UNIVERSITY OF CALIFORNIA

Los Angeles

Multibody Dynamics, Control-Oriented Model, and 6-DOF Motion Control of a Thrust-Vectored Quadrotor

A thesis submitted in partial satisfaction
of the requirements for the degree
Master of Science in Mechanical Engineering

by

Tyler Austin McCown

2021

ABSTRACT OF THE THESIS

Multibody Dynamics, Control-Oriented Model, and 6-DOF Motion Control of a Thrust-Vectored Quadrotor

by

Tyler Austin McCown

Master of Science in Mechanical Engineering
University of California, Los Angeles, 2021
Professor Tsu-Chin Tsao, Chair

Traditional quadcopters possess only four controllable inputs and are inherently under-actuated, limiting their ability to interact with an environment or manipulate a payload. This work discusses a quadcopter architecture incorporating twisting and tilting joints to fully decouple the position and attitude dynamics, permitting full six-degree-of-freedom maneuvering. A dynamic model is presented which includes both the gyroscopic effects of the propellers and the configuration-dependent inertia of the articulated components. A control framework is developed first for a quarter copter model, then generalized to the full copter on a spherical joint, and finally to the full copter with unconstrained base motion on the special Euclidean group SE(3). Simulations are conducted on a Simscape multibody model, and the results are presented to demonstrate the capabilities of the craft.

The thesis of Tyler Austin McCown is approved.

Tetsuya Iwasaki

Robert Thomas M'Closkey

Tsu-Chin Tsao, Committee Chair

University of California, Los Angeles

2021

To my family,

Thank you

For your infinite love and support.

Contents

List of Symbols viii

List of Figures xiii

Acknowledgements xiv

1 Introduction 1

2 Twist-Tilt Copter Architecture 4

2.1 Body and Frame Definitions 4

2.1.1 Base Link 5

2.1.2 Arm Subsystems 7

2.2 Mass Properties 10

2.3 End-Effector Kinetics 11

2.4 Rigid Body Dynamics Model 12

3 Quarter Copter 16

3.1 Decoupled SISO Control 16

3.1.1 Simplified Models 17

3.1.2 Control Design 18

3.2 Lagrange Formulation 27

3.2.1 Arc Energy 28

3.2.2 Shaft Energy 29

3.2.3 Propeller Energy 31

3.2.4 Generalized Forces . . . 33
3.2.5 Equations of Motion . . . 36
3.2.6 Sample Trajectory . . . 39
3.3 Centralized MIMO Control . . . 41

4 Full Copter with Base Rotation **45**
4.1 Full Copter Lagrangian . . . 46
4.2 Base Energy . . . 47
4.3 Arm Energy . . . 49
4.3.1 Arc . . . 50
4.3.2 Shaft . . . 53
4.3.3 Propeller . . . 56
4.4 Generalized Forces . . . 58
4.5 Roll-Axis Arms . . . 60
4.5.1 Arm 1 Energy . . . 61
4.5.2 Arm 3 Energy . . . 65
4.5.3 Generalized Forces . . . 68
4.6 Pitch-Axis Arms . . . 69
4.6.1 Arm 2 Energy . . . 70
4.6.2 Arm 4 Energy . . . 73
4.6.3 Generalized Forces . . . 76
4.7 Equations of Motion . . . 78
4.7.1 Inertia Matrix . . . 78
4.7.2 Coupling Matrix . . . 82
4.7.3 Vector Terms . . . 85
4.8 Sample Trajectory . . . 92
4.9 Hierarchical Control . . . 95

5 Full Copter 6-DOF **104**

5.1 Base Translation 104
5.1.1 Effects on Arm Energy 105
5.1.2 Generalized Forces 107
5.2 Equations of Motion 108
5.3 6-DOF Tracking Control 109
5.3.1 On-point Rotation 112
5.3.2 Level Flight 119

6 Conclusion **122**

A Simulation Parameters **128**

References **132**

List of Symbols

α	Twist angle; rotation angle between base frame and arc frame
β	Tilt angle; rotation angle between arc frame and shaft frame
γ	Rotation angle between shaft frame and propeller frame
i	Indexing variable corresponding to an arm subsystem
$\mathcal{N}$	Inertial fixed frame
$\mathcal{O}$	Origin of inertial fixed frame
$\hat{\boldsymbol{n}}$	Unit vector for inertial frame
$\mathcal{B}$	Rotating frame attached to the base link, or origin of such frame
$\hat{\boldsymbol{b}}$	Unit vector for base frames
$\boldsymbol{p}$	Base link position vector
ψ	Yaw angle of base link
θ	Pitch angle of base link
φ	Roll angle of base link
$\boldsymbol{R}_{F_1F_2}$	Direction cosine matrix relating frames F_1 and F_2
$\mathcal{A}$	Rotating frame attached to an arc, or origin of such frame
$\hat{\boldsymbol{a}}$	Unit vector for arc frames
$\mathcal{S}$	Rotating frame attached to a shaft, or origin of such frame
$\hat{\boldsymbol{s}}$	Unit vector for shaft frames
$\mathcal{P}$	Rotating frame attached to a propeller, or origin of such frame
$\hat{\boldsymbol{p}}$	Unit vector for propeller frames
ℓ_B	Length dimension describing the position of the center of mass of body B
m_B	Mass of body B
$\boldsymbol{I}_B$	Inertia matrix of body B reflected in the body's rotating frame
$\bar{\boldsymbol{F}}$	Propeller thrust force vector
$\bar{\boldsymbol{\tau}}$	Propeller drag-induced torque vector
c_p	Propeller thrust coefficient
c_t	Propeller drag torque coefficient

$\boldsymbol{r}^{P^1/P^2}$	Position vector for point P^1 relative to point P^2
$\boldsymbol{v}^{PF}$	Velocity vector for point P as seen in frame F
$\boldsymbol{a}^{PF}$	Acceleration vector for point P as seen in frame F
g_0	Standard gravitational acceleration (positive scalar)
$\boldsymbol{g}$	Vector of gravitational torques
$\boldsymbol{\omega}^{F_1F_2}$	Angular velocity vector of frame F_1 with respect to frame F_2
$\boldsymbol{q}$	Vector of generalized coordinates
$\boldsymbol{q}_d$	Desired trajectory of generalized coordinates
$\boldsymbol{u}$	Control wrench on the base link
$\boldsymbol{E}$	Identity matrix
τ_μ	Motor torque applied by motor μ
n	Scalar nonlinearities in equations of motion
$\boldsymbol{K}$	Controller gain matrix
k	Scalar control gain
$\boldsymbol{e}$	Error state vector
P	Plant model
$\boldsymbol{Q}$	State weighting matrix for LQR
$\boldsymbol{R}$	Input weighting matrix for LQR
T	Kinetic energy
U	Potential energy
$\mathcal{L}$	Lagrangian
ξ	Generalized force
$\boldsymbol{\sigma}_B$	Torque associated with the gyroscopic precession of body B
$\boldsymbol{M}$	Inertia matrix in Euler-Lagrange equations
$\boldsymbol{C}$	Velocity coupling matrix in Euler-Lagrange equations
$\boldsymbol{f}$	Vector of thrust-induced torques
$\boldsymbol{d}$	Vector of drag-induced torques
$\boldsymbol{\tau}$	Vector of motor input torques

$\boldsymbol{N}$	Vector nonlinearities in equations of motion
$\dot{\Psi}$	Generalized yaw rate of the base link
$\dot{\Theta}$	Generalized pitch rate of the base link
$\dot{\Phi}$	Generalized roll rate of the base link
$\mathfrak{A}$	Full arm composed of an arc, a shaft, and a propeller
$\boldsymbol{\tau}_{\mathcal{B}}$	Commanded torque about the base link
$\boldsymbol{\Xi}$	Commanded forces on the base link
$\boldsymbol{W}$	Weight force vector in the inertial frame
$\boldsymbol{e}_i$	Integrated error state vector

List of Figures

2.1 Twist-tilt copter 5

2.2 Base link rotation sequence 7

2.3 Arm rotation sequence 8

2.4 Rigid body hierarchical control model 12

3.1 Block diagram for the simplified propeller dynamics with P control . . . 19

3.2 Block diagram for the simplified tilt dynamics with PD control 20

3.3 Block diagram for the simplified twist dynamics with PD control 21

3.4 Nominal step response for SISO propeller speed controller 22

3.5 Nominal step response for SISO tilt angle controller 23

3.6 Nominal step response for SISO twist angle controller 24

3.7 Simulated tracking performance with three independent SISO controllers on the quarter copter model 26

3.8 Sample trajectory for validation of the coupled equations of motion for the quarter copter model 40

3.9 Torque calculation with coupled equations of motion for the quarter copter model 40

3.10 Simulated tracking performance with the centralized MIMO controller on the quarter copter 43

3.11 Commanded motor torques for trajectory tracking with the MIMO controller on the quarter copter 43

4.1 Sample trajectory for validation of the coupled equations of motion for the full copter with base rotation . . . 93
4.2 Base link torque calculation with coupled equations of motion for the full copter with base rotation . . . 93
4.3 Arm motor torque calculation with coupled equations of motion for the full copter with base rotation . . . 94
4.4 Adapted hierarchical control model for full copter attitude control . . . 97
4.5 Simulated tracking performance of the rotating base link for a yaw-pitch attitude trajectory . . . 98
4.6 Simulated tracking performance of the arm motors for a yaw-pitch attitude trajectory . . . 99
4.7 Simulated tracking performance of the rotating base link for a yaw-roll attitude trajectory . . . 101
4.8 Simulated tracking performance of the arm motors for a yaw-roll attitude trajectory . . . 102

5.1 Block diagram for the position dynamics with LQI control . . . 110
5.2 Hierarchical control model for full copter 6-DOF control . . . 111
5.3 Simulated tracking performance of the base attitude for a 6-DOF yaw-pitch trajectory . . . 113
5.4 Simulated tracking performance of the base position for a 6-DOF yaw-pitch trajectory . . . 114
5.5 Simulated tracking performance of the arm motors for a 6-DOF yaw-pitch trajectory . . . 115
5.6 Simulated tracking performance of the base attitude for a 6-DOF yaw-roll trajectory . . . 116
5.7 Simulated tracking performance of the base position for a 6-DOF yaw-roll trajectory . . . 117

5.8 Simulated tracking performance of the arm motors for a 6-DOF yaw-roll trajectory 118
5.9 Simulated tracking performance of the base position on a 6-DOF level-flight trajectory 119
5.10 Simulated tracking performance of the base attitude on a 6-DOF level-flight trajectory 120
5.11 Simulated tracking performance of the arm motors on a 6-DOF level-flight trajectory 121

Acknowledgements

My deepest gratitude goes to my advisor, Dr. Tsu-Chin Tsao. Thank you for all of your guidance and support of my goals, both academic and professional. And to my mentor, Dr. Matthew J. Gerber. From my undergraduate design work to my master's thesis, your experience and insight has been an invaluable resource.

I would also like to thank Abdulaziz Alawadhi, Omar Curiel, and the whole quadcopter group in the Mechatronics and Controls Lab. No success occurs in isolation, and my achievements are built upon the years of dedicated work from those who came before me.

Finally, I offer my sincerest appreciation to Dr. Robert T. M'Closkey, Dr. Dennis Dongjoon Kim, Dr. Tetsuya "teD" Iwasaki, Dr. Joshua W. Clemens, and the many other outstanding faculty who have guided me throughout my time at UCLA. Your expertise is truly inspiring, and your profound perspectives have changed the way that I see the world. It has been an honor to study under you.

Chapter 1

Introduction

Multirotor aircraft, and in particular quadcopters, have risen to prominence over the past several years due to their mechanical simplicity and high maneuverability. Advances in low-cost inertial sensors and flight controllers have made multirotor platforms more accessible to both hobbyists as well as researchers, resulting in accelerated development for a variety applications. Among these are geological surveying, infrastructure inspection, and disaster response, all situations in which a nimble craft can navigate an open environment and provide visual information to a human operator [1]. A major shortcoming of typical quadrotor systems is their inherent underactuation; the presence of only four controllable inputs prevents arbitary maneuvering in 3D space, limiting utility in tasks such as object manipulation and environmental interaction.

Many multirotor platforms exist which expand upon the capabilities of the standard quadcopter by including additional controllable degrees of freedom. One common method that preserves mechanical simplicity is to increase the number of rotors to six or more [2], [3], [4]. Simply possessing six rotors does not guarantee full actuation due to redundancy in parallel thrusts, and some groups have conducted design optimizations to study the trade-offs between efficiency and agility of various actuator configurations [5], [6], [7], [8]. Despite the optimization, these architectures all involve conflicting thrust components which lead to internal forces and wasted control energy.

Another class of multirotor crafts solves the underactuation problem by replacing each

rotor with a traditional quadcopter. Early implementations connected these copters to a base link by flexible cables as in [9], or by spherical joints as in [10]. An improvement on these attachment mechanisms is shown in [11], which utilizes an in-line revolute joint to eliminate angle limitations between the individual copters and the base. One challenge associated with these configurations is their distributed nature; each copter includes on-board sensors and compute modules, but must communicate synchronously with a centralized controller to coordinate with the other copters.

More variants of fully and overactuated craft introduce controllable degrees of freedom between the base link and the propeller motors. [12] and [13] approach this by separating the main body from the thruster component with a gimbal-like mechanism between the two. This allows six-degree-of-freedom (6-DOF) control of the main body, but with limited range of motion due to the joint construction. Another approach is to add a single degree of articulation to each propeller as in [14], [15], [16]. These designs achieve overactuation while also allowing internal forces to be reduced by reorienting thrust vectors to minimize conflicting components.

This work concerns the articulated-rotor type craft first proposed in [17], a variant of quadcopter with includes two controllable degrees of freedom at each of the four propellers. The resulting gimbal-like mechanism allows each propeller to assume an arbitrary orientation relative to the base link as well as to the other propellers. This craft is fully actuated and can hover with all parallel thrust vectors in any body orientation, maximizing thrust efficiency. Chapter 2 discusses the architecture of this copter in more detail and describes previous work related to its control under a rigid body assumption. A detailed set of coupled equations of motion is derived in Chapter 3 for one of the articulated arms in isolation (the "quarter copter"). An accompanying control law is presented for comparison with the rigid body results. Chapter 4 generalizes the quarter copter model to the full copter with the base link constrained on a spherical joint, presenting equations of motion and a modified control architecture. Finally Chapter 5 removes the spherical joint constraint and presents the final equations of motion for the full copter

with a rotating and translating base link. The resulting controller is capable of tracking an arbitrary trajectory on the special Euclidean group SE(3). The work is concluded in Chapter 6.

Chapter 2

Twist-Tilt Copter Architecture

2.1 Body and Frame Definitions

The copter discussed in this work is the twist-tilt quadrotor introduced by Gerber and Tsao in [17] and shown in Fig. 2.1. It is composed of four identical subsystems, referred to as arms, connected to a rigid base through revolute joints. Each arm includes three more rigid bodies, referred to as the arc, shaft, and propeller. These bodies are connected in a serial fashion through revolute joints so that each arm i can be modeled as an open kinematic chain, with the joint between the base and the arc referred to as the "twist" angle and denoted α_i, the joint between the arc and the shaft referred to as the "tilt" angle and denoted β_i, and the propeller angle denoted γ_i, where $i \in \{1, \ldots, 4\}$. The defining feature of this architecture is that the configuration space of each arm is three-dimensional, permitting each thrust vector to achieve arbitrary magnitude and direction independent of the overall copter configuration and therefore independent of the other arms. The copter thus has 12 independent controllable inputs, fully decoupling the attitude and position dynamics to achieve arbitrary 6-DOF control while retaining a six-dimensional configuration nullspace for optimization.

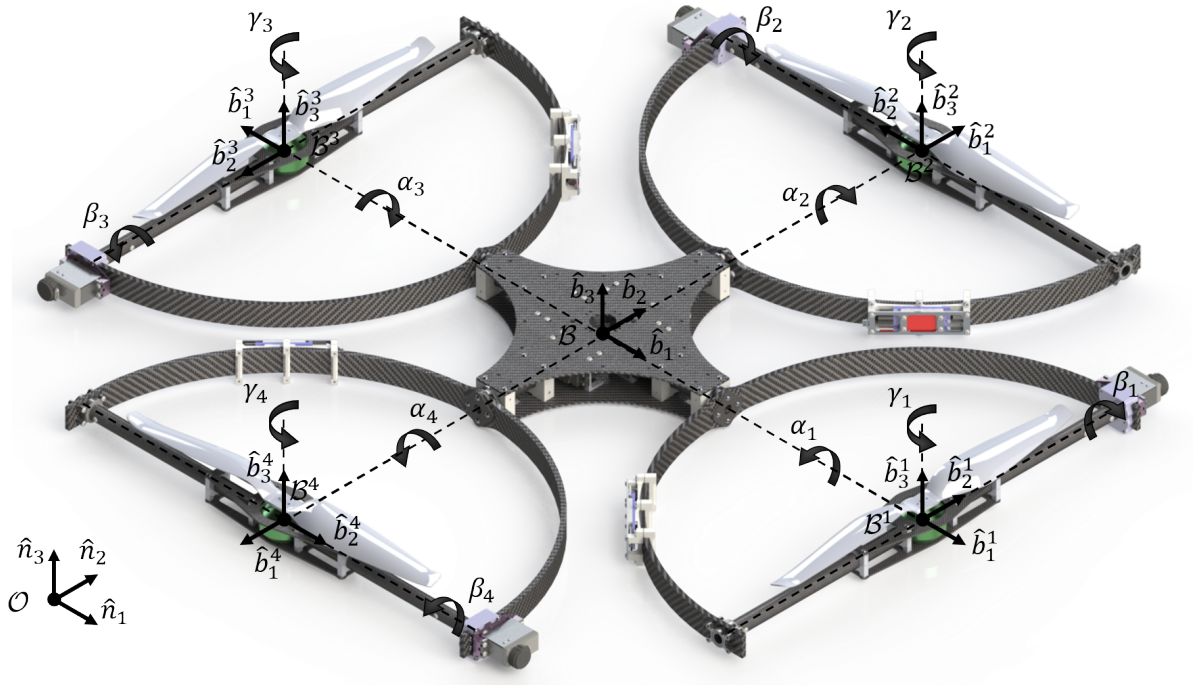

Figure 2.1: The full twist-tilt copter, composed of four identical arms connected to a base link. Each arm has three controllable inputs $\{\alpha_i, \beta_i, \gamma_i\}$ for a total of 12 internal degrees of freedom.

2.1.1 Base Link

Coordinate frames will be denoted throughout this work by capital script letters. The unit vectors associated with a given frame will be denoted by the same letter as the frame in non-script lower case, with a subscript index such that the axis order 1-2-3 forms a right-handed system. Axes are denoted by the same capital script letter as the frame with a subscript index to match the corresponding unit vector.

An inertial fixed frame $\mathcal{N} = \left(\mathcal{O}, \{\hat{\boldsymbol{n}}_1, \hat{\boldsymbol{n}}_2, \hat{\boldsymbol{n}}_3\}\right)$ is defined with the origin $\mathcal{O}$ acting as the reference point for all motion. The $\mathcal{N}_3$ axis is antiparallel to standard gravity so that the $\mathcal{N}_1\mathcal{N}_2$ plane defines the horizontal. A rotating body frame $\mathcal{B} = \left(\mathcal{B}, \{\hat{\boldsymbol{b}}_1, \hat{\boldsymbol{b}}_2, \hat{\boldsymbol{b}}_3\}\right)$ is defined with the origin at the intersection of all four twist axes. The first two unit vectors $\hat{\boldsymbol{b}}_1$ and $\hat{\boldsymbol{b}}_2$ are colinear with the twist axes of the first two arcs, and $\hat{\boldsymbol{b}}_3$ completes a right-handed coordinate system. The position of base origin $\mathcal{B}$ with respect to the inertial origin $\mathcal{O}$ is denoted by

$$\boldsymbol{p} = x\,\hat{\boldsymbol{n}}_1 + y\,\hat{\boldsymbol{n}}_2 + z\,\hat{\boldsymbol{n}}_3. \tag{2.1}$$

A Z-Y-X (yaw-pitch-roll) Tait-Bryan angle sequence is used to describe the mapping from the $\mathcal{N}$ frame to the $\mathcal{B}$ frame. The sequence of elemental rotations is depicted in Fig. 2.2 and includes two intermediate frames, $\mathcal{B}' = \left(\mathcal{B}, \{\hat{\boldsymbol{b}}'_1, \hat{\boldsymbol{b}}'_2, \hat{\boldsymbol{b}}'_3\}\right)$ and $\mathcal{B}'' = \left(\mathcal{B}, \{\hat{\boldsymbol{b}}''_1, \hat{\boldsymbol{b}}''_2, \hat{\boldsymbol{b}}''_3\}\right)$. The yaw angle is denoted ψ and describes an elemental rotation about $\hat{\boldsymbol{n}}_3$, resulting in the $\mathcal{B}'$ frame. The pitch angle is denoted θ and describes an elemental rotation about $\hat{\boldsymbol{b}}'_2$, resulting in the $\mathcal{B}''$ frame. Finally, the roll angle is denoted φ and describes an elemental rotation about $\hat{\boldsymbol{b}}''_1$, resulting in the $\mathcal{B}$ frame. These elemental rotations can be represented with the following direction cosine matrices (DCM)

$$\begin{bmatrix}\hat{\boldsymbol{n}}_1 & \hat{\boldsymbol{n}}_2 & \hat{\boldsymbol{n}}_3\end{bmatrix} = \underbrace{\begin{bmatrix} c_\psi & -s_\psi & 0 \\ s_\psi & c_\psi & 0 \\ 0 & 0 & 1 \end{bmatrix}}_{\boldsymbol{R}_{\mathcal{N}\mathcal{B}'}} \begin{bmatrix}\hat{\boldsymbol{b}}'_1 & \hat{\boldsymbol{b}}'_2 & \hat{\boldsymbol{b}}'_3\end{bmatrix}, \tag{2.2}$$

$$\begin{bmatrix}\hat{\boldsymbol{b}}'_1 & \hat{\boldsymbol{b}}'_2 & \hat{\boldsymbol{b}}'_3\end{bmatrix} = \underbrace{\begin{bmatrix} c_\theta & 0 & s_\theta \\ 0 & 1 & 0 \\ -s_\theta & 0 & c_\theta \end{bmatrix}}_{\boldsymbol{R}_{\mathcal{B}'\mathcal{B}''}} \begin{bmatrix}\hat{\boldsymbol{b}}''_1 & \hat{\boldsymbol{b}}''_2 & \hat{\boldsymbol{b}}''_3\end{bmatrix}, \tag{2.3}$$

$$\begin{bmatrix}\hat{\boldsymbol{b}}''_1 & \hat{\boldsymbol{b}}''_2 & \hat{\boldsymbol{b}}''_3\end{bmatrix} = \underbrace{\begin{bmatrix} 1 & 0 & 0 \\ 0 & c_\varphi & -s_\varphi \\ 0 & s_\varphi & c_\varphi \end{bmatrix}}_{\boldsymbol{R}_{\mathcal{B}''\mathcal{B}}} \begin{bmatrix}\hat{\boldsymbol{b}}_1 & \hat{\boldsymbol{b}}_2 & \hat{\boldsymbol{b}}_3\end{bmatrix}, \tag{2.4}$$

where sine and cosine have been abbreviated for concise notation. The overall rotation matrix relating the $\mathcal{N}$ frame to the $\mathcal{B}$ frame is found by successive multiplication of the elemental rotations

$$\boldsymbol{R}_{\mathcal{N}\mathcal{B}} = \boldsymbol{R}_{\mathcal{N}\mathcal{B}'}\boldsymbol{R}_{\mathcal{B}'\mathcal{B}''}\boldsymbol{R}_{\mathcal{B}''\mathcal{B}} = \begin{bmatrix} c_\psi c_\theta & c_\psi s_\theta s_\varphi - s_\psi c_\varphi & c_\psi s_\theta c_\varphi + s_\psi s_\varphi \\ s_\psi c_\theta & s_\psi s_\theta s_\varphi + c_\psi c_\varphi & s_\psi s_\theta c_\varphi - c_\psi s_\varphi \\ -s_\theta & c_\theta s_\varphi & c_\theta c_\varphi \end{bmatrix}. \tag{2.5}$$

Four more rotating frames $\mathcal{B}^i = \left(\mathcal{B}^i, \{\hat{\boldsymbol{b}}^i_1, \hat{\boldsymbol{b}}^i_2, \hat{\boldsymbol{b}}^i_3\}\right)$ are defined for notational convenience. The origin of $\mathcal{B}^i$ lies at the intersection of twist axis α_i and tilt axis β_i, the $\hat{\boldsymbol{b}}^i_1$ unit vector is colinear with twist axis α_i, the $\hat{\boldsymbol{b}}^i_3$ unit vector is parallel to $\hat{\boldsymbol{b}}_3$, and the

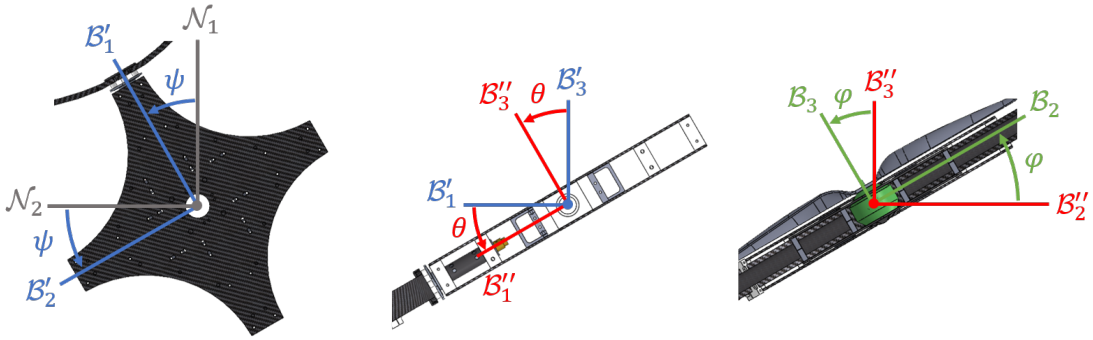

(a) Yaw angle ψ. (b) Pitch angle θ. (c) Roll angle φ.

Figure 2.2: Tait-Bryan angle sequence describing the rotation of the $\mathcal{B}$ frame with respect to the $\mathcal{N}$ frame. The sequence proceeds through two intermediate frames, $\mathcal{B}'$ and $\mathcal{B}''$, both of which are centered at $\mathcal{B}$. The $\mathcal{B}'$ frame is generated by a rotation of ψ about the $\mathcal{N}_3$ axis, the $\mathcal{B}''$ frame is generated by a rotation of θ about the $\mathcal{B}'_2$ axis, and the $\mathcal{B}$ frame is generated by a rotation of φ about the $\mathcal{B}''_1$ axis.

$\hat{\boldsymbol{b}}_2^i$ unit vector completes a right-handed coordinate system. This allows each arm to be described identically by writing its dynamics in frame $\mathcal{B}^i$, which is just an elemental rotation of the base frame $\mathcal{B}$ about $\hat{\boldsymbol{b}}_3$ by $(i-1)\frac{\pi}{2}$. The DCM $\boldsymbol{R}_{\mathcal{B}\mathcal{B}^i}$ relating the $\mathcal{B}$ frame to the $\mathcal{B}^i$ frame is given by

$$\begin{bmatrix}\hat{\boldsymbol{b}}_1 & \hat{\boldsymbol{b}}_2 & \hat{\boldsymbol{b}}_3\end{bmatrix} = \underbrace{\begin{bmatrix}\cos\frac{\pi}{2} & -\sin\frac{\pi}{2} & 0\\ \sin\frac{\pi}{2} & \cos\frac{\pi}{2} & 0\\ 0 & 0 & 1\end{bmatrix}^{(i-1)}}_{\boldsymbol{R}_{\mathcal{B}\mathcal{B}^i}} \begin{bmatrix}\hat{\boldsymbol{b}}_1^i & \hat{\boldsymbol{b}}_2^i & \hat{\boldsymbol{b}}_3^i\end{bmatrix}, \tag{2.6}$$

and will be abbreviated as $\boldsymbol{R}_i$ where

$$\boldsymbol{R}_1 = \begin{bmatrix}1 & 0 & 0\\ 0 & 1 & 0\\ 0 & 0 & 1\end{bmatrix}, \quad \boldsymbol{R}_2 = \begin{bmatrix}0 & -1 & 0\\ 1 & 0 & 0\\ 0 & 0 & 1\end{bmatrix}, \quad \boldsymbol{R}_3 = \begin{bmatrix}-1 & 0 & 0\\ 0 & -1 & 0\\ 0 & 0 & 1\end{bmatrix}, \quad \boldsymbol{R}_4 = \begin{bmatrix}0 & 1 & 0\\ -1 & 0 & 0\\ 0 & 0 & 1\end{bmatrix}.$$

Note that the $\mathcal{B}^i$ frames rotate with the base link but not with the twist/tilt angles.

2.1.2 Arm Subsystems

The 3-dimensional configuration space for the arm subsystems is described by the Tait-Bryan angle sequence shown in Fig. 2.3. The description for arm i as seen in frame $\mathcal{B}^i$

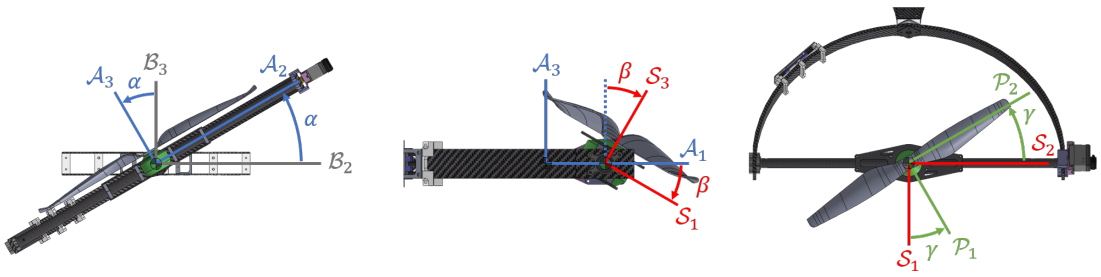

(a) Twist angle α. (b) Tilt angle β. (c) Propeller angle γ.

Figure 2.3: Tait-Bryan angle sequence describing the rotation of the $\mathcal{P}^i$ frame with respect to the $\mathcal{B}^i$ frame. Arm indices have been omitted in the figure for simplicity. The sequence proceeds through two intermediate frames, $\mathcal{A}$ and $\mathcal{S}$, which are rotating frames attached to the arc and shaft bodies at the respective centers of mass.

is identical for all $i \in \{1, \ldots, 4\}$, thus the notation can be introduced without index and then applied to any arm.

The rotation sequence proceeds through three rotating frames which are attached to the three rigid bodies in the arm subsystem. First, an arc frame $\mathcal{A} = \left(\mathcal{A}, \{\hat{\boldsymbol{a}}_1, \hat{\boldsymbol{a}}_2, \hat{\boldsymbol{a}}_3\}\right)$ is defined with origin at the center of mass of the arc, assumed to lie at a fixed distance $\ell_{\mathcal{A}}$ along the twist axis with respect to the base link origin. The $\hat{\boldsymbol{a}}_1$ unit vector is colinear with the twist axis, the $\hat{\boldsymbol{a}}_2$ unit vector rotates to stay parallel with the shaft, and the $\hat{\boldsymbol{a}}_3$ unit vector completes a right-handed coordinate system. The twist angle α is then the angle between the $\mathcal{B}_2$ and $\mathcal{A}_2$ axes, or between the $\mathcal{B}_3$ and $\mathcal{A}_3$ axes. Fig. 2.3a shows a detailed view of the twist angle, and Fig. 2.3b shows the location of the $\mathcal{A}$ origin along the twist axis. The DCM relating the $\mathcal{B}$ frame and the $\mathcal{A}$ frame is given by

$$\begin{bmatrix} \hat{\boldsymbol{b}}_1 & \hat{\boldsymbol{b}}_2 & \hat{\boldsymbol{b}}_3 \end{bmatrix} = \underbrace{\begin{bmatrix} 1 & 0 & 0 \\ 0 & c_\alpha & -s_\alpha \\ 0 & s_\alpha & c_\alpha \end{bmatrix}}_{\boldsymbol{R}_{\mathcal{B}\mathcal{A}}} \begin{bmatrix} \hat{\boldsymbol{a}}_1 & \hat{\boldsymbol{a}}_2 & \hat{\boldsymbol{a}}_3 \end{bmatrix}. \tag{2.7}$$

Next, a shaft frame $\mathcal{S} = \left(\mathcal{S}, \{\hat{\boldsymbol{s}}_1, \hat{\boldsymbol{s}}_2, \hat{\boldsymbol{s}}_3\}\right)$ is defined with origin at the center of mass of the shaft, assumed to lie at the intersection of the twist and tilt axes, which is a fixed distance $\ell_{\mathcal{S}}$ along the twist axis with respect to the base link origin. The $\hat{\boldsymbol{s}}_1$ unit vector is colinear with the twist axis, the $\hat{\boldsymbol{s}}_2$ unit vector is colinear with the tilt axis, and the $\hat{\boldsymbol{s}}_3$ unit vector completes a right-handed coordinate frame. The tilt angle β is the angle

between the $\mathcal{A}_1$ and $\mathcal{S}_1$ axes, or between the $\mathcal{A}_3$ and $\mathcal{S}_3$ axes. Fig. 2.3b shows a detailed view of the tilt angle, and Fig. 2.3c shows the location of the $\mathcal{S}$ origin at the intersection of all three motor axes. The DCM relating the $\mathcal{A}$ frame to the $\mathcal{S}$ frame is given by

$$\begin{bmatrix} \hat{\boldsymbol{a}}_1 & \hat{\boldsymbol{a}}_2 & \hat{\boldsymbol{a}}_3 \end{bmatrix} = \underbrace{\begin{bmatrix} c_\beta & 0 & s_\beta \\ 0 & 1 & 0 \\ -s_\beta & 0 & c_\beta \end{bmatrix}}_{\boldsymbol{R}_{\mathcal{AS}}} \begin{bmatrix} \hat{\boldsymbol{s}}_1 & \hat{\boldsymbol{s}}_2 & \hat{\boldsymbol{s}}_3 \end{bmatrix}. \tag{2.8}$$

Finally, a propeller frame $\mathcal{P} = \left(\mathcal{P}, \{\hat{\boldsymbol{p}}_1, \hat{\boldsymbol{p}}_2, \hat{\boldsymbol{p}}_3\}\right)$ is defined with origin at the center of mass of the propeller, assumed to lie at a fixed distance $\ell_{\mathcal{P}}$ along the propeller axis with respect to the $\mathcal{S}$ origin. The $\hat{\boldsymbol{p}}_3$ unit vector is colinear with the propeller axis. The remaining two unit vectors $\hat{\boldsymbol{p}}_1$ and $\hat{\boldsymbol{p}}_2$ complete a right-handed coordinate system such that γ is the angle between the $\mathcal{S}_1$ and $\mathcal{P}_1$ axes, or between the $\mathcal{S}_2$ and $\mathcal{P}_2$ axes, however the propeller angle is not of interest for defining the arm dynamics. The propeller kinetics discussed in Section 2.3 and the equations of motion developed in Chapter 3 are both written in terms of angular velocity rather than angular position, and thus the propeller's configuration is better described by $\dot{\gamma}$. The DCM relating the $\mathcal{S}$ frame to the $\mathcal{P}$ frame is given by

$$\begin{bmatrix} \hat{\boldsymbol{s}}_1 & \hat{\boldsymbol{s}}_2 & \hat{\boldsymbol{s}}_3 \end{bmatrix} = \underbrace{\begin{bmatrix} c_\gamma & -s_\gamma & 0 \\ s_\gamma & c_\gamma & 0 \\ 0 & 0 & 1 \end{bmatrix}}_{\boldsymbol{R}_{\mathcal{SP}}} \begin{bmatrix} \hat{\boldsymbol{p}}_1 & \hat{\boldsymbol{p}}_2 & \hat{\boldsymbol{p}}_3 \end{bmatrix}. \tag{2.9}$$

Embedded in these frame definitions are assumptions about the mass properties of the three rigid bodies comprising an arm; each body is assumed to have a mass distribution which is symmetric about its relevant axes of rotation. These modeling choices are reflected on the real system, where components have been designed with the foresight that mass symmetry leads to great simplifications in the dynamics. From an energy standpoint, a fixed center of mass means that there is no translational contribution to kinetic energy, reducing the complexity of the resulting Lagrange equations. From a kinematics standpoint, a fixed center of mass implies zero linear acceleration and generates a constraint on the kinetics rather than an additional equation of motion. The twist-tilt

copter is designed to leverage these desirable traits, and thus the assumptions about mass symmetry are considered safe.

All definitions in this section were made without a frame index due to the fourth order rotational symmetry of the copter. Chapter 3 will use these definitions to implicitly describe the motion of arm 1, and Chapter 4 will then explicitly generalize the dynamics to the other three arms.

2.2 Mass Properties

Masses and inertia matrices will be denoted throughout this work by m and $\boldsymbol{I}$, respectively, with a subscript to denote the relevant rigid body. Inertia matrices are understood to be reflected in the rotating frame attached to the relevant body. As a consequence of the assumptions made in Section 2.1.2 regarding the placement of the mass centers and the symmetry of mass distributions, all inertia matrices are diagonal and described with only three parameters.

Following these notations, the mass of the base link is denoted $m_{\mathcal{B}}$, and the inertia reflected in the $\mathcal{B}$ frame is

$$\boldsymbol{I}_{\mathcal{B}} = \operatorname{diag}\left(I^x_{\mathcal{B}},\, I^y_{\mathcal{B}},\, I^z_{\mathcal{B}}\right), \tag{2.10}$$

where the superscript x, y, or z indicates the inertia about axis $\mathcal{B}_1$, $\mathcal{B}_2$, or $\mathcal{B}_3$, respectively.[1] Similarly, the mass of each arc is denoted $m_{\mathcal{A}}$, and the inertia of arc i reflected in the $\mathcal{A}^i$ frame is

$$\boldsymbol{I}_{\mathcal{A}} = \operatorname{diag}\left(I^x_{\mathcal{A}},\, I^y_{\mathcal{A}},\, I^z_{\mathcal{A}}\right), \tag{2.11}$$

where the superscript x, y, or z indicates the inertia about axis $\mathcal{A}^i_1$, $\mathcal{A}^i_2$, or $\mathcal{A}^i_3$, respectively. Note that no index is necessary on either the mass or the inertia since all arcs are identical with respect to their rotating frames.

The masses of the shafts and propellers are defined analogously as $m_{\mathcal{S}}$ and $m_{\mathcal{P}}$. The

[1] The use of superscript letters rather than numbers is intended to avoid confusion with the common notation for the first, second, and third principal moments of inertia, which do not necessarily correspond to the ordering of elements shown here.

inertia of shaft i reflected in the $\mathcal{S}^i$ frame is

$$\boldsymbol{I}_{\mathcal{S}} = \mathrm{diag}\left(I^x_{\mathcal{S}},\, I^y_{\mathcal{S}},\, I^z_{\mathcal{S}}\right), \tag{2.12}$$

and the inertia of propeller i reflected in the $\mathcal{P}^i$ frame is

$$\boldsymbol{I}_{\mathcal{P}} = \mathrm{diag}\left(I^x_{\mathcal{P}},\, I^y_{\mathcal{P}},\, I^z_{\mathcal{P}}\right). \tag{2.13}$$

2.3 End-Effector Kinetics

In modeling the arm subsystems as open kinematic chains it is natural to regard the propellers as end-effectors which interact with the surrounding atmosphere. Motion of a propeller results in application of a thrust force $\bar{\boldsymbol{F}}$ and a drag torque $\bar{\boldsymbol{\tau}}$ on the propeller by the environment. The bar notation is used to indicate kinetics which originate from external sources rather than from within the copter. The thrust generated by propeller i is modeled by

$$\bar{\boldsymbol{F}}_i = c_p \dot{\gamma}_i^2\, \hat{\boldsymbol{p}}_3^i, \tag{2.14}$$

where c_p is a positive-definite constant relating the angular velocity of the propeller to the generated thrust. The drag torque experienced by propeller i is similarly modeled by

$$\bar{\boldsymbol{\tau}}_i = (-1)^i c_t \dot{\gamma}_i^2\, \hat{\boldsymbol{p}}_3^i, \tag{2.15}$$

where c_t is another positive-definite constant relating the angular velocity of the propeller to the induced drag torque. The factor $(-1)^i$ is included to account for the spinning direction of the propeller, which alternates between arms to cancel internal yawing moments.

The wrench formed by the combined thrust force and drag torque is assumed to be applied at the center of mass of the corresponding propeller, which lies at a fixed location on the $\mathcal{S}_3^i$ axis.

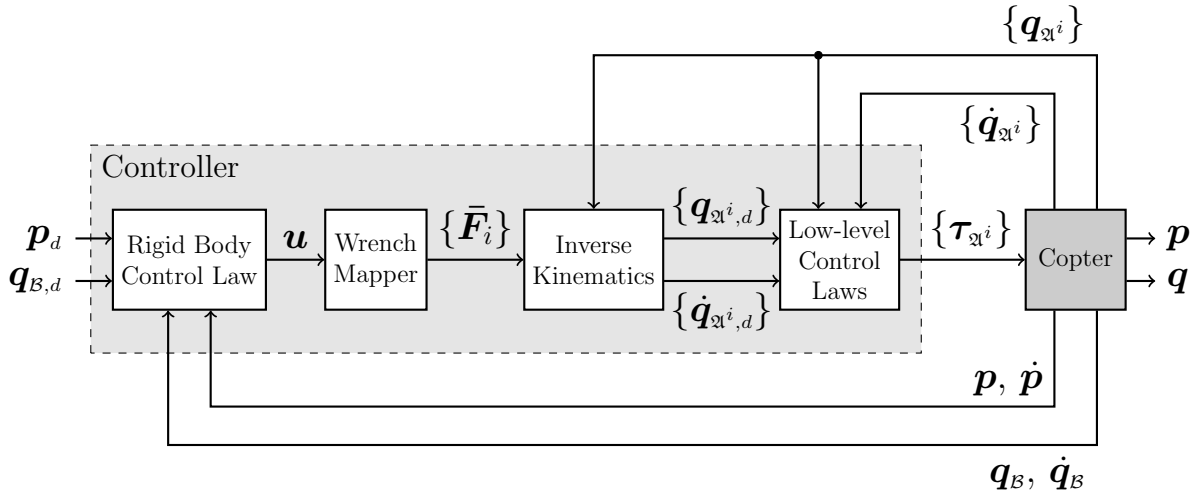

Figure 2.4: Hierarchical control model for the twist-tilt copter proposed in [17]. The trajectory specifies the desired 3-DOF position and 3-DOF attitude of the base link. A high-level control law based on a rigid body model generates an overall 6-DOF control wrench for trajectory tracking. A least-norms mapper and inverse kinematics scheme converts the rigid body wrench into reference commands for the 12 controllable inputs, which are then tracked with decoupled low-level controllers.

2.4 Rigid Body Dynamics Model

Previously, Gerber and Tsao proposed the hierarchical control model shown in Fig. 2.4. The copter is modeled as a rigid body with mass m and constant inertia $\boldsymbol{I}$. The translational dynamics under these assumptions are

$$m\boldsymbol{a}^{\mathcal{B}/\mathcal{O}} = -mg_0\,\hat{\boldsymbol{n}}_3 + \sum_{i=1}^{4} \bar{\boldsymbol{F}}_i \tag{2.16}$$

where $\boldsymbol{a}^{\mathcal{B}/\mathcal{O}}$ is the linear acceleration of the base link with respect to the origin, and g_0 is the standard gravitational acceleration, assumed positive for convention. The rotational dynamics are given by

$$\boldsymbol{I}\dot{\boldsymbol{\omega}}^{\mathcal{BN}} + \boldsymbol{\omega}^{\mathcal{BN}} \times \left(\boldsymbol{I}\boldsymbol{\omega}^{\mathcal{BN}}\right) = \boldsymbol{g}(\theta,\varphi) + \sum_{i=i}^{4} \left(\boldsymbol{r}^{\mathcal{S}^i/\mathcal{B}} \times \bar{\boldsymbol{F}}_i + \bar{\boldsymbol{\tau}}_i\right), \tag{2.17}$$

where $\boldsymbol{\omega}^{\mathcal{BN}}$ and $\dot{\boldsymbol{\omega}}^{\mathcal{BN}}$ are the angular velocity and angular acceleration of the base relative to the inertial frame, $\boldsymbol{g}$ is an attitude-dependent gravitational torque, and $\boldsymbol{r}^{\mathcal{S}^i/\mathcal{B}}$ is the moment arm of thrust i acting about the base. Based on the assumptions in Section 2.1.2,

the moment arm is the constant vector $\boldsymbol{r}^{\mathcal{S}^i/\mathcal{B}} = \ell_{\mathcal{S}}\,\hat{\boldsymbol{b}}_1^i$. The cross product for the thrust-induced torque can also be written as $\ell_{\mathcal{S}}\big(\hat{\boldsymbol{b}}_1^i\big)^{\wedge}\bar{\boldsymbol{F}}_i$, where $(\cdot)^{\wedge}$ is the linear bijection given by

$$\boldsymbol{x}^{\wedge} = \begin{bmatrix} x_1 \\ x_2 \\ x_3 \end{bmatrix}^{\wedge} = \begin{bmatrix} 0 & -x_3 & x_2 \\ x_3 & 0 & -x_1 \\ -x_2 & x_1 & 0 \end{bmatrix}, \tag{2.18}$$

which maps a vector in $\mathbb{R}^3$ to a skew-symmetric matrix reproducing the cross product.

The desired copter trajectory $\boldsymbol{q}_{\mathcal{B},d}$ includes 3-DOF position and attitude set-points which are used as the inputs to a rigid body control scheme. Full actuation allows the position and attitude components to be decoupled for use with independent position and attitude feedback control laws. The position controller is based on feedback linearization of Equation (2.16) and given by

$$\boldsymbol{u}_1 = m\left(g_0\,\hat{\boldsymbol{n}}_3 - \boldsymbol{K}_r\boldsymbol{e}_r - \boldsymbol{K}_v\boldsymbol{e}_v\right), \tag{2.19}$$

where $\boldsymbol{K}$ denotes a state-feedback gain matrix, $\boldsymbol{e}$ denotes an error state, and the subscripts r and v denote position and velocity. The output $\boldsymbol{u}_1$ is a resultant force vector which should be applied to the copter for position tracking. The attitude controller is a feedback linearization of Equation (2.17), resulting in

$$\boldsymbol{u}_2 = \boldsymbol{\omega}^{\mathcal{BN}} \times \left(\boldsymbol{I}\boldsymbol{\omega}^{\mathcal{BN}}\right) - \boldsymbol{g}(\theta,\varphi) - \boldsymbol{K}_R\boldsymbol{e}_R - \boldsymbol{K}_\omega\boldsymbol{e}_\omega \tag{2.20}$$

where the subscripts R and ω denote angular position and angular velocity. The output $\boldsymbol{u}_2$ is a resultant torque vector which should be applied to the copter for attitude tracking. Combining $\boldsymbol{u}_1$ and $\boldsymbol{u}_2$ results in a 6-DOF control wrench $\boldsymbol{u}$ which, if applied to the copter as a rigid body, would cause the copter's 6-DOF pose to track the desired trajectory.

To convert the wrench into motor commands, substitute the definitions from Section 2.3 into the equations of motion to obtain

$$m\boldsymbol{a}^{\mathcal{B}/\mathcal{O}} = -mg_0\,\hat{\boldsymbol{n}}_3 + \boldsymbol{u}_1 \tag{2.21}$$

$$\boldsymbol{I}\dot{\boldsymbol{\omega}}^{\mathcal{BN}} + \boldsymbol{\omega}^{\mathcal{BN}} \times \left(\boldsymbol{I}\boldsymbol{\omega}^{\mathcal{BN}}\right) = \boldsymbol{g}(\theta, \varphi) + \boldsymbol{u}_2 \tag{2.22}$$

where

$$\boldsymbol{u}_1 = \sum_{i=1}^{4} \bar{\boldsymbol{F}}_i, \tag{2.23}$$

$$\boldsymbol{u}_2 = \sum_{i=1}^{4} \left(\boldsymbol{r}^{\mathcal{S}^i/\mathcal{B}} \times \bar{\boldsymbol{F}}_i + \bar{\boldsymbol{\tau}}_i\right) \tag{2.24}$$

Defining the new quantity $\bar{\boldsymbol{t}}_i = \dot{\gamma}_i^2\, \hat{\boldsymbol{p}}_3^i$ allows the wrench to be written as a matrix multiplication

$$\boldsymbol{u} = \begin{bmatrix} \boldsymbol{u}_1 \\ \boldsymbol{u}_2 \end{bmatrix} = \boldsymbol{A}\bar{\boldsymbol{t}}, \qquad \bar{\boldsymbol{t}} = \begin{bmatrix} \bar{\boldsymbol{t}}_1 \\ \vdots \\ \bar{\boldsymbol{t}}_4 \end{bmatrix}, \tag{2.25}$$

with the constant allocation matrix given by

$$\boldsymbol{A} = \begin{bmatrix} c_p\boldsymbol{E}_3 & \cdots & c_p\boldsymbol{E}_3 \\ \boldsymbol{J}_1 & \cdots & \boldsymbol{J}_4 \end{bmatrix} \in \mathbb{R}^{6\times 12}, \qquad \boldsymbol{J}_i = c_p \ell_{\mathcal{S}} \left(\hat{\boldsymbol{b}}_1^i\right)^{\wedge} + (-1)^i c_t \boldsymbol{E}_3 \tag{2.26}$$

where $\boldsymbol{E}_3$ is the (3×3) identity matrix. The allocation matrix is configuration-independent and therefore full row-rank at all times, with the Moore-Penrose right pseudoinverse offering a mapping from the control wrench $\boldsymbol{u}$ to the vector $\bar{\boldsymbol{t}}$

$$\bar{\boldsymbol{t}} = \boldsymbol{A}^{\dagger}\boldsymbol{u}, \qquad \boldsymbol{A}^{\dagger} = \boldsymbol{A}^T\left(\boldsymbol{A}\boldsymbol{A}^T\right)^{-1}. \tag{2.27}$$

The right pseudoinverse is equivalent to a least-norms mapping, which leverages the six-dimensional configuration nullspace to determine the combination of thrust vectors which realizes the desired control wrench with minimal Euclidean norm. This has the effect of minimizing the counteracting thrust components between arms and thus reducing the required motor torques.

An inverse kinematics scheme fully described in [17] is then used to find the unique set of $\{\alpha_i, \beta_i, \dot{\gamma}_i\}$ parameters that produce the desired $\{\bar{\boldsymbol{t}}_i\}$. Finally, low-level independent

feedback control loops are used at each motor to track the desired twist/tilt angles and propeller speeds.

This hierarchical model neglects two key factors in the copter dynamics. First, the position and attitude control laws model the copter as a rigid body, which disregards configuration-dependent fluctuations in the inertia. Second, the independent nature of the low-level motor control laws cannot account for the gyroscopic coupling that occurs when deflecting an existing angular momentum vector, e.g. when using the twist/tilt motors to manipulate the thrust direction. Both of these effects have been found to be non negligible in experiments with the real system and thus must be addressed through modeling. The principal focus of this work is the development of a dynamic model which incorporates these complex effects while remaining sufficiently parsimonious for use in controller design.

Chapter 3

Quarter Copter

Rotational symmetry of the full twist-tilt copter allows the modeling problem to be reduced to several smaller models which are coupled through the base link. This chapter applies a Lagrangian approach to develop equations of motion for a single arm subsystem under the assumption of a stationary base link. While this assumption is highly restrictive, it serves as a starting point to establish the potential benefit of a centralized multi-input-multi-output (MIMO) controller over a set of decoupled single-input-single-output (SISO) controllers. The results are then generalized in Chapter 4 to include all four arcs and permit general base motion.

3.1 Decoupled SISO Control

Before diving into a rigorous dynamic model, it is important to establish a baseline for comparison. This section discusses a pseudo model-based approach for designing decoupled SISO controllers using very simple rigid body dynamics derived by inspection. The arm indexing subscript is dropped throughout this chapter, and can be regarded as 1 where strictly required.

3.1.1 Simplified Models

First, consider the propeller motor in isolation. The axis of rotation is $\hat{\boldsymbol{p}}_3$, the rotation angle is γ, and the effective inertia is $I^z_{\mathcal{P}}$. The relevant applied torques include the control torque from the motor and the resistive drag torque described in Section 2.3. The scalar equation of motion describing these dynamics is

$$I^z_{\mathcal{P}}\ddot{\gamma} = \tau_\gamma - c_t\dot{\gamma}^2, \tag{3.1}$$

where τ_γ is the torque from the propeller motor.

Next, consider the tilt motor in isolation. The axis of rotation is $\hat{\boldsymbol{s}}_2$, the rotation angle is β, and the effective inertia includes $I^y_{\mathcal{S}}$ as well as a constant parallel axis component from the propeller. The main torque applied along this axis is the control torque from the motor τ_β. A configuration-dependent gravitational torque also exists due to the propeller center of mass being offset from the tilt axis, however this torque is neglected for SISO design. The scalar equation of motion describing these dynamics is

$$\left(I^y_{\mathcal{S}} + m_{\mathcal{P}}\ell^2_{\mathcal{P}}\right)\ddot{\beta} = \tau_\beta, \tag{3.2}$$

which is a simple double integrator with respect to the input τ_β and output β.

Finally, consider the twist motor in isolation. The axis of rotation is $\hat{\boldsymbol{a}}_1$, the rotation angle is α, the effective inertia is $I^x_{\mathcal{A}} + I^x_{\mathcal{S}}$, and the applied torque from the motor is τ_α. The offset of the propeller from the twist axis also generates a configuration-dependent parallel axis term in the inertia as well as a configuration-dependent gravitational torque, however these effects are neglected for SISO design. The scalar equation of motion is then

$$\left(I^x_{\mathcal{A}} + I^x_{\mathcal{S}}\right)\ddot{\alpha} = \tau_\alpha, \tag{3.3}$$

which is another double integrator with respect to the input τ_α and output α. Together, Equations (3.1), (3.2), and (3.3) are a complete description of the simplified dynamics

for one arm subsystem.

3.1.2 Control Design

Many frameworks exist for control design aimed at reference tracking with integrator plants. This section applies the state-feedback linear quadratic regulator (LQR) design methodology because the tuning weights can be reused in Section 3.3 when designing the centralized controller, allowing for direct comparison between the SISO and MIMO designs. The choice of state variables as the position and velocity of a given motor makes state-feedback LQR equivalent to proportional-derivative (PD) control, which is sufficient for stabilization of double-integrator dynamics. A general framework will first be developed which is adapted from [18, Appendix C.2]. This framework is then applied to each of the models in Section 3.1.1 and the results combined for simulation.

First, consider the scalar nonlinear equation of motion for a general coordinate q

$$I(q)\ddot{q} + n(q, \dot{q}) = \tau, \tag{3.4}$$

where I is a (possibly) configuration dependent inertia, n is a general nonlinear function, and τ is an input torque affecting the dynamics. The goal is to design a feedback control law for τ which compensates for the nonlinearities and tracks a desired trajectory q_d. The trajectory is assumed to be known and twice differentiable in order to define error dynamics, however in application differentiation will not be necessary.

Define a linearizing change of variables according to

$$\tau = I(q)\left(\ddot{q}_d - u\right) + n(q, \dot{q}), \tag{3.5}$$

where u is a new control input. Next, define an error state to include the position and velocity tracking errors

$$\boldsymbol{e} = \begin{bmatrix} q_d - q \\ \dot{q}_d - \dot{q} \end{bmatrix}. \tag{3.6}$$

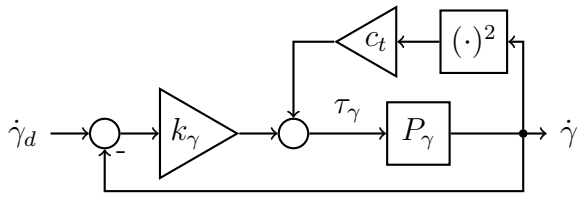

Figure 3.1: Control block diagram for the simplified propeller dynamics in Equation (3.1), represented as the plant P_γ, and the P controller with nonlinear compensation described by Equation (3.10). The operation $(\cdot)^2$ indicates a nonlinear block of which the output is the square of the input.

Differentiating Equation (3.6) and combining (3.4)-(3.5) results in a state-space model for the error system

$$\dot{\boldsymbol{e}} = \begin{bmatrix} \dot{q}_d - \dot{q} \\ \ddot{q}_d - \ddot{q} \end{bmatrix} = \begin{bmatrix} 0 & 1 \\ 0 & 0 \end{bmatrix} \begin{bmatrix} q_d - q \\ \dot{q}_d - \dot{q} \end{bmatrix} + \begin{bmatrix} 0 \\ 1 \end{bmatrix} u, \tag{3.7}$$

which has double-integrator dynamics. Notice that the state-space matrices are not dependent on either the inertia matrix or the nonlinear dynamics, and therefore this error model can be recycled for any equation of motion of the form in Equation (3.4). The standard LQR framework can be applied to the system $\dot{\boldsymbol{e}} = \boldsymbol{A}\boldsymbol{e} + \boldsymbol{B}u$ to select gains for the state-feedback control law given by

$$u(\boldsymbol{e}) = -\boldsymbol{K}\boldsymbol{e} = -k_p(q_d - q) - k_d(\dot{q}_d - \dot{q}). \tag{3.8}$$

Substituting into Equation (3.5) gives the full control law

$$\tau = I(q)\left[\ddot{q}_d + k_p(q_d - q) + k_d(\dot{q}_d - \dot{q})\right] + n(q, \dot{q}). \tag{3.9}$$

In practice only one of the desired trajectory terms will be kept, with the selection depending on whether the controller is primarily meant to track position or velocity. The other trajectory terms will be set to zero.

Now consider applying this controller to the propeller motor. From Equation (3.4), selecting $I = I^z_{\mathcal{P}}$ and $n = c_t\dot{\gamma}^2$ reconstructs the propeller dynamics used in Section 3.1.1. The variable of interest for the propeller is the speed $\dot{\gamma}$, and so the desired position γ_d

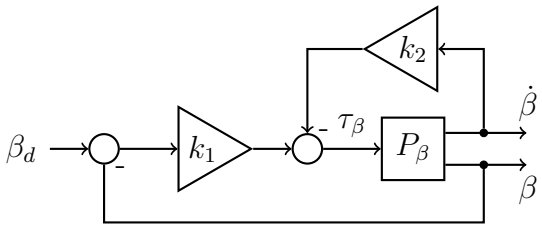

Figure 3.2: Control block diagram for the simplified tilt dynamics in Equation (3.2), represented as the plant P_β, and the state-feedback control law described by Equation (3.11).

and acceleration $\ddot{\gamma}_d$ will both be assumed zero to simplify the control law. By selecting the LQR weight associated with γ to be small compared to the weight for $\dot{\gamma}$, the resulting position gain will be small compared to the velocity gain and can be neglected. The control law for the propeller motor is then given by

$$\begin{aligned} \tau_\gamma &= I_{\mathcal{P}}^z k_d(\dot{\gamma}_d - \dot{\gamma}) + c_t\dot{\gamma}^2 \\ &\triangleq k_\gamma(\dot{\gamma}_d - \dot{\gamma}) + c_t\dot{\gamma}^2, \end{aligned} \tag{3.10}$$

which is a proportional (P) type controller in terms of the propeller speed, with nonlinear compensation for the drag-induced torque. A block diagram for this controller is shown in Fig. 3.1.

Next, a controller is designed for the tilt motor. The tilt dynamics are already in the form of a double integrator, therefore the choice of $I = I_{\mathcal{S}}^y + m_{\mathcal{P}}\ell_{\mathcal{P}}^2$ and $n = 0$ reconstructs the simplified equation of motion in Section 3.1.1. The tilt motor is meant to track a desired position, so the reference values for velocity $\dot{\beta}_d$ and acceleration $\ddot{\beta}_d$ will be set to zero for simplification. The control law for the tilt motor is then given by

$$\begin{aligned} \tau_\beta &= \left(I_{\mathcal{S}}^y + m_{\mathcal{P}}\ell_{\mathcal{P}}^2\right)\left[k_p(\beta_d - \beta) - k_d\dot{\beta}\right] \\ &\triangleq k_1(\beta_d - \beta) - k_2\dot{\beta}, \end{aligned} \tag{3.11}$$

which is a PD type controller in terms of the tilt angle. The corresponding block diagram is shown in Fig. 3.2.

The same pattern can be applied to the twist motor, which is also a pure double integrator. The choice of $I = I_{\mathcal{A}}^x + I_{\mathcal{S}}^x$ and $n = 0$ reconstructs the simplified dynamics,

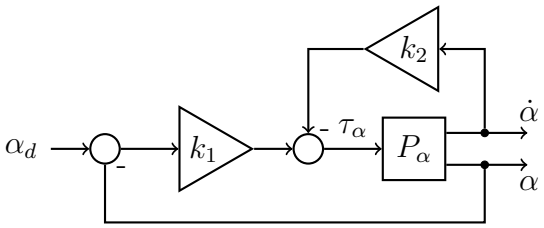

Figure 3.3: Control block diagram for the simplified twist dynamics in Equation (3.3), represented as the plant P_α, and the state-feedback control law described by Equation (3.12).

$\dot{\alpha}_d = \ddot{\alpha}_d = 0$ simplifies the controller for position tracking, and the final control law is given by

$$\begin{aligned} \tau_\alpha &= (I_{\mathcal{A}}^x + I_{\mathcal{S}}^x)\left[k_p(\alpha_d - \alpha) - k_d\dot{\alpha}\right] \\ &\triangleq k_1(\alpha_d - \alpha) - k_2\dot{\alpha}, \end{aligned} \tag{3.12}$$

which is another PD type controller with block diagram shown in Fig. 3.3.

The baseline controller performance is established by selecting tuning weights for the LQR problems above. For the propeller dynamics, the state weighting is chosen to be $\boldsymbol{Q}_\gamma = \mathrm{diag}\,(1 \times 10^{-6},\, 1)$, and the control weighting is chosen to be $R_\gamma = 1 \times 10^{-3}$. The weight corresponding to γ is retained so that Equation (3.6) applies, however it is simple to rewrite the error system in terms of a single state variable corresponding to velocity error only. Both approaches are equivalent when k_p is neglected to obtain Equation (3.10). The nominal closed-loop step response from an initial speed of $\dot{\gamma}(0) = 2600\,\mathrm{RPM}$[1] to a desired speed of $\dot{\gamma}_d = 3100\,\mathrm{RPM}$ is shown in Fig. 3.4.

The weightings for the twist and tilt states are chosen to be the same since the motors are identical on the real system, however the cost associated with τ_α is made larger than that associated with τ_β since the twist actuator wields a larger inertial load, requiring greater torque to achieve the same acceleration. The state weightings are chosen to be $\boldsymbol{Q}_\alpha = \boldsymbol{Q}_\beta = \mathrm{diag}\,(10,\, 0.1)$, and the control weightings are chosen to be $R_\alpha = 0.1$, $R_\beta = 1 \times 10^{-3}$. This leads to the nominal step responses shown in Fig. 3.5 and Fig. 3.6, where the initial conditions are $\alpha(0) = \beta(0) = 0$, and the desired positions are $\alpha_d = \beta_d = 30°$. The tilt controller is able to command large control inputs relative to its effective inertia

[1] With the assumed system parameters, 2600 RPM is the required speed of each propeller for steady level flight.

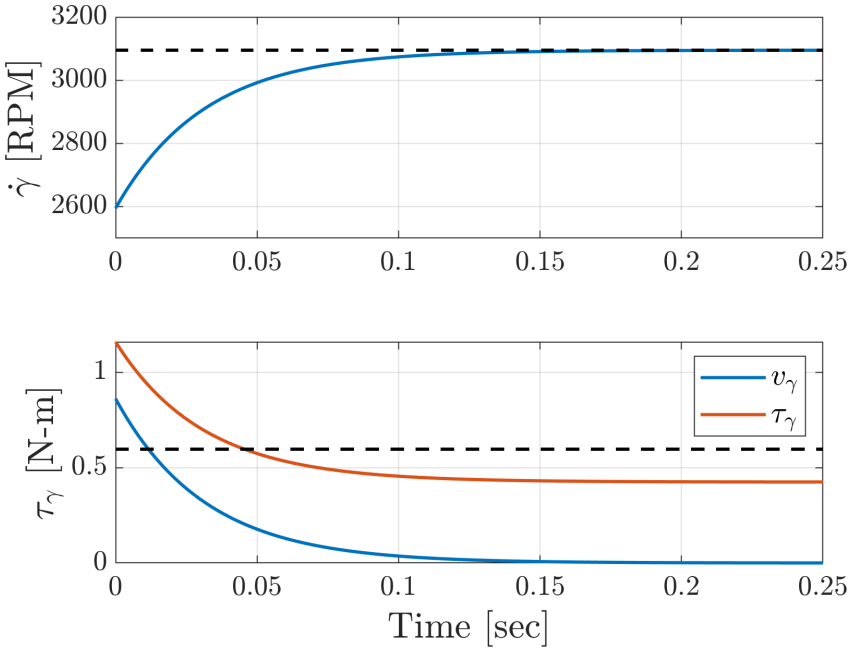

Figure 3.4: Nominal step response of the propeller speed from an initial condition of $\dot{\gamma}(0) = 2600\,\text{RPM}$ to a desired speed of $\dot{\gamma}_d = 3100\,\text{RPM}$, shown as a black dashed line on the speed plot. The dynamics are simulated according to Equation (3.1) with the control law in Equation (3.10). The torque trace v_γ includes only the state-feedback control term while the trace τ_γ includes the full nonlinear compensation. The control command exceeds the maximum torque of the motor for a significant portion of the rise time due to the large drag-induced torque, indicating that the copter is thrust limited in this regime of response speed. The maximum motor torque is shown as a black dashed line on the torque plot and is taken to be $0.6\,\text{N m}$ according to the hardware datasheet.

while remaining well within the actuator limitations, denoted on the torque plot by a black dashed line. The same cannot be said for the alpha controller, which operates in saturation for a large portion of its rise time. While saturation is generally undesirable as it leads to nonlinear plant behavior from the perspective of the controller, the degraded performance is tolerable in this case in order to maintain a fast response. Real trajectories of interest for the copter are unlikely to include discontinuous position commands, and so saturation is of less concern in practice. The propeller motor also operates in saturation for a large portion of its transient phase, which is not surprising as the bound on dynamic response speed of multirotor craft often comes in the form of thrust limitations. These limits are known by the craft designer and thus can be incorporated into trajectory planning algorithms to avoid motion commands which saturate the hardware capabilities.

While the nominal step responses look reasonable in isolation, the tracking perfor-

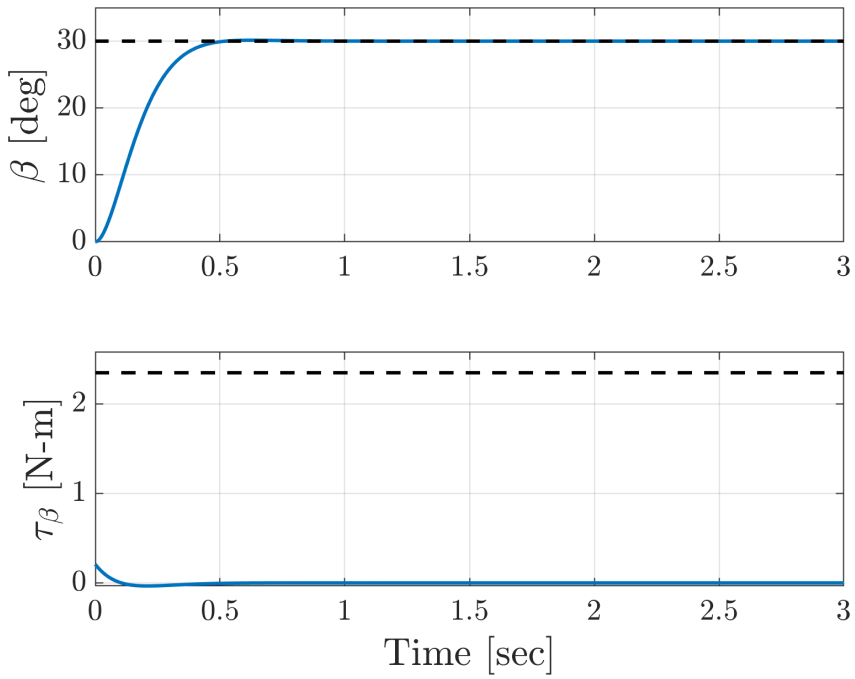

Figure 3.5: Nominal step response of the tilt angle from an initial condition of $\beta(0) = 0$ to a desired position of $\beta_d = 30°$, shown as a black dashed line on the position plot. The dynamics are simulated according to Equation (3.2) with the control law in Equation (3.11). The maximum torque of the motor is indicated on the torque plot by a black dashed line and taken to be 2.35 N m according to the hardware datasheet. The commanded torque remains far below this maximum at all times due to the relatively small inertial load experienced by the tilt motor.

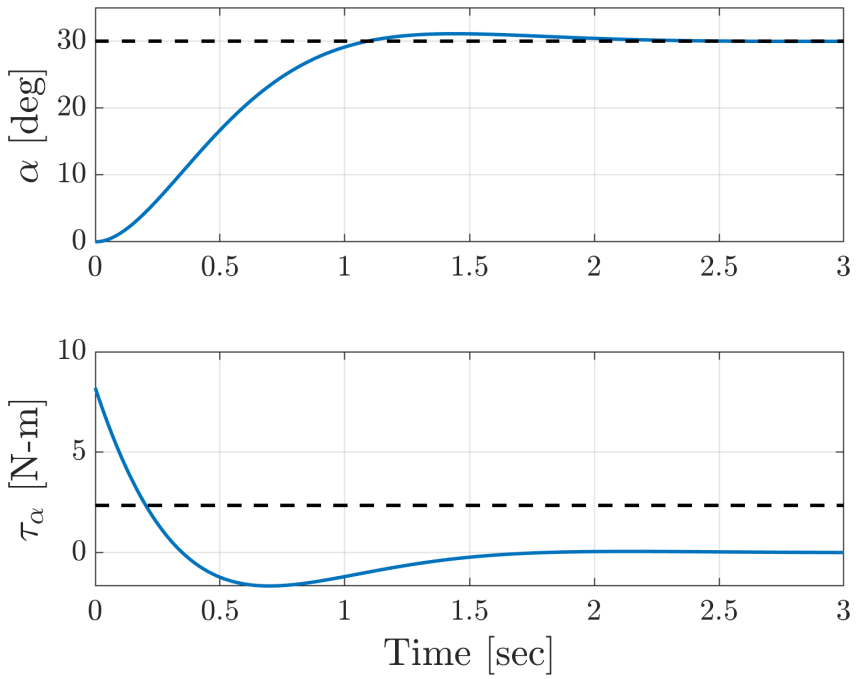

Figure 3.6: Nominal step response of the twist angle from an initial condition of $\alpha(0) = 0$ to a desired position of $\alpha_d = 30°$, shown as a black dashed line on the position plot. The dynamics are simulated according to Equation (3.3) with the control law in Equation (3.12). The commanded torque exceeds the maximum torque of the motor for a notable portion of the transient response due to the relatively large inertial load experienced by the twist motor. The maximum motor torque is shown on the torque plot by a black dashed line and taken to be 2.35 N m according to the hardware datasheet.

mance suffers when multiple actions are occurring simultaneously. To demonstrate this, consider a reference signal r that changes from an initial value r_i to a final value r_f with a cycloid velocity profile over time T. This signal is characterized by

$$r(t) = \frac{r_f - r_i}{T}\left(t - \sin\frac{2\pi t}{T}\right) + r_i, \quad t \in [0, T], \tag{3.13}$$

$$r(0) = r_i, \quad r(T) = r_f,$$

which is continuous and continuously differentiable on the defined time interval. By taking r to represent various motor angles, a smooth reference trajectory can be obtained between any two points in the arm configuration space.

A simulation was developed using Simscape Multibody[2] to evaluate the above controllers. The Simscape model is built using an imported CAD assembly connected by specified joints. Actuator saturation limits are enforced to better represent the mechanical components. Inertial parameters are obtained directly from the CAD files and therefore make no assumptions about center of mass locations or products of inertia, such as those made in Section 2.1.2 for ease of modeling. Equations of motion are formulated and solved by the software, meaning the dynamics are independent of any models derived in this paper. The only exception is in simulating the aerodynamic thrust and drag, which are applied to the propeller explicitly according to the equations outlined in Section 2.3. The result is a platform for virtual experiments which approximates the true system insofar as the CAD model is correct. Parameters used for simulation are described in Appendix A.

Fig. 3.7 shows the simulated performance of the three SISO controllers acting simultaneously to track a given cycloidal trajectory. The twist and tilt angles are alternately varied and held constant so that the thrust vector traces out a square in the configuration space, while the propeller speed is varied sinusoidally to act as a disturbance on the twist/tilt motors. Immediately apparent in this response are the large deviations in

[2]Trademarked.

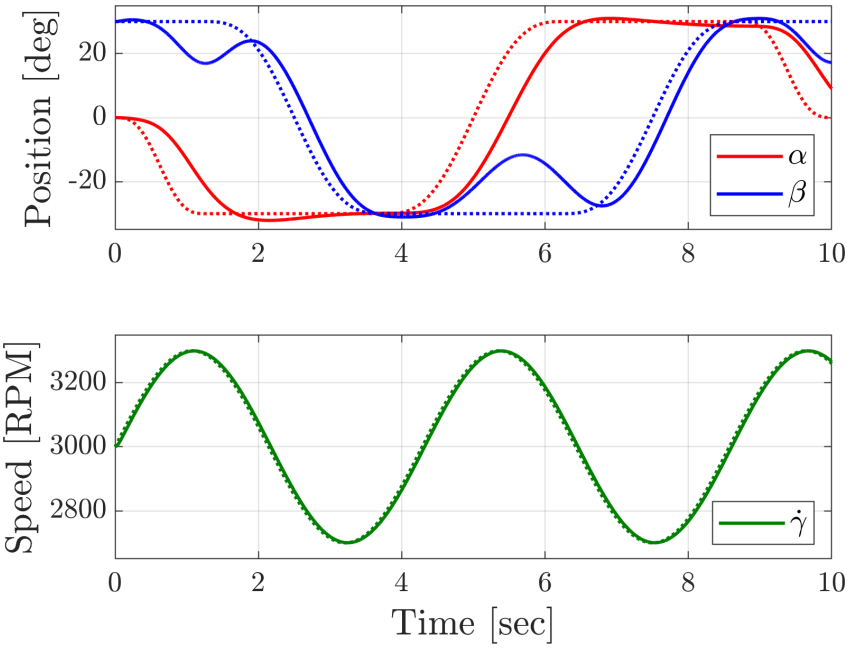

Figure 3.7: Simulated tracking performance of the three independent SISO controllers. The reference trajectory shown in dashed lines is generated by applying the cycloid signal Equation (3.13) to the twist and tilt angles in sequence, resulting in the thrust direction tracing a square pattern with continuously differentiable transitions between the corner points. The reference propeller speed is varied sinusoidally to act as a disturbance on the twist/tilt axes. Large tracking errors in β arise during the motion stages of α, and smaller but noticeable errors in α arise during motion stages of β. These errors occur due to unmodeled coupling between the two axes.

the β angle during periods of α rotation, with the β perturbation following the direction of α motion. A smaller but still visible deviation in the α occurs during periods of β rotation, with the α perturbation opposing the direction of β motion. These effects arise due to the gyroscopic coupling of the two axes which both act to change the direction of the spinning propeller. This experiment occurs under the constraint of a fixed base link, however it is easy to imagine how gyroscopic deviations occurring in all four arms simultaneously would cause the full copter to spin out beyond recovery. It is therefore necessary to account for these gyroscopic couplings in the dynamic model in order to compensate for their effects in the controller.

3.2 Lagrange Formulation

An energy method can be applied to derive the coupled equations of motion for one arm subsystem. Assuming for now that the base link is fixed to ground with $\psi = \theta = \phi = 0$, the arm configuration can be described by three generalized coordinates corresponding to the three control inputs. The vectors of generalized coordinates and generalized speeds are defined as

$$\boldsymbol{q} = \begin{bmatrix} q_1 \\ q_2 \\ q_3 \end{bmatrix} = \begin{bmatrix} \alpha \\ \beta \\ \gamma \end{bmatrix}, \quad \dot{\boldsymbol{q}} = \begin{bmatrix} \dot{q}_1 \\ \dot{q}_2 \\ \dot{q}_3 \end{bmatrix} = \begin{bmatrix} \dot{\alpha} \\ \dot{\beta} \\ \dot{\gamma} \end{bmatrix}. \tag{3.14}$$

Let the total kinetic energy of the arm subsystem be denoted by T, and the total potential energy by U. These energies are obtained from the sum of energies of each component

$$T = T_{\mathcal{A}} + T_{\mathcal{S}} + T_{\mathcal{P}}, \tag{3.15}$$

$$U = U_{\mathcal{A}} + U_{\mathcal{S}} + U_{\mathcal{P}}, \tag{3.16}$$

where the subscripts denote the arc, shaft, and propeller rigid bodies. The Lagrangian can then be defined in the usual way

$$\mathcal{L} = T - U = (T_{\mathcal{A}} + T_{\mathcal{S}} + T_{\mathcal{P}}) - (U_{\mathcal{A}} + U_{\mathcal{S}} + U_{\mathcal{P}}). \tag{3.17}$$

Denoting the vector of generalized forces acting along the generalized coordinates as $\boldsymbol{\xi}$, and noting that mechanical potential energy is not dependent on any generalized speed, the Euler-Lagrange equations of motion are given by

$$\frac{d}{dt}\left(\frac{\partial T}{\partial \dot{\boldsymbol{q}}}\right)^T - \left(\frac{\partial T}{\partial \boldsymbol{q}}\right)^T + \left(\frac{\partial U}{\partial \boldsymbol{q}}\right)^T = \boldsymbol{\xi}, \tag{3.18}$$

which can be expanded using Equations (3.15) and (3.16) to give

$$\frac{d}{dt}\begin{bmatrix} \frac{\partial T_{\mathcal{A}}}{\partial \dot{\alpha}} + \frac{\partial T_{\mathcal{S}}}{\partial \dot{\alpha}} + \frac{\partial T_{\mathcal{P}}}{\partial \dot{\alpha}} \\ \frac{\partial T_{\mathcal{A}}}{\partial \dot{\beta}} + \frac{\partial T_{\mathcal{S}}}{\partial \dot{\beta}} + \frac{\partial T_{\mathcal{P}}}{\partial \dot{\beta}} \\ \frac{\partial T_{\mathcal{A}}}{\partial \dot{\gamma}} + \frac{\partial T_{\mathcal{S}}}{\partial \dot{\gamma}} + \frac{\partial T_{\mathcal{P}}}{\partial \dot{\gamma}} \end{bmatrix} - \begin{bmatrix} \frac{\partial T_{\mathcal{A}}}{\partial \alpha} + \frac{\partial T_{\mathcal{S}}}{\partial \alpha} + \frac{\partial T_{\mathcal{P}}}{\partial \alpha} \\ \frac{\partial T_{\mathcal{A}}}{\partial \beta} + \frac{\partial T_{\mathcal{S}}}{\partial \beta} + \frac{\partial T_{\mathcal{P}}}{\partial \beta} \\ \frac{\partial T_{\mathcal{A}}}{\partial \gamma} + \frac{\partial T_{\mathcal{S}}}{\partial \gamma} + \frac{\partial T_{\mathcal{P}}}{\partial \gamma} \end{bmatrix} + \begin{bmatrix} \frac{\partial U_{\mathcal{P}}}{\partial \alpha} \\ \frac{\partial U_{\mathcal{P}}}{\partial \beta} \\ \frac{\partial U_{\mathcal{P}}}{\partial \gamma} \end{bmatrix} = \begin{bmatrix} \xi_\alpha \\ \xi_\beta \\ \xi_\gamma \end{bmatrix}. \tag{3.19}$$

The ensuing sections will evaluate the many terms of this Lagrange equation one rigid body at a time, addressing the arc, shaft, and propeller in sequence. The generalized forces are then treated separately, and the results are combined to form the final equations of motion.

3.2.1 Arc Energy

Based on the assumptions in Section 2.1.2, the position of the center of mass of the arc with respect to the base frame origin is given by

$$\boldsymbol{r}^{\mathcal{A}/\mathcal{B}} = \ell_{\mathcal{A}}\, \hat{\boldsymbol{a}}_1, \tag{3.20}$$

and the angular velocity of the $\mathcal{A}$ frame relative to the $\mathcal{B}$ frame is given by

$$\boldsymbol{\omega}^{\mathcal{A}\mathcal{B}} = \dot{\alpha}\, \hat{\boldsymbol{a}}_1. \tag{3.21}$$

Because the arc center of mass is fixed along the $\mathcal{A}_1$ axis and aligned with the arc rotation, the velocity of the arc center of mass as seen in the $\mathcal{B}$ frame is constrained to be zero at all times

$$\boldsymbol{v}^{\mathcal{A}\mathcal{B}} = \boldsymbol{0}. \tag{3.22}$$

The kinetic energy of the arc can be found with the inertial parameters defined in

Section 2.2 and the velocities above

$$\begin{aligned} T_{\mathcal{A}} &= \frac{1}{2} m_{\mathcal{A}} \cancel{\left(\boldsymbol{v}^{\mathcal{AB}}\right)^T \left(\boldsymbol{v}^{\mathcal{AB}}\right)}^{0} + \frac{1}{2} \left(\boldsymbol{\omega}^{\mathcal{AB}}\right)^T \boldsymbol{I}_{\mathcal{A}} \left(\boldsymbol{\omega}^{\mathcal{AB}}\right) \\ &= \frac{1}{2} I^x_{\mathcal{A}} \dot{\alpha}^2. \end{aligned} \tag{3.23}$$

From this equation it is clear that all partial derivatives of $T_{\mathcal{A}}$ in Equation (3.19) are zero except for the partial with respect to $\dot{\alpha}$, which is given by

$$\frac{d}{dt}\left(\frac{\partial T_{\mathcal{A}}}{\partial \dot{\alpha}}\right) = I^x_{\mathcal{A}} \ddot{\alpha}. \tag{3.24}$$

Noting that the center of mass of the arc is fixed on the $\mathcal{A}_1$ axis, which is constrained to be horizontal by assumption of $\theta = 0$, the base link origin can be used as the reference point for gravitational potential energy, resulting in the configuration-independent energy description

$$U_{\mathcal{A}} = 0. \tag{3.25}$$

Clearly all partial derivatives of $U_{\mathcal{A}}$ are zero, and thus Equation (3.24) gives a complete description of the arc energy for Equation (3.19).

3.2.2 Shaft Energy

Similar to the arc, the center of mass of the shaft is located at a fixed distance from the base frame origin given by

$$\boldsymbol{r}^{\mathcal{S}/\mathcal{B}} = \ell_{\mathcal{S}}\, \hat{\boldsymbol{a}}_1. \tag{3.26}$$

The rotation of the $\mathcal{S}$ frame relative to the $\mathcal{B}$ frame includes components from both the twist and tilt axes, given by

$$\begin{aligned} \boldsymbol{\omega}^{\mathcal{SB}} &= \boldsymbol{\omega}^{\mathcal{AB}} + \boldsymbol{\omega}^{\mathcal{SA}} = \dot{\alpha}\, \hat{\boldsymbol{a}}_1 + \dot{\beta}\, \hat{\boldsymbol{s}}_2 \\ &= \dot{\alpha} c_\beta\, \hat{\boldsymbol{s}}_1 + \dot{\beta}\, \hat{\boldsymbol{s}}_2 + \dot{\alpha} s_\beta\, \hat{\boldsymbol{s}}_3 \end{aligned} \tag{3.27}$$

Due to the shaft center of mass being fixed along the $\mathcal{A}_1$ axis and aligned with the arc rotation, the velocity of the shaft center of mass as seen in the $\mathcal{B}$ frame will be zero for all time

$$\boldsymbol{v}^{\mathcal{SB}} = \mathbf{0}. \tag{3.28}$$

From the inertial parameters defined in Section 2.2 and the velocities above, the shaft kinetic energy is given by

$$\begin{aligned} T_{\mathcal{S}} &= \frac{1}{2} m_{\mathcal{S}} \cancelto{0}{\left(\boldsymbol{v}^{\mathcal{SB}}\right)^T \left(\boldsymbol{v}^{\mathcal{SB}}\right)} + \frac{1}{2} \left(\boldsymbol{\omega}^{\mathcal{SB}}\right)^T \boldsymbol{I}_{\mathcal{S}} \left(\boldsymbol{\omega}^{\mathcal{SB}}\right) \\ &= \frac{1}{2} I_{\mathcal{S}}^x \dot{\alpha}^2 c_\beta^2 + \frac{1}{2} I_{\mathcal{S}}^y \dot{\beta}^2 + \frac{1}{2} I_{\mathcal{S}}^z \dot{\alpha}^2 s_\beta^2. \end{aligned} \tag{3.29}$$

The geometry of the shaft body is very nearly symmetric about the $\mathcal{S}_2$ axis, permitting the approximation $I_{\mathcal{S}}^x \approx I_{\mathcal{S}}^z$. This allows a slight simplification of Equation (3.29) to

$$T_{\mathcal{S}} \approx \frac{1}{2} I_{\mathcal{S}}^{xz} \dot{\alpha}^2 + \frac{1}{2} I_{\mathcal{S}}^y \dot{\beta}^2, \tag{3.30}$$

where $I_{\mathcal{S}}^{xz}$ is used to denote the shaft moment of inertia about either the $\mathcal{S}_1$ or $\mathcal{S}_3$ axes. This energy is dependent on two of the generalized speeds and none of the generalized coordinates, therefore the only nonzero partial derivatives for Equation (3.19) are

$$\frac{d}{dt}\left(\frac{\partial T_{\mathcal{S}}}{\partial \dot{\alpha}}\right) = I_{\mathcal{S}}^{xz} \ddot{\alpha} \tag{3.31}$$

and

$$\frac{d}{dt}\left(\frac{\partial T_{\mathcal{S}}}{\partial \dot{\beta}}\right) = I_{\mathcal{S}}^{y} \ddot{\beta}. \tag{3.32}$$

Again similar to the arc, the shaft center of mass lies along the $\mathcal{A}_1$ axis, resulting in zero potential energy for any configuration of the arm.

$$U_{\mathcal{S}} = 0 \tag{3.33}$$

All partial derivatives of $U_{\mathcal{S}}$ are zero, and thus Equations (3.31) and (3.32) give a complete

description of the shaft energy in Equation (3.19).

3.2.3 Propeller Energy

The propeller center of mass is offset by a fixed distance from the shaft center of mass, but is located on a rotating axis which will result in a nonzero values for the center of mass velocity and potential energy. The position with respect to the base frame origin is given by

$$\boldsymbol{r}^{\mathcal{P}/\mathcal{B}} = \boldsymbol{r}^{\mathcal{S}/\mathcal{B}} + \boldsymbol{r}^{\mathcal{P}/\mathcal{S}} = \ell_{\mathcal{S}}\,\hat{\boldsymbol{a}}_1 + \ell_{\mathcal{P}}\,\hat{\boldsymbol{p}}_3, \tag{3.34}$$

and the rotation of the $\mathcal{P}$ frame relative to the $\mathcal{B}$ frame includes components from all three motor axes, described by

$$\begin{aligned}\boldsymbol{\omega}^{\mathcal{P}\mathcal{B}} &= \boldsymbol{\omega}^{\mathcal{A}\mathcal{B}} + \boldsymbol{\omega}^{\mathcal{S}\mathcal{A}} + \boldsymbol{\omega}^{\mathcal{P}\mathcal{S}} = \dot{\alpha}\,\hat{\boldsymbol{a}}_1 + \dot{\beta}\,\hat{\boldsymbol{s}}_2 + \dot{\gamma}\,\hat{\boldsymbol{p}}_3 \\ &= \big(\dot{\alpha}c_\beta c_\gamma + \dot{\beta}s_\gamma\big)\hat{\boldsymbol{p}}_1 + \big(-\dot{\alpha}c_\beta s_\gamma + \dot{\beta}c_\gamma\big)\hat{\boldsymbol{p}}_2 + \big(\dot{\alpha}s_\beta + \dot{\gamma}\big)\hat{\boldsymbol{p}}_3.\end{aligned} \tag{3.35}$$

The velocity of the center of mass is obtained by differentiating Equation (3.34) and accounting for the rotating frame

$$\begin{aligned}\boldsymbol{v}^{\mathcal{P}\mathcal{B}} &= \cancelto{0}{\boldsymbol{v}^{\mathcal{S}\mathcal{B}}} + \boldsymbol{\omega}^{\mathcal{S}\mathcal{B}} \times (\ell_{\mathcal{P}}\,\hat{\boldsymbol{p}}_3) \\ &= \ell_{\mathcal{P}}\dot{\beta}\,\hat{\boldsymbol{s}}_1 - \ell_{\mathcal{P}}\dot{\alpha}c_\beta\,\hat{\boldsymbol{s}}_2\end{aligned} \tag{3.36}$$

With the inertial parameters defined in Section 2.2 and the velocities derived here, the propeller kinetic energy is given by

$$\begin{aligned}T_{\mathcal{P}} &= \frac{1}{2}m_{\mathcal{P}}\Big(\boldsymbol{v}^{\mathcal{P}\mathcal{B}}\Big)^T\Big(\boldsymbol{v}^{\mathcal{P}\mathcal{B}}\Big) + \frac{1}{2}\big(\boldsymbol{\omega}^{\mathcal{P}\mathcal{B}}\big)^T\boldsymbol{I}_{\mathcal{P}}\big(\boldsymbol{\omega}^{\mathcal{P}\mathcal{B}}\big) \\ &= \frac{1}{2}m_{\mathcal{P}}\ell_{\mathcal{P}}^2\left(\dot{\beta}^2 + \dot{\alpha}^2c_\beta^2\right) \\ &\quad + \frac{1}{2}I_{\mathcal{P}}^x\Big(\dot{\alpha}c_\beta c_\gamma + \dot{\beta}s_\gamma\Big)^2 + \frac{1}{2}I_{\mathcal{P}}^y\Big(-\dot{\alpha}c_\beta s_\gamma + \dot{\beta}c_\gamma\Big)^2 + \frac{1}{2}I_{\mathcal{P}}^z\Big(\dot{\alpha}s_\beta + \dot{\gamma}\Big)^2.\end{aligned} \tag{3.37}$$

This is a very cumbersome expression compared to the kinetic energies of the arc and shaft, and includes a dependence on the propeller angle which would be highly impractical

for implementation. Fortunately this equation can be simplified greatly by leveraging the vast differences in the expected motor speeds. Recall from Section 3.1.2 that the nominal propeller speed for level hovering is $\dot{\gamma} = 2600\,\text{RPM}$. In contrast, the maximum speed of the twist/tilt motors seen in the sample trajectory from Fig. 3.7 is only about 5 RPM, multiple orders of magnitude slower than the propeller. The approximations $\dot{\alpha}/\dot{\gamma} \ll 1$ and $\dot{\beta}/\dot{\gamma} \ll 1$ are thus very sound but lead to great simplifications in Equation (3.37)

$$\begin{aligned} T_{\mathcal{P}} &= \frac{1}{2} m_{\mathcal{P}} \ell_{\mathcal{P}}^2 \left(\dot{\beta}^2 + \dot{\alpha}^2 c_\beta^2 \right) \\ &\quad + \frac{1}{2} \left[I_{\mathcal{P}}^x \left(\frac{\dot{\alpha} c_\beta c_\gamma + \dot{\beta} s_\gamma}{\dot{\gamma}} \right)^2 + I_{\mathcal{P}}^y \left(\frac{-\dot{\alpha} c_\beta s_\gamma + \dot{\beta} c_\gamma}{\dot{\gamma}} \right)^2 + I_{\mathcal{P}}^z \left(\frac{\dot{\alpha} s_\beta}{\dot{\gamma}} + 1 \right)^2 \right] \dot{\gamma}^2 \\ &\approx \frac{1}{2} m_{\mathcal{P}} \ell_{\mathcal{P}}^2 \left(\dot{\beta}^2 + \dot{\alpha}^2 c_\beta^2 \right) + \frac{1}{2} I_{\mathcal{P}}^z \dot{\gamma}^2. \end{aligned} \tag{3.38}$$

Note that the same approximation of speed ratios could have been used to eliminate the first term entirely. This term corresponds to the energy contribution from the propeller linear velocity, which is very small relative to the contribution from angular velocity due not only to the speed ratio but also to the relatively small values of $m_{\mathcal{P}}$ and $\ell_{\mathcal{P}}$ in comparison to the larger value of $I_{\mathcal{P}}^z$. The linear velocity term is retained here for interpretation in Section 3.2.5, but will be neglected in Chapter 4 for simplicity.

This form of the propeller kinetic energy is dependent on all three generalized speeds but only one of the generalized coordinates. The relevant partial derivatives for Equation (3.19) are

$$\frac{d}{dt} \left(\frac{\partial T_{\mathcal{P}}}{\partial \dot{\alpha}} \right) = m_{\mathcal{P}} \ell_{\mathcal{P}}^2 \ddot{\alpha} c_\beta^2 - 2 m_{\mathcal{P}} \ell_{\mathcal{P}}^2 \dot{\alpha} \dot{\beta} s_\beta c_\beta, \tag{3.39}$$

$$\frac{d}{dt} \left(\frac{\partial T_{\mathcal{P}}}{\partial \dot{\beta}} \right) = m_{\mathcal{P}} \ell_{\mathcal{P}}^2 \ddot{\beta}, \tag{3.40}$$

$$\frac{d}{dt} \left(\frac{\partial T_{\mathcal{P}}}{\partial \dot{\gamma}} \right) = I_{\mathcal{P}}^z \ddot{\gamma}, \tag{3.41}$$

and

$$\frac{\partial T_{\mathcal{P}}}{\partial \beta} = -m_{\mathcal{P}} \ell_{\mathcal{P}}^2 \dot{\alpha}^2 s_\beta c_\beta. \tag{3.42}$$

With the reference point for gravitational potential energy at the base link origin, the potential energy of the propeller can be obtained by multiplying its weight with the projection of its position onto the $\mathcal{B}_3$ axis according to

$$U_{\mathcal{P}} = \boldsymbol{r}^{\mathcal{P}/\mathcal{B}} \cdot \hat{\boldsymbol{b}}_3 = m_{\mathcal{P}} g_0 \ell_{\mathcal{P}} c_\alpha c_\beta. \tag{3.43}$$

This energy is dependent on two of the generalized coordinates and none of the generalized speeds, therefore the nonzero partial derivatives for Equation (3.19) are

$$\frac{\partial U_{\mathcal{P}}}{\partial \alpha} = -m_{\mathcal{P}} g_0 \ell_{\mathcal{P}} s_\alpha c_\beta \tag{3.44}$$

and

$$\frac{\partial U_{\mathcal{P}}}{\partial \beta} = -m_{\mathcal{P}} g_0 \ell_{\mathcal{P}} c_\alpha s_\beta. \tag{3.45}$$

Equations (3.39)-(3.42) and (3.44)-(3.45) are a complete description for the propeller energy in Equation (3.19).

3.2.4 Generalized Forces

Because each of the generalized coordinates in Equation (3.14) corresponds to a controllable input, each element of $\boldsymbol{\xi}$ in Equation (3.19) will include a motor torque τ applied along the coordinate. Other generalized forces include the end-effector terms described in Section 2.3, as well as the torques associated with gyroscopic precession. The gyroscopic effect arises when a spinning body experiences a torque which is not aligned with its existing angular momentum, resulting in a rotation not aligned with either the angular momentum or the applied torque. Intuitively this corresponds to the moment required to change the direction of an angular momentum vector, given by the cross product of the new rotation with the existing angular momentum. The gyroscopic torque is orthogonal

to the applied torque by virtue of the cross product, and therefore must be included separately from the motor torque τ.

Torques associated with gyroscopic precession will be denoted by $\boldsymbol{\sigma}$. No such torque arises for the arc because it is constrained to rotate about the twist axis only. This is a direct consequence of fixing the orientation of the base link and will not be the case once the base is allowed to rotate.

$$\boldsymbol{\sigma}_{\mathcal{A}} = \cancelto{0}{\boldsymbol{\omega}^{\mathcal{B}\mathcal{N}}} \times \boldsymbol{I}_{\mathcal{A}} \boldsymbol{\omega}^{\mathcal{A}\mathcal{B}} = 0 \tag{3.46}$$

A gyroscopic torque does exist for the shaft, as it experiences the rotation of the arc in addition to its own rotation about the tilt axis. The torque is calculated by the rotation of the shaft due to the arc (equal to the rotation of the arc itself) crossed with the angular momentum of the shaft as seen by the arc

$$\boldsymbol{\sigma}_{\mathcal{S}} = \boldsymbol{\omega}^{\mathcal{A}\mathcal{B}} \times \boldsymbol{I}_{\mathcal{S}} \boldsymbol{\omega}^{\mathcal{S}\mathcal{A}} = I^y_{\mathcal{S}} \dot{\alpha} \dot{\beta}\, \hat{\boldsymbol{a}}_3. \tag{3.47}$$

A similar torque exists for the propeller, which experiences rotation due to the arc and the shaft in addition to its own rotation about the γ axis. The torque is calculated by the total rotation of the shaft crossed with the angular momentum of the propeller as seen by the shaft

$$\begin{aligned} \boldsymbol{\sigma}_{\mathcal{P}} &= \boldsymbol{\omega}^{\mathcal{S}\mathcal{B}} \times \boldsymbol{I}_{\mathcal{P}} \boldsymbol{\omega}^{\mathcal{P}\mathcal{S}} \\ &= I^z_{\mathcal{P}} \dot{\beta} \dot{\gamma} \hat{\boldsymbol{s}}_1 - I^z_{\mathcal{P}} \dot{\alpha} \dot{\gamma} c_\beta \hat{\boldsymbol{s}}_2 \\ &= I^z_{\mathcal{P}} \dot{\beta} \dot{\gamma} c_\beta \hat{\boldsymbol{a}}_1 - I^z_{\mathcal{P}} \dot{\alpha} \dot{\gamma} c_\beta \hat{\boldsymbol{a}}_2 - I^z_{\mathcal{P}} \dot{\beta} \dot{\gamma} s_\beta \hat{\boldsymbol{a}}_3, \end{aligned} \tag{3.48}$$

where the result has been expressed in both the $\mathcal{A}$ frame and the $\mathcal{S}$ frame for easy projection onto the various coordinates.

Finally, the generalized force for a given coordinate can be written as the sum of the motor torque for that coordinate, the end-effector terms projected onto the coordinate, and the gyroscopic torques of all downstream bodies projected onto the coordinate. For

coordinate j in a serial mechanism of n links, this is described by

$$\xi_{q_j} = \tau_{q_j} + \left(\boldsymbol{\rho} \times \bar{\boldsymbol{F}}\right) \cdot \hat{\boldsymbol{q}}_j + \bar{\boldsymbol{\tau}} \cdot \hat{\boldsymbol{q}}_j - \sum_{k=j+1}^{n} \boldsymbol{\sigma}_k \cdot \hat{\boldsymbol{q}}_j, \tag{3.49}$$

where $\hat{\boldsymbol{q}}_j$ denotes the unit vector associated with coordinate j, and $\boldsymbol{\rho}$ is the moment arm for the end effector force with respect to $\hat{\boldsymbol{q}}_j$. Note that the gyroscopic torques of the downstream bodies $\boldsymbol{\sigma}_k$ enter with a negative sign because they are associated with a kinematic phenomenon rather than an external torque, similar to so-called "inertial forces" in other classical mechanics formulations.

For the generalized coordinates considered in this section, the line of action of the thrust force $\bar{\boldsymbol{F}}$ intersects all three motor axes and thus no thrust-induced torque will appear in the right-hand side of Equation (3.19). This is a consequence of the design of the twist-tilt copter and will still hold for the arm coordinates once the base is allowed to rotate, however thrust-induced torques will appear in Chapter 4 when considering the generalized forces about applied to the base rotation axes.

Applying Equation (3.49) to the three generalized coordinates yields the following generalized forces

$$\begin{aligned} \xi_\alpha &= \tau_\alpha + \left(-c_t \dot{\gamma}^2 \hat{\boldsymbol{p}}_3\right) \cdot \hat{\boldsymbol{a}}_1 - \cancelto{0}{\boldsymbol{\sigma}_{\mathcal{S}} \cdot \hat{\boldsymbol{a}}_1} - \boldsymbol{\sigma}_{\mathcal{P}} \cdot \hat{\boldsymbol{a}}_1 \\ &= \tau_\alpha - c_t \dot{\gamma}^2 s_\beta - I^z_{\mathcal{P}} \dot{\beta} \dot{\gamma} c_\beta, \end{aligned} \tag{3.50}$$

$$\begin{aligned} \xi_\beta &= \tau_\beta + \cancelto{0}{\left(-c_t \dot{\gamma}^2 \hat{\boldsymbol{p}}_3\right) \cdot \hat{\boldsymbol{s}}_2} - \boldsymbol{\sigma}_{\mathcal{P}} \cdot \hat{\boldsymbol{s}}_2 \\ &= \tau_\beta + I^z_{\mathcal{P}} \dot{\alpha} \dot{\gamma} c_\beta, \end{aligned} \tag{3.51}$$

$$\begin{aligned} \xi_\gamma &= \tau_\gamma + \left(-c_t \dot{\gamma}^2 \hat{\boldsymbol{p}}_3\right) \cdot \hat{\boldsymbol{p}}_3 \\ &= \tau_\gamma - c_t \dot{\gamma}^2. \end{aligned} \tag{3.52}$$

Note that the α joint supports gyroscopic torques from both the shaft and propeller since both of these links are downstream with respect to the arc. The β joint only supports gyroscopic torques from the propeller, and the γ joint supports no gyroscopic torques

because it is the final link in the open kinematic chain.

3.2.5 Equations of Motion

Substituting the elements of Equation (3.19) and rearranging yields a matrix equation of motion in the form

$$\boldsymbol{M}(\boldsymbol{q})\ddot{\boldsymbol{q}} + \boldsymbol{C}(\boldsymbol{q},\dot{\boldsymbol{q}})\dot{\boldsymbol{q}} + \boldsymbol{d}(\boldsymbol{q},\dot{\boldsymbol{q}}) + \boldsymbol{g}(\boldsymbol{q}) = \boldsymbol{\tau}, \tag{3.53}$$

which represents an undamped gyroscopic system with the definitions in Equations (3.54)-(3.58).

The matrix $\boldsymbol{M}$ is a symmetric positive-definite inertia matrix given by

$$\boldsymbol{M}(\boldsymbol{q}) = \begin{bmatrix} I_{\mathcal{A}}^x + I_{\mathcal{S}}^x + m_{\mathcal{P}}\ell_{\mathcal{P}}^2 c_\beta^2 & 0 & 0 \\ 0 & I_{\mathcal{S}}^y + m_{\mathcal{P}}\ell_{\mathcal{P}}^2 & 0 \\ 0 & 0 & I_{\mathcal{P}}^z \end{bmatrix}, \tag{3.54}$$

which can be decomposed into a constant matrix and a configuration-dependent matrix. For this model the only configuration-dependent element is the parallel axis contribution of the propeller rotating about the twist axis, which occurs at a variable distance based on the tilt angle. This parallel axis term arises from the decision to keep the translational contribution to Equation (3.38) despite it being negligible relative to the rotational contribution. Here as well the contribution of the propeller mass is small relative to the arc and shaft inertias, further justifying its omission. The propeller parallel axis term will thus be dropped in Chapter 4 for simplicity.

The matrix $\boldsymbol{C}$ is a coupling matrix which, when multiplied by $\dot{\boldsymbol{q}}$, results in quadratic velocity terms. This matrix is given by

$$\boldsymbol{C}(\boldsymbol{q},\dot{\boldsymbol{q}}) = \underbrace{m_{\mathcal{P}}\ell_{\mathcal{P}}^2 s_\beta c_\beta \begin{bmatrix} -\dot{\beta} & -\dot{\alpha} & 0 \\ \dot{\alpha} & 0 & 0 \\ 0 & 0 & 0 \end{bmatrix}}_{\tilde{\boldsymbol{C}}(\boldsymbol{q},\dot{\boldsymbol{q}})} + \underbrace{I_{\mathcal{P}}^z c_\beta \begin{bmatrix} 0 & \dot{\gamma} & 0 \\ -\dot{\gamma} & 0 & 0 \\ 0 & 0 & 0 \end{bmatrix}}_{\bar{\boldsymbol{C}}(\boldsymbol{q},\dot{\boldsymbol{q}})}, \tag{3.55}$$

where the matrices $\tilde{\boldsymbol{C}}$ and $\bar{\boldsymbol{C}}$ are defined temporarily for ease of reference. The $\dot{\alpha}^2$ element of $\tilde{\boldsymbol{C}}(\boldsymbol{q}, \dot{\boldsymbol{q}})\dot{\boldsymbol{q}}$ represents the centrifugal effect on the β axis due to the rotation of $\dot{\alpha}$, and the $\dot{\alpha}\dot{\beta}$ elements represent the Coriolis effects on the α axis due to simultaneous rotations of $\dot{\alpha}$ and $\dot{\beta}$. Both of these effects disappear when $s_\beta c_\beta = 0$, which occurs at 90° intervals of the tilt angle. No Coriolis effects are present in the β row because the distance to the propeller center of mass is fixed with respect to the tilt axis. The vector $\bar{\boldsymbol{C}}(\boldsymbol{q}, \dot{\boldsymbol{q}})\dot{\boldsymbol{q}}$ represents gyroscopic effects associated with changing the direction of the propeller angular momentum. The effect on the twist axis is dependent on $\dot{\beta}\dot{\gamma}$ whereas the effect on the tilt axis is dependent on $\dot{\alpha}\dot{\gamma}$, producing an inherent coupling between the two motors which increases with speed. Once again the magnitude of the propeller parallel axis term $\tilde{\boldsymbol{C}}$ is small compared to the surrounding terms, a final justification for dropping the linear velocity contribution to Equation (3.38) for the remainder of this work.

A notable property of equations in the form of (3.53) is the skew-symmetry relation between the inertia matrix and the velocity coupling matrix. Specifically, the quantity $\dot{\boldsymbol{M}} - 2\boldsymbol{C}$ should be a skew-symmetric matrix [see 18, sec. 7.2]. Applying this relation to Equations (3.54) and (3.55):

$$\dot{\boldsymbol{M}} - 2\boldsymbol{C} = 2m_{\mathcal{P}}\ell_{\mathcal{P}}^2 s_\beta c_\beta \begin{bmatrix} 0 & \dot{\alpha} & 0 \\ -\dot{\alpha} & 0 & 0 \\ 0 & 0 & 0 \end{bmatrix} + 2I_{\mathcal{P}}^z c_\beta \begin{bmatrix} 0 & -\dot{\gamma} & 0 \\ \dot{\gamma} & 0 & 0 \\ 0 & 0 & 0 \end{bmatrix},$$

which is indeed skew-symmetric. This property is not only useful for validation of the obtained model but will also be applied in Chapter 4 to supplement some simplifying approximations.

Returning to the final terms of Equation (3.53), the vector $\boldsymbol{d}$ represents the drag torques coming from the generalized forces, given by

$$\boldsymbol{d}(\boldsymbol{q}, \dot{\boldsymbol{q}}) = c_t \dot{\gamma}^2 \begin{bmatrix} s_\beta \\ 0 \\ 1 \end{bmatrix}. \tag{3.56}$$

The γ axis feels the full effect of the drag torque at all times due to the definition in Equation (2.15). In contrast, the β axis feels no effect from the drag torque at any time since it is orthogonal to the propeller axis by construction. The drag torque felt by the α axis varies by configuration and is projected through the tilt angle.

The vector $\boldsymbol{g}$ represents the gravitational torque felt at the twist and tilt axes due to the offset of the propeller center of mass. It is given by

$$\boldsymbol{g}(\boldsymbol{q}) = -m_{\mathcal{P}} g_0 \ell_{\mathcal{P}} \begin{bmatrix} s_\alpha c_\beta \\ c_\alpha s_\beta \\ 0 \end{bmatrix}, \tag{3.57}$$

which comes directly from the partials of propeller potential energy with respect to the various coordinates.

Finally, the vector $\boldsymbol{\tau}$ includes the applied torques from the motors

$$\boldsymbol{\tau} = \begin{bmatrix} \tau_\alpha \\ \tau_\beta \\ \tau_\gamma \end{bmatrix}. \tag{3.58}$$

These torques represent the controllable inputs and are crucial for the control design in Section 3.3.

A comparison of these coupled equations of motion to the simplified models in Section 3.1.1 reveals exactly which dynamics are neglected in the simplified forms. If the velocity coupling, drag torque, gravitational torque, and configuration-dependent inertia are all removed from Equation (3.53), the first two rows reduce to Equations (3.2) and (3.3). The third row of Equation (3.53) is already equivalent to Equation (3.1) due to simplification of the propeller kinetic energy when deriving the Lagrangian. Using the full kinetic energy in Equation (3.37) would create coupling terms in both the $\boldsymbol{M}$ and $\boldsymbol{C}$ matrices, however these contributions would be small relative to the already included terms. In summary, the equation of motion for the propeller replicates the simplified model, while the new equations for the twist and tilt axes include certain Coriolis, centrifugal, gyroscopic, gravitational, and configuration-dependent inertial effects which were ignored

in the initial model.

3.2.6 Sample Trajectory

A virtual experiment is conducted on the Simscape model to validate these equations of motion. The square sample trajectory shown in Fig. 3.8 is used as a prescribed input motion and the required torques to achieve this motion are calculated automatically. The timeseries of joint angles, velocities, and accelerations can be extracted and used in Equation (3.53) to calculate the expected motor torques $\boldsymbol{\tau}$, which are then compared to the actual torques applied in the simulation. Fig. 3.9 shows the simulation measurements (solid) compared to the model predictions (dashed) for the three motor torques. The near-constant offset in the α motor torque is due to the unmodeled offsets in the center of mass of each component, contributing small gravitational torques about the twist axis. The initial deviation of the α prediction is due to the unmodeled coupling between the propeller acceleration and the alpha motor torque, a consequence of the simplification of the propeller kinetic energy. Despite the approximations, the model performs extremely well after an initial settling period, confirming its use as a predictive tool.

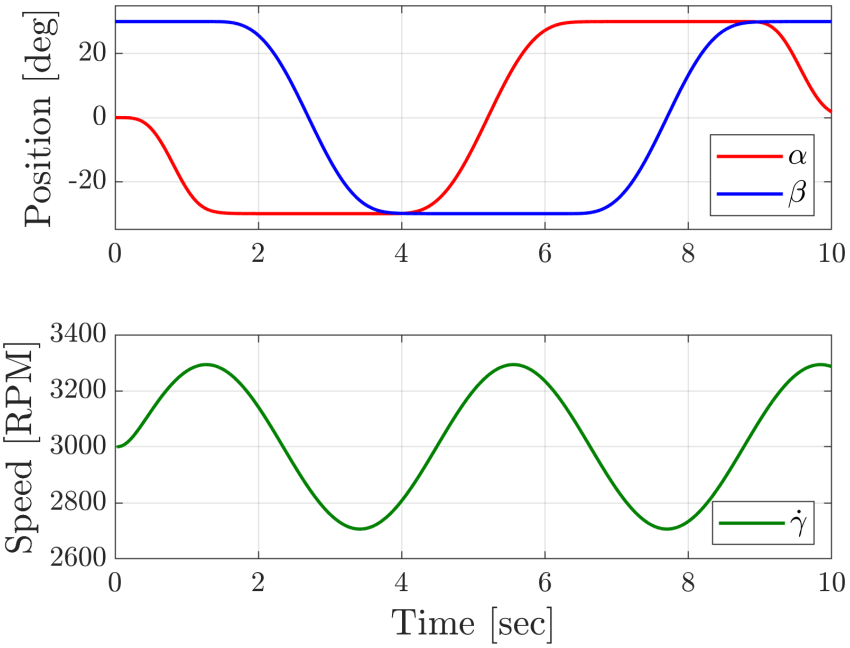

Figure 3.8: Sample trajectory for validation of the coupled equations of motion. Joint motion is prescribed directly to the Simscape model and the torques required to realize that motion are calculated within the software.

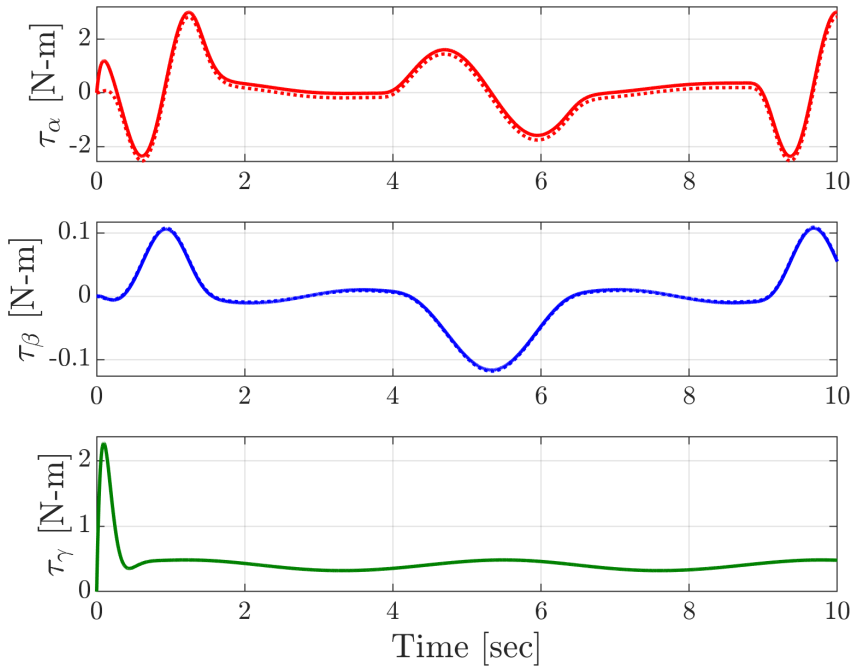

Figure 3.9: Comparison of predicted (dashed) and measured (solid) torques for a virtual experiment on the Simscape model. The measured torques are generated by the simulation in order to realize the prescribed trajectory in Fig. 3.8. Predicted torques are calculated by applying Equation (3.53) to the measured joint angles, velocities, and accelerations.

3.3 Centralized MIMO Control

The coupled equations of motion can be used to develop a single MIMO controller for the entire arm subsystem. The same control strategy applied in Section 3.1.2 is repeated here so that the tracking performance is a direct comparison between the SISO and MIMO frameworks.

Starting from Equation (3.53), grouping all of the nonlinear terms into a general vector-valued function produces a vector version of Equation (3.4),

$$\boldsymbol{M}(\boldsymbol{q})\ddot{\boldsymbol{q}} + \boldsymbol{N}(\boldsymbol{q}, \dot{\boldsymbol{q}}) = \boldsymbol{\tau}, \tag{3.59}$$

with

$$\boldsymbol{N}(\boldsymbol{q}, \dot{\boldsymbol{q}}) = \boldsymbol{C}(\boldsymbol{q}, \dot{\boldsymbol{q}})\dot{\boldsymbol{q}} + \boldsymbol{d}(\boldsymbol{q}, \dot{\boldsymbol{q}}) + \boldsymbol{g}(\boldsymbol{q}). \tag{3.60}$$

Define the linearizing change of variables according to

$$\boldsymbol{\tau} = \boldsymbol{M}(\boldsymbol{q})\left(\ddot{\boldsymbol{q}}_d - \boldsymbol{u}\right) + \boldsymbol{N}(\boldsymbol{q}, \dot{\boldsymbol{q}}), \tag{3.61}$$

where $\boldsymbol{u}$ is the new control input. The augmented error state composed of position and velocity tracking error is given by

$$\boldsymbol{e} = \begin{bmatrix} \boldsymbol{q}_d - \boldsymbol{q} \\ \dot{\boldsymbol{q}}_d - \dot{\boldsymbol{q}} \end{bmatrix}, \tag{3.62}$$

and the error dynamics are obtained by combining Equations (3.59)-(3.61) to form the double-integrator system

$$\dot{\boldsymbol{e}} = \begin{bmatrix} \dot{\boldsymbol{q}}_d - \dot{\boldsymbol{q}} \\ \ddot{\boldsymbol{q}}_d - \ddot{\boldsymbol{q}} \end{bmatrix} = \begin{bmatrix} \boldsymbol{0} & \boldsymbol{E} \\ \boldsymbol{0} & \boldsymbol{0} \end{bmatrix} \begin{bmatrix} \boldsymbol{q}_d - \boldsymbol{q} \\ \dot{\boldsymbol{q}}_d - \dot{\boldsymbol{q}} \end{bmatrix} + \begin{bmatrix} \boldsymbol{0} \\ \boldsymbol{E} \end{bmatrix} \boldsymbol{u}, \tag{3.63}$$

where $\boldsymbol{E}$ is the identity matrix of appropriate dimension. The standard LQR framework

can be applied to select gains for the state-feedback control law given by

$$\boldsymbol{u}(\boldsymbol{e}) = -\boldsymbol{K}\boldsymbol{e} = -\boldsymbol{K}_p(\boldsymbol{q}_d - \boldsymbol{q}) - \boldsymbol{K}_d(\dot{\boldsymbol{q}}_d - \dot{\boldsymbol{q}}), \tag{3.64}$$

and the full control law is obtained by substituting into Equation (3.61)

$$\boldsymbol{\tau} = \boldsymbol{M}(\boldsymbol{q})\left[\ddot{\boldsymbol{q}}_d + \boldsymbol{K}_p(\boldsymbol{q}_d - \boldsymbol{q}) + \boldsymbol{K}_d(\dot{\boldsymbol{q}}_d - \dot{\boldsymbol{q}})\right] + \boldsymbol{N}(\boldsymbol{q}, \dot{\boldsymbol{q}}). \tag{3.65}$$

To apply this controller to the arm subsystem, note that the trajectory of interest is composed of $\{\alpha, \beta, \dot{\gamma}\}$. For tracking purposes it is sufficient to set the other reference variables to zero, i.e. $\gamma_d = 0$, $\dot{\alpha}_d = \dot{\beta}_d = 0$, and $\ddot{\boldsymbol{q}}_d = \boldsymbol{0}$, since these variables would not be specified by a provided trajectory. Choosing the state weighting for γ to be small relative to the weighting for $\dot{\gamma}$ makes the corresponding column in $\boldsymbol{K}_p$ negligible so that the propeller control law again approximates a P type controller for the speed.

To make the comparison between architectures as direct as possible, the same weightings used in SISO control design are recycled for the MIMO controller. The state weighting matrix is then $\boldsymbol{Q} = \text{diag}\,(10,\ 10,\ 1 \times 10^{-6},\ 0.1,\ 0.1,\ 1)$, and the control weighting matrix is $\boldsymbol{R} = \text{diag}\,(0.1,\ 1 \times 10^{-3},\ 1 \times 10^{-3})$, where the values have been rearranged to match the ordering of the $\boldsymbol{q}$ and $\dot{\boldsymbol{q}}$ state vectors.

Fig. 3.10 shows the simulated performance of the MIMO controller tracking the square sample trajectory. Comparing this to the performance of the SISO controllers shown in Fig. 3.7, it can be seen that the deviations due to gyroscopic coupling have been almost completely eliminated. There is no noticeable disturbance to β due to the motion of α, and only a slight disturbance in α due to the motion of β. This is an absolutely essential characteristic for scaling these controllers to the whole twist-tilt copter, where perturbations in the arm angles results in unexpected thrust directions that can quickly lead to divergent behavior.

The commanded motor torques associated with this trajectory are shown in Fig. 3.11. All three commands remain within the motor capabilities at all times, meaning that there

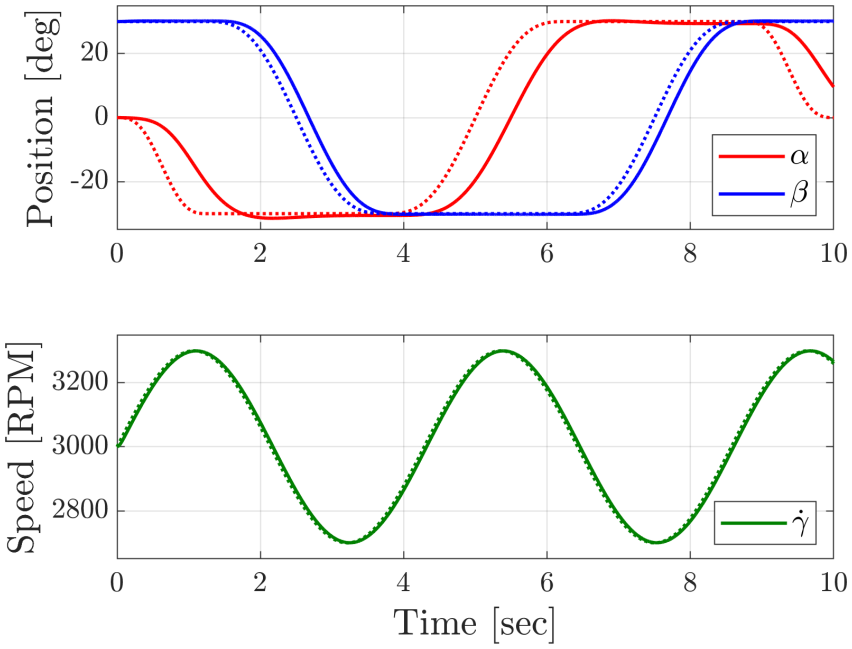

Figure 3.10: Simulated tracking performance of the MIMO controller. The reference trajectory shown in dashed lines is identical to Fig. 3.7 for comparison. Including coupling effects in the dynamic compensation has eliminated any significant perturbations in β due to the motion of α, and vice versa.

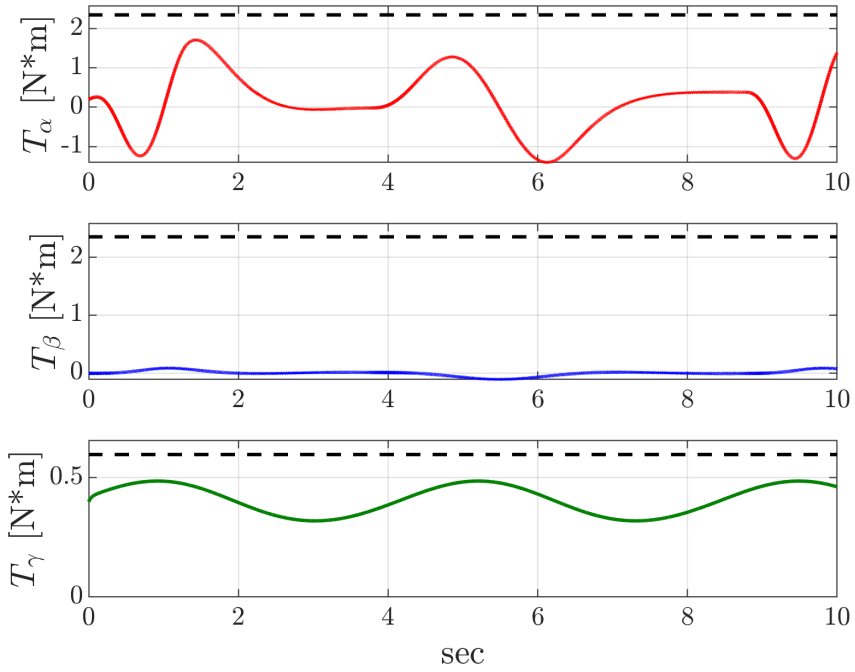

Figure 3.11: Commanded motor torques associated with the trajectory tracking shown in Fig. 3.10. Maximum motor torques obtained from the hardware datasheets are shown as black dashed lines. All motors remain below their torque limits at all times.

is some freedom to increase the response speed while still avoiding actuator saturation. In particular it may be desirable to shorten the rise time of the twist axis so that it more closely matches the tilt axis, which can be achieved by decreasing the weight in $\boldsymbol{R}$ corresponding to τ_α.

This chapter has demonstrated that a naïve modeling approach which ignores the couplings between motor axes is insufficient for control design, even for a single arm in isolation. Using an energy method, a model was developed for the coupled equations of motion of a single arm that considers certain Coriolis, centrifugal, gyroscopic, gravitational, and configuration-dependent inertial effects which were ignored in the initial model. While the coupled equations are certainly more complex, they are made computationally tractable by certain approximations from a priori knowledge of the system. Most notably, the large difference in speed regimes between the twist/tilt motors and the propeller motor allows the kinetic energy of the propeller to be approximated by a much simpler expression, dependent on fewer generalized coordinates and speeds. This set of coupled equations was used to synthesize a controller of identical form to the SISO controllers, and using identical LQR weightings, with nonlinear compensation to account for coupled dynamics. The result is a nonlinear controller which very nearly eliminates coupling perturbations and improves the tracking performance, even in a simulation which includes the full non-diagonal inertia matrices and center of mass offsets for the various bodies. The following chapter focuses on generalizing this modeling approach to include more arms and allow motion of the base link.

Chapter 4

Full Copter with Base Rotation

With the insight gained from Chapter 3 in modeling a single arm on a fixed base, this chapter focuses on the development of equations of motion describing all four arcs and allowing the base to rotate. The same Lagrangian approach is applied with increased complexity due to the base rotation, modeled as a 3-DOF spherical joint located at the base origin $\mathcal{B}$. The resulting model is expected to show a special coupling structure where the arms are independent of each other but are inherently linked through the rotating base. Finally, a modified hierarchical control structure is developed to track a specified attitude trajectory for the base link through command inputs to the arm motors.

While the arm subsystem was simple enough for approximate modeling by inspection, the full copter with base rotation includes 15 degrees of freedom, quickly rendering intuitive modeling infeasible. Hand-tuning gains for 15 controllers with coupled dynamics is a formidable task, and the author was unable to synthesize a controller by inspection which stabilizes the full copter for attitude tracking. For this reason, no baseline performance will be presented and a model-based approach which accounts for the nonlinear couplings is assumed necessary for stabilization.

4.1 Full Copter Lagrangian

The attitude of the twist-tilt copter is described by the 3-2-1 Tait-Bryan angle sequence from Section 2.1.1. These three angles are combined with the three motor angles of each arm to form the full vectors of 15 generalized coordinates and generalized speeds

$$\boldsymbol{q} = \begin{bmatrix} q_1 \\ q_2 \\ q_3 \\ \hdashline q_4 \\ q_5 \\ q_6 \\ \hdashline \vdots \\ \hdashline q_{13} \\ q_{14} \\ q_{15} \end{bmatrix} = \begin{bmatrix} \psi \\ \theta \\ \varphi \\ \hdashline \alpha_1 \\ \beta_1 \\ \gamma_1 \\ \hdashline \vdots \\ \hdashline \alpha_4 \\ \beta_4 \\ \gamma_4 \end{bmatrix}, \quad \dot{\boldsymbol{q}} = \begin{bmatrix} \dot{q}_1 \\ \dot{q}_2 \\ \dot{q}_3 \\ \hdashline \dot{q}_4 \\ \dot{q}_5 \\ \dot{q}_6 \\ \hdashline \vdots \\ \hdashline \dot{q}_{13} \\ \dot{q}_{14} \\ \dot{q}_{15} \end{bmatrix} = \begin{bmatrix} \dot{\psi} \\ \dot{\theta} \\ \dot{\varphi} \\ \hdashline \dot{\alpha}_1 \\ \dot{\beta}_1 \\ \dot{\gamma}_1 \\ \hdashline \vdots \\ \hdashline \dot{\alpha}_4 \\ \dot{\beta}_4 \\ \dot{\gamma}_4 \end{bmatrix}. \tag{4.1}$$

Let the total kinetic energy of the copter be denoted by T, and the total potential energy by U. The total energy is the sum of the base energy and all four arm energies, i.e.

$$T = T_{\mathcal{B}} + \sum_{i=1}^{4} \left(T_{\mathcal{A}^i} + T_{\mathcal{S}^i} + T_{\mathcal{P}^i} \right), \tag{4.2}$$

$$U = U_{\mathcal{B}} + \sum_{i=1}^{4} \left(U_{\mathcal{A}^i} + U_{\mathcal{S}^i} + U_{\mathcal{P}^i} \right). \tag{4.3}$$

The Lagrangian is defined in the usual way as

$$\mathcal{L} = T - U = T_{\mathcal{B}} + \sum_{i=1}^{4} \left(T_{\mathcal{A}^i} + T_{\mathcal{S}^i} + T_{\mathcal{P}^i} \right) - U_{\mathcal{B}} - \sum_{i=1}^{4} \left(U_{\mathcal{A}^i} + U_{\mathcal{S}^i} + U_{\mathcal{P}^i} \right), \tag{4.4}$$

and the Euler-Lagrange equations of motion are then formulated by

$$\frac{d}{dt} \left(\frac{\partial T}{\partial \dot{\boldsymbol{q}}} \right)^T - \left(\frac{\partial T}{\partial \boldsymbol{q}} \right)^T + \left(\frac{\partial U}{\partial \boldsymbol{q}} \right)^T = \boldsymbol{\xi}, \tag{4.5}$$

where $\boldsymbol{\xi}$ is the 15-vector of generalized forces. The scalar expansion of Equation (4.5) is omitted for brevity, but resembles an augmented version of Equation (3.19). The

following sections will evaluate the many partials of the Lagrangian addressing one body at a time before recombining to form the final equations of motion. The three sets of partial derivatives in Equation (4.5) will be referred to throughout this chapter as the kinetic energy speed partials, kinetic energy position partials, and potential energy partials respectively for shorthand.

4.2 Base Energy

The position of the base link center of mass is assumed fixed at the origin $\mathcal{O}$ by virtue of a spherical joint. The position and velocity vectors are thus zero for all time

$$\boldsymbol{r}^{\mathcal{B}/\mathcal{O}} = \boldsymbol{0}, \tag{4.6}$$

$$\boldsymbol{v}^{\mathcal{BN}} = \boldsymbol{0}. \tag{4.7}$$

The angular velocity of the base is obtained by combining rotations about the various axes described in Section 2.1.1, expressed in the $\mathcal{B}$ frame for ease of use

$$\begin{aligned} \boldsymbol{\omega}^{\mathcal{BN}} &= \dot{\psi}\,\hat{\boldsymbol{n}}_3 + \dot{\theta}\,\hat{\boldsymbol{b}}_2' + \dot{\varphi}\,\hat{\boldsymbol{b}}_1'' \\ &= \big(-\dot{\psi}s_\theta + \dot{\varphi}\big)\hat{\boldsymbol{b}}_1 + \big(\dot{\psi}c_\theta s_\varphi + \dot{\theta}c_\varphi\big)\hat{\boldsymbol{b}}_2 + \big(\dot{\psi}c_\theta c_\varphi - \dot{\theta}s_\varphi\big)\hat{\boldsymbol{b}}_3. \end{aligned} \tag{4.8}$$

With the inertial properties discussed in Section 2.2, the kinetic energy of the base link is calculated as

$$\begin{aligned} T_{\mathcal{B}} &= \frac{1}{2}m_{\mathcal{B}}\cancelto{0}{\big(\boldsymbol{v}^{\mathcal{BN}}\big)^T\big(\boldsymbol{v}^{\mathcal{BN}}\big)} + \frac{1}{2}\left(\boldsymbol{\omega}^{\mathcal{BN}}\right)^T \boldsymbol{I}_{\mathcal{B}}\left(\boldsymbol{\omega}^{\mathcal{BN}}\right) \\ &= \frac{1}{2}I_{\mathcal{B}}^x\big(-\dot{\psi}s_\theta + \dot{\varphi}\big)^2 + \frac{1}{2}I_{\mathcal{B}}^y\big(\dot{\psi}c_\theta s_\varphi + \dot{\theta}c_\varphi\big)^2 + \frac{1}{2}I_{\mathcal{B}}^z\big(\dot{\psi}c_\theta c_\varphi - \dot{\theta}s_\varphi\big)^2, \end{aligned} \tag{4.9}$$

which is dependent on two of the angles and all three of the base angular rates. In this form no statements can be made about the relative importance of one term over another since all angular rates are expected to be comparable in magnitude; however, consider

evaluating the kinetic energy speed partial corresponding to ψ:

$$\frac{d}{dt}\left(\frac{\partial T_{\mathcal{B}}}{\partial \dot{\psi}}\right) = I^x_{\mathcal{B}}\big(\ddot{\psi}s^2_\theta + \dot{\psi}\dot{\theta}s_{2\theta} - \ddot{\varphi}s_\theta - \dot{\theta}\dot{\varphi}c_\theta\big) + \big(I^y_{\mathcal{B}} - I^z_{\mathcal{B}}\big)\dot{\psi}\dot{\varphi}c^2_\theta s_{2\varphi}$$
$$+ \big(I^y_{\mathcal{B}}s^2_\varphi + I^z_{\mathcal{B}}c^2_\varphi\big)\ddot{\psi}c^2_\theta - \big(I^y_{\mathcal{B}}s^2_\varphi + I^z_{\mathcal{B}}c^2_\varphi\big)\dot{\psi}\dot{\theta}s_{2\theta}$$
$$+ \big(I^y_{\mathcal{B}} - I^z_{\mathcal{B}}\big)\left(\frac{1}{2}\ddot{\theta}c_\theta s_{2\varphi} - \frac{1}{2}\dot{\theta}^2 s_\theta s_{2\varphi} + \dot{\theta}\dot{\varphi}c_\theta c_{2\varphi}\right)$$

This expression contains a mixture of inertial terms, corresponding to angular accelerations; and coupling terms, corresponding to products of angular rates. The acceleration terms must be retained in order to form meaningful equations of motion, however the coupling terms can be neglected. As justification, consider that each row of Equation (4.5) will contain many coupling terms corresponding to various pairings of generalized speeds. Due to the large discrepancy in angular rates, the gyroscopic effects depending on some $\dot{\gamma}_i$ term will far outweigh the centrifugal and Coriolis effects which do not depend on any $\dot{\gamma}_i$ terms. The energy speed partial above can thus be reduced without great effect on the final equations of motion

$$\frac{d}{dt}\left(\frac{\partial T_{\mathcal{B}}}{\partial \dot{\psi}}\right) \approx I^x_{\mathcal{B}}\ddot{\psi}s^2_\theta + \big(I^y_{\mathcal{B}}s^2_\varphi + I^z_{\mathcal{B}}c^2_\varphi\big)\ddot{\psi}c^2_\theta + \frac{1}{2}\big(I^y_{\mathcal{B}} - I^z_{\mathcal{B}}\big)\ddot{\theta}c_\theta s_{2\varphi} - I^x_{\mathcal{B}}\ddot{\varphi}s_\theta. \tag{4.10}$$

Similar approximations can be made to obtain the partials of the Lagrangian with respect to the other base speeds

$$\frac{d}{dt}\left(\frac{\partial T_{\mathcal{B}}}{\partial \dot{\theta}}\right) \approx \frac{1}{2}\big(I^y_{\mathcal{B}} - I^z_{\mathcal{B}}\big)\ddot{\psi}c_\theta s_{2\varphi} + \big(I^y_{\mathcal{B}}c^2_\varphi + I^z_{\mathcal{B}}s^2_\varphi\big)\ddot{\theta}, \tag{4.11}$$

$$\frac{d}{dt}\left(\frac{\partial T_{\mathcal{B}}}{\partial \dot{\varphi}}\right) \approx -I^x_{\mathcal{B}}\ddot{\psi}s_\theta + I^x_{\mathcal{B}}\ddot{\varphi}. \tag{4.12}$$

In neglecting certain terms one must take care to maintain certain properties of the final model, such as symmetry and positive-definiteness of the inertia matrix. These properties can be directly observed in the approximated partials by noting that the cross

coefficients are identical and the diagonal terms are nonnegative. For example, the coefficient for $\ddot{\theta}$ in Equation (4.10) is equivalent to the coefficient for $\ddot{\psi}$ in Equation (4.11). This symmetry also holds for $\ddot{\varphi}$ in Equation (4.10) with $\ddot{\psi}$ in Equation (4.12). Additionally, the coefficients for $\ddot{\psi}$ in Equation (4.10), for $\ddot{\theta}$ in Equation (4.11), and for $\ddot{\varphi}$ in Equation (4.12) are nonnegative.

Continuing with the kinetic energy position partials, note that Equation (4.9) is not dependent on any $\dot{\gamma}_i$ terms. This means that none of the partial derivatives with respect to generalized coordinates will depend on a $\dot{\gamma}_i$ term, and thus all of the kinetic energy position partials can be neglected with the same justification used above for simplifying the kinetic energy speed partials. This pattern will also hold for the arc and shaft kinetic energies, greatly reducing the number of terms in the final model.

Finally, taking the reference point for gravitational potential energy to be the origin $\mathcal{O}$, the base potential energy remains zero at all times by assumption of the spherical joint. The potential energy partials for the base are thus zero for all time.

With all of these simplifications, Equations (4.10)-(4.12) are a complete description of the base energy for the equations of motion.

4.3 Arm Energy

In order to adapt the findings from Chapter 3 for a rotating base, the angular velocity of each body must incorporate extra terms corresponding to the base link rotation. Equation (4.8) describes this angular velocity in the $\mathcal{B}$ frame, however it is useful to express the base rotation in the various $\mathcal{B}^i$ frames and develop a general expression for the Lagrangian partials of arm i which can be applied to each arm in sequence. This is more convenient than rotating the inertia matrices of every arm component into the $\mathcal{B}$ frame.

Let the angular velocity of the base link be given by

$$\boldsymbol{\omega}^{\mathcal{BN}} = \dot{\Phi}_i \, \hat{\boldsymbol{b}}_1^i + \dot{\Theta}_i \, \hat{\boldsymbol{b}}_2^i + \dot{\Psi} \, \hat{\boldsymbol{b}}_3^i, \tag{4.13}$$

where $\dot{\Phi}_i$, $\dot{\Theta}_i$, $\dot{\Psi}_i$ are the effective roll, pitch, and yaw rates as seen in the $\mathcal{B}^i$ frame. These rates are obtained by multiplying the components of Equation (4.8) with the corresponding DCM defined in Equation (2.6)

$$\begin{bmatrix} \dot{\Phi}_i \\ \dot{\Theta}_i \\ \dot{\Psi}_i \end{bmatrix} = \boldsymbol{R}_i^T \begin{bmatrix} -\dot{\psi} s_\theta + \dot{\varphi} \\ \dot{\psi} c_\theta s_\varphi + \dot{\theta} c_\varphi \\ \dot{\psi} c_\theta c_\varphi - \dot{\theta} s_\varphi \end{bmatrix}. \tag{4.14}$$

Note that the yaw rate is the same for all i because the $\mathcal{B}^i$ frames are related by constant rotations about the yaw axis. The following sections incorporate the base angular velocity into the arm components to derive generic equations for the Lagrange partials.

4.3.1 Arc

To generalize Section 3.2.1 for any arm on a rotating base, the position is written in terms of unit vectors for arm i

$$\boldsymbol{r}^{\mathcal{A}^i/\mathcal{B}} = \ell_{\mathcal{A}}\, \hat{\boldsymbol{b}}_1^i = \ell_{\mathcal{A}}\, \hat{\boldsymbol{a}}_1^i. \tag{4.15}$$

The angular velocity is expanded to include the base rotation according to

$$\begin{aligned} \boldsymbol{\omega}^{\mathcal{A}^i\mathcal{N}} &= \boldsymbol{\omega}^{\mathcal{A}^i\mathcal{B}} + \boldsymbol{\omega}^{\mathcal{B}\mathcal{N}} \\ &= \left(\dot{\alpha}_i + \dot{\Phi}_i\right) \hat{\boldsymbol{b}}_1^i + \dot{\Theta}_i\, \hat{\boldsymbol{b}}_2^i + \dot{\Psi}\, \hat{\boldsymbol{b}}_3^i. \end{aligned} \tag{4.16}$$

Though the arc center of mass is fixed with respect to the $\mathcal{B}^i$ frame, the rotation of the base link confers a linear velocity to the arc center of mass, given by

$$\begin{aligned} \boldsymbol{v}^{\mathcal{A}^i\mathcal{N}} &= \boldsymbol{\omega}^{\mathcal{B}^i\mathcal{N}} \times \boldsymbol{r}^{\mathcal{A}^i/\mathcal{B}} \\ &= \ell_{\mathcal{A}} \dot{\Psi}\, \hat{\boldsymbol{b}}_2^i - \ell_{\mathcal{A}} \dot{\Theta}_i\, \hat{\boldsymbol{b}}_3^i. \end{aligned} \tag{4.17}$$

With the linear and angular velocity expressed in the $\mathcal{B}^i$ frame, the inertia matrix must be rotated into the $\mathcal{B}^i$ frame by projecting Equation (2.11) through the proper DCM

$$\boldsymbol{R}_{\mathcal{B}^i\mathcal{A}^i}\boldsymbol{I}_{\mathcal{A}}\boldsymbol{R}_{\mathcal{A}^i\mathcal{B}^i} = \begin{bmatrix} I^x_{\mathcal{A}} & 0 & 0 \\ 0 & I^y_{\mathcal{A}}c^2_{\alpha_i} + I^z_{\mathcal{A}}s^2_{\alpha_i} & \left(I^y_{\mathcal{A}} - I^z_{\mathcal{A}}\right)s_{\alpha_i}c_{\alpha_i} \\ 0 & \left(I^y_{\mathcal{A}} - I^z_{\mathcal{A}}\right)s_{\alpha_i}c_{\alpha_i} & I^y_{\mathcal{A}}s^2_{\alpha_i} + I^z_{\mathcal{A}}c^2_{\alpha_i} \end{bmatrix}. \tag{4.18}$$

It is useful to split the kinetic energy into translational and rotational contributions defined by

$$\begin{aligned} T^v_{\mathcal{A}^i} &= \frac{1}{2}m_{\mathcal{A}}\left(\boldsymbol{v}^{\mathcal{A}^i\mathcal{N}}\right)^T\left(\boldsymbol{v}^{\mathcal{A}^i\mathcal{N}}\right) \\ &= \frac{1}{2}m_{\mathcal{A}}\ell^2_{\mathcal{A}}\dot{\Theta}^2_i + \frac{1}{2}m_{\mathcal{A}}\ell^2_{\mathcal{A}}\dot{\Psi}^2 \end{aligned} \tag{4.19}$$

and

$$\begin{aligned} T^{\omega}_{\mathcal{A}^i} &= \frac{1}{2}\left(\boldsymbol{\omega}^{\mathcal{A}^i\mathcal{N}}\right)^T\boldsymbol{R}_{\mathcal{B}^i\mathcal{A}^i}\boldsymbol{I}_{\mathcal{A}}\boldsymbol{R}_{\mathcal{A}^i\mathcal{B}^i}\left(\boldsymbol{\omega}^{\mathcal{A}^i\mathcal{N}}\right) \\ &= \frac{1}{2}\left(I^y_{\mathcal{A}}c^2_{\alpha_i} + I^z_{\mathcal{A}}s^2_{\alpha_i}\right)\dot{\Theta}^2_i + \frac{1}{2}\left(I^y_{\mathcal{A}}s^2_{\alpha_i} + I^z_{\mathcal{A}}c^2_{\alpha_i}\right)\dot{\Psi}^2 + \left(I^y_{\mathcal{A}} - I^z_{\mathcal{A}}\right)s_{\alpha_i}c_{\alpha_i}\dot{\Theta}_i\dot{\Psi}. \end{aligned} \tag{4.20}$$

The total kinetic energy of the arc is then

$$T_{\mathcal{A}^i} = T^v_{\mathcal{A}^i} + T^{\omega}_{\mathcal{A}^i}. \tag{4.21}$$

The nonzero Lagrange speed partials of the translational kinetic energy in Equation (4.19) are

$$\frac{\partial T^v_{\mathcal{A}^i}}{\partial\dot{\psi}} = m_{\mathcal{A}}\ell^2_{\mathcal{A}}\left(\dot{\Theta}_i\frac{\partial\dot{\Theta}_i}{\partial\dot{\psi}} + \dot{\Psi}_i\frac{\partial\dot{\Psi}_i}{\partial\dot{\psi}}\right), \tag{4.22}$$

$$\frac{\partial T^v_{\mathcal{A}^i}}{\partial\dot{\theta}} = m_{\mathcal{A}}\ell^2_{\mathcal{A}}\left(\dot{\Theta}_i\frac{\partial\dot{\Theta}_i}{\partial\dot{\theta}} + \dot{\Psi}_i\frac{\partial\dot{\Psi}_i}{\partial\dot{\theta}}\right), \tag{4.23}$$

$$\frac{\partial T^v_{\mathcal{A}^i}}{\partial\dot{\varphi}} = m_{\mathcal{A}}\ell^2_{\mathcal{A}}\dot{\Theta}_i\frac{\partial\dot{\Theta}_i}{\partial\dot{\varphi}}, \tag{4.24}$$

where the partial with respect to $\dot{\varphi}$ has simplified slightly because $\dot{\Psi}$ has no dependence on $\dot{\varphi}$. The nonzero speed partials of the rotational kinetic energy in Equation (4.20) are

$$\frac{\partial T^{\omega}_{\mathcal{A}^i}}{\partial \dot{\psi}} = I^x_{\mathcal{A}}\big(\dot{\alpha}_i + \dot{\Phi}_i\big)\frac{\partial \dot{\Phi}_i}{\partial \dot{\psi}} + \big(I^y_{\mathcal{A}} c^2_{\alpha_i} + I^z_{\mathcal{A}} s^2_{\alpha_i}\big)\dot{\Theta}_i \frac{\partial \dot{\Theta}_i}{\partial \dot{\psi}} + \big(I^y_{\mathcal{A}} s^2_{\alpha_i} + I^z_{\mathcal{A}} c^2_{\alpha_i}\big)\dot{\Psi}\frac{\partial \dot{\Psi}}{\partial \dot{\psi}} + \big(I^y_{\mathcal{A}} - I^z_{\mathcal{A}}\big)s_{\alpha_i} c_{\alpha_i}\left(\frac{\partial \dot{\Theta}_i}{\partial \dot{\psi}}\dot{\Psi} + \dot{\Theta}_i \frac{\partial \dot{\Psi}}{\partial \dot{\psi}}\right), \quad (4.25)$$

$$\frac{\partial T^{\omega}_{\mathcal{A}^i}}{\partial \dot{\theta}} = I^x_{\mathcal{A}}\big(\dot{\alpha}_i + \dot{\Phi}_i\big)\frac{\partial \dot{\Phi}_i}{\partial \dot{\theta}} + \big(I^y_{\mathcal{A}} c^2_{\alpha_i} + I^z_{\mathcal{A}} s^2_{\alpha_i}\big)\dot{\Theta}_i \frac{\partial \dot{\Theta}_i}{\partial \dot{\theta}} + \big(I^y_{\mathcal{A}} s^2_{\alpha_i} + I^z_{\mathcal{A}} c^2_{\alpha_i}\big)\dot{\Psi}\frac{\partial \dot{\Psi}}{\partial \dot{\theta}} + \big(I^y_{\mathcal{A}} - I^z_{\mathcal{A}}\big)s_{\alpha_i} c_{\alpha_i}\left(\frac{\partial \dot{\Theta}_i}{\partial \dot{\theta}}\dot{\Psi} + \dot{\Theta}_i \frac{\partial \dot{\Psi}}{\partial \dot{\theta}}\right), \quad (4.26)$$

$$\frac{\partial T^{\omega}_{\mathcal{A}^i}}{\partial \dot{\varphi}} = I^x_{\mathcal{A}}\big(\dot{\alpha}_i + \dot{\Phi}_i\big)\frac{\partial \dot{\Phi}_i}{\partial \dot{\varphi}} + \big(I^y_{\mathcal{A}} c^2_{\alpha_i} + I^z_{\mathcal{A}} s^2_{\alpha_i}\big)\dot{\Theta}_i \frac{\partial \dot{\Theta}_i}{\partial \dot{\varphi}} + \big(I^y_{\mathcal{A}} - I^z_{\mathcal{A}}\big)s_{\alpha_i} c_{\alpha_i}\frac{\partial \dot{\Theta}_i}{\partial \dot{\varphi}}\dot{\Psi}, \quad (4.27)$$

$$\frac{\partial T^{\omega}_{\mathcal{A}^i}}{\partial \dot{\alpha}_i} = I^x_{\mathcal{A}}\big(\dot{\alpha}_i + \dot{\Phi}_i\big). \quad (4.28)$$

The final Lagrange equations depend on the time derivatives of the above partials, however further differentiation is impractical in this general form. The operation will be carried out in subsequent sections which apply to specific arms.

Similar to the base, the kinetic energy of the arcs is not dependent on any $\dot{\gamma}_i$ terms. Therefore none of the position partials will depend on $\dot{\gamma}_i$ terms, and so the position partials can be neglected relative to the gyroscopic couplings which will arise in the generalized forces.

The potential energy obtained by projecting the center of mass position onto the vertical axis and multiplying by the weight

$$\begin{aligned} U_{\mathcal{A}^i} &= m_{\mathcal{A}} g_0 \, \boldsymbol{r}^{\mathcal{A}^i/\mathcal{B}} \cdot \hat{\boldsymbol{n}}_3 \\ &= m_{\mathcal{A}} g_0 \big(\ell_{\mathcal{A}} \, \hat{\boldsymbol{b}}^i_1\big) \cdot \big(- s_\theta \, \hat{\boldsymbol{b}}^1_1 + c_\theta s_\varphi \, \hat{\boldsymbol{b}}^1_2 + c_\theta c_\varphi \, \hat{\boldsymbol{b}}^1_3\big). \end{aligned} \quad (4.29)$$

This expression will have different coordinate dependencies for the various arms, and so

the partial derivatives will be evaluated in subsequent sections.

4.3.2 Shaft

The previous results for the shaft can be generalized in the same way as the arc. The position, angular velocity, and linear velocity of the shaft are now given by

$$\boldsymbol{r}^{\mathcal{S}^i/\mathcal{B}} = \ell_{\mathcal{S}}\,\hat{\boldsymbol{b}}_1^i = \ell_{\mathcal{S}}\,\hat{\boldsymbol{a}}_1^i, \tag{4.30}$$

$$\begin{aligned}\boldsymbol{\omega}^{\mathcal{S}^i\mathcal{N}} &= \boldsymbol{\omega}^{\mathcal{S}^i\mathcal{B}} + \boldsymbol{\omega}^{\mathcal{B}\mathcal{N}} \\ &= \left(\dot{\alpha}_i + \dot{\Phi}_i\right)\hat{\boldsymbol{b}}_1^i + \left(\dot{\beta}_i c_{\alpha_i} + \dot{\Theta}_i\right)\hat{\boldsymbol{b}}_2^i + \left(\dot{\beta}_i s_{\alpha_i} + \dot{\Psi}\right)\hat{\boldsymbol{b}}_3^i,\end{aligned} \tag{4.31}$$

$$\begin{aligned}\boldsymbol{v}^{\mathcal{S}^i\mathcal{N}} &= \boldsymbol{\omega}^{\mathcal{B}\mathcal{N}} \times \boldsymbol{r}^{\mathcal{S}^i/\mathcal{B}} \\ &= \ell_{\mathcal{S}}\dot{\Psi}\,\hat{\boldsymbol{b}}_2^i - \ell_{\mathcal{S}}\dot{\Theta}_i\,\hat{\boldsymbol{b}}_3^i,\end{aligned} \tag{4.32}$$

which are all expressed in the $\mathcal{B}^i$ frame. Rotating the shaft inertia into the $\mathcal{B}^i$ frame using the proper DCMs results in

$$\boldsymbol{R}_{\mathcal{B}^i\mathcal{A}^i}\boldsymbol{R}_{\mathcal{A}^i\mathcal{S}^i}\boldsymbol{I}_{\mathcal{S}}\boldsymbol{R}_{\mathcal{S}^i\mathcal{A}^i}\boldsymbol{R}_{\mathcal{A}^i\mathcal{B}^i} =$$
$$\begin{bmatrix} I_{\mathcal{S}}^x c_{\beta_i}^2 + I_{\mathcal{S}}^z s_{\beta_i}^2 & \left(I_{\mathcal{S}}^x - I_{\mathcal{S}}^z\right)s_{\alpha_i}s_{\beta_i}c_{\beta_i} & \left(I_{\mathcal{S}}^z - I_{\mathcal{S}}^x\right)c_{\alpha_i}s_{\beta_i}c_{\beta_i} \\ \left(I_{\mathcal{S}}^x - I_{\mathcal{S}}^z\right)s_{\alpha_i}s_{\beta_i}c_{\beta_i} & I_{\mathcal{S}}^y c_{\alpha_i}^2 + \left(I_{\mathcal{S}}^x s_{\beta_i}^2 + I_{\mathcal{S}}^z c_{\beta_i}^2\right)s_{\alpha_i}^2 & I_{\mathcal{S}}^y s_{\alpha_i}c_{\alpha_i} - \left(I_{\mathcal{S}}^x s_{\beta_i}^2 + I_{\mathcal{S}}^z c_{\beta_i}^2\right)s_{\alpha_i}c_{\alpha_i} \\ \left(I_{\mathcal{S}}^z - I_{\mathcal{S}}^x\right)c_{\alpha_i}s_{\beta_i}c_{\beta_i} & I_{\mathcal{S}}^y s_{\alpha_i}c_{\alpha_i} - \left(I_{\mathcal{S}}^x s_{\beta_i}^2 + I_{\mathcal{S}}^z c_{\beta_i}^2\right)s_{\alpha_i}c_{\alpha_i} & I_{\mathcal{S}}^y s_{\alpha_i}^2 + \left(I_{\mathcal{S}}^x s_{\beta_i}^2 + I_{\mathcal{S}}^z c_{\beta_i}^2\right)c_{\alpha_i}^2 \end{bmatrix}.$$

Recalling that the shaft is nearly symmetric about the $\mathcal{S}_2^i$ axis, the approximation $I_{\mathcal{S}}^x \approx I_{\mathcal{S}}^z$ allows for simplification

$$\boldsymbol{R}_{\mathcal{B}^i\mathcal{A}^i}\boldsymbol{R}_{\mathcal{A}^i\mathcal{S}^i}\boldsymbol{I}_{\mathcal{S}}\boldsymbol{R}_{\mathcal{S}^i\mathcal{A}^i}\boldsymbol{R}_{\mathcal{A}^i\mathcal{B}^i} \approx \begin{bmatrix} I_{\mathcal{S}}^{xz} & 0 & 0 \\ 0 & I_{\mathcal{S}}^y c_{\alpha_i}^2 + I_{\mathcal{S}}^{xz} s_{\alpha_i}^2 & \left(I_{\mathcal{S}}^y - I_{\mathcal{S}}^{xz}\right)s_{\alpha_i}c_{\alpha_i} \\ 0 & \left(I_{\mathcal{S}}^y - I_{\mathcal{S}}^{xz}\right)s_{\alpha_i}c_{\alpha_i} & I_{\mathcal{S}}^y s_{\alpha_i}^2 + I_{\mathcal{S}}^{xz} c_{\alpha_i}^2 \end{bmatrix}. \tag{4.33}$$

The kinetic energy is split into translational and rotational contributions defined by

$$\begin{aligned} T_{\mathcal{S}^i}^v &= \frac{1}{2} m_{\mathcal{S}} \left(\boldsymbol{v}^{\mathcal{S}^i\mathcal{N}}\right)^T \left(\boldsymbol{v}^{\mathcal{S}^i\mathcal{N}}\right) \\ &= \frac{1}{2} m_{\mathcal{S}} \ell_{\mathcal{S}}^2 \dot{\Theta}_i^2 + \frac{1}{2} m_{\mathcal{S}} \ell_{\mathcal{S}}^2 \dot{\Psi}^2 \end{aligned} \tag{4.34}$$

and

$$\begin{aligned} T_{\mathcal{S}^i}^\omega &= \frac{1}{2} \left(\boldsymbol{\omega}^{\mathcal{S}^i\mathcal{N}}\right)^T \boldsymbol{R}_{\mathcal{B}^i\mathcal{A}^i} \boldsymbol{R}_{\mathcal{A}^i\mathcal{S}^i} \boldsymbol{I}_{\mathcal{S}} \boldsymbol{R}_{\mathcal{S}^i\mathcal{A}^i} \boldsymbol{R}_{\mathcal{A}^i\mathcal{B}^i} \left(\boldsymbol{\omega}^{\mathcal{S}^i\mathcal{N}}\right) \\ &= \frac{1}{2} I_{\mathcal{S}}^{xz} \left(\dot{\alpha}_i^2 + \dot{\Phi}_i\right)^2 + \frac{1}{2} \left(I_{\mathcal{S}}^y c_{\alpha_i}^2 + I_{\mathcal{S}}^{xz} s_{\alpha_i}^2\right) \left(\dot{\beta}_i c_{\alpha_i} + \dot{\Theta}_i\right)^2 + \frac{1}{2} \left(I_{\mathcal{S}}^y s_{\alpha_i}^2 + I_{\mathcal{S}}^{xz} c_{\alpha_i}^2\right) \left(\dot{\beta}_i s_{\alpha_i} + \dot{\Psi}\right)^2 \\ &\quad + \left(I_{\mathcal{S}}^y - I_{\mathcal{S}}^{xz}\right) s_{\alpha_i} c_{\alpha_i} \left(\dot{\beta}_i c_{\alpha_i} + \dot{\Theta}_i\right) \left(\dot{\beta}_i s_{\alpha_i} + \dot{\Psi}\right), \end{aligned} \tag{4.35}$$

with the total kinetic energy of the shaft given by

$$T_{\mathcal{S}^i} = T_{\mathcal{S}^i}^v + T_{\mathcal{S}^i}^\omega. \tag{4.36}$$

The nonzero speed partials of the translational kinetic energy in Equation (4.34) are

$$\frac{\partial T_{\mathcal{S}^i}^v}{\partial \dot{\psi}} = m_{\mathcal{S}} \ell_{\mathcal{S}}^2 \left(\dot{\Theta}_i \frac{\partial \dot{\Theta}_i}{\partial \dot{\psi}} + \dot{\Psi}_i \frac{\partial \dot{\Psi}_i}{\partial \dot{\psi}}\right), \tag{4.37}$$

$$\frac{\partial T_{\mathcal{S}^i}^v}{\partial \dot{\theta}} = m_{\mathcal{S}} \ell_{\mathcal{S}}^2 \left(\dot{\Theta}_i \frac{\partial \dot{\Theta}_i}{\partial \dot{\theta}} + \dot{\Psi}_i \frac{\partial \dot{\Psi}_i}{\partial \dot{\theta}}\right), \tag{4.38}$$

$$\frac{\partial T_{\mathcal{S}^i}^v}{\partial \dot{\varphi}} = m_{\mathcal{S}} \ell_{\mathcal{S}}^2 \dot{\Theta}_i \frac{\partial \dot{\Theta}_i}{\partial \dot{\varphi}}, \tag{4.39}$$

which are very similar in form to the translational kinetic energy speed partials of the arc. This is expected because the linear velocities of the arc and shaft centers of mass behave in exactly in the same way due to their fixed locations on the $\mathcal{B}_1^i$ axis. The nonzero speed partials of the rotational kinetic energy in Equation (4.35) are

$$\frac{\partial T_{\mathcal{S}^i}^\omega}{\partial \dot{\psi}} = I_{\mathcal{S}}^{xz} \left(\dot{\alpha}_i + \dot{\Phi}_i\right) \frac{\partial \dot{\Phi}_i}{\partial \dot{\psi}} + \left(I_{\mathcal{S}}^y c_{\alpha_i}^2 + I_{\mathcal{S}}^{xz} s_{\alpha_i}^2\right) \left(\dot{\beta}_i c_{\alpha_i} + \dot{\Theta}_i\right) \frac{\partial \dot{\Theta}_i}{\partial \dot{\psi}}$$

$$+\left(I_{\mathcal{S}}^{y}s_{\alpha_i}^{2}+I_{\mathcal{S}}^{xz}c_{\alpha_i}^{2}\right)\left(\dot{\beta}_i s_{\alpha_i}+\dot{\Psi}_i\right)\frac{\partial\dot{\Psi}_i}{\partial\dot{\psi}}$$
$$+\left(I_{\mathcal{S}}^{y}-I_{\mathcal{S}}^{xz}\right)s_{\alpha_i}c_{\alpha_i}\left[\frac{\partial\dot{\Theta}_i}{\partial\dot{\psi}}\left(\dot{\beta}_i s_{\alpha_i}+\dot{\Psi}\right)+\left(\dot{\beta}_i c_{\alpha_i}+\dot{\Theta}_i\right)\frac{\partial\dot{\Psi}}{\partial\dot{\psi}}\right], \quad (4.40)$$

$$\frac{\partial T_{\mathcal{S}^i}^{\omega}}{\partial\dot{\theta}}=I_{\mathcal{S}}^{xz}\left(\dot{\alpha}_i+\dot{\Phi}_i\right)\frac{\partial\dot{\Phi}_i}{\partial\dot{\theta}}+\left(I_{\mathcal{S}}^{y}c_{\alpha_i}^{2}+I_{\mathcal{S}}^{xz}s_{\alpha_i}^{2}\right)\left(\dot{\beta}_i c_{\alpha_i}+\dot{\Theta}_i\right)\frac{\partial\dot{\Theta}_i}{\partial\dot{\theta}}$$
$$+\left(I_{\mathcal{S}}^{y}s_{\alpha_i}^{2}+I_{\mathcal{S}}^{xz}c_{\alpha_i}^{2}\right)\left(\dot{\beta}_i s_{\alpha_i}+\dot{\Psi}_i\right)\frac{\partial\dot{\Psi}_i}{\partial\dot{\theta}}$$
$$+\left(I_{\mathcal{S}}^{y}-I_{\mathcal{S}}^{xz}\right)s_{\alpha_i}c_{\alpha_i}\left[\frac{\partial\dot{\Theta}_i}{\partial\dot{\theta}}\left(\dot{\beta}_i s_{\alpha_i}+\dot{\Psi}\right)+\left(\dot{\beta}_i c_{\alpha_i}+\dot{\Theta}_i\right)\frac{\partial\dot{\Psi}}{\partial\dot{\theta}}\right], \quad (4.41)$$

$$\frac{\partial T_{\mathcal{S}^i}^{\omega}}{\partial\dot{\varphi}}=I_{\mathcal{S}}^{xz}\left(\dot{\alpha}_i+\dot{\Phi}_i\right)\frac{\partial\dot{\Phi}_i}{\partial\dot{\varphi}}+\left(I_{\mathcal{S}}^{y}c_{\alpha_i}^{2}+I_{\mathcal{S}}^{xz}s_{\alpha_i}^{2}\right)\left(\dot{\beta}_i c_{\alpha_i}+\dot{\Theta}_i\right)\frac{\partial\dot{\Theta}_i}{\partial\dot{\varphi}}$$
$$+\left(I_{\mathcal{S}}^{y}-I_{\mathcal{S}}^{xz}\right)s_{\alpha_i}c_{\alpha_i}\frac{\partial\dot{\Theta}_i}{\partial\dot{\varphi}}\left(\dot{\beta}_i s_{\alpha_i}+\dot{\Psi}\right) \quad (4.42)$$

$$\frac{\partial T_{\mathcal{S}^i}^{\omega}}{\partial\dot{\alpha}_i}=I_{\mathcal{S}}^{xz}\left(\dot{\alpha}_i+\dot{\Phi}_i\right), \quad (4.43)$$

$$\frac{\partial T_{\mathcal{S}^i}^{\omega}}{\partial\dot{\beta}_i}=\left(I_{\mathcal{S}}^{y}c_{\alpha_i}^{2}+I_{\mathcal{S}}^{xz}s_{\alpha_i}^{2}\right)\left(\dot{\beta}_i c_{\alpha_i}+\dot{\Theta}_i\right)c_{\alpha_i}+\left(I_{\mathcal{S}}^{y}s_{\alpha_i}^{2}+I_{\mathcal{S}}^{xz}c_{\alpha_i}^{2}\right)\left(\dot{\beta}_i s_{\alpha_i}+\dot{\Psi}_i\right)s_{\alpha_i}$$
$$+\left(I_{\mathcal{S}}^{y}-I_{\mathcal{S}}^{xz}\right)s_{\alpha_i}c_{\alpha_i}\left[c_{\alpha_i}\left(\dot{\beta}_i s_{\alpha_i}+\dot{\Psi}\right)+\left(\dot{\beta}_i c_{\alpha_i}+\dot{\Theta}_i\right)s_{\alpha_i}\right]. \quad (4.44)$$

The time derivatives of the above partials will be calculated in subsequent sections, and the kinetic energy position partials will be neglected due to a lack of dependence on the large magnitude $\dot{\gamma}_i$ terms.

The potential energy is obtained by projecting the center of mass position onto the

vertical axis and multiplying by the weight

$$\begin{aligned} U_{\mathcal{S}^i} &= m_{\mathcal{S}} g_0 \, \boldsymbol{r}^{\mathcal{S}^i/\mathcal{B}} \cdot \hat{\boldsymbol{n}}_3 \\ &= m_{\mathcal{S}} g_0 \big(\ell_{\mathcal{S}} \, \hat{\boldsymbol{b}}_1^i\big) \cdot \big(- s_\theta \, \hat{\boldsymbol{b}}_1^1 + c_\theta s_\varphi \, \hat{\boldsymbol{b}}_2^1 + c_\theta c_\varphi \, \hat{\boldsymbol{b}}_3^1\big). \end{aligned} \tag{4.45}$$

which again is similar in form to the potential energy of the arc due to the identical behavior of the arc center of mass. The partial derivatives will be evaluated in later sections which pertain to particular arms.

4.3.3 Propeller

Unlike the arc and shaft, the position of the propeller center of mass depends on the arm configuration and is thus a much more complicated expression. The position relative to the base origin is given by

$$\boldsymbol{r}^{\mathcal{P}^i/\mathcal{B}} = \ell_{\mathcal{S}} \, \hat{\boldsymbol{a}}_1^i + \ell_{\mathcal{P}} \, \hat{\boldsymbol{s}}_3^i \tag{4.46}$$

The angular velocity includes terms for the rotations of the base, arc, shaft, and propeller combined

$$\boldsymbol{\omega}^{\mathcal{P}^i\mathcal{N}} = \big(\dot{\alpha}_i + \dot{\gamma}_i s_{\beta_i} + \dot{\Phi}_i\big)\hat{\boldsymbol{b}}_1^i + \big(\dot{\beta}_i c_{\alpha_i} - \dot{\gamma}_i s_{\alpha_i} c_{\beta_i} + \dot{\Theta}_i\big)\hat{\boldsymbol{b}}_2^i + \big(\dot{\beta}_i s_{\alpha_i} + \dot{\gamma}_i c_{\alpha_i} c_{\beta_i} + \dot{\Psi}\big)\hat{\boldsymbol{b}}_3^i \tag{4.47}$$

Taking the cross product of the angular velocity with the position would yield a rather complex equation for the linear velocity, leading to an even more complex equation for the linear contribution to kinetic energy; however recall from Chapter 3 that all terms arising from the propeller linear velocity were found to be negligible in the final equations of motion. The same reasoning will be applied here to neglect calculating the linear velocity and the linear kinetic energy.

To aid in calculating the rotational kinetic energy, temporarily define another set of angular rates so that the base angular velocity can be quickly represented in the $\mathcal{P}^i$ frame

$$\boldsymbol{\omega}^{\mathcal{B}\mathcal{N}} = \dot{\tilde{\Phi}}_i \, \hat{\boldsymbol{p}}_1^i + \dot{\tilde{\Theta}}_i \, \hat{\boldsymbol{p}}_2^i + \dot{\tilde{\Psi}}_i \, \hat{\boldsymbol{p}}_3^i. \tag{4.48}$$

Equation (4.47) can then be rewritten in the $\mathcal{P}^i$ frame as

$$\boldsymbol{\omega}^{\mathcal{P}^i\mathcal{N}} = \big(\dot{\beta}_i s_{\gamma_i} + \dot{\alpha}_i c_{\beta_i} c_{\gamma_i} + \dot{\tilde{\Phi}}_i\big)\hat{\boldsymbol{p}}_1^i + \big(\dot{\beta}_i c_{\gamma_i} - \dot{\alpha}_i c_{\beta_i} s_{\gamma_i} + \dot{\tilde{\Theta}}_i\big)\hat{\boldsymbol{p}}_2^i + \big(\dot{\gamma}_i + \dot{\alpha}_i s_{\beta_i} + \dot{\tilde{\Psi}}_i\big)\hat{\boldsymbol{p}}_3^i \quad (4.49)$$

and the rotational kinetic energy can be calculated without projecting the inertia matrix into any other frames

$$\begin{aligned} T_{\mathcal{P}^i}^{\omega} &= \frac{1}{2}\big(\boldsymbol{\omega}^{\mathcal{P}^i\mathcal{N}}\big)^T \boldsymbol{I}_{\mathcal{P}}\big(\boldsymbol{\omega}^{\mathcal{P}^i\mathcal{N}}\big) \\ &= \frac{1}{2} I_{\mathcal{P}}^x\big(\dot{\beta}_i s_{\gamma_i} + \dot{\alpha}_i c_{\beta_i} c_{\gamma_i} + \dot{\tilde{\Phi}}_i\big)^2 + \frac{1}{2} I_{\mathcal{P}}^y\big(\dot{\beta}_i c_{\gamma_i} + \dot{\alpha}_i c_{\beta_i} s_{\gamma_i} + \dot{\tilde{\Theta}}_i\big)^2 + \frac{1}{2} I_{\mathcal{P}}^z\big(\dot{\gamma}_i + \dot{\alpha}_i s_{\beta_i} + \dot{\tilde{\Psi}}_i\big)^2 \end{aligned} \quad (4.50)$$

Assuming that all body rates and twist/tilt speeds will be significantly smaller than the propeller speeds, the propeller kinetic energy can be greatly simplified in the same way as Equation (3.38)

$$\begin{aligned} T_{\mathcal{P}^i}^{\omega} &= \frac{1}{2}\Bigg[I_{\mathcal{P}}^x \left(\frac{\dot{\beta}_i s_{\gamma_i} + \dot{\alpha}_i c_{\beta_i} c_{\gamma_i} + \dot{\tilde{\Phi}}_i}{\dot{\gamma}_i} \right)^2 + I_{\mathcal{P}}^y \left(\frac{\dot{\beta}_i c_{\gamma_i} + \dot{\alpha}_i c_{\beta_i} s_{\gamma_i} + \dot{\tilde{\Theta}}_i}{\dot{\gamma}_i} \right)^2 \\ &\qquad + I_{\mathcal{P}}^z \left(\frac{\dot{\alpha}_i s_{\beta_i} + \dot{\tilde{\Psi}}_i}{\dot{\gamma}_i} + 1 \right)^2 \Bigg] \dot{\gamma}_i^2 \\ &\approx \frac{1}{2} I_{\mathcal{P}}^z \dot{\gamma}_i^2. \end{aligned} \quad (4.51)$$

In this form it is clear that the only kinetic energy partial derivative is given by

$$\frac{d}{dt}\left(\frac{\partial T_{\mathcal{P}^i}^{\omega}}{\partial \dot{\gamma}_i}\right) = I_{\mathcal{P}}^z \ddot{\gamma}_i. \quad (4.52)$$

The potential energy is obtained by projecting the position vector onto the vertical axis, given by

$$\begin{aligned} U_{\mathcal{P}} &= m_{\mathcal{P}} g_0 \, \boldsymbol{r}^{\mathcal{P}^i/\mathcal{B}} \cdot \hat{\boldsymbol{n}}_3 \\ &= \Big[\big(\ell_{\mathcal{S}} + \ell_{\mathcal{P}} s_{\beta_i}\big)\hat{\boldsymbol{b}}_1^i - \ell_{\mathcal{P}} s_{\alpha_i} c_{\beta_i}\, \hat{\boldsymbol{b}}_2^i + \ell_{\mathcal{P}} c_{\alpha_i} c_{\beta_i}\, \hat{\boldsymbol{b}}_3^i\Big] \cdot \big(- s_\theta\, \hat{\boldsymbol{b}}_1^1 + c_\theta s_\varphi\, \hat{\boldsymbol{b}}_2^1 + c_\theta c_\varphi\, \hat{\boldsymbol{b}}_3^1\big), \end{aligned} \quad (4.53)$$

for which the partial derivatives will be evaluated in later sections.

An obvious but noteworthy property is that the equations for arm i do not depend on the configurations of arms $j \neq i$. This will lead to a special block structure of the final equations of motion where the inertia and coupling matrices are fully populated for the rows and columns corresponding to the base coordinates, but block diagonal for the rows and columns corresponding to the arm coordinates.

4.4 Generalized Forces

The generalized forces for the full copter involve the motor torques, drag-induced torques, and gyroscopic torques discussed in Section 3.2.4, as well as thrust-induced torques that act on the base rotation axes. Equation (3.49) developed for the arm subsystem is a general form which still holds for the full copter, and the various terms will be reconsidered here.

From Equation (2.14), the thrust force from propeller i acts along the $\mathcal{P}_3^i$ axis and thus exerts no torque about the twist or tilt coordinates. The torque exerted about the base origin is given by

$$\boldsymbol{r}^{\mathcal{P}^i/\mathcal{B}} \times \bar{\boldsymbol{F}}_i = -c_p \ell_{\mathcal{S}} \dot{\gamma}_i^2 c_{\beta_i} \big(c_{\alpha_i} \, \hat{\boldsymbol{b}}_2^i + s_{\alpha_i} \, \hat{\boldsymbol{b}}_3^i \big),$$

which can then be projected onto the three base rotation coordinates defined by the Tait-Bryan sequence in Section 2.1.1

$$\psi : \big(\boldsymbol{r}^{\mathcal{P}^i/\mathcal{B}} \times \bar{\boldsymbol{F}}_i \big) \cdot \hat{\boldsymbol{n}}_3 = -c_p \ell_{\mathcal{S}} \dot{\gamma}_i^2 c_{\beta_i} \big(c_{\alpha_i} \, \hat{\boldsymbol{b}}_2^i + s_{\alpha_i} \, \hat{\boldsymbol{b}}_3^i \big) \cdot \big(- s_\theta \, \hat{\boldsymbol{b}}_1^1 + c_\theta s_\varphi \, \hat{\boldsymbol{b}}_2^1 + c_\theta c_\varphi \, \hat{\boldsymbol{b}}_3^1 \big), \tag{4.54}$$

$$\theta : \big(\boldsymbol{r}^{\mathcal{P}^i/\mathcal{B}} \times \bar{\boldsymbol{F}}_i \big) \cdot \hat{\boldsymbol{b}}_2' = -c_p \ell_{\mathcal{S}} \dot{\gamma}_i^2 c_{\beta_i} \big(c_{\alpha_i} \, \hat{\boldsymbol{b}}_2^i + s_{\alpha_i} \, \hat{\boldsymbol{b}}_3^i \big) \cdot \big(c_\varphi \, \hat{\boldsymbol{b}}_2^1 - s_\varphi \, \hat{\boldsymbol{b}}_3^1 \big), \tag{4.55}$$

$$\varphi : \big(\boldsymbol{r}^{\mathcal{P}^i/\mathcal{B}} \times \bar{\boldsymbol{F}}_i \big) \cdot \hat{\boldsymbol{b}}_1 = -c_p \ell_{\mathcal{S}} \dot{\gamma}_i^2 c_{\beta_i} \big(c_{\alpha_i} \, \hat{\boldsymbol{b}}_2^i + s_{\alpha_i} \, \hat{\boldsymbol{b}}_3^i \big) \cdot \big(\hat{\boldsymbol{b}}_1^1 \big). \tag{4.56}$$

The drag torque from propeller i given in Equation (2.15) can be rotated into the $\mathcal{B}^i$

frame and then projected onto the base rotation coordinates in the same way

$$\psi : \bar{\boldsymbol{\tau}}_i \cdot \hat{\boldsymbol{n}}_3 = (-1)^i c_t \dot{\gamma}_i^2 \big(s_{\beta_i}\, \hat{\boldsymbol{b}}_1^i - s_{\alpha_i} c_{\beta_i}\, \hat{\boldsymbol{b}}_2^i + c_{\alpha_i} c_{\beta_i}\, \hat{\boldsymbol{b}}_3^i\big) \cdot \big(- s_\theta\, \hat{\boldsymbol{b}}_1^1 + c_\theta s_\varphi\, \hat{\boldsymbol{b}}_2^1 + c_\theta c_\varphi\, \hat{\boldsymbol{b}}_3^1\big), \tag{4.57}$$

$$\theta : \bar{\boldsymbol{\tau}}_i \cdot \hat{\boldsymbol{b}}_2' = (-1)^i c_t \dot{\gamma}_i^2 \big(s_{\beta_i}\, \hat{\boldsymbol{b}}_1^i - s_{\alpha_i} c_{\beta_i}\, \hat{\boldsymbol{b}}_2^i + c_{\alpha_i} c_{\beta_i}\, \hat{\boldsymbol{b}}_3^i\big) \cdot \big(c_\varphi\, \hat{\boldsymbol{b}}_2^1 - s_\varphi\, \hat{\boldsymbol{b}}_3^1\big), \tag{4.58}$$

$$\varphi : \bar{\boldsymbol{\tau}}_i \cdot \hat{\boldsymbol{b}}_1 = (-1)^i c_t \dot{\gamma}_i^2 \big(s_{\beta_i}\, \hat{\boldsymbol{b}}_1^i - s_{\alpha_i} c_{\beta_i}\, \hat{\boldsymbol{b}}_2^i + c_{\alpha_i} c_{\beta_i}\, \hat{\boldsymbol{b}}_3^i\big) \cdot \big(\hat{\boldsymbol{b}}_1^1\big). \tag{4.59}$$

Projections of the drag torque onto the arm coordinates are unchanged from Section 3.2.4.

When considering the arm subsystem in isolation, the only gyroscopic torques which appeared in the final equations of motion were those due to precession of the propeller. This was not the result of an approximation but a byproduct of fixing the base to ground. Allowing the base link to rotate permits gyroscopic precession of the arc and shaft, and associated torques arise along the base rotation axes. Though these gyroscopic torques do exist in the system, their contributions to the resultant torque about any given axis will be small relative to the contribution from the propeller gyroscopic torque due to the large difference in motor speeds. The arc and shaft gyroscopic effects can thus be neglected using the same approximation which justified neglect of the Coriolis and centrifugal effects.

The remaining gyroscopic torque associated with the propeller is given by the following, written in three coordinate frames to facilitate projection in future sections

$$\begin{aligned}
\boldsymbol{\sigma}_{\mathcal{P}^i} &= \boldsymbol{\omega}^{\mathcal{S}^i\mathcal{N}} \times \boldsymbol{I}_{\mathcal{P}} \boldsymbol{\omega}^{\mathcal{P}^i\mathcal{S}^i} \\
&= \Big[\big(\dot{\alpha}_i + \dot{\Phi}_i\big)\hat{\boldsymbol{b}}_1^i + \big(\dot{\beta}_i c_{\alpha_i} \dot{\Theta}_i\big)\hat{\boldsymbol{b}}_2^i + \big(\dot{\beta}_i s_{\alpha_i} + \dot{\Psi}\big)\hat{\boldsymbol{b}}_3^i\Big] \times I_{\mathcal{P}}^z \dot{\gamma}_i \big(s_{\beta_i}\hat{\boldsymbol{b}}_1^i - s_{\alpha_i} c_{\beta_i}\hat{\boldsymbol{b}}_2^i + c_{\alpha_i} c_{\beta_i}\hat{\boldsymbol{b}}_3^i\big) \\
&= I_{\mathcal{P}}^z \dot{\gamma}_i \Big[\big(\dot{\beta}_i c_{\alpha_i} + \dot{\Theta}_i\big) c_{\alpha_i} c_{\beta_i} + \big(\dot{\beta}_i s_{\alpha_i} + \dot{\Psi}\big) s_{\alpha_i} c_{\beta_i}\Big]\, \hat{\boldsymbol{b}}_1^i \\
&\quad + I_{\mathcal{P}}^z \dot{\gamma}_i \Big[\big(\dot{\beta}_i s_{\alpha_i} + \dot{\Psi}\big) s_{\beta_i} - \big(\dot{\alpha}_i + \dot{\Phi}_i\big) c_{\alpha_i} c_{\beta_i}\Big]\, \hat{\boldsymbol{b}}_2^i \\
&\quad + I_{\mathcal{P}}^z \dot{\gamma}_i \Big[-\big(\dot{\alpha}_i + \dot{\Phi}_i\big) s_{\alpha_i} c_{\beta_i} - \big(\dot{\beta}_i c_{\alpha_i} + \dot{\Theta}\big) s_{\beta_i}\Big]\, \hat{\boldsymbol{b}}_3^i
\end{aligned} \tag{4.60}$$

$$
\begin{aligned}
&= I^z_{\mathcal{P}}\dot{\gamma}_i\left[\left(\dot{\beta}_i c_{\alpha_i}+\dot{\Theta}_i\right)c_{\alpha_i}c_{\beta_i}+\left(\dot{\beta}_i s_{\alpha_i}+\dot{\Psi}\right)s_{\alpha_i}c_{\beta_i}\right]\hat{\boldsymbol{a}}^i_1 \\
&\quad + I^z_{\mathcal{P}}\dot{\gamma}_i\left[\left(\dot{\beta}_i s_{\alpha_i}+\dot{\Psi}\right)c_{\alpha_i}s_{\beta_i}-\left(\dot{\alpha}_i+\dot{\Phi}_i\right)c_{\beta_i}-\left(\dot{\beta}_i c_{\alpha_i}+\dot{\Theta}_i\right)s_{\alpha_i}s_{\beta_i}\right]\hat{\boldsymbol{a}}^i_2 \qquad (4.61)\\
&\quad + I^z_{\mathcal{P}}\dot{\gamma}_i\left[-\left(\dot{\beta}_i s_{\alpha_i}+\dot{\Psi}\right)s_{\alpha_i}s_{\beta_i}-\left(\dot{\beta}_i c_{\alpha_i}+\dot{\Theta}_i\right)c_{\alpha_i}c_{\beta_i}\right]\hat{\boldsymbol{a}}^i_3 \\
&= I^z_{\mathcal{P}}\dot{\gamma}_i\left[\left(\dot{\beta}_i c_{\alpha_i}+\dot{\Theta}_i\right)c_{\alpha_i}c^2_{\beta_i}+\left(\dot{\beta}_i s_{\alpha_i}+\dot{\Psi}\right)s_{\alpha_i}+\left(\dot{\beta}_i c_{\alpha_i}+\dot{\Theta}_i\right)c_{\alpha_i}s_{\beta_i}c_{\beta_i}\right]\hat{\boldsymbol{s}}^i_1 \\
&\quad + I^z_{\mathcal{P}}\dot{\gamma}_i\left[\left(\dot{\beta}_i s_{\alpha_i}+\dot{\Psi}\right)c_{\alpha_i}s_{\beta_i}-\left(\dot{\alpha}_i+\dot{\Phi}_i\right)c_{\beta_i}-\left(\dot{\beta}_i c_{\alpha_i}+\dot{\Theta}_i\right)s_{\alpha_i}s_{\beta_i}\right]\hat{\boldsymbol{s}}^i_2 \qquad (4.62)\\
&\quad + I^z_{\mathcal{P}}\dot{\gamma}_i\left[\left(\dot{\beta}_i c_{\alpha_i}+\dot{\Theta}_i\right)c_{\alpha_i}s_{\beta_i}c_{\beta_i}-\left(\dot{\beta}_i c_{\alpha_i}+\dot{\Theta}_i\right)c_{\alpha_i}c^2_{\beta_i}\right]\hat{\boldsymbol{s}}^i_3.
\end{aligned}
$$

The final piece of the generalized forces is the vector of motor input torques, which can be written as

$$
\boldsymbol{\tau} = \begin{bmatrix} 0 \\ 0 \\ 0 \\ \hdashline \tau_{\alpha_1} \\ \tau_{\beta_1} \\ \tau_{\gamma_1} \\ \hdashline \vdots \\ \hdashline \tau_{\alpha_4} \\ \tau_{\beta_4} \\ \tau_{\gamma_4} \end{bmatrix}. \qquad (4.63)
$$

Unlike the arm subsystems, the coordinates for the base link rotation do not have dedicated actuators and therefore rely solely on the thrust-induced torques for control. An adaptation to the control structure in Section 3.3 which addresses the zero elements in $\boldsymbol{\tau}$ is discussed at the end of this chapter.

4.5 Roll-Axis Arms

When assembling the Euler-Lagrange equations for the full copter, it is useful to work simultaneously with opposing arms to make use of symmetry relations. This section evaluates the general partial derivatives outlined in Section 4.3 for arms 1 and 3, which lie along the copter's roll axis.

4.5.1 Arm 1 Energy

Based on Equation (2.6), the $\mathcal{B}^1$ frame is aligned with the $\mathcal{B}$ frame and thus requires no rotation to obtain the generalized angular rates as

$$\dot{\Phi}_1 = -\dot{\psi}s_\theta + \dot{\varphi}, \tag{4.64}$$

$$\dot{\Theta}_1 = \dot{\psi}c_\theta s_\varphi + \dot{\theta}c_\varphi, \tag{4.65}$$

$$\dot{\Psi}_1 = \dot{\psi}c_\theta c_\varphi - \dot{\theta}s_\varphi, \tag{4.66}$$

which can then be used to evaluate the necessary partial derivatives for the Lagrange equations. Starting with the speed partial of the translational component of the arc kinetic energy with respect to $\dot{\psi}$, Equation (4.22) simplifies to

$$\frac{\partial T^v_{\mathcal{A}^1}}{\partial \dot{\psi}} = m_{\mathcal{A}}\ell^2_{\mathcal{A}}\dot{\psi}c^2_\theta,$$

and differentiating with respect to time results in

$$\frac{d}{dt}\left(\frac{\partial T^v_{\mathcal{A}^1}}{\partial \dot{\psi}}\right) = m_{\mathcal{A}}\ell^2_{\mathcal{A}}\left(\ddot{\psi}c^2_\theta - \dot{\psi}\dot{\theta}s_{2\theta}\right).$$

This equation includes an inertial term as well as a Coriolis term.[1] The inertial term is retained to preserve symmetry properties of the final inertia matrix, however the Coriolis term may be neglected due to its small magnitude relative to the gyroscopic couplings which will also appear in the final equations of motion. The same justification is applied to neglect all other quadratic velocity terms which do not depend on propeller speed. With this approximation, the speed partials of the arc linear kinetic energy from Equations (4.22)-(4.24) become

$$\frac{d}{dt}\left(\frac{\partial T^v_{\mathcal{A}^1}}{\partial \dot{\psi}}\right) \approx m_{\mathcal{A}}\ell^2_{\mathcal{A}}\ddot{\psi}c^2_\theta, \tag{4.67}$$

[1]Though the arc center of mass lies at a fixed distance from the base origin, Coriolis accelerations can still arise in certain axes due to the use of a Tait-Bryan sequence.

$$\frac{d}{dt}\left(\frac{\partial T^v_{\mathcal{A}^1}}{\partial \dot{\theta}}\right) \approx m_{\mathcal{A}} \ell^2_{\mathcal{A}} \ddot{\theta}, \tag{4.68}$$

$$\frac{d}{dt}\left(\frac{\partial T^v_{\mathcal{A}^1}}{\partial \dot{\varphi}}\right) = 0, \tag{4.69}$$

where the last equation is exact because $\dot{\Theta}_1$ is not dependent on $\dot{\varphi}$. Applying the same approximation along with much algebraic manipulation, the nonzero speed partials of the arc rotational kinetic energy from Equations (4.25)-(4.28) become

$$\frac{d}{dt}\left(\frac{\partial T^\omega_{\mathcal{A}^1}}{\partial \dot{\psi}}\right) \approx I^x_{\mathcal{A}}\big(\ddot{\psi} s^2_\theta - \ddot{\varphi} s_\theta - \ddot{\alpha}_1 s_\theta\big) + \big(I^y_{\mathcal{A}} s^2_{\varphi+\alpha_1} + I^z_{\mathcal{A}} c^2_{\varphi+\alpha_1}\big)\ddot{\psi} c^2_\theta + \frac{1}{2}\big(I^y_{\mathcal{A}} - I^z_{\mathcal{A}}\big)\ddot{\theta} c_\theta s_{2\varphi+2\alpha_1}, \tag{4.70}$$

$$\frac{d}{dt}\left(\frac{\partial T^\omega_{\mathcal{A}^1}}{\partial \dot{\theta}}\right) \approx \big(I^y_{\mathcal{A}} c^2_{\varphi+\alpha_1} + I^z_{\mathcal{A}} s^2_{\varphi+\alpha_1}\big)\ddot{\theta} + \frac{1}{2}\big(I^y_{\mathcal{A}} - I^z_{\mathcal{A}}\big)\ddot{\psi} c_\theta s_{2\varphi+2\alpha_1}, \tag{4.71}$$

$$\frac{d}{dt}\left(\frac{\partial T^\omega_{\mathcal{A}^1}}{\partial \dot{\varphi}}\right) \approx I^x_{\mathcal{A}}\big(-\ddot{\psi} s_\theta + \ddot{\varphi} + \ddot{\alpha}_1\big), \tag{4.72}$$

$$\frac{d}{dt}\left(\frac{\partial T^\omega_{\mathcal{A}^1}}{\partial \dot{\alpha}_1}\right) \approx I^x_{\mathcal{A}}\big(-\ddot{\psi} s_\theta + \ddot{\varphi} + \ddot{\alpha}_1\big). \tag{4.73}$$

This set of partials will define a portion of the final inertia matrix and must satisfy symmetry and nonnegativity. For example, the coefficient corresponding to $\ddot{\psi}$ in Equation (4.70) is nonnegative, as is the coefficient corresponding to $\ddot{\theta}$ in Equation (4.71), etc. For symmetry, the coefficient corresponding to $\ddot{\alpha}_1$ in Equation (4.72) matches the coefficient corresponding to $\ddot{\varphi}$ in Equation (4.73), etc. Thus the approximation preserves the expected properties of the final dynamic model.

From Equation (4.29), the potential energy of arc 1 is given by

$$U_{\mathcal{A}^1} = -m_{\mathcal{A}} g_0 \ell_{\mathcal{A}} s_\theta, \tag{4.74}$$

of which the only nonzero partial derivative is

$$\frac{\partial U_{\mathcal{A}^1}}{\partial \theta} = -m_{\mathcal{A}} g_0 \ell_{\mathcal{A}} c_\theta. \tag{4.75}$$

The same process is applied to Equations (4.37)-(4.39) to obtain the following set of linear kinetic energy speed partials for the shaft

$$\frac{d}{dt}\left(\frac{\partial T^v_{\mathcal{S}^1}}{\partial \dot{\psi}}\right) \approx m_{\mathcal{S}}\ell^2_{\mathcal{S}}\ddot{\psi}c^2_\theta, \tag{4.76}$$

$$\frac{d}{dt}\left(\frac{\partial T^v_{\mathcal{S}^1}}{\partial \dot{\theta}}\right) \approx m_{\mathcal{S}}\ell^2_{\mathcal{S}}\ddot{\theta}, \tag{4.77}$$

$$\frac{d}{dt}\left(\frac{\partial T^v_{\mathcal{S}^1}}{\partial \dot{\varphi}}\right) = 0, \tag{4.78}$$

which are of identical form to the linear kinetic energy speed partials for the arc because the arc and shaft centers of mass behave in the same way by construction. The shaft rotational kinetic energy speed partials from Equations (4.40)-(4.44) are

$$\begin{aligned}\frac{d}{dt}\left(\frac{\partial T^\omega_{\mathcal{S}^1}}{\partial \dot{\psi}}\right) \approx{}& I^{xz}_{\mathcal{S}}\big(\ddot{\psi}s^2_\theta - \ddot{\varphi}s_\theta - \ddot{\alpha}_1 s_\theta\big) + \big(I^y_{\mathcal{S}}s^2_{\varphi+\alpha_1} + I^{xz}_{\mathcal{S}}c^2_{\varphi+\alpha_1}\big)\ddot{\psi}c^2_\theta + I^y_{\mathcal{S}}\ddot{\beta}_1 c_\theta s_{\varphi+\alpha_1} \\ &+ \frac{1}{2}\big(I^y_{\mathcal{S}} - I^{xz}_{\mathcal{S}}\big)\ddot{\theta}c_\theta s_{2\varphi+2\alpha_1},\end{aligned} \tag{4.79}$$

$$\frac{d}{dt}\left(\frac{\partial T^\omega_{\mathcal{S}^1}}{\partial \dot{\theta}}\right) \approx \big(I^y_{\mathcal{S}}c^2_{\varphi+\alpha_1} + I^{xz}_{\mathcal{S}}s^2_{\varphi+\alpha_1}\big)\ddot{\theta} + \frac{1}{2}\big(I^y_{\mathcal{S}} - I^{xz}_{\mathcal{S}}\big)\ddot{\psi}c_\theta s_{2\varphi+2\alpha_1} + I^y_{\mathcal{S}}\ddot{\beta}_1 c_{\varphi+\alpha_1}, \tag{4.80}$$

$$\frac{d}{dt}\left(\frac{\partial T^\omega_{\mathcal{S}^1}}{\partial \dot{\varphi}}\right) \approx I^{xz}_{\mathcal{S}}\big(-\ddot{\psi}s_\theta + \ddot{\varphi} + \ddot{\alpha}_1\big), \tag{4.81}$$

$$\frac{d}{dt}\left(\frac{\partial T^\omega_{\mathcal{S}^1}}{\partial \dot{\alpha}_1}\right) \approx I^{xz}_{\mathcal{S}}\big(-\ddot{\psi}s_\theta + \ddot{\varphi} + \ddot{\alpha}_1\big), \tag{4.82}$$

$$\frac{d}{dt}\left(\frac{\partial T^\omega_{\mathcal{S}^1}}{\partial \dot{\beta}_1}\right) \approx I^y_{\mathcal{S}}\big(\ddot{\psi}c_\theta s_{\varphi+\alpha_1} + \ddot{\theta}c_{\varphi+\alpha_1} + \ddot{\beta}_1\big), \tag{4.83}$$

which are again largely the same as the arc equations but with additional terms for the tilt rotation in certain coordinates. From Equation (4.45) The potential energy of shaft 1 is given by

$$U_{\mathcal{S}^1} = -m_{\mathcal{S}}g_0\ell_{\mathcal{S}}s_\theta, \tag{4.84}$$

of which the only nonzero partial derivative is

$$\frac{\partial U_{\mathcal{S}^1}}{\partial \theta} = -m_{\mathcal{S}} g_0 \ell_{\mathcal{S}} c_\theta. \tag{4.85}$$

Finally, the only nonzero speed partial of the propeller kinetic energy from Equation (4.52) is

$$\frac{d}{dt}\left(\frac{\partial T^{\omega}_{\mathcal{P}^1}}{\partial \dot{\gamma}_1}\right) = I^z_{\mathcal{P}} \ddot{\gamma}_1. \tag{4.86}$$

The propeller potential energy from Equation (4.53) is

$$U_{\mathcal{P}^1} = m_{\mathcal{P}} g_0 \Big[-\ell_{\mathcal{S}} s_\theta + \ell_{\mathcal{P}} (-s_\theta s_{\beta_1} + c_\theta c_{\beta_1} c_{\varphi+\alpha_1}) \Big], \tag{4.87}$$

and the necessary position partials are given by

$$\frac{\partial U_{\mathcal{P}^1}}{\partial \theta} = -m_{\mathcal{P}} g_0 \Big[\ell_{\mathcal{S}} c_\theta + \ell_{\mathcal{P}} (c_\theta s_{\beta_1} + s_\theta c_{\beta_1} c_{\varphi+\alpha_1}) \Big], \tag{4.88}$$

$$\frac{\partial U_{\mathcal{P}^1}}{\partial \varphi} = -m_{\mathcal{P}} g_0 \ell_{\mathcal{P}} c_\theta c_{\beta_1} s_{\varphi+\alpha_1}, \tag{4.89}$$

$$\frac{\partial U_{\mathcal{P}^1}}{\partial \alpha_1} = -m_{\mathcal{P}} g_0 \ell_{\mathcal{P}} c_\theta c_{\beta_1} s_{\varphi+\alpha_1}, \tag{4.90}$$

$$\frac{\partial U_{\mathcal{P}^1}}{\partial \beta_1} = -m_{\mathcal{P}} g_0 \ell_{\mathcal{P}} (s_\theta c_{\beta_1} + c_\theta s_{\beta_1} c_{\varphi+\alpha_1}). \tag{4.91}$$

At this point it is possible to assemble Euler-Lagrange equations that describe the rotation of the base link controlled by a single arm. Rotation of the base link has expanded the configuration space by adding three more degrees of freedom, but has not included additional actuators. The result is an underactuated system for which designing a controller would be a digression from the goal of full 6-DOF control. For this reason, equations of motion will be delayed until all four arcs can be incorporated simultaneously.

4.5.2 Arm 3 Energy

arm 3 is considered next because the resulting equations will be similar to arm 1 due to symmetry. From Equation (4.14), the generalized angular rates for this arm are

$$\dot{\Phi}_3 = \dot{\psi} s_\theta - \dot{\varphi}, \tag{4.92}$$

$$\dot{\Theta}_3 = -\dot{\psi} c_\theta s_\varphi - \dot{\theta} c_\varphi, \tag{4.93}$$

$$\dot{\Psi}_3 = \dot{\psi} c_\theta c_\varphi - \dot{\theta} s_\varphi. \tag{4.94}$$

Applying the approximation of neglecting quadratic velocity terms which do not depend on propeller speeds, the kinetic energy speed partials for arc 3 are given by

$$\frac{d}{dt}\left(\frac{\partial T^v_{\mathcal{A}^3}}{\partial \dot{\psi}}\right) \approx m_{\mathcal{A}} \ell^2_{\mathcal{A}} \ddot{\psi} c^2_\theta, \tag{4.95}$$

$$\frac{d}{dt}\left(\frac{\partial T^v_{\mathcal{A}^3}}{\partial \dot{\theta}}\right) \approx m_{\mathcal{A}} \ell^2_{\mathcal{A}} \ddot{\theta}, \tag{4.96}$$

$$\frac{d}{dt}\left(\frac{\partial T^v_{\mathcal{A}^3}}{\partial \dot{\varphi}}\right) = 0, \tag{4.97}$$

$$\frac{d}{dt}\left(\frac{\partial T^\omega_{\mathcal{A}^3}}{\partial \dot{\psi}}\right) \approx I^x_{\mathcal{A}}\big(\ddot{\psi} s^2_\theta - \ddot{\varphi} s_\theta + \ddot{\alpha}_3 s_\theta\big) + \big(I^y_{\mathcal{A}} s^2_{\varphi-\alpha_3} + I^z_{\mathcal{A}} c^2_{\varphi-\alpha_3}\big)\ddot{\psi} c^2_\theta + \frac{1}{2}\big(I^y_{\mathcal{A}} - I^z_{\mathcal{A}}\big)\ddot{\theta} c_\theta s_{2\varphi-2\alpha_3}, \tag{4.98}$$

$$\frac{d}{dt}\left(\frac{\partial T^\omega_{\mathcal{A}^3}}{\partial \dot{\theta}}\right) \approx \big(I^y_{\mathcal{A}} c^2_{\varphi-\alpha_3} + I^z_{\mathcal{A}} s^2_{\varphi-\alpha_3}\big)\ddot{\theta} + \frac{1}{2}\big(I^y_{\mathcal{A}} - I^z_{\mathcal{A}}\big)\ddot{\psi} c_\theta s_{2\varphi-2\alpha_3}, \tag{4.99}$$

$$\frac{d}{dt}\left(\frac{\partial T^\omega_{\mathcal{A}^3}}{\partial \dot{\varphi}}\right) \approx I^x_{\mathcal{A}}\big(-\ddot{\psi} s_\theta + \ddot{\varphi} - \ddot{\alpha}_3\big), \tag{4.100}$$

$$\frac{d}{dt}\left(\frac{\partial T^\omega_{\mathcal{A}^3}}{\partial \dot{\alpha}_3}\right) \approx I^x_{\mathcal{A}}\big(\ddot{\psi} s_\theta - \ddot{\varphi} + \ddot{\alpha}_3\big). \tag{4.101}$$

Notice that these equations are equivalent to Equations (4.67)-(4.73) with $\dot{\alpha}_1$ replaced by $-\dot{\alpha}_3$. For Equation (4.101) the variable of differentiation must receive this sign change as well in order to make it equivalent to Equation (4.73). This is expected as the $\hat{\boldsymbol{a}}^1_1$ and $\hat{\boldsymbol{a}}^3_1$

directions are related by a 180° rotation and thus will have opposing effects on the base coordinates.

The potential energy for arc 3 from Equation (4.29) is given by

$$U_{\mathcal{A}^3} = m_{\mathcal{A}} g_0 \ell_{\mathcal{A}} s_\theta, \tag{4.102}$$

with the single partial derivative

$$\frac{\partial U_{\mathcal{A}^3}}{\partial \theta} = m_{\mathcal{A}} g_0 \ell_{\mathcal{A}} c_\theta, \tag{4.103}$$

which varies from Equation (4.75) by a negative sign. This is expected because a positive pitch maneuver has the opposite effect on the vertical position of arm 1 compared to arm 3. When the equations of motion are assembled, the gravitational torque of arc 3 will balance that of arc 1 in all configurations.

The kinetic energy speed partials for shaft 3 are given by

$$\frac{d}{dt}\left(\frac{\partial T^v_{\mathcal{S}^3}}{\partial \dot{\psi}}\right) \approx m_{\mathcal{S}} \ell_{\mathcal{S}}^2 \ddot{\psi} c_\theta^2, \tag{4.104}$$

$$\frac{d}{dt}\left(\frac{\partial T^v_{\mathcal{S}^3}}{\partial \dot{\theta}}\right) \approx m_{\mathcal{S}} \ell_{\mathcal{S}}^2 \ddot{\theta}, \tag{4.105}$$

$$\frac{d}{dt}\left(\frac{\partial T^v_{\mathcal{S}^3}}{\partial \dot{\varphi}}\right) = 0, \tag{4.106}$$

$$\begin{aligned}\frac{d}{dt}\left(\frac{\partial T^\omega_{\mathcal{S}^3}}{\partial \dot{\psi}}\right) \approx\ & I^{xz}_{\mathcal{S}}\big(\ddot{\psi} s_\theta^2 - \ddot{\varphi} s_\theta + \ddot{\alpha}_3 s_\theta\big) + \big(I^y_{\mathcal{S}} s^2_{\varphi-\alpha_3} + I^{xz}_{\mathcal{S}} c^2_{\varphi-\alpha_3}\big)\ddot{\psi} c_\theta^2 - I^y_{\mathcal{S}} \ddot{\beta}_3 c_\theta s_{\varphi-\alpha_3} \\ & + \frac{1}{2}\big(I^y_{\mathcal{S}} - I^{xz}_{\mathcal{S}}\big)\ddot{\theta} c_\theta s_{2\varphi-2\alpha_3},\end{aligned} \tag{4.107}$$

$$\frac{d}{dt}\left(\frac{\partial T^\omega_{\mathcal{S}^3}}{\partial \dot{\theta}}\right) \approx \big(I^y_{\mathcal{S}} c^2_{\varphi-\alpha_3} + I^{xz}_{\mathcal{S}} s^2_{\varphi-\alpha_3}\big)\ddot{\theta} + \frac{1}{2}\big(I^y_{\mathcal{S}} - I^{xz}_{\mathcal{S}}\big)\ddot{\psi} c_\theta s_{2\varphi-2\alpha_3} - I^y_{\mathcal{S}} \ddot{\beta}_3 c_{\varphi-\alpha_3}, \tag{4.108}$$

$$\frac{d}{dt}\left(\frac{\partial T^\omega_{\mathcal{S}^3}}{\partial \dot{\varphi}}\right) \approx I^{xz}_{\mathcal{S}}\big(-\ddot{\psi} s_\theta + \ddot{\varphi} - \ddot{\alpha}_3\big), \tag{4.109}$$

$$\frac{d}{dt}\left(\frac{\partial T^\omega_{\mathcal{S}^3}}{\partial \dot{\alpha}_3}\right) \approx I^{xz}_{\mathcal{S}}\big(\ddot{\psi} s_\theta - \ddot{\varphi} + \ddot{\alpha}_3\big), \tag{4.110}$$

$$\frac{d}{dt}\left(\frac{\partial T^{\omega}_{\mathcal{S}^3}}{\partial \dot{\beta}_3}\right) \approx I^y_{\mathcal{S}}\big(- \ddot{\psi} c_\theta s_{\varphi-\alpha_3} - \ddot{\theta} c_{\varphi-\alpha_3} + \ddot{\beta}_3\big), \tag{4.111}$$

which are equivalent to Equations (4.76)-(4.83) with $\dot{\alpha}_1$ replaced by $-\dot{\alpha}_3$, and $\dot{\beta}_1$ replaced by $-\dot{\beta}_3$, including as the variable of differentiation where applicable. The potential energy of shaft 3 from Equation (4.45) is

$$U_{\mathcal{S}^3} = m_{\mathcal{S}} g_0 \ell_{\mathcal{S}} s_\theta, \tag{4.112}$$

and the only nonzero partial derivative is

$$\frac{\partial U_{\mathcal{S}^3}}{\partial \theta} = m_{\mathcal{S}} g_0 \ell_{\mathcal{S}} c_\theta. \tag{4.113}$$

This again differs from the equation for arm 1 by a negative sign, and will cancel the gravitational torque of shaft 1 in the final equations of motion.

The only nonzero speed partial of the propeller kinetic energy from Equation (4.51) is

$$\frac{d}{dt}\left(\frac{\partial T^{\omega}_{\mathcal{P}^3}}{\partial \dot{\gamma}_3}\right) = I^z_{\mathcal{P}} \ddot{\gamma}_3. \tag{4.114}$$

The propeller potential energy from Equation (4.53) is

$$U_{\mathcal{P}^3} = m_{\mathcal{P}} g_0 \big[\ell_{\mathcal{S}} s_\theta + \ell_{\mathcal{P}} (s_\theta s_{\beta_3} + c_\theta c_{\beta_3} c_{\varphi-\alpha_3})\big], \tag{4.115}$$

and the necessary position partials are given by

$$\frac{\partial U_{\mathcal{P}^3}}{\partial \theta} = m_{\mathcal{P}} g_0 \Big[\ell_{\mathcal{S}} c_\theta + \ell_{\mathcal{P}} (c_\theta s_{\beta_3} - s_\theta c_{\beta_3} c_{\varphi-\alpha_3})\Big], \tag{4.116}$$

$$\frac{\partial U_{\mathcal{P}^3}}{\partial \varphi} = -m_{\mathcal{P}} g_0 \ell_{\mathcal{P}} c_\theta c_{\beta_3} s_{\varphi-\alpha_3}, \tag{4.117}$$

$$\frac{\partial U_{\mathcal{P}^3}}{\partial \alpha_3} = m_{\mathcal{P}} g_0 \ell_{\mathcal{P}} c_\theta c_{\beta_3} s_{\varphi-\alpha_3}, \tag{4.118}$$

$$\frac{\partial U_{\mathcal{P}^3}}{\partial \beta_3} = m_{\mathcal{P}} g_0 \ell_{\mathcal{P}} (s_\theta c_{\beta_3} - c_\theta s_{\beta_3} c_{\varphi-\alpha_3}). \tag{4.119}$$

4.5.3 Generalized Forces

Equations (4.54)-(4.59) are used to project the thrust- and drag-induced torques from arms 1 and 3 onto the base rotation axes according to

$$\psi : \left(\boldsymbol{r}^{\mathcal{P}^1/\mathcal{B}} \times \bar{\boldsymbol{F}}_1\right) \cdot \hat{\boldsymbol{n}}_3 = -c_p \ell_{\mathcal{S}} \dot{\gamma}_1^2 c_\theta c_{\beta_1} s_{\varphi+\alpha_1}, \tag{4.120}$$

$$\left(\boldsymbol{r}^{\mathcal{P}^3/\mathcal{B}} \times \bar{\boldsymbol{F}}_3\right) \cdot \hat{\boldsymbol{n}}_3 = c_p \ell_{\mathcal{S}} \dot{\gamma}_3^2 c_\theta c_{\beta_3} s_{\varphi-\alpha_3}, \tag{4.121}$$

$$\bar{\boldsymbol{\tau}}_1 \cdot \hat{\boldsymbol{n}}_3 = -c_t \dot{\gamma}_1^2 (-s_\theta s_{\beta_1} + c_\theta c_{\beta_1} c_{\varphi+\alpha_1}), \tag{4.122}$$

$$\bar{\boldsymbol{\tau}}_3 \cdot \hat{\boldsymbol{n}}_3 = -c_t \dot{\gamma}_3^2 (s_\theta s_{\beta_3} + c_\theta c_{\beta_3} c_{\varphi-\alpha_3}), \tag{4.123}$$

$$\theta : \left(\boldsymbol{r}^{\mathcal{P}^1/\mathcal{B}} \times \bar{\boldsymbol{F}}_1\right) \cdot \hat{\boldsymbol{b}}_2' = -c_p \ell_{\mathcal{S}} \dot{\gamma}_1^2 c_{\beta_1} c_{\varphi+\alpha_1}, \tag{4.124}$$

$$\left(\boldsymbol{r}^{\mathcal{P}^3/\mathcal{B}} \times \bar{\boldsymbol{F}}_3\right) \cdot \hat{\boldsymbol{b}}_2' = c_p \ell_{\mathcal{S}} \dot{\gamma}_3^2 c_{\beta_3} c_{\varphi-\alpha_3}, \tag{4.125}$$

$$\bar{\boldsymbol{\tau}}_1 \cdot \hat{\boldsymbol{b}}_2' = c_t \dot{\gamma}_1^2 c_{\beta_1} s_{\varphi+\alpha_1}, \tag{4.126}$$

$$\bar{\boldsymbol{\tau}}_3 \cdot \hat{\boldsymbol{b}}_2' = c_t \dot{\gamma}_3^2 c_{\beta_3} s_{\varphi-\alpha_3}, \tag{4.127}$$

$$\varphi : \left(\boldsymbol{r}^{\mathcal{P}^1/\mathcal{B}} \times \bar{\boldsymbol{F}}_1\right) \cdot \hat{\boldsymbol{b}}_1 = 0, \tag{4.128}$$

$$\left(\boldsymbol{r}^{\mathcal{P}^3/\mathcal{B}} \times \bar{\boldsymbol{F}}_3\right) \cdot \hat{\boldsymbol{b}}_1 = 0, \tag{4.129}$$

$$\bar{\boldsymbol{\tau}}_1 \cdot \hat{\boldsymbol{b}}_1 = -c_t \dot{\gamma}_1^2 s_{\beta_1}, \tag{4.130}$$

$$\bar{\boldsymbol{\tau}}_3 \cdot \hat{\boldsymbol{b}}_1 = c_t \dot{\gamma}_3^2 s_{\beta_3}. \tag{4.131}$$

Similar to the energy partial derivatives, the effects of the thrust and drag torques for arms 1 and 3 are related by the substitution $(\alpha_1, \beta_1) \leftrightarrow (-\alpha_3, -\beta_3)$. The thrust-induced torques vary by an additional negative sign due to the opposing directions of the moment arms about the base. Projections of these end-effector torques onto the arm coordinates remain unchanged from Section 3.2.4 and so are not repeated here.

Lastly, the gyroscopic torques associated with precession of the propellers given by Equation (4.60) can be projected onto the various coordinates according to

$$\psi : \boldsymbol{\sigma}_{\mathcal{P}^1} \cdot \hat{\boldsymbol{n}}_3 = I_{\mathcal{P}}^z \dot{\gamma}_1 \big(- \dot{\theta} c_\theta s_{\beta_1} - \dot{\theta} s_\theta c_{\beta_1} c_{\varphi+\alpha_1} - \dot{\varphi} c_\theta c_{\beta_1} s_{\varphi+\alpha_1} - \dot{\alpha}_1 c_\theta c_{\beta_1} s_{\varphi+\alpha_1}$$

$$- \dot{\beta}_1 s_\theta c_{\beta_1} - \dot{\beta}_1 c_\theta s_{\beta_1} c_{\varphi+\alpha_1}\big), \tag{4.132}$$

$$\boldsymbol{\sigma}_{\mathcal{P}^3} \cdot \hat{\boldsymbol{n}}_3 = I^z_{\mathcal{P}} \dot{\gamma}_3 \big(\dot{\theta} c_\theta s_{\beta_3} - \dot{\theta} s_\theta c_{\beta_3} c_{\varphi-\alpha_3} - \dot{\varphi} c_\theta c_{\beta_3} s_{\varphi-\alpha_3} + \dot{\alpha}_3 c_\theta c_{\beta_3} s_{\varphi-\alpha_3} + \dot{\beta}_3 s_\theta c_{\beta_3} - \dot{\beta}_3 c_\theta s_{\beta_3} c_{\varphi-\alpha_3} \big), \tag{4.133}$$

$$\theta : \boldsymbol{\sigma}_{\mathcal{P}^1} \cdot \hat{\boldsymbol{b}}'_2 = I^z_{\mathcal{P}} \dot{\gamma}_1 \big(\dot{\psi} c_\theta s_{\beta_1} + \dot{\psi} s_\theta c_{\beta_1} c_{\varphi+\alpha_1} - \dot{\varphi} c_{\beta_1} c_{\varphi+\alpha_1} - \dot{\alpha}_1 c_{\beta_1} c_{\varphi+\alpha_1} + \dot{\beta}_1 s_{\beta_1} s_{\varphi+\alpha_1} \big), \tag{4.134}$$

$$\boldsymbol{\sigma}_{\mathcal{P}^3} \cdot \hat{\boldsymbol{b}}'_2 = I^z_{\mathcal{P}} \dot{\gamma}_3 \big(- \dot{\psi} c_\theta s_{\beta_3} + \dot{\psi} s_\theta c_{\beta_3} c_{\varphi-\alpha_3} - \dot{\varphi} c_{\beta_3} c_{\varphi-\alpha_3} + \dot{\alpha}_3 c_{\beta_3} c_{\varphi-\alpha_3} + \dot{\beta}_3 s_{\beta_3} s_{\varphi-\alpha_3} \big), \tag{4.135}$$

$$\varphi : \boldsymbol{\sigma}_{\mathcal{P}^1} \cdot \hat{\boldsymbol{b}}_1 = I^z_{\mathcal{P}} \dot{\gamma}_1 \big(\dot{\psi} c_\theta c_{\beta_1} s_{\varphi+\alpha_1} + \dot{\theta} c_{\beta_1} c_{\varphi+\alpha_1} + \dot{\beta}_1 c_{\beta_1} \big), \tag{4.136}$$

$$\boldsymbol{\sigma}_{\mathcal{P}^3} \cdot \hat{\boldsymbol{b}}_1 = I^z_{\mathcal{P}} \dot{\gamma}_3 \big(\dot{\psi} c_\theta c_{\beta_3} s_{\varphi-\alpha_3} + \dot{\theta} c_{\beta_3} c_{\varphi-\alpha_3} - \dot{\beta}_3 c_{\beta_3} \big), \tag{4.137}$$

$$\alpha_1 : \boldsymbol{\sigma}_{\mathcal{P}^1} \cdot \hat{\boldsymbol{a}}^1_1 = I^z_{\mathcal{P}} \dot{\gamma}_1 \big(\dot{\psi} c_\theta c_{\beta_1} s_{\varphi+\alpha_1} + \dot{\theta} c_{\beta_1} c_{\varphi+\alpha_1} + \dot{\beta}_1 c_{\beta_1} \big), \tag{4.138}$$

$$\alpha_3 : \boldsymbol{\sigma}_{\mathcal{P}^3} \cdot \hat{\boldsymbol{a}}^3_1 = I^z_{\mathcal{P}} \dot{\gamma}_3 \big(- \dot{\psi} c_\theta c_{\beta_3} s_{\varphi-\alpha_3} - \dot{\theta} c_{\beta_3} c_{\varphi-\alpha_3} + \dot{\beta}_3 c_{\beta_3} \big), \tag{4.139}$$

$$\beta_1 : \boldsymbol{\sigma}_{\mathcal{P}^1} \cdot \hat{\boldsymbol{s}}^1_2 = I^z_{\mathcal{P}} \dot{\gamma}_1 \big(\dot{\psi} s_\theta c_{\beta_1} + \dot{\psi} c_\theta s_{\beta_1} c_{\varphi+\alpha_1} - \dot{\theta} s_{\beta_1} s_{\varphi+\alpha_1} - \dot{\varphi} c_{\beta_1} - \dot{\alpha}_1 c_{\beta_1} \big), \tag{4.140}$$

$$\beta_3 : \boldsymbol{\sigma}_{\mathcal{P}^3} \cdot \hat{\boldsymbol{s}}^3_2 = I^z_{\mathcal{P}} \dot{\gamma}_3 \big(- \dot{\psi} s_\theta c_{\beta_3} + \dot{\psi} c_\theta s_{\beta_3} c_{\varphi-\alpha_3} - \dot{\theta} s_{\beta_3} s_{\varphi-\alpha_3} + \dot{\varphi} c_{\beta_3} - \dot{\alpha}_3 c_{\beta_3} \big). \tag{4.141}$$

Once again the equations for arm 3 can be obtained from those for arm 1 by the substitution $(\alpha_1, \beta_1) \leftrightarrow (-\alpha_3, -\beta_3)$.

This completes all of the components necessary to assemble the Euler-Lagrange equations for arms 1 and 3.

4.6 Pitch-Axis Arms

Section 4.5 demonstrated the utility of evaluating opposing arms simultaneously in order to compare their effects via symmetry. The same approach will be taken for arms 2 and 4, which lie along the copter's nominal pitch axis. Though the nominal pitch axis does

not stay aligned with the θ axis of the base rotation sequence, arms 2 and 4 will still be referred to colloquially as the pitch-axis arms.

4.6.1 Arm 2 Energy

From Equation (4.14), the generalized angular rates for arm 2 are

$$\dot{\Phi}_2 = \dot{\psi} c_\theta s_\varphi + \dot{\theta} c_\varphi, \tag{4.142}$$

$$\dot{\Theta}_2 = \dot{\psi} s_\theta - \dot{\varphi}, \tag{4.143}$$

$$\dot{\Psi}_2 = \dot{\psi} c_\theta c_\varphi - \dot{\theta} s_\varphi. \tag{4.144}$$

Misalignment of the true pitch axis with the $\mathcal{B}_2$ axis at nonzero roll angles leads to additional terms in the Lagrangian, complicating the partial derivatives of the pitch-axis arms compared to the roll-axis arms. This is immediately apparent when evaluating the kinetic energy speed partials. For example, consider the linear kinetic energy speed partial of arc 2 with respect to $\dot{\psi}$, with quadratic velocity terms neglected as per the preceding sections

$$\frac{d}{dt}\left(\frac{\partial T^v_{\mathcal{A}^2}}{\partial \dot{\psi}}\right) \approx m_{\mathcal{A}} \ell^2_{\mathcal{A}} \Big[\big(s^2_\theta + c^2_\theta c^2_\varphi\big) \ddot{\psi} - s_\theta \ddot{\varphi} - c_\theta s_\varphi c_\varphi \ddot{\theta} \Big]. \tag{4.145}$$

When the copter rotation is zero, the $\mathcal{B}_2$ axis aligns with the pitch axis and Equation (4.145) reduces to Equation (4.67), however for nontrivial rotations the energy of arm 2 becomes dependent on multiple angles and multiple accelerations. This pattern continues for the other arc linear kinetic energy speed partials, given by

$$\frac{d}{dt}\left(\frac{\partial T^v_{\mathcal{A}^2}}{\partial \dot{\theta}}\right) \approx m_{\mathcal{A}} \ell^2_{\mathcal{A}} \big(- c_\theta s_\varphi c_\varphi \ddot{\psi} + s^2_\varphi \ddot{\theta} \big), \tag{4.146}$$

$$\frac{d}{dt}\left(\frac{\partial T^v_{\mathcal{A}^2}}{\partial \dot{\varphi}}\right) \approx m_{\mathcal{A}} \ell^2_{\mathcal{A}} \big(- s_\theta \ddot{\psi} + \ddot{\varphi} \big). \tag{4.147}$$

At zero base rotation, Equation (4.146) reduces to Equation (4.69) and Equation (4.147)

reduces to the negative of Equation (4.68). This is consistent with the frame definitions as the 1-axis of arm 1 matches the negative 2-axis of arm 2, and the 2-axis of arm 1 matches the 1-axis of arm 2.

With this understanding, the remaining partial derivatives for arm 2 are evaluated and quadratic velocity terms neglected.

$$\begin{aligned}\frac{d}{dt}\left(\frac{\partial T^{\omega}_{\mathcal{A}^2}}{\partial \dot{\psi}}\right) \approx\ & I^x_{\mathcal{A}}\big(c^2_\theta s^2_\varphi \ddot{\psi} + c_\theta s_\varphi c_\varphi \ddot{\theta} + c_\theta s_\varphi \ddot{\alpha}_2\big) \\ & + \Big[I^y_{\mathcal{A}}(s_\theta c_{\alpha_2} + c_\theta c_\varphi s_{\alpha_2})^2 + I^z_{\mathcal{A}}(s_\theta s_{\alpha_2} - c_\theta c_\varphi c_{\alpha_2})^2\Big]\ddot{\psi} \\ & - \Big[\big(I^y_{\mathcal{A}} s^2_{\alpha_2} + I^z_{\mathcal{A}} c^2_{\alpha_2}\big) c_\theta s_\varphi c_\varphi + \big(I^y_{\mathcal{A}} - I^z_{\mathcal{A}}\big) s_\theta s_\varphi s_{\alpha_2} c_{\alpha_2}\Big]\ddot{\theta} \\ & - \Big[\big(I^y_{\mathcal{A}} c^2_{\alpha_2} + I^z_{\mathcal{A}} s^2_{\alpha_2}\big) s_\theta + \big(I^y_{\mathcal{A}} - I^z_{\mathcal{A}}\big) c_\theta c_\varphi s_{\alpha_2} c_{\alpha_2}\Big]\ddot{\varphi},\end{aligned} \tag{4.148}$$

$$\begin{aligned}\frac{d}{dt}\left(\frac{\partial T^{\omega}_{\mathcal{A}^2}}{\partial \dot{\theta}}\right) \approx\ & I^x_{\mathcal{A}}\big(c_\theta s_\varphi c_\varphi \ddot{\psi} + c^2_\varphi \ddot{\theta} + c_\varphi \ddot{\alpha}_2\big) \\ & - \Big[\big(I^y_{\mathcal{A}} s^2_{\alpha_2} + I^z_{\mathcal{A}} c^2_{\alpha_2}\big) c_\theta s_\varphi c_\varphi + \big(I^y_{\mathcal{A}} - I^z_{\mathcal{A}}\big) s_\theta s_\varphi s_{\alpha_2} c_{\alpha_2}\Big]\ddot{\psi} \\ & + \big(I^y_{\mathcal{A}} s^2_{\alpha_2} + I^z_{\mathcal{A}} c^2_{\alpha_2}\big) s^2_\varphi \ddot{\theta} + \big(I^y_{\mathcal{A}} - I^z_{\mathcal{A}}\big) s_\varphi s_{\alpha_2} c_{\alpha_2} \ddot{\varphi},\end{aligned} \tag{4.149}$$

$$\begin{aligned}\frac{d}{dt}\left(\frac{\partial T^{\omega}_{\mathcal{A}^2}}{\partial \dot{\varphi}}\right) \approx\ & -\Big[\big(I^y_{\mathcal{A}} c^2_{\alpha_2} + I^z_{\mathcal{A}} s^2_{\alpha_2}\big) s_\theta + \big(I^y_{\mathcal{A}} - I^z_{\mathcal{A}}\big) c_\theta c_\varphi s_{\alpha_2} c_{\alpha_2}\Big]\ddot{\psi} \\ & + \big(I^y_{\mathcal{A}} - I^z_{\mathcal{A}}\big) s_\varphi s_{\alpha_2} c_{\alpha_2} \ddot{\theta} + \big(I^y_{\mathcal{A}} c^2_{\alpha_2} + I^z_{\mathcal{A}} s^2_{\alpha_2}\big)\ddot{\varphi},\end{aligned} \tag{4.150}$$

$$\frac{d}{dt}\left(\frac{\partial T^{\omega}_{\mathcal{A}^2}}{\partial \dot{\alpha}_2}\right) \approx I^x_{\mathcal{A}}\big(c_\theta s_\varphi \ddot{\psi} + c_\varphi \ddot{\theta} + \ddot{\alpha}_2\big), \tag{4.151}$$

$$U_{\mathcal{A}^2} = -m_{\mathcal{A}} g_0 \ell_{\mathcal{A}} c_\theta s_\varphi, \tag{4.152}$$

$$\frac{\partial U_{\mathcal{A}^2}}{\partial \theta} = m_{\mathcal{A}} g_0 \ell_{\mathcal{A}} s_\theta s_\varphi, \tag{4.153}$$

$$\frac{\partial U_{\mathcal{A}^2}}{\partial \varphi} = -m_{\mathcal{A}} g_0 \ell_{\mathcal{A}} c_\theta c_\varphi, \tag{4.154}$$

$$\frac{d}{dt}\left(\frac{\partial T^{v}_{\mathcal{S}^2}}{\partial \dot{\psi}}\right) \approx m_{\mathcal{S}} \ell^2_{\mathcal{S}}\Big[\big(s^2_\theta + c^2_\theta c^2_\varphi\big)\ddot{\psi} - s_\theta \ddot{\varphi} - c_\theta s_\varphi c_\varphi \ddot{\theta}\Big], \tag{4.155}$$

$$\frac{d}{dt}\left(\frac{\partial T^{v}_{\mathcal{S}^2}}{\partial \dot{\theta}}\right) \approx m_{\mathcal{S}}\ell^2_{\mathcal{S}}\big(- c_\theta s_\varphi c_\varphi \ddot{\psi} + s^2_\varphi \ddot{\theta}\ \big), \tag{4.156}$$

$$\frac{d}{dt}\left(\frac{\partial T^{v}_{\mathcal{S}^2}}{\partial \dot{\varphi}}\right) \approx m_{\mathcal{S}}\ell^2_{\mathcal{S}}\big(- s_\theta \ddot{\psi} + \ddot{\varphi}\big), \tag{4.157}$$

$$\begin{aligned}\frac{d}{dt}\left(\frac{\partial T^{\omega}_{\mathcal{S}^2}}{\partial \dot{\psi}}\right) \approx\ & I^x_{\mathcal{S}}\big(c^2_\theta s^2_\varphi \ddot{\psi} + c_\theta s_\varphi c_\varphi \ddot{\theta} + c_\theta s_\varphi \ddot{\alpha}_2\big) \\ & + \Big[I^y_{\mathcal{S}}(s_\theta c_{\alpha_2} + c_\theta c_\varphi s_{\alpha_2})^2 + I^{xz}_{\mathcal{S}}(s_\theta s_{\alpha_2} - c_\theta c_\varphi c_{\alpha_2})^2\Big]\ddot{\psi} \\ & - \Big[\big(I^y_{\mathcal{S}} s^2_{\alpha_2} + I^{xz}_{\mathcal{S}} c^2_{\alpha_2}\big)c_\theta s_\varphi c_\varphi + \big(I^y_{\mathcal{S}} - I^{xz}_{\mathcal{S}}\big)s_\theta s_\varphi s_{\alpha_2} c_{\alpha_2}\Big]\ddot{\theta} \\ & - \Big[\big(I^y_{\mathcal{S}} c^2_{\alpha_2} + I^{xz}_{\mathcal{S}} s^2_{\alpha_2}\big)s_\theta + \big(I^y_{\mathcal{S}} - I^{xz}_{\mathcal{S}}\big)c_\theta c_\varphi s_{\alpha_2} c_{\alpha_2}\Big]\ddot{\varphi} \\ & + I^y_{\mathcal{S}}\big(s_\theta c_{\alpha_2} + c_\theta c_\varphi s_{\alpha_2}\big)\ddot{\beta}_2,\end{aligned} \tag{4.158}$$

$$\begin{aligned}\frac{d}{dt}\left(\frac{\partial T^{\omega}_{\mathcal{S}^2}}{\partial \dot{\theta}}\right) \approx\ & I^x_{\mathcal{S}}\big(c_\theta s_\varphi c_\varphi \ddot{\psi} + c^2_\varphi \ddot{\theta} + c_\varphi \ddot{\alpha}_2\big) \\ & - \Big[\big(I^y_{\mathcal{S}} s^2_{\alpha_2} + I^{xz}_{\mathcal{S}} c^2_{\alpha_2}\big)c_\theta s_\varphi c_\varphi + \big(I^y_{\mathcal{S}} - I^{xz}_{\mathcal{S}}\big)s_\theta s_\varphi s_{\alpha_2} c_{\alpha_2}\Big]\ddot{\psi} \\ & + \big(I^y_{\mathcal{S}} s^2_{\alpha_2} + I^{xz}_{\mathcal{S}} c^2_{\alpha_2}\big)s^2_\varphi \ddot{\theta} + \big(I^y_{\mathcal{S}} - I^{xz}_{\mathcal{S}}\big)s_\varphi s_{\alpha_2} c_{\alpha_2}\ddot{\varphi} - I^y_{\mathcal{S}} s_\varphi s_{\alpha_2}\ddot{\beta}_2,\end{aligned} \tag{4.159}$$

$$\begin{aligned}\frac{d}{dt}\left(\frac{\partial T^{\omega}_{\mathcal{S}^2}}{\partial \dot{\varphi}}\right) \approx\ & -\Big[\big(I^y_{\mathcal{S}} c^2_{\alpha_2} + I^{xz}_{\mathcal{S}} s^2_{\alpha_2}\big)s_\theta + \big(I^y_{\mathcal{S}} - I^{xz}_{\mathcal{S}}\big)c_\theta c_\varphi s_{\alpha_2} c_{\alpha_2}\Big]\ddot{\psi} \\ & + \big(I^y_{\mathcal{S}} - I^{xz}_{\mathcal{S}}\big)s_\varphi s_{\alpha_2} c_{\alpha_2}\ddot{\theta} + \big(I^y_{\mathcal{S}} c^2_{\alpha_2} + I^{xz}_{\mathcal{S}} s^2_{\alpha_2}\big)\ddot{\varphi} - I^y_{\mathcal{S}} c_{\alpha_2}\ddot{\beta}_2,\end{aligned} \tag{4.160}$$

$$\frac{d}{dt}\left(\frac{\partial T^{\omega}_{\mathcal{S}^2}}{\partial \dot{\alpha}_2}\right) \approx I^{xz}_{\mathcal{S}}\big(c_\theta s_\varphi \ddot{\psi} + c_\varphi \ddot{\theta} + \ddot{\alpha}_2\big), \tag{4.161}$$

$$\frac{d}{dt}\left(\frac{\partial T^{\omega}_{\mathcal{S}^2}}{\partial \dot{\beta}_2}\right) \approx I^y_{\mathcal{S}}\Big[\big(s_\theta c_{\alpha_2} + c_\theta c_\varphi s_{\alpha_2}\big)\ddot{\psi} - s_\varphi s_{\alpha_2}\ddot{\theta} - c_{\alpha_2}\ddot{\varphi} + \ddot{\beta}_2\Big], \tag{4.162}$$

$$U_{\mathcal{S}^2} = -m_{\mathcal{S}} g_0 \ell_{\mathcal{S}} c_\theta s_\varphi, \tag{4.163}$$

$$\frac{\partial U_{\mathcal{S}^2}}{\partial \theta} = m_{\mathcal{S}} g_0 \ell_{\mathcal{S}} s_\theta s_\varphi, \tag{4.164}$$

$$\frac{\partial U_{\mathcal{S}^2}}{\partial \varphi} = -m_{\mathcal{S}} g_0 \ell_{\mathcal{S}} c_\theta c_\varphi, \tag{4.165}$$

$$\frac{d}{dt}\left(\frac{\partial T^{\omega}_{\mathcal{P}^2}}{\partial \dot{\gamma}_2}\right) = I^z_{\mathcal{P}}\ddot{\gamma}_2, \tag{4.166}$$

$$U_{\mathcal{P}^2} = m_{\mathcal{P}} g_0 \Big[\big(\ell_{\mathcal{S}} + \ell_{\mathcal{P}} s_{\beta_2}\big) c_\theta s_\varphi - \ell_{\mathcal{P}} s_\theta s_{\alpha_2} c_{\beta_2} + \ell_{\mathcal{P}} c_\theta c_\varphi c_{\alpha_2} c_{\beta_2} \Big], \tag{4.167}$$

$$\frac{\partial U_{\mathcal{P}^2}}{\partial \theta} = m_{\mathcal{P}} g_0 \Big[-\big(\ell_{\mathcal{S}} + \ell_{\mathcal{P}} s_{\beta_2}\big) s_\theta s_\varphi - \ell_{\mathcal{P}} c_\theta s_{\alpha_2} c_{\beta_2} - \ell_{\mathcal{P}} s_\theta c_\varphi c_{\alpha_2} c_{\beta_2} \Big], \tag{4.168}$$

$$\frac{\partial U_{\mathcal{P}^2}}{\partial \varphi} = m_{\mathcal{P}} g_0 \Big[\big(\ell_{\mathcal{S}} + \ell_{\mathcal{P}} s_{\beta_2}\big) c_\theta c_\varphi - \ell_{\mathcal{P}} c_\theta s_\varphi c_{\alpha_2} c_{\beta_2} \Big], \tag{4.169}$$

$$\frac{\partial U_{\mathcal{P}^2}}{\partial \alpha_2} = m_{\mathcal{P}} g_0 \big(-\ell_{\mathcal{P}} s_\theta c_{\alpha_2} c_{\beta_2} - \ell_{\mathcal{P}} c_\theta c_\varphi s_{\alpha_2} c_{\beta_2} \big), \tag{4.170}$$

$$\frac{\partial U_{\mathcal{P}^2}}{\partial \beta_2} = m_{\mathcal{P}} g_0 \big(\ell_{\mathcal{P}} c_\theta s_\varphi c_{\beta_2} + \ell_{\mathcal{P}} s_\theta s_{\alpha_2} s_{\beta_2} - \ell_{\mathcal{P}} c_\theta c_\varphi c_{\alpha_2} s_{\beta_2} \big). \tag{4.171}$$

4.6.2 Arm 4 Energy

Similar to the relationship between the two roll-axis arms, the equations for the two pitch-axis arms are related by a substitution of the twist and tilt coordinates with their negative counterparts. Beginning from Equation (4.14), the generalized angular rates for arm 4 are

$$\dot{\Phi}_4 = -\dot{\psi} c_\theta s_\varphi - \dot{\theta} c_\varphi, \tag{4.172}$$

$$\dot{\Theta}_4 = -\dot{\psi} s_\theta + \dot{\varphi}, \tag{4.173}$$

$$\dot{\Psi}_4 = \dot{\psi} c_\theta c_\varphi - \dot{\theta} s_\varphi. \tag{4.174}$$

The Lagrangian partials can then be evaluated and quadratic velocity terms neglected.

$$\frac{d}{dt}\left(\frac{\partial T^v_{\mathcal{A}^4}}{\partial \dot{\psi}}\right) \approx m_{\mathcal{A}} \ell^2_{\mathcal{A}} \Big[\big(s^2_\theta + c^2_\theta c^2_\varphi\big) \ddot{\psi} - s_\theta \ddot{\varphi} - c_\theta s_\varphi c_\varphi \ddot{\theta} \Big], \tag{4.175}$$

$$\frac{d}{dt}\left(\frac{\partial T^v_{\mathcal{A}^4}}{\partial \dot{\theta}}\right) \approx m_{\mathcal{A}} \ell^2_{\mathcal{A}} \big(-c_\theta s_\varphi c_\varphi \ddot{\psi} + s^2_\varphi \ddot{\theta} \big), \tag{4.176}$$

$$\frac{d}{dt}\left(\frac{\partial T^v_{\mathcal{A}^4}}{\partial \dot{\varphi}}\right) \approx m_{\mathcal{A}} \ell^2_{\mathcal{A}} \big(-s_\theta \ddot{\psi} + \ddot{\varphi} \big), \tag{4.177}$$

$$\begin{aligned}\frac{d}{dt}\left(\frac{\partial T^{\omega}_{\mathcal{A}^4}}{\partial\dot{\psi}}\right) \approx\ & I^x_{\mathcal{A}}\big(c^2_\theta s^2_\varphi\ddot{\psi} + c_\theta s_\varphi c_\varphi\ddot{\theta} - c_\theta s_\varphi\ddot{\alpha}_4\big)\\ &+ \Big[I^y_{\mathcal{A}}(s_\theta c_{\alpha_4} - c_\theta c_\varphi s_{\alpha_4})^2 + I^z_{\mathcal{A}}(s_\theta s_{\alpha_4} + c_\theta c_\varphi c_{\alpha_4})^2\Big]\ddot{\psi}\\ &- \Big[\big(I^y_{\mathcal{A}}s^2_{\alpha_4} + I^z_{\mathcal{A}}c^2_{\alpha_4}\big)c_\theta s_\varphi c_\varphi - \big(I^y_{\mathcal{A}} - I^z_{\mathcal{A}}\big)s_\theta s_\varphi s_{\alpha_4}c_{\alpha_4}\Big]\ddot{\theta}\\ &- \Big[\big(I^y_{\mathcal{A}}c^2_{\alpha_4} + I^z_{\mathcal{A}}s^2_{\alpha_4}\big)s_\theta - \big(I^y_{\mathcal{A}} - I^z_{\mathcal{A}}\big)c_\theta c_\varphi s_{\alpha_4}c_{\alpha_4}\Big]\ddot{\varphi},\end{aligned} \tag{4.178}$$

$$\begin{aligned}\frac{d}{dt}\left(\frac{\partial T^{\omega}_{\mathcal{A}^4}}{\partial\dot{\theta}}\right) \approx\ & I^x_{\mathcal{A}}\big(c_\theta s_\varphi c_\varphi\ddot{\psi} + c^2_\varphi\ddot{\theta} - c_\varphi\ddot{\alpha}_4\big)\\ &- \Big[\big(I^y_{\mathcal{A}}s^2_{\alpha_4} + I^z_{\mathcal{A}}c^2_{\alpha_4}\big)c_\theta s_\varphi c_\varphi - \big(I^y_{\mathcal{A}} - I^z_{\mathcal{A}}\big)s_\theta s_\varphi s_{\alpha_4}c_{\alpha_4}\Big]\ddot{\psi}\\ &+ \big(I^y_{\mathcal{A}}s^2_{\alpha_4} + I^z_{\mathcal{A}}c^2_{\alpha_4}\big)s^2_\varphi\ddot{\theta} - \big(I^y_{\mathcal{A}} - I^z_{\mathcal{A}}\big)s_\varphi s_{\alpha_4}c_{\alpha_4}\ddot{\varphi},\end{aligned} \tag{4.179}$$

$$\begin{aligned}\frac{d}{dt}\left(\frac{\partial T^{\omega}_{\mathcal{A}^4}}{\partial\dot{\varphi}}\right) \approx\ & -\Big[\big(I^y_{\mathcal{A}}c^2_{\alpha_4} + I^z_{\mathcal{A}}s^2_{\alpha_4}\big)s_\theta - \big(I^y_{\mathcal{A}} - I^z_{\mathcal{A}}\big)c_\theta c_\varphi s_{\alpha_4}c_{\alpha_4}\Big]\ddot{\psi}\\ &- \big(I^y_{\mathcal{A}} - I^z_{\mathcal{A}}\big)s_\varphi s_{\alpha_4}c_{\alpha_4}\ddot{\theta} + \big(I^y_{\mathcal{A}}c^2_{\alpha_4} + I^z_{\mathcal{A}}s^2_{\alpha_4}\big)\ddot{\varphi},\end{aligned} \tag{4.180}$$

$$\frac{d}{dt}\left(\frac{\partial T^{\omega}_{\mathcal{A}^4}}{\partial\dot{\alpha}_4}\right) \approx I^x_{\mathcal{A}}\big(-c_\theta s_\varphi\ddot{\psi} - c_\varphi\ddot{\theta} + \ddot{\alpha}_4\big), \tag{4.181}$$

$$U_{\mathcal{A}^4} = m_{\mathcal{A}}g_0\ell_{\mathcal{A}}c_\theta s_\varphi, \tag{4.182}$$

$$\frac{\partial U_{\mathcal{A}^4}}{\partial\theta} = -m_{\mathcal{A}}g_0\ell_{\mathcal{A}}s_\theta s_\varphi, \tag{4.183}$$

$$\frac{\partial U_{\mathcal{A}^4}}{\partial\varphi} = m_{\mathcal{A}}g_0\ell_{\mathcal{A}}c_\theta c_\varphi, \tag{4.184}$$

$$\frac{d}{dt}\left(\frac{\partial T^{v}_{\mathcal{S}^4}}{\partial\dot{\psi}}\right) \approx m_{\mathcal{S}}\ell^2_{\mathcal{S}}\Big[\big(s^2_\theta + c^2_\theta c^2_\varphi\big)\ddot{\psi} - s_\theta\ddot{\varphi} - c_\theta s_\varphi c_\varphi\ddot{\theta}\Big], \tag{4.185}$$

$$\frac{d}{dt}\left(\frac{\partial T^{v}_{\mathcal{S}^4}}{\partial\dot{\theta}}\right) \approx m_{\mathcal{S}}\ell^2_{\mathcal{S}}\big(-c_\theta s_\varphi c_\varphi\ddot{\psi} + s^2_\varphi\ddot{\theta}\ \big), \tag{4.186}$$

$$\frac{d}{dt}\left(\frac{\partial T^{v}_{\mathcal{S}^4}}{\partial\dot{\varphi}}\right) \approx m_{\mathcal{S}}\ell^2_{\mathcal{S}}\big(-s_\theta\ddot{\psi} + \ddot{\varphi}\big), \tag{4.187}$$

$$\frac{d}{dt}\left(\frac{\partial T^{\omega}_{\mathcal{S}^4}}{\partial \dot{\psi}}\right) \approx I^{x}_{\mathcal{S}}\big(c^2_{\theta}s^2_{\varphi}\ddot{\psi} + c_{\theta}s_{\varphi}c_{\varphi}\ddot{\theta} - c_{\theta}s_{\varphi}\ddot{\alpha}_4\big)$$
$$+ \Big[I^{y}_{\mathcal{S}}(s_{\theta}c_{\alpha_4} - c_{\theta}c_{\varphi}s_{\alpha_4})^2 + I^{xz}_{\mathcal{S}}(s_{\theta}s_{\alpha_4} + c_{\theta}c_{\varphi}c_{\alpha_4})^2\Big]\ddot{\psi}$$
$$- \Big[\big(I^{y}_{\mathcal{S}}s^2_{\alpha_4} + I^{xz}_{\mathcal{S}}c^2_{\alpha_4}\big)c_{\theta}s_{\varphi}c_{\varphi} - \big(I^{y}_{\mathcal{S}} - I^{xz}_{\mathcal{S}}\big)s_{\theta}s_{\varphi}s_{\alpha_4}c_{\alpha_4}\Big]\ddot{\theta} \tag{4.188}$$
$$- \Big[\big(I^{y}_{\mathcal{S}}c^2_{\alpha_4} + I^{xz}_{\mathcal{S}}s^2_{\alpha_4}\big)s_{\theta} - \big(I^{y}_{\mathcal{S}} - I^{xz}_{\mathcal{S}}\big)c_{\theta}c_{\varphi}s_{\alpha_4}c_{\alpha_4}\Big]\ddot{\varphi}$$
$$- I^{y}_{\mathcal{S}}\big(s_{\theta}c_{\alpha_4} - c_{\theta}c_{\varphi}s_{\alpha_4}\big)\ddot{\beta}_4,$$

$$\frac{d}{dt}\left(\frac{\partial T^{\omega}_{\mathcal{S}^4}}{\partial \dot{\theta}}\right) \approx I^{x}_{\mathcal{S}}\big(c_{\theta}s_{\varphi}c_{\varphi}\ddot{\psi} + c^2_{\varphi}\ddot{\theta} - c_{\varphi}\ddot{\alpha}_4\big)$$
$$- \Big[\big(I^{y}_{\mathcal{S}}s^2_{\alpha_4} + I^{xz}_{\mathcal{S}}c^2_{\alpha_4}\big)c_{\theta}s_{\varphi}c_{\varphi} - \big(I^{y}_{\mathcal{S}} - I^{xz}_{\mathcal{S}}\big)s_{\theta}s_{\varphi}s_{\alpha_4}c_{\alpha_4}\Big]\ddot{\psi} \tag{4.189}$$
$$+ \big(I^{y}_{\mathcal{S}}s^2_{\alpha_4} + I^{xz}_{\mathcal{S}}c^2_{\alpha_4}\big)s^2_{\varphi}\ddot{\theta} - \big(I^{y}_{\mathcal{S}} - I^{xz}_{\mathcal{S}}\big)s_{\varphi}s_{\alpha_4}c_{\alpha_4}\ddot{\varphi} - I^{y}_{\mathcal{S}}s_{\varphi}s_{\alpha_4}\ddot{\beta}_4,$$

$$\frac{d}{dt}\left(\frac{\partial T^{\omega}_{\mathcal{S}^4}}{\partial \dot{\varphi}}\right) \approx -\Big[\big(I^{y}_{\mathcal{S}}c^2_{\alpha_4} + I^{xz}_{\mathcal{S}}s^2_{\alpha_4}\big)s_{\theta} - \big(I^{y}_{\mathcal{S}} - I^{xz}_{\mathcal{S}}\big)c_{\theta}c_{\varphi}s_{\alpha_4}c_{\alpha_4}\Big]\ddot{\psi}$$
$$- \big(I^{y}_{\mathcal{S}} - I^{xz}_{\mathcal{S}}\big)s_{\varphi}s_{\alpha_4}c_{\alpha_4}\ddot{\theta} + \big(I^{y}_{\mathcal{S}}c^2_{\alpha_4} + I^{xz}_{\mathcal{S}}s^2_{\alpha_4}\big)\ddot{\varphi} + I^{y}_{\mathcal{S}}c_{\alpha_4}\ddot{\beta}_4, \tag{4.190}$$

$$\frac{d}{dt}\left(\frac{\partial T^{\omega}_{\mathcal{S}^4}}{\partial \dot{\alpha}_4}\right) \approx I^{xz}_{\mathcal{S}}\big(-c_{\theta}s_{\varphi}\ddot{\psi} - c_{\varphi}\ddot{\theta} + \ddot{\alpha}_4\big), \tag{4.191}$$

$$\frac{d}{dt}\left(\frac{\partial T^{\omega}_{\mathcal{S}^4}}{\partial \dot{\beta}_4}\right) \approx I^{y}_{\mathcal{S}}\Big[\big(-s_{\theta}c_{\alpha_4} + c_{\theta}c_{\varphi}s_{\alpha_4}\big)\ddot{\psi} - s_{\varphi}s_{\alpha_4}\ddot{\theta} + c_{\alpha_4}\ddot{\varphi} + \ddot{\beta}_4\Big], \tag{4.192}$$

$$U_{\mathcal{S}^4} = m_{\mathcal{S}}g_0\ell_{\mathcal{S}}c_{\theta}s_{\varphi}, \tag{4.193}$$

$$\frac{\partial U_{\mathcal{S}^4}}{\partial \theta} = -m_{\mathcal{S}}g_0\ell_{\mathcal{S}}s_{\theta}s_{\varphi}, \tag{4.194}$$

$$\frac{\partial U_{\mathcal{S}^4}}{\partial \varphi} = m_{\mathcal{S}}g_0\ell_{\mathcal{S}}c_{\theta}c_{\varphi}, \tag{4.195}$$

$$\frac{d}{dt}\left(\frac{\partial T^{\omega}_{\mathcal{P}^4}}{\partial \dot{\gamma}_4}\right) = I^{z}_{\mathcal{P}}\ddot{\gamma}_4, \tag{4.196}$$

$$U_{\mathcal{P}^4} = m_{\mathcal{P}}g_0\Big[-\big(\ell_{\mathcal{S}} + \ell_{\mathcal{P}}s_{\beta_4}\big)c_{\theta}s_{\varphi} + \ell_{\mathcal{P}}s_{\theta}s_{\alpha_4}c_{\beta_4} + \ell_{\mathcal{P}}c_{\theta}c_{\varphi}c_{\alpha_4}c_{\beta_4}\Big], \tag{4.197}$$

$$\frac{\partial U_{\mathcal{P}^4}}{\partial \theta} = m_{\mathcal{P}} g_0 \Big[\big(\ell_{\mathcal{S}} + \ell_{\mathcal{P}} s_{\beta_4}\big) s_\theta s_\varphi + \ell_{\mathcal{P}} c_\theta s_{\alpha_4} c_{\beta_4} - \ell_{\mathcal{P}} s_\theta c_\varphi c_{\alpha_4} c_{\beta_4} \Big], \tag{4.198}$$

$$\frac{\partial U_{\mathcal{P}^4}}{\partial \varphi} = m_{\mathcal{P}} g_0 \Big[-\big(\ell_{\mathcal{S}} + \ell_{\mathcal{P}} s_{\beta_4}\big) c_\theta c_\varphi - \ell_{\mathcal{P}} c_\theta s_\varphi c_{\alpha_4} c_{\beta_4} \Big], \tag{4.199}$$

$$\frac{\partial U_{\mathcal{P}^4}}{\partial \alpha_4} = m_{\mathcal{P}} g_0 \big(\ell_{\mathcal{P}} s_\theta c_{\alpha_4} c_{\beta_4} - \ell_{\mathcal{P}} c_\theta c_\varphi s_{\alpha_4} c_{\beta_4}\big), \tag{4.200}$$

$$\frac{\partial U_{\mathcal{P}^4}}{\partial \beta_4} = m_{\mathcal{P}} g_0 \big(-\ell_{\mathcal{P}} c_\theta s_\varphi c_{\beta_4} - \ell_{\mathcal{P}} s_\theta s_{\alpha_4} s_{\beta_4} - \ell_{\mathcal{P}} c_\theta c_\varphi c_{\alpha_4} s_{\beta_4}\big). \tag{4.201}$$

4.6.3 Generalized Forces

The thrust and drag torques for the pitch-axis arms are projected onto the base rotation axes using Equations (4.54)-(4.59).

$$\psi : \big(\boldsymbol{r}^{\mathcal{P}^2/\mathcal{B}} \times \bar{\boldsymbol{F}}_2\big) \cdot \hat{\boldsymbol{n}}_3 = c_p \ell_{\mathcal{S}} \dot{\gamma}_2^2 c_{\beta_2} \big(-s_\theta c_{\alpha_2} - c_\theta c_\varphi s_{\alpha_2}\big), \tag{4.202}$$

$$\big(\boldsymbol{r}^{\mathcal{P}^4/\mathcal{B}} \times \bar{\boldsymbol{F}}_4\big) \cdot \hat{\boldsymbol{n}}_3 = c_p \ell_{\mathcal{S}} \dot{\gamma}_4^2 c_{\beta_4} \big(s_\theta c_{\alpha_4} - c_\theta c_\varphi s_{\alpha_4}\big), \tag{4.203}$$

$$\bar{\boldsymbol{\tau}}_2 \cdot \hat{\boldsymbol{n}}_3 = c_t \dot{\gamma}_2^2 (-s_\theta s_{\alpha_2} c_{\beta_2} + c_\theta s_\varphi s_{\beta_2} + c_\theta c_\varphi c_{\alpha_2} c_{\beta_2}), \tag{4.204}$$

$$\bar{\boldsymbol{\tau}}_4 \cdot \hat{\boldsymbol{n}}_3 = c_t \dot{\gamma}_4^2 (s_\theta s_{\alpha_4} c_{\beta_4} - c_\theta s_\varphi s_{\beta_4} + c_\theta c_\varphi c_{\alpha_4} c_{\beta_4}), \tag{4.205}$$

$$\theta : \big(\boldsymbol{r}^{\mathcal{P}^2/\mathcal{B}} \times \bar{\boldsymbol{F}}_2\big) \cdot \hat{\boldsymbol{b}}_2' = c_p \ell_{\mathcal{S}} \dot{\gamma}_2^2 s_\varphi s_{\alpha_2} c_{\beta_2}, \tag{4.206}$$

$$\big(\boldsymbol{r}^{\mathcal{P}^4/\mathcal{B}} \times \bar{\boldsymbol{F}}_4\big) \cdot \hat{\boldsymbol{b}}_2' = c_p \ell_{\mathcal{S}} \dot{\gamma}_4^2 s_\varphi s_{\alpha_4} c_{\beta_4}, \tag{4.207}$$

$$\bar{\boldsymbol{\tau}}_2 \cdot \hat{\boldsymbol{b}}_2' = c_t \dot{\gamma}_2^2 \big(c_\varphi s_{\beta_2} - s_\varphi c_{\alpha_2} c_{\beta_2}\big), \tag{4.208}$$

$$\bar{\boldsymbol{\tau}}_4 \cdot \hat{\boldsymbol{b}}_2' = c_t \dot{\gamma}_4^2 \big(-c_\varphi s_{\beta_4} - s_\varphi c_{\alpha_4} c_{\beta_4}\big), \tag{4.209}$$

$$\varphi : \big(\boldsymbol{r}^{\mathcal{P}^2/\mathcal{B}} \times \bar{\boldsymbol{F}}_2\big) \cdot \hat{\boldsymbol{b}}_1 = c_p \ell_{\mathcal{S}} \dot{\gamma}_2^2 c_{\alpha_2} c_{\beta_2}, \tag{4.210}$$

$$\big(\boldsymbol{r}^{\mathcal{P}^4/\mathcal{B}} \times \bar{\boldsymbol{F}}_4\big) \cdot \hat{\boldsymbol{b}}_1 = -c_p \ell_{\mathcal{S}} \dot{\gamma}_4^2 c_{\alpha_4} c_{\beta_4}, \tag{4.211}$$

$$\bar{\boldsymbol{\tau}}_2 \cdot \hat{\boldsymbol{b}}_1 = c_t \dot{\gamma}_2^2 s_{\alpha_2} c_{\beta_2}, \tag{4.212}$$

$$\bar{\boldsymbol{\tau}}_4 \cdot \hat{\boldsymbol{b}}_1 = -c_t \dot{\gamma}_4^2 s_{\alpha_4} c_{\beta_4}. \tag{4.213}$$

Neglecting gyroscopic torques for the arcs and shafts, the gyroscopic torques of the

propellers given by Equation (4.60) are projected onto the various coordinates.

$$\psi : \boldsymbol{\sigma}_{\mathcal{P}^2} \cdot \hat{\boldsymbol{n}}_3 = I^z_{\mathcal{P}} \dot{\gamma}_2 \Big[- \dot{\theta} c_\theta s_{\alpha_2} c_{\beta_2} - \dot{\theta} s_\theta \big(s_\varphi s_{\beta_2} + c_\varphi c_{\alpha_2} c_{\beta_2} \big) + \dot{\varphi} c_\theta \big(c_\varphi s_{\beta_2} - s_\varphi c_{\alpha_2} c_{\beta_2} \big) \\ - \dot{\alpha} c_{\beta_2} \big(s_\theta c_{\alpha_2} + c_\theta c_\varphi s_{\alpha_2} \big) + \dot{\beta}_2 c_\theta s_\varphi c_{\beta_2} + \dot{\beta}_2 s_{\beta_2} \big(s_\theta s_{\alpha_2} - c_\theta c_\varphi c_{\alpha_2} \big) \Big] \tag{4.214}$$

$$\boldsymbol{\sigma}_{\mathcal{P}^4} \cdot \hat{\boldsymbol{n}}_3 = I^z_{\mathcal{P}} \dot{\gamma}_4 \Big[\dot{\theta} c_\theta s_{\alpha_4} c_{\beta_4} + \dot{\theta} s_\theta \big(s_\varphi s_{\beta_4} - c_\varphi c_{\alpha_4} c_{\beta_4} \big) - \dot{\varphi} c_\theta \big(c_\varphi s_{\beta_4} + s_\varphi c_{\alpha_4} c_{\beta_4} \big) \\ + \dot{\alpha} c_{\beta_4} \big(s_\theta c_{\alpha_4} - c_\theta c_\varphi s_{\alpha_4} \big) - \dot{\beta}_4 c_\theta s_\varphi c_{\beta_4} - \dot{\beta}_4 s_{\beta_4} \big(s_\theta s_{\alpha_4} + c_\theta c_\varphi c_{\alpha_4} \big) \Big] \tag{4.215}$$

$$\theta : \boldsymbol{\sigma}_{\mathcal{P}^2} \cdot \hat{\boldsymbol{b}}'_2 = I^z_{\mathcal{P}} \dot{\gamma}_2 \Big[\dot{\psi} c_\theta s_{\alpha_2} c_{\beta_2} + \dot{\psi} s_\theta \big(s_\varphi s_{\beta_2} + c_\varphi c_{\alpha_2} c_{\beta_2} \big) - \dot{\varphi} \big(c_\varphi c_{\alpha_2} c_{\beta_2} + s_\varphi s_{\beta_2} \big) \\ + \dot{\alpha}_2 s_\varphi s_{\alpha_2} c_{\beta_2} + \dot{\beta}_2 \big(c_\varphi c_{\beta_2} + s_\varphi c_{\alpha_2} s_{\beta_2} \big) \Big] \tag{4.216}$$

$$\boldsymbol{\sigma}_{\mathcal{P}^4} \cdot \hat{\boldsymbol{b}}'_2 = I^z_{\mathcal{P}} \dot{\gamma}_4 \Big[- \dot{\psi} c_\theta s_{\alpha_4} c_{\beta_4} - \dot{\psi} s_\theta \big(s_\varphi s_{\beta_4} - c_\varphi c_{\alpha_4} c_{\beta_4} \big) + \dot{\varphi} \big(s_\varphi s_{\beta_4} - c_\varphi c_{\alpha_4} c_{\beta_4} \big) \\ + \dot{\alpha}_4 s_\varphi s_{\alpha_4} c_{\beta_4} - \dot{\beta}_4 \big(c_\varphi c_{\beta_4} - s_\varphi c_{\alpha_4} s_{\beta_4} \big) \Big] \tag{4.217}$$

$$\varphi : \boldsymbol{\sigma}_{\mathcal{P}^2} \cdot \hat{\boldsymbol{b}}_1 = I^z_{\mathcal{P}} \dot{\gamma}_2 \Big[- \dot{\psi} c_\theta \big(c_\varphi s_{\beta_2} - s_\varphi c_{\alpha_2} c_{\beta_2} \big) + \dot{\theta} \big(s_\varphi s_{\beta_2} + c_\varphi c_{\alpha_2} c_{\beta_2} \big) \\ + \dot{\alpha}_2 c_{\alpha_2} c_{\beta_2} - \dot{\beta}_2 s_{\alpha_2} s_{\beta_2} \Big] \tag{4.218}$$

$$\boldsymbol{\sigma}_{\mathcal{P}^4} \cdot \hat{\boldsymbol{b}}_1 = I^z_{\mathcal{P}} \dot{\gamma}_4 \Big[\dot{\psi} c_\theta \big(c_\varphi s_{\beta_4} + s_\varphi c_{\alpha_4} c_{\beta_4} \big) - \dot{\theta} \big(s_\varphi s_{\beta_4} - c_\varphi c_{\alpha_4} c_{\beta_4} \big) \\ - \dot{\alpha}_4 c_{\alpha_4} c_{\beta_4} + \dot{\beta}_4 s_{\alpha_4} s_{\beta_4} \Big] \tag{4.219}$$

$$\alpha_2 : \boldsymbol{\sigma}_{\mathcal{P}^2} \cdot \hat{\boldsymbol{a}}^2_1 = I^z_{\mathcal{P}} \dot{\gamma}_2 \Big[\dot{\psi} c_{\beta_2} \big(s_\theta c_{\alpha_2} + c_\theta c_\varphi s_{\alpha_2} \big) - \dot{\theta} s_\varphi s_{\alpha_2} c_{\beta_2} - \dot{\varphi} c_{\alpha_2} c_{\beta_2} + \dot{\beta}_2 c_{\beta_2} \Big] \tag{4.220}$$

$$\alpha_4 : \boldsymbol{\sigma}_{\mathcal{P}^4} \cdot \hat{\boldsymbol{a}}^4_1 = I^z_{\mathcal{P}} \dot{\gamma}_4 \Big[- \dot{\psi} c_{\beta_4} \big(s_\theta c_{\alpha_4} - c_\theta c_\varphi s_{\alpha_4} \big) - \dot{\theta} s_\varphi s_{\alpha_4} c_{\beta_4} + \dot{\varphi} c_{\alpha_4} c_{\beta_4} + \dot{\beta}_4 c_{\beta_4} \Big] \tag{4.221}$$

$$\beta_2 : \boldsymbol{\sigma}_{\mathcal{P}^2} \cdot \hat{\boldsymbol{s}}^2_2 = I^z_{\mathcal{P}} \dot{\gamma}_2 \Big[\dot{\psi} \big(c_\theta c_\varphi c_{\alpha_2} s_{\beta_2} - c_\theta s_\varphi c_{\beta_2} - s_\theta s_{\alpha_2} s_{\beta_2} \big) - \dot{\theta} \big(c_\varphi c_{\beta_2} + s_\varphi c_{\alpha_2} s_{\beta_2} \big) \\ + \dot{\varphi} s_{\alpha_2} s_{\beta_2} - \dot{\alpha}_2 c_{\beta_2} \Big] \tag{4.222}$$

$$\beta_4 : \boldsymbol{\sigma}_{\mathcal{P}^4} \cdot \hat{\boldsymbol{s}}^4_2 = I^z_{\mathcal{P}} \dot{\gamma}_4 \Big[\dot{\psi} \big(c_\theta c_\varphi c_{\alpha_4} s_{\beta_4} + c_\theta s_\varphi c_{\beta_4} + s_\theta s_{\alpha_4} s_{\beta_4} \big) + \dot{\theta} \big(c_\varphi c_{\beta_4} - s_\varphi c_{\alpha_4} s_{\beta_4} \big) \\ - \dot{\varphi} s_{\alpha_4} s_{\beta_4} - \dot{\alpha}_4 c_{\beta_4} \Big] \tag{4.223}$$

4.7 Equations of Motion

The full Euler-Lagrange equations are assembled by combining the results from the last several sections and substituting into Equation (4.5). The resulting matrix equation is of the form

$$\boldsymbol{M}(\boldsymbol{q})\ddot{\boldsymbol{q}} + \boldsymbol{C}(\boldsymbol{q}, \dot{\boldsymbol{q}})\dot{\boldsymbol{q}} + \boldsymbol{f}(\boldsymbol{q}, \dot{\boldsymbol{q}}) + \boldsymbol{d}(\boldsymbol{q}, \dot{\boldsymbol{q}}) + \boldsymbol{g}(\boldsymbol{q}) = \boldsymbol{\tau}, \tag{4.224}$$

which is similar to Equation (3.53) with larger dimensions and including the thrust-induced torques. The matrix terms $\boldsymbol{M}$ and $\boldsymbol{C}$ are described individually in the following sections, and the vector terms are grouped into another section.

4.7.1 Inertia Matrix

The inertia matrix $\boldsymbol{M}$ is composed of the coefficients to acceleration terms arising from the kinetic energy speed partials. It takes the following block structure

$$\boldsymbol{M}(\boldsymbol{q}) = \begin{bmatrix} \boldsymbol{M}_{\mathcal{B}\mathcal{B}} & \boldsymbol{M}_{\mathcal{B}\mathfrak{A}^1} & \boldsymbol{M}_{\mathcal{B}\mathfrak{A}^2} & \boldsymbol{M}_{\mathcal{B}\mathfrak{A}^3} & \boldsymbol{M}_{\mathcal{B}\mathfrak{A}^4} \\ \boldsymbol{M}_{\mathfrak{A}^1\mathcal{B}} & \boldsymbol{M}_{\mathfrak{A}^1\mathfrak{A}^1} & \boldsymbol{0} & \boldsymbol{0} & \boldsymbol{0} \\ \boldsymbol{M}_{\mathfrak{A}^2\mathcal{B}} & \boldsymbol{0} & \boldsymbol{M}_{\mathfrak{A}^2\mathfrak{A}^2} & \boldsymbol{0} & \boldsymbol{0} \\ \boldsymbol{M}_{\mathfrak{A}^3\mathcal{B}} & \boldsymbol{0} & \boldsymbol{0} & \boldsymbol{M}_{\mathfrak{A}^3\mathfrak{A}^3} & \boldsymbol{0} \\ \boldsymbol{M}_{\mathfrak{A}^4\mathcal{B}} & \boldsymbol{0} & \boldsymbol{0} & \boldsymbol{0} & \boldsymbol{M}_{\mathfrak{A}^4\mathfrak{A}^4} \end{bmatrix}, \tag{4.225}$$

where $\mathcal{B}$ denote the base link and $\mathfrak{A}^i$ denotes arm i. It can be seen that while each arm has inertial couplings to the base link, the arms are not directly coupled to each other. This structure arises because the energy for arm i depends only on the base coordinates and the coordinates of arm i, resulting in zero partial derivatives with respect to the coordinates of arms $j \neq i$.

The first block represents the moments of inertia of the whole copter about the base rotation axes. It is a symmetric positive-definite matrix with the following structure and

elements

$$\boldsymbol{M}_{\mathcal{BB}} = \begin{bmatrix} M_{\psi\psi} & M_{\psi\theta} & M_{\psi\varphi} \\ M_{\theta\psi} & M_{\theta\theta} & M_{\theta\varphi} \\ M_{\varphi\psi} & M_{\varphi\theta} & M_{\varphi\varphi} \end{bmatrix}, \tag{4.226}$$

$$\begin{aligned} M_{\psi\psi} = {} & I^x_{\mathcal{B}} s^2_\theta + \big(I^y_{\mathcal{B}} s^2_\varphi + I^z_{\mathcal{B}} c^2_\varphi\big) c^2_\theta + \big(2m_{\mathcal{A}}\ell^2_{\mathcal{A}} + 2m_{\mathcal{S}}\ell^2_{\mathcal{S}}\big)\left(1 + c^2_\theta c^2_\varphi\right) \\ & + \big(2I^x_{\mathcal{A}} + 2I^x_{\mathcal{S}}\big)\big(s^2_\theta + c^2_\theta s^2_\varphi\big) \\ & + \big(I^y_{\mathcal{A}} + I^y_{\mathcal{S}}\big) c^2_\theta s^2_{\varphi+\alpha_1} + \big(I^z_{\mathcal{A}} + I^z_{\mathcal{S}}\big) c^2_\theta c^2_{\varphi+\alpha_1} \\ & + \left(I^y_{\mathcal{A}} + I^y_{\mathcal{S}}\right)\left(s_\theta c_{\alpha_2} + c_\theta c_\varphi s_{\alpha_2}\right)^2 + \left(I^z_{\mathcal{A}} + I^z_{\mathcal{S}}\right)\left(s_\theta s_{\alpha_2} - c_\theta c_\varphi c_{\alpha_2}\right)^2 \\ & + \big(I^y_{\mathcal{A}} + I^y_{\mathcal{S}}\big) c^2_\theta s^2_{\varphi-\alpha_3} + \big(I^z_{\mathcal{A}} + I^z_{\mathcal{S}}\big) c^2_\theta c^2_{\varphi-\alpha_3} \\ & + \left(I^y_{\mathcal{A}} + I^y_{\mathcal{S}}\right)\left(s_\theta c_{\alpha_4} - c_\theta c_\varphi s_{\alpha_4}\right)^2 + \left(I^z_{\mathcal{A}} + I^z_{\mathcal{S}}\right)\left(s_\theta s_{\alpha_4} + c_\theta c_\varphi c_{\alpha_4}\right)^2, \end{aligned} \tag{4.227}$$

$$\begin{aligned} M_{\psi\theta} = M_{\theta\psi} = {} & \frac{1}{2}\big(I^y_{\mathcal{B}} - I^z_{\mathcal{B}}\big) c_\theta s_{2\varphi} - \big(2m_A\ell^2_A + 2m_S\ell^2_S\big)\, c_\theta s_\varphi c_\varphi + \big(2I^x_{\mathcal{A}} + 2I^x_{\mathcal{S}}\big) c_\theta s_\varphi c_\varphi \\ & + \frac{1}{2}\big(I^y_{\mathcal{A}} - I^z_{\mathcal{A}}\big)\big(s_{2\varphi+2\alpha_1} + s_{2\varphi-2\alpha_3}\big) c_\theta + \frac{1}{2}\big(I^y_{\mathcal{S}} - I^z_{\mathcal{S}}\big)\big(s_{2\varphi+2\alpha_1} + s_{2\varphi-2\alpha_3}\big) c_\theta \\ & - \big(I^y_{\mathcal{A}} + I^y_{\mathcal{S}}\big)\big(s_\theta c_{\alpha_2} + c_\theta c_\varphi s_{\alpha_2}\big) s_\varphi s_{\alpha_2} + \left(I^z_A + I^z_S\right)\left(s_\theta s_{\alpha_2} - c_\theta c_\varphi c_{\alpha_2}\right) s_\varphi c_{\alpha_2} \\ & + \big(I^y_{\mathcal{A}} + I^y_{\mathcal{S}}\big)\big(s_\theta c_{\alpha_4} - c_\theta c_\varphi s_{\alpha_4}\big) s_\varphi s_{\alpha_4} - \left(I^z_A + I^z_S\right)\left(s_\theta s_{\alpha_4} + c_\theta c_\varphi c_{\alpha_4}\right) s_\varphi c_{\alpha_4}, \end{aligned} \tag{4.228}$$

$$\begin{aligned} M_{\psi\varphi} = M_{\varphi\psi} = {} & -\big(I^x_{\mathcal{B}} + 2I^x_{\mathcal{A}} + 2I^x_{\mathcal{S}}\big) s_\theta - \big(2m_{\mathcal{A}}\ell^2_{\mathcal{A}} + 2m_{\mathcal{S}}\ell^2_{\mathcal{S}}\big) s_\theta \\ & - \big(I^y_{\mathcal{A}} + I^y_{\mathcal{S}}\big)\big(s_\theta c_{\alpha_2} + c_\theta c_\varphi s_{\alpha_2}\big) c_{\alpha_2} - \big(I^z_{\mathcal{A}} + I^z_{\mathcal{S}}\big)\big(s_\theta s_{\alpha_2} - c_\theta c_\varphi c_{\alpha_2}\big) s_{\alpha_2} \\ & - \big(I^y_{\mathcal{A}} + I^y_{\mathcal{S}}\big)\big(s_\theta c_{\alpha_4} - c_\theta c_\varphi s_{\alpha_4}\big) c_{\alpha_4} - \big(I^z_{\mathcal{A}} + I^z_{\mathcal{S}}\big)\big(s_\theta s_{\alpha_4} + c_\theta c_\varphi c_{\alpha_4}\big) s_{\alpha_4}, \end{aligned} \tag{4.229}$$

$$\begin{aligned} M_{\theta\theta} = {} & \big(I^y_{\mathcal{B}} c^2_\varphi + I^z_{\mathcal{B}} s^2_\varphi\big) + \big(2m_{\mathcal{A}}\ell^2_{\mathcal{A}} + 2m_{\mathcal{S}}\ell^2_{\mathcal{S}}\big)\big(1 + s^2_\varphi\big) + \big(2I^x_{\mathcal{A}} + 2I^x_{\mathcal{S}}\big) c^2_\varphi \\ & + \big(I^y_{\mathcal{A}} + I^y_{\mathcal{S}}\big) c^2_{\varphi+\alpha_1} + \big(I^z_{\mathcal{A}} + I^z_{\mathcal{S}}\big) s^2_{\varphi+\alpha_1} \\ & + \big(I^y_{\mathcal{A}} + I^y_{\mathcal{S}}\big) s^2_\varphi s^2_{\alpha_2} + \big(I^z_{\mathcal{A}} + I^z_{\mathcal{S}}\big) s^2_\varphi c^2_{\alpha_2} \\ & + \big(I^y_{\mathcal{A}} + I^y_{\mathcal{S}}\big) c^2_{\varphi-\alpha_3} + \big(I^z_{\mathcal{A}} + I^z_{\mathcal{S}}\big) s^2_{\varphi-\alpha_3} \\ & + \big(I^y_{\mathcal{A}} + I^y_{\mathcal{S}}\big) s^2_\varphi s^2_{\alpha_4} + \big(I^z_{\mathcal{A}} + I^z_{\mathcal{S}}\big) s^2_\varphi c^2_{\alpha_4}, \end{aligned} \tag{4.230}$$

$$M_{\theta\varphi} = M_{\varphi\theta} = \Big[\big(I^y_{\mathcal{A}} + I^y_{\mathcal{S}}\big) - \big(I^z_{\mathcal{A}} + I^z_{\mathcal{S}}\big)\Big]\big(s_{\alpha_2}c_{\alpha_2} - s_{\alpha_4}c_{\alpha_4}\big)s_{\varphi}, \tag{4.231}$$

$$\begin{aligned} M_{\varphi\varphi} = {} & \big(I^x_{\mathcal{B}} + 2I^x_{\mathcal{A}} + 2I^x_{\mathcal{S}}\big) + 2m_{\mathcal{A}}\ell^2_{\mathcal{A}} + 2m_{\mathcal{S}}\ell^2_{\mathcal{S}} \\ & + \big(I^y_{\mathcal{A}} + I^y_{\mathcal{S}}\big)\big(c^2_{\alpha_2} + c^2_{\alpha_4}\big) + \big(I^z_{\mathcal{A}} + I^z_{\mathcal{S}}\big)\big(s^2_{\alpha_2} + s^2_{\alpha_4}\big). \end{aligned} \tag{4.232}$$

Clearly these elements include dependencies on all 12 of the arm coordinates, and therefore this block reflects inertias of the complete copter. The off-diagonal blocks of Equation (4.225) represent the products of inertia between the arms and the base link, and each block reflects the inertia of a single arm. The structures and elements, with transposed versions shown explicitly to emphasize symmetry, are given by

$$\boldsymbol{M}_{\mathcal{B}\mathfrak{A}^1} = \begin{bmatrix} M_{\psi\alpha_1} & M_{\psi\beta_1} & 0 \\ 0 & M_{\theta\beta_1} & 0 \\ M_{\varphi\alpha_1} & 0 & 0 \end{bmatrix}, \qquad \boldsymbol{M}_{\mathfrak{A}^1\mathcal{B}} = \begin{bmatrix} M_{\alpha_1\psi} & 0 & M_{\alpha_1\varphi} \\ M_{\beta_1\psi} & M_{\beta_1\theta} & 0 \\ 0 & 0 & 0 \end{bmatrix}, \tag{4.233}$$

$$M_{\psi\alpha_1} = M_{\alpha_1\psi} = -\big(I^x_{\mathcal{A}} + I^x_{\mathcal{S}}\big)s_{\theta}, \tag{4.234}$$

$$M_{\psi\beta_1} = M_{\beta_1\psi} = I^y_{\mathcal{S}}c_{\theta}s_{\varphi+\alpha_1}, \tag{4.235}$$

$$M_{\theta\beta_1} = M_{\beta_1\theta} = I^y_{\mathcal{S}}c_{\varphi+\alpha_1}, \tag{4.236}$$

$$M_{\varphi\alpha_1} = M_{\alpha_1\varphi} = \big(I^x_{\mathcal{A}} + I^x_{\mathcal{S}}\big), \tag{4.237}$$

$$\boldsymbol{M}_{\mathcal{B}\mathfrak{A}^2} = \begin{bmatrix} M_{\psi\alpha_2} & M_{\psi\beta_2} & 0 \\ M_{\theta\alpha_2} & M_{\theta\beta_2} & 0 \\ 0 & M_{\varphi\beta_2} & 0 \end{bmatrix}, \qquad \boldsymbol{M}_{\mathfrak{A}^2\mathcal{B}} = \begin{bmatrix} M_{\alpha_2\psi} & M_{\alpha_2\theta} & 0 \\ M_{\beta_2\psi} & M_{\beta_2\theta} & M_{\beta_2\varphi} \\ 0 & 0 & 0 \end{bmatrix}, \tag{4.238}$$

$$M_{\psi\alpha_2} = M_{\alpha_2\psi} = \big(I^x_{\mathcal{A}} + I^x_{\mathcal{S}}\big)c_{\theta}s_{\varphi}, \tag{4.239}$$

$$M_{\psi\beta_2} = M_{\beta_2\psi} = I^y_{\mathcal{S}}\big(s_{\theta}c_{\alpha_2} + c_{\theta}c_{\varphi}s_{\alpha_2}\big), \tag{4.240}$$

$$M_{\theta\alpha_2} = M_{\alpha_2\theta} = \big(I^x_{\mathcal{A}} + I^x_{\mathcal{S}}\big)c_{\varphi}, \tag{4.241}$$

$$M_{\theta\beta_2} = M_{\beta_2\theta} = -I^y_{\mathcal{S}}s_{\varphi}s_{\alpha_2}, \tag{4.242}$$

$$M_{\varphi\beta_2} = M_{\beta_2\varphi} = -I^y_{\mathcal{S}}c_{\alpha_2}, \tag{4.243}$$

$$\boldsymbol{M}_{\mathcal{B}\mathfrak{A}^3} = \begin{bmatrix} M_{\psi\alpha_3} & M_{\psi\beta_3} & 0 \\ 0 & M_{\theta\beta_3} & 0 \\ M_{\varphi\alpha_3} & 0 & 0 \end{bmatrix}, \qquad \boldsymbol{M}_{\mathfrak{A}^3\mathcal{B}} = \begin{bmatrix} M_{\alpha_3\psi} & 0 & M_{\alpha_3\varphi} \\ M_{\beta_3\psi} & M_{\beta_3\theta} & 0 \\ 0 & 0 & 0 \end{bmatrix}, \tag{4.244}$$

$$M_{\psi\alpha_3} = M_{\alpha_3\psi} = \big(I^x_{\mathcal{A}} + I^x_{\mathcal{S}}\big)s_\theta, \tag{4.245}$$

$$M_{\psi\beta_3} = M_{\beta_3\psi} = -I^y_{\mathcal{S}}c_\theta s_{\varphi-\alpha_3}, \tag{4.246}$$

$$M_{\theta\beta_3} = M_{\beta_3\theta} = -I^y_{\mathcal{S}}c_{\varphi-\alpha_3}, \tag{4.247}$$

$$M_{\varphi\alpha_3} = M_{\alpha_3\varphi} = -\big(I^x_{\mathcal{A}} + I^x_{\mathcal{S}}\big), \tag{4.248}$$

$$\boldsymbol{M}_{\mathcal{B}\mathfrak{A}^4} = \begin{bmatrix} M_{\psi\alpha_4} & M_{\psi\beta_4} & 0 \\ M_{\theta\alpha_4} & M_{\theta\beta_4} & 0 \\ 0 & M_{\varphi\beta_4} & 0 \end{bmatrix}, \qquad \boldsymbol{M}_{\mathfrak{A}^4\mathcal{B}} = \begin{bmatrix} M_{\alpha_4\psi} & M_{\alpha_4\theta} & 0 \\ M_{\beta_4\psi} & M_{\beta_4\theta} & M_{\beta_4\varphi} \\ 0 & 0 & 0 \end{bmatrix}, \tag{4.249}$$

$$M_{\psi\alpha_4} = M_{\alpha_4\psi} = -\big(I^x_{\mathcal{A}} + I^x_{\mathcal{S}}\big)c_\theta s_\varphi, \tag{4.250}$$

$$M_{\psi\beta_4} = M_{\beta_4\psi} = -I^y_{\mathcal{S}}\big(s_\theta c_{\alpha_4} - c_\theta c_\varphi s_{\alpha_4}\big), \tag{4.251}$$

$$M_{\theta\alpha_4} = M_{\alpha_4\theta} = -\big(I^x_{\mathcal{A}} + I^x_{\mathcal{S}}\big)c_\varphi, \tag{4.252}$$

$$M_{\theta\beta_4} = M_{\beta_4\theta} = -I^y_{\mathcal{S}}s_\varphi s_{\alpha_4}, \tag{4.253}$$

$$M_{\varphi\beta_4} = M_{\beta_4\varphi} = I^y_{\mathcal{S}}c_{\alpha_4}. \tag{4.254}$$

The symmetry between the two roll-axis arms first discussed in Section 4.5 has resulted in an identical block structure in the full equations of motion, with the blocks $\boldsymbol{M}_{\mathcal{B}\mathfrak{A}^1}$ and $\boldsymbol{M}_{\mathcal{B}\mathfrak{A}^3}$ related by the substitution $(\alpha_1, \beta_1) \leftrightarrow (-\alpha_3, -\beta_3)$. A similar pattern relates the two pitch-axis arms with blocks $\boldsymbol{M}_{\mathcal{B}\mathfrak{A}^2}$ and $\boldsymbol{M}_{\mathcal{B}\mathfrak{A}^4}$. Lastly, the remaining diagonal blocks of Equation (4.225) represent the moments of inertia of each arm about its own coordinates. They are identical constant matrices given by

$$\boldsymbol{M}_{\mathfrak{A}^i\mathfrak{A}^i} = \begin{bmatrix} I^x_{\mathcal{A}} + I^x_{\mathcal{S}} & 0 & 0 \\ 0 & I^y_{\mathcal{S}} & 0 \\ 0 & 0 & I^z_{\mathcal{P}} \end{bmatrix}, \tag{4.255}$$

which matches Equation (3.54) for one arm with the propeller mass neglected.

4.7.2 Coupling Matrix

The coupling matrix $\boldsymbol{C}$ can be written with a similar structure block structure to the inertia matrix, given by

$$\boldsymbol{C}(\boldsymbol{q}, \dot{\boldsymbol{q}}) = \left[\begin{array}{c|c|c|c|c} \boldsymbol{C}_{\mathcal{BB}} & \boldsymbol{C}_{\mathcal{B}\mathfrak{A}^1} & \boldsymbol{C}_{\mathcal{B}\mathfrak{A}^2} & \boldsymbol{C}_{\mathcal{B}\mathfrak{A}^3} & \boldsymbol{C}_{\mathcal{B}\mathfrak{A}^4} \\ \hline \boldsymbol{C}_{\mathfrak{A}^1\mathcal{B}} & \boldsymbol{C}_{\mathfrak{A}^1\mathfrak{A}^1} & \boldsymbol{0} & \boldsymbol{0} & \boldsymbol{0} \\ \hline \boldsymbol{C}_{\mathfrak{A}^2\mathcal{B}} & \boldsymbol{0} & \boldsymbol{C}_{\mathfrak{A}^2\mathfrak{A}^2} & \boldsymbol{0} & \boldsymbol{0} \\ \hline \boldsymbol{C}_{\mathfrak{A}^3\mathcal{B}} & \boldsymbol{0} & \boldsymbol{0} & \boldsymbol{C}_{\mathfrak{A}^3\mathfrak{A}^3} & \boldsymbol{0} \\ \hline \boldsymbol{C}_{\mathfrak{A}^4\mathcal{B}} & \boldsymbol{0} & \boldsymbol{0} & \boldsymbol{0} & \boldsymbol{C}_{\mathfrak{A}^4\mathfrak{A}^4} \end{array}\right]. \tag{4.256}$$

Because all quadratic velocity terms were neglected which did not include a $\dot{\gamma}_i$, the blocks of the $\boldsymbol{C}$ matrix include only the propeller gyroscopic couplings arising from the projection of Equation (4.60) onto each coordinate. Each block represents the couplings between two sets of coordinates. The many blocks of zeros arise because the arms are not directly coupled to each other and are only connected through the base link. The $\boldsymbol{C}_{\mathcal{BB}}$ block includes couplings with all four propellers and can be further broken down into

$$\boldsymbol{C}_{\mathcal{BB}} = \boldsymbol{C}^1_{\mathcal{BB}} + \boldsymbol{C}^2_{\mathcal{BB}} + \boldsymbol{C}^3_{\mathcal{BB}} + \boldsymbol{C}^4_{\mathcal{BB}}, \tag{4.257}$$

where $\boldsymbol{C}^i_{\mathcal{BB}}$ is a skew-symmetric matrix which includes the gyroscopic coupling of propeller i with the base angular rates, affecting the base rotation coordinates. These effects are described by

$$\boldsymbol{C}^1_{\mathcal{BB}} = I^z_{\mathcal{P}}\dot{\gamma}_1 \begin{bmatrix} 0 & -c_\theta s_{\beta_1} - s_\theta c_{\beta_1} c_{\varphi+\alpha_1} & -c_\theta c_{\beta_1} s_{\varphi+\alpha_1} \\ c_\theta s_{\beta_1} + s_\theta c_{\beta_1} c_{\varphi+\alpha_1} & 0 & -c_{\beta_1} c_{\varphi+\alpha_1} \\ c_\theta c_{\beta_1} s_{\varphi+\alpha_1} & c_{\beta_1} c_{\varphi+\alpha_1} & 0 \end{bmatrix}, \tag{4.258}$$

$$\boldsymbol{C}^2_{\mathcal{BB}} = I^z_{\mathcal{P}}\dot{\gamma}_2 \begin{bmatrix} 0 & C^2_{\psi\theta} & C^2_{\psi\varphi} \\ C^2_{\theta\psi} & 0 & C^2_{\theta\varphi} \\ C^2_{\varphi\psi} & C^2_{\varphi\theta} & 0 \end{bmatrix}, \tag{4.259}$$

$$C^2_{\psi\theta} = -C^2_{\theta\psi} = -s_\theta s_\varphi s_{\beta_2} - c_\theta s_{\alpha_2} c_{\beta_2} - s_\theta c_\varphi c_{\alpha_2} c_{\beta_2}, \tag{4.260}$$

$$C^2_{\psi\varphi} = -C^2_{\varphi\psi} = c_\theta \left(c_\varphi s_{\beta_2} - s_\varphi c_{\alpha_2} c_{\beta_2}\right), \tag{4.261}$$

$$C^2_{\theta\varphi} = -C^2_{\varphi\theta} = -s_\varphi s_{\beta_2} - c_\varphi c_{\alpha_2} c_{\beta_2}, \tag{4.262}$$

$$\boldsymbol{C}^3_{\mathcal{BB}} = I^z_{\mathcal{P}}\dot{\gamma}_3 \begin{bmatrix} 0 & c_\theta s_{\beta_3} - s_\theta c_{\beta_3} c_{\varphi-\alpha_3} & -c_\theta c_{\beta_3} s_{\varphi-\alpha_3}, \\ -c_\theta s_{\beta_3} + s_\theta c_{\beta_3} c_{\varphi-\alpha_3} & 0 & -c_{\beta_3} c_{\varphi-\alpha_3}, \\ c_\theta c_{\beta_3} s_{\varphi-\alpha_3} & c_{\beta_3} c_{\varphi-\alpha_3} & 0, \end{bmatrix}, \tag{4.263}$$

$$\boldsymbol{C}^4_{\mathcal{BB}} = I^z_{\mathcal{P}}\dot{\gamma}_4 \begin{bmatrix} 0 & C^4_{\psi\theta} & C^4_{\psi\varphi} \\ C^4_{\theta\psi} & 0 & C^4_{\theta\varphi} \\ C^4_{\varphi\psi} & C^4_{\varphi\theta} & 0 \end{bmatrix}, \tag{4.264}$$

$$C^4_{\psi\theta} = -C^4_{\theta\psi} = s_\theta s_\varphi s_{\beta_4} + c_\theta s_{\alpha_4} c_{\beta_4} - s_\theta c_\varphi c_{\alpha_4} c_{\beta_4}, \tag{4.265}$$

$$C^4_{\psi\varphi} = -C^4_{\varphi\psi} = -c_\theta \left(c_\varphi s_{\beta_4} + s_\varphi c_{\alpha_4} c_{\beta_4}\right), \tag{4.266}$$

$$C^4_{\theta\varphi} = -C^4_{\varphi\theta} = s_\varphi s_{\beta_4} - c_\varphi c_{\alpha_4} c_{\beta_4}. \tag{4.267}$$

The off-diagonal blocks in the first row of Equation (4.256) represent the gyroscopic coupling of propeller i with the angular rates of arm i, affecting the base rotation coordinates. They are the negative transposes of the off-diagonal blocks in the first column of Equation (4.256) , which represent the gyroscopic coupling of propeller i with the base angular rates, affecting the coordinates of arm i.

$$\boldsymbol{C}_{\mathcal{B}\mathfrak{A}^1} = I^z_{\mathcal{P}}\dot{\gamma}_1 \begin{bmatrix} -c_\theta c_{\beta_1} s_{\varphi+\alpha_1} & -s_\theta c_{\beta_1} - c_\theta s_{\beta_1} c_{\varphi+\alpha_1} & 0 \\ -c_{\beta_1} c_{\varphi+\alpha_1} & s_{\beta_1} s_{\varphi+\alpha_1} & 0 \\ 0 & c_{\beta_1} & 0 \end{bmatrix} \tag{4.268}$$

$$\boldsymbol{C}_{\mathfrak{A}^1\mathcal{B}} = I^z_{\mathcal{P}}\dot{\gamma}_1 \begin{bmatrix} c_\theta c_{\beta_1} s_{\varphi+\alpha_1} & c_{\beta_1} c_{\varphi+\alpha_1} & 0 \\ s_\theta c_{\beta_1} + c_\theta s_{\beta_1} c_{\varphi+\alpha_1} & -s_{\beta_1} s_{\varphi+\alpha_1} & -c_{\beta_1} \\ 0 & 0 & 0 \end{bmatrix} \tag{4.269}$$

$$\boldsymbol{C}_{\mathcal{B}\mathfrak{A}^2} = I^z_{\mathcal{P}}\dot{\gamma}_2 \begin{bmatrix} -c_{\beta_2}\left(s_\theta c_{\alpha_2} + c_\theta c_\varphi s_{\alpha_2}\right) & c_\theta s_\varphi c_{\beta_2} + s_\theta s_{\alpha_2} s_{\beta_2} - c_\theta c_\varphi c_{\alpha_2} s_{\beta_2} & 0 \\ s_\varphi s_{\alpha_2} c_{\beta_2} & c_\varphi c_{\beta_2} + s_\varphi c_{\alpha_2} s_{\beta_2} & 0 \\ c_{\alpha_2} c_{\beta_2} & -s_{\alpha_2} s_{\beta_2} & 0 \end{bmatrix} \tag{4.270}$$

$$\boldsymbol{C}_{\mathfrak{A}^2\mathcal{B}} = I^z_{\mathcal{P}}\dot{\gamma}_2 \begin{bmatrix} c_{\beta_2}\left(s_\theta c_{\alpha_2} + c_\theta c_\varphi s_{\alpha_2}\right) & -s_\varphi s_{\alpha_2} c_{\beta_2} & -c_{\alpha_2} c_{\beta_2} \\ -c_\theta s_\varphi c_{\beta_2} - s_\theta s_{\alpha_2} s_{\beta_2} + c_\theta c_\varphi c_{\alpha_2} s_{\beta_2} & -c_\varphi c_{\beta_2} - s_\varphi c_{\alpha_2} s_{\beta_2} & s_{\alpha_2} s_{\beta_2} \\ 0 & 0 & 0 \end{bmatrix} \tag{4.271}$$

$$\boldsymbol{C}_{\mathcal{B}\mathfrak{A}^3} = I^z_{\mathcal{P}}\dot{\gamma}_3 \begin{bmatrix} c_\theta c_{\beta_3} s_{\varphi-\alpha_3} & s_\theta c_{\beta_3} - c_\theta s_{\beta_3} c_{\varphi-\alpha_3} & 0 \\ c_{\beta_3} c_{\varphi-\alpha_3} & s_{\beta_3} s_{\varphi-\alpha_3} & 0 \\ 0 & -c_{\beta_3} & 0 \end{bmatrix} \tag{4.272}$$

$$\boldsymbol{C}_{\mathfrak{A}^3\mathcal{B}} = I^z_{\mathcal{P}}\dot{\gamma}_3 \begin{bmatrix} -c_\theta c_{\beta_3} s_{\varphi-\alpha_3} & -c_{\beta_3} c_{\varphi-\alpha_3} & 0 \\ -s_\theta c_{\beta_3} + c_\theta s_{\beta_3} c_{\varphi-\alpha_3} & -s_{\beta_3} s_{\varphi-\alpha_3} & c_{\beta_3} \\ 0 & 0 & 0 \end{bmatrix} \tag{4.273}$$

$$\boldsymbol{C}_{\mathcal{B}\mathfrak{A}^4} = I^z_{\mathcal{P}}\dot{\gamma}_4 \begin{bmatrix} c_{\beta_4}\left(s_\theta c_{\alpha_4} - c_\theta c_\varphi s_{\alpha_4}\right) & -s_\theta s_{\alpha_4} s_{\beta_4} - c_\theta s_\varphi c_{\beta_4} - c_\theta c_\varphi c_{\alpha_4} s_{\beta_4} & 0 \\ s_\varphi s_{\alpha_4} c_{\beta_4} & -c_\varphi c_{\beta_4} + s_\varphi c_{\alpha_4} s_{\beta_4} & 0 \\ -c_{\alpha_4} c_{\beta_4} & s_{\alpha_4} s_{\beta_4} & 0 \end{bmatrix} \tag{4.274}$$

$$\boldsymbol{C}_{\mathfrak{A}^4\mathcal{B}} = I^z_{\mathcal{P}}\dot{\gamma}_4 \begin{bmatrix} -c_{\beta_4}\left(s_\theta c_{\alpha_4} - c_\theta c_\varphi s_{\alpha_4}\right) & -s_\varphi s_{\alpha_4} c_{\beta_4} & c_{\alpha_4} c_{\beta_4} \\ s_\theta s_{\alpha_4} s_{\beta_4} + c_\theta s_\varphi c_{\beta_4} + c_\theta c_\varphi c_{\alpha_4} s_{\beta_4} & c_\varphi c_{\beta_4} - s_\varphi c_{\alpha_4} s_{\beta_4} & -s_{\alpha_4} s_{\beta_4} \\ 0 & 0 & 0 \end{bmatrix} \tag{4.275}$$

The remaining diagonal blocks of Equation (4.256) represent the gyroscopic coupling of propeller i with the angular rates of arm i affecting the coordinates of arm i. They are

identical skew-symmetric matrices given by

$$\boldsymbol{C}_{\mathfrak{A}^i\mathfrak{A}^i} = I^z_{\mathcal{P}}\dot{\gamma}_i \begin{bmatrix} 0 & c_{\beta_i} & 0 \\ -c_{\beta_i} & 0 & 0 \\ 0 & 0 & 0 \end{bmatrix}, \tag{4.276}$$

which matches Equation (3.55) for a single arm with the propeller mass neglected.

An important property of Equation (4.256) is that it includes entries in every row. This means that there propeller gyroscopic terms affecting every generalized coordinate, which justifies the neglect of other quadratic velocity terms even in Lagrange partial derivatives which did not include $\dot{\gamma}_i$.

4.7.3 Vector Terms

Equation (4.224) includes effects from the thrust-induced torque, drag-induced torque, gravitational torque, and the motor torques. The gravitational terms arise from the potential energy partial derivatives, while the others originate from the generalized forces acting on each coordinate.

The thrust-induced torque can be written as the sum of torques from each arm

$$\boldsymbol{f}(\boldsymbol{q}, \dot{\boldsymbol{q}}) = \boldsymbol{f}_1 + \boldsymbol{f}_2 + \boldsymbol{f}_3 + \boldsymbol{f}_4. \tag{4.277}$$

Each arm exerts a thrust torque about the base coordinates but has no effect on any of the arm coordinates. This is consistent with the discussion in Section 3.2.4 and is the

reason no thrust appeared in Equation (3.53). The four thrust terms are given by

$$\boldsymbol{f}_1 = c_p \ell_S \dot{\gamma}_1^2 \left[\begin{array}{c} c_\theta c_{\beta_1} s_{\varphi+\alpha_1} \\ c_{\beta_1} c_{\varphi+\alpha_1} \\ 0 \\ \hdashline 0 \\ 0 \\ 0 \\ \hdashline 0 \\ 0 \\ 0 \\ \hdashline 0 \\ 0 \\ 0 \end{array}\right], \tag{4.278}$$

$$\boldsymbol{f}_2 = c_p \ell_S \dot{\gamma}_2^2 \left[\begin{array}{c} c_{\beta_2}\left(s_\theta c_{\alpha_2} + c_\theta c_\varphi s_{\alpha_2}\right) \\ -s_\varphi s_{\alpha_2} c_{\beta_2} \\ -c_{\alpha_2} c_{\beta_2} \\ \hdashline 0 \\ 0 \\ 0 \\ \hdashline 0 \\ 0 \\ 0 \\ \hdashline 0 \\ 0 \\ 0 \end{array}\right], \tag{4.279}$$

$$\boldsymbol{f}_3 = c_p \ell_S \dot{\gamma}_3^2 \left[\begin{array}{c} -c_\theta c_{\beta_3} s_{\varphi-\alpha_3} \\ -c_{\beta_3} c_{\varphi-\alpha_3} \\ 0 \\ \hdashline 0 \\ 0 \\ 0 \\ \hdashline 0 \\ 0 \\ 0 \\ \hdashline 0 \\ 0 \\ 0 \end{array}\right], \tag{4.280}$$

$$\boldsymbol{f}_4 = c_p \ell_S \dot{\gamma}_4^2 \left[\begin{array}{c} -c_{\beta_4}\left(s_\theta c_{\alpha_4} - c_\theta c_\varphi s_{\alpha_4}\right) \\ -s_\varphi s_{\alpha_4} c_{\beta_4} \\ c_{\alpha_4} c_{\beta_4} \\ \hdashline 0 \\ 0 \\ 0 \\ \hdashline 0 \\ 0 \\ 0 \\ \hdashline 0 \\ 0 \\ 0 \end{array}\right]. \tag{4.281}$$

The drag-induced torque can also be written as a sum of contributions from each arm

$$\boldsymbol{d}(\boldsymbol{q}, \dot{\boldsymbol{q}}) = \boldsymbol{d}_1 + \boldsymbol{d}_2 + \boldsymbol{d}_3 + \boldsymbol{d}_4. \tag{4.282}$$

Each arm exerts a drag torque about the base coordinates and its own coordinates, but not the coordinates of the other arms. The effect of the drag from propeller i on the coordinates of arm i is identical for each arm, and equal to Equation (3.56) with a sign

adjustment to account for the direction of propeller spin. The four contributions are

$$\boldsymbol{d}_1 = c_t\dot{\gamma}_1^2 \begin{bmatrix} -s_\theta s_{\beta_1} + c_\theta c_{\beta_1} c_{\varphi+\alpha_1} \\ c_{\beta_1} s_{\varphi+\alpha_1} \\ s_{\beta_1} \\ \hdashline s_{\beta_1} \\ 0 \\ 1 \\ \hdashline 0 \\ 0 \\ 0 \\ \hdashline 0 \\ 0 \\ 0 \\ \hdashline 0 \\ 0 \\ 0 \end{bmatrix}, \tag{4.283}$$

$$\boldsymbol{d}_2 = c_t\dot{\gamma}_2^2 \begin{bmatrix} s_\theta s_{\alpha_2} c_{\beta_2} - c_\theta s_\varphi s_{\beta_2} - c_\theta c_\varphi c_{\alpha_2} c_{\beta_2} \\ -c_\varphi s_{\beta_2} + s_\varphi c_{\alpha_2} c_{\beta_2} \\ -s_{\alpha_2} c_{\beta_2} \\ \hdashline 0 \\ 0 \\ 0 \\ \hdashline -s_{\beta_2} \\ 0 \\ -1 \\ \hdashline 0 \\ 0 \\ 0 \\ \hdashline 0 \\ 0 \\ 0 \end{bmatrix}, \tag{4.284}$$

$$\boldsymbol{d}_3 = c_t\dot{\gamma}_3^2 \begin{bmatrix} s_\theta s_{\beta_3} + c_\theta c_{\beta_3} c_{\varphi-\alpha_3} \\ -c_{\beta_3} s_{\varphi-\alpha_3} \\ -s_{\beta_3} \\ \hdashline 0 \\ 0 \\ 0 \\ \hdashline 0 \\ 0 \\ 0 \\ \hdashline s_{\beta_3} \\ 0 \\ 1 \\ \hdashline 0 \\ 0 \\ 0 \end{bmatrix}, \tag{4.285}$$

$$\boldsymbol{d}_4 = c_t\dot{\gamma}_4^2 \begin{bmatrix} -s_\theta s_{\alpha_4} c_{\beta_4} + c_\theta s_\varphi s_{\beta_4} - c_\theta c_\varphi c_{\alpha_4} c_{\beta_4} \\ c_\varphi s_{\beta_4} + s_\varphi c_{\alpha_4} c_{\beta_4} \\ s_{\alpha_4} c_{\beta_4} \\ \hdashline 0 \\ 0 \\ 0 \\ \hdashline 0 \\ 0 \\ 0 \\ \hdashline 0 \\ 0 \\ 0 \\ \hdashline -s_{\beta_4} \\ 0 \\ -1 \end{bmatrix}. \tag{4.286}$$

The gravitational torque of the arcs and shafts are balanced in all configurations due to symmetry about the base origin, however the gravitational torque of the propellers can exert unbalanced torques depending on the configuration. These torques are described by the following terms

$$\boldsymbol{g}(\boldsymbol{q}) = \boldsymbol{g}_1 + \boldsymbol{g}_2 + \boldsymbol{g}_3 + \boldsymbol{g}_4, \tag{4.287}$$

$$\boldsymbol{g}_1 = m_{\mathcal{P}} g_0 \begin{bmatrix} 0 \\ -\ell_{\mathcal{P}} \left(c_\theta s_{\beta_1} + s_\theta c_{\beta_1} c_{\varphi+\alpha_1} \right) \\ -\ell_{\mathcal{P}} c_\theta c_{\beta_1} s_{\varphi+\alpha_1} \\ \hdashline -\ell_{\mathcal{P}} c_\theta c_{\beta_1} s_{\varphi+\alpha_1} \\ -\ell_{\mathcal{P}} \left(s_\theta c_{\beta_1} + c_\theta s_{\beta_1} c_{\varphi+\alpha_1} \right) \\ 0 \\ \hdashline 0 \\ 0 \\ 0 \\ \hdashline 0 \\ 0 \\ 0 \\ \hdashline 0 \\ 0 \\ 0 \end{bmatrix}, \tag{4.288}$$

$$\boldsymbol{g}_2 = m_{\mathcal{P}} g_0 \begin{bmatrix} 0 \\ -\ell_{\mathcal{P}} \left(s_\theta s_\varphi s_{\beta_2} + c_\theta s_{\alpha_2} c_{\beta_2} + s_\theta c_\varphi c_{\alpha_2} c_{\beta_2} \right) \\ \ell_{\mathcal{P}} \left(c_\theta c_\varphi s_{\beta_2} - c_\theta s_\varphi c_{\alpha_2} c_{\beta_2} \right) \\ \hdashline 0 \\ 0 \\ 0 \\ \hdashline -\ell_{\mathcal{P}} \left(s_\theta c_{\alpha_2} c_{\beta_2} + c_\theta c_\varphi s_{\alpha_2} c_{\beta_2} \right) \\ \ell_{\mathcal{P}} \left(c_\theta s_\varphi c_{\beta_2} + s_\theta s_{\alpha_2} s_{\beta_2} - c_\theta c_\varphi c_{\alpha_2} s_{\beta_2} \right) \\ 0 \\ \hdashline 0 \\ 0 \\ 0 \\ \hdashline 0 \\ 0 \\ 0 \end{bmatrix}, \tag{4.289}$$

$$\boldsymbol{g}_3 = m_{\mathcal{P}} g_0 \begin{bmatrix} 0 \\ \ell_{\mathcal{P}} \left(c_\theta s_{\beta_3} - s_\theta c_{\beta_3} c_{\varphi - \alpha_3} \right) \\ -\ell_{\mathcal{P}} c_\theta c_{\beta_3} s_{\varphi - \alpha_3} \\ \hdashline 0 \\ 0 \\ 0 \\ \hdashline 0 \\ 0 \\ 0 \\ \hdashline \ell_{\mathcal{P}} c_\theta c_{\beta_3} s_{\varphi - \alpha_3} \\ \ell_{\mathcal{P}} \left(s_\theta c_{\beta_3} - c_\theta s_{\beta_3} c_{\varphi - \alpha_3} \right) \\ 0 \\ \hdashline 0 \\ 0 \\ 0 \end{bmatrix}, \tag{4.290}$$

$$\boldsymbol{g}_4 = m_{\mathcal{P}} g_0 \begin{bmatrix} 0 \\ \ell_{\mathcal{P}} \left(s_\theta s_\varphi s_{\beta_4} + c_\theta s_{\alpha_4} c_{\beta_4} - s_\theta c_\varphi c_{\alpha_4} c_{\beta_4} \right) \\ -\ell_{\mathcal{P}} \left(c_\theta c_\varphi s_{\beta_4} + c_\theta s_\varphi c_{\alpha_4} c_{\beta_4} \right) \\ \hdashline 0 \\ 0 \\ 0 \\ \hdashline 0 \\ 0 \\ 0 \\ \hdashline 0 \\ 0 \\ 0 \\ \hdashline \ell_{\mathcal{P}} \left(s_\theta c_{\alpha_4} c_{\beta_4} - c_\theta c_\varphi s_{\alpha_4} c_{\beta_4} \right) \\ -\ell_{\mathcal{P}} \left(c_\theta s_\varphi c_{\beta_4} + s_\theta s_{\alpha_4} s_{\beta_4} + c_\theta c_\varphi c_{\alpha_4} s_{\beta_4} \right) \\ 0 \end{bmatrix}. \tag{4.291}$$

The final piece of the equations of motion is the vector of motor input torques, given by Equation (4.63) and not repeated here. While the overall copter is highly overactuated with respect to 3-DOF attitude control, the coordinates for the base link rotation do not have dedicated actuators and thus rely on the end-effector torques and couplings for motion. This requires an adaptation to the control scheme developed in Section 3.3,

which will be discussed at the end of this chapter.

4.8 Sample Trajectory

Another virtual experiment is conducted on the Simscape model to compare the torques predicted by Equation (4.224) with those measured in simulation. The square sample trajectory shown in Fig. 3.8 is extended over 20 sec and prescribed as the motion for all four arms simultaneously. The base angles are also varied sequentially between 0-90° using the cycloid trajectory as described by Equation (3.13) and shown in Fig. 4.1. Note that for this experiment artificial actuators have been added to the base link to give full authority over the motion of the copter. The joint angles, velocities, and accelerations are used as the inputs to the left-hand side of Equation (4.224) to calculate the predicted torques about each coordinate based on the derived equations of motion, and these predictions are compared to the measurements made in the simulation. The resulting torques about the base rotation axes are shown in Fig. 4.2, and the torques about the arm axes are shown in Fig. 4.3.

Clearly the most notable deviations of the model occur during intervals of high base velocity about multiple axes, occurring between 5-10 sec and 10-15 sec. This is expected as the quadratic velocity effects due to the base were neglected to simplify the equations of motion. Note that the maximum angular rate of the base in this trajectory is approximately 9.5 RPM, which is much faster than would be commanded in application. The arm actuators are also prescribed motion rates beyond what would typically arise for controlled steady flight. This sample trajectory thus represents a fairly extreme case where the neglected dynamics are exaggerated. Despite this, the model predicts the motor torques for the tilt and propeller motors almost exactly, and captures the trend for the alpha motors and base rotations very well. The derived equations of motion thus provide a reliable approximation for use in model-based control design.

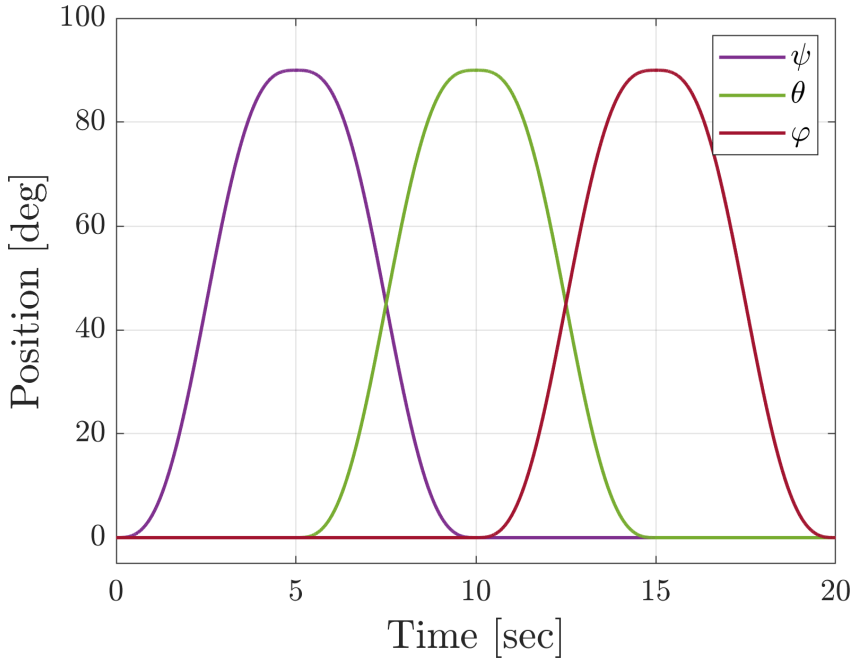

Figure 4.1: Sample trajectory for validation of the derived equations of motion. Each of the base rotation angles is varied from 0-90° using a smooth cycloid trajectory, with overlap in the rotation intervals to excite Coriolis couplings between the coordinates. Joint motion is prescribed directly to the Simscape model and the torques required to realize that motion are calculated within the software.

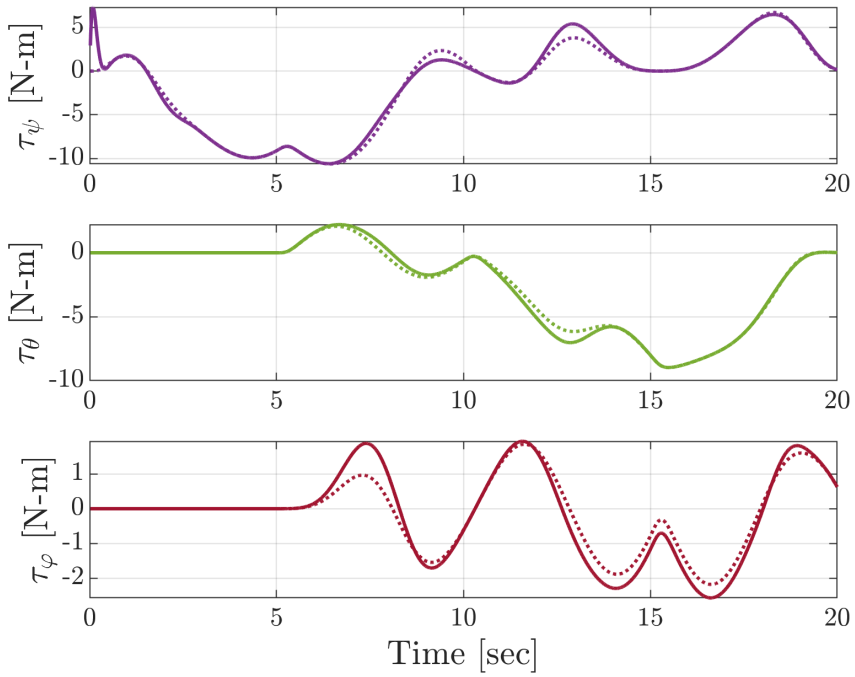

Figure 4.2: Comparison of predicted (dashed) and measured (solid) torques for the base rotation axes. The measured torques are generated by the Simscape model in order to realize the prescribed trajectory in Fig. 4.1. Predicted torques are calculated with Equation (4.224) to the measured joint angles, velocities, and accelerations.

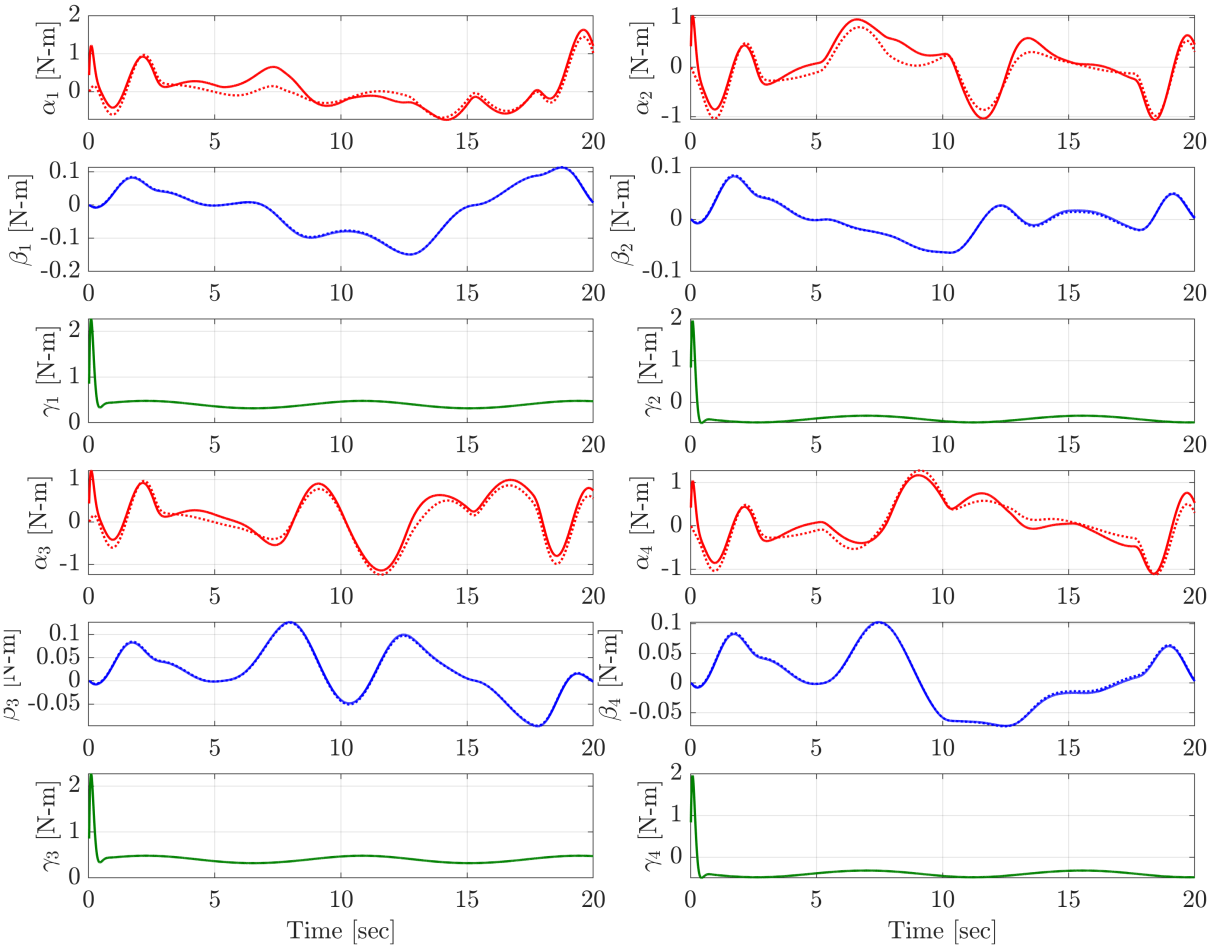

Figure 4.3: Predicted (dashed) and measured (solid) torques for the arm motors. Measurements are taken from Simscape simulation to generate the trajectory in Fig. 4.1. Predicted torques are calculated from the derived equations of motion using the measured joint angles, velocities, and accelerations.

4.9 Hierarchical Control

For the full copter with base rotation, the control objective is to apply propeller thrusts such that the base link tracks a 3-DOF attitude trajectory composed of desired roll, pitch, and yaw angles. Desired values for the arm angles are not provided by the trajectory but must be generated within the control architecture. To begin, the nonlinear terms in Equation (4.224) are grouped into a general vector-valued function to produce

$$\boldsymbol{M}(\boldsymbol{q})\ddot{\boldsymbol{q}} + \boldsymbol{N}(\boldsymbol{q}, \dot{\boldsymbol{q}}) = \boldsymbol{\tau}, \tag{4.292}$$

with

$$\boldsymbol{N}(\boldsymbol{q}, \dot{\boldsymbol{q}}) = \boldsymbol{C}(\boldsymbol{q}, \dot{\boldsymbol{q}})\dot{\boldsymbol{q}} + \boldsymbol{f}(\boldsymbol{q}, \dot{\boldsymbol{q}}) + \boldsymbol{d}(\boldsymbol{q}, \dot{\boldsymbol{q}}) + \boldsymbol{g}(\boldsymbol{q}). \tag{4.293}$$

Equation (4.292) is identical to Equation (3.59) with larger dimensions, and the control strategy from Section 3.3 can be repeated to obtain the control law

$$\boldsymbol{\tau} = \boldsymbol{M}(\boldsymbol{q})\big[\boldsymbol{K}_p(\boldsymbol{q}_d - \boldsymbol{q}) + \boldsymbol{K}_d(\dot{\boldsymbol{q}}_d - \dot{\boldsymbol{q}})\big] + \boldsymbol{N}(\boldsymbol{q}, \dot{\boldsymbol{q}}). \tag{4.294}$$

The problem with this approach is that the torque vector $\boldsymbol{\tau}$ is implicitly assumed to include a controllable input in every row, which is not the case for the base rotation coordinates. Thus an adaptation is necessary to generalize this strategy for attitude control.

Consider partitioning the motor input vector in Equation (4.63) in the following way

$$\boldsymbol{\tau} = \begin{bmatrix} \boldsymbol{\tau}_{\mathcal{B}} \\ \hdashline \boldsymbol{\tau}_{\mathfrak{A}^1} \\ \hdashline \vdots \\ \hdashline \boldsymbol{\tau}_{\mathfrak{A}^4} \end{bmatrix}, \tag{4.295}$$

where $\boldsymbol{\tau}_{\mathfrak{A}^i}$ represents the vector of commanded motor torques associated with arm i, and $\boldsymbol{\tau}_{\mathcal{B}}$ represents the vector of torques about the base rotation axes which would be

commanded if there were dedicated actuators to do so. The generalized coordinates and speeds can also be partitioned in the same way for ease of representation on a block diagram

$$\boldsymbol{q} = \begin{bmatrix} \boldsymbol{q}_{\mathcal{B}} \\ \hdashline \boldsymbol{q}_{\mathfrak{A}^1} \\ \hdashline \vdots \\ \hdashline \boldsymbol{q}_{\mathfrak{A}^4} \end{bmatrix}, \qquad \dot{\boldsymbol{q}} = \begin{bmatrix} \dot{\boldsymbol{q}}_{\mathcal{B}} \\ \hdashline \dot{\boldsymbol{q}}_{\mathfrak{A}^1} \\ \hdashline \vdots \\ \hdashline \dot{\boldsymbol{q}}_{\mathfrak{A}^4} \end{bmatrix}. \tag{4.296}$$

While the arm torques $\boldsymbol{\tau}_{\mathfrak{A}^i}$ can be sent directly to the motors as commands, the base torque $\boldsymbol{\tau}_{\mathcal{B}}$ must be converted into another form. Recall the wrench mapper described in Section 2.4, which was a least-norms mapping from a control wrench about the base axes to a set of thrust vectors with minimal Euclidean norm. The same mapper[2] and subsequent inverse kinematics scheme can be used to convert the base torque $\boldsymbol{\tau}_{\mathcal{B}}$ into unique sets of desired arm angles $\{\alpha_{i,d}, \beta_{i,d}\}$ and propeller speeds $\{\dot{\gamma}_{i,d}\}$, which are gathered into generalized coordinate and speed vectors according to

$$\boldsymbol{q}_{\mathfrak{A}^i,d} = \begin{bmatrix} \alpha_{i,d} \\ \beta_{i,d} \\ 0 \end{bmatrix}, \qquad \dot{\boldsymbol{q}}_{\mathfrak{A}^i,d} = \begin{bmatrix} 0 \\ 0 \\ \dot{\gamma}_{i,d} \end{bmatrix}. \tag{4.297}$$

The full vectors of desired coordinates and speeds for Equation (4.294) are obtained by combining the arm set-points with the provided base trajectory

$$\boldsymbol{q}_d = \begin{bmatrix} \boldsymbol{q}_{\mathcal{B},d} \\ \hdashline \boldsymbol{q}_{\mathfrak{A}^1,d} \\ \hdashline \vdots \\ \hdashline \boldsymbol{q}_{\mathfrak{A}^4,d} \end{bmatrix}, \qquad \dot{\boldsymbol{q}}_d = \begin{bmatrix} \boldsymbol{0} \\ \hdashline \dot{\boldsymbol{q}}_{\mathfrak{A}^1,d} \\ \hdashline \vdots \\ \hdashline \dot{\boldsymbol{q}}_{\mathfrak{A}^4,d} \end{bmatrix}. \tag{4.298}$$

Fig. 4.4 offers a block diagram depiction of the proposed control scheme. Upon com-

[2]The wrench mapper in Section 2.4 operates on a 6-vector wrench containing both force and torque. In this chapter $\boldsymbol{\tau}_{\mathcal{B}}$ is only a 3-vector torque, so in simulation it is concatenated with a 3-vector force which is equal and opposite to the copter's weight. This is done to maintain propeller speeds near those necessary for flight, since the propeller speeds have a strong effect on the system response due to the gyroscopic couplings.

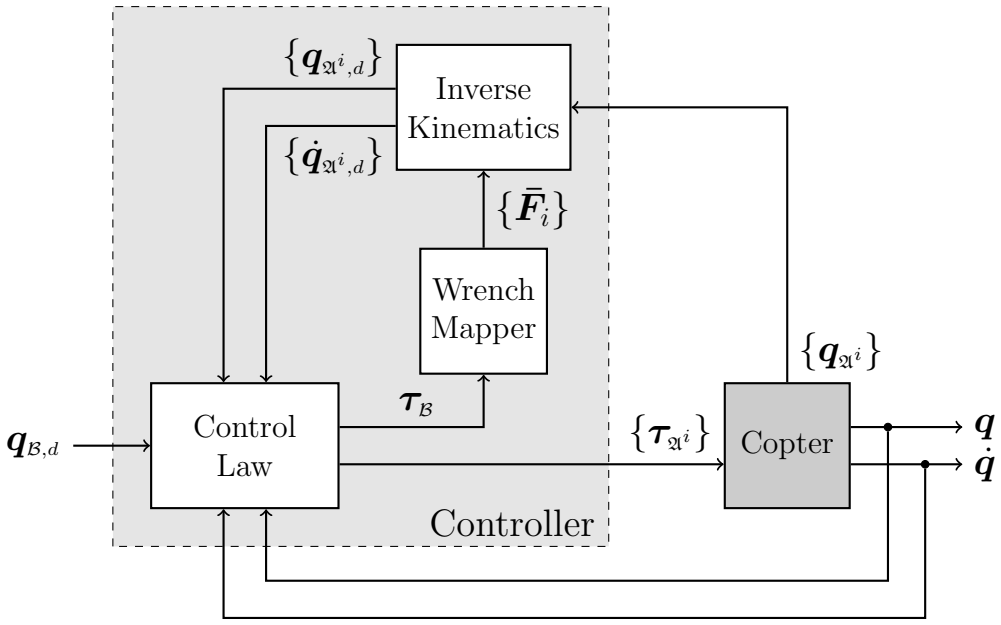

Figure 4.4: Adapted hierarchical control model (compare Fig. 2.4). The desired trajectory is specified for the base link while the arm set-points are determined within the controller. A single centralized control law computes both the low-level motors torques and the high-level control wrench for the base. The control wrench is then used to solve for the unique set of motor angles and propeller speeds that realizes the wrench with minimal thrust magnitudes, which are fed back to the control law as set-points.

parison with the original hierarchical control scheme shown in Fig. 2.4, the number of independent control laws has been reduced from six (two high-level plus four low-level) down to just one. Having a single centralized controller which generates both the rigid body control wrench and the low-level motor torques allows for compensation of the configuration-dependent inertia and gyroscopic couplings, assumed to be necessary for synthesis of a stabilizing controller.

Reuse of the control law structure from previous chapters allows for reuse of the tuning weights as well. To select the gains for Equation (4.294), the LQR framework is applied to the feedback-linearized double integrator system with the base state weightings $\boldsymbol{Q}_{\mathcal{B}} = \mathrm{diag}\,(10,\, 10,\, 10,\, 5,\, 5,\, 5)$ and base control weightings $\boldsymbol{R}_{\mathcal{B}} = \mathrm{diag}\,(1,\, 1,\, 1)$. The state and control weights for the arms are $\boldsymbol{Q}_{\mathfrak{A}} = \mathrm{diag}\,(10,\, 10,\, 1 \times 10^{-6},\, 0.1,\, 0.1,\, 1)$ and $\boldsymbol{R}_{\mathfrak{A}} = \mathrm{diag}\,(0.1,\, 1 \times 10^{-3},\, 1 \times 10^{-3})$, which are recycled from Section 3.3 and repeated for each arm.

The tracking performance is first tested on the Simscape model with the trajectory

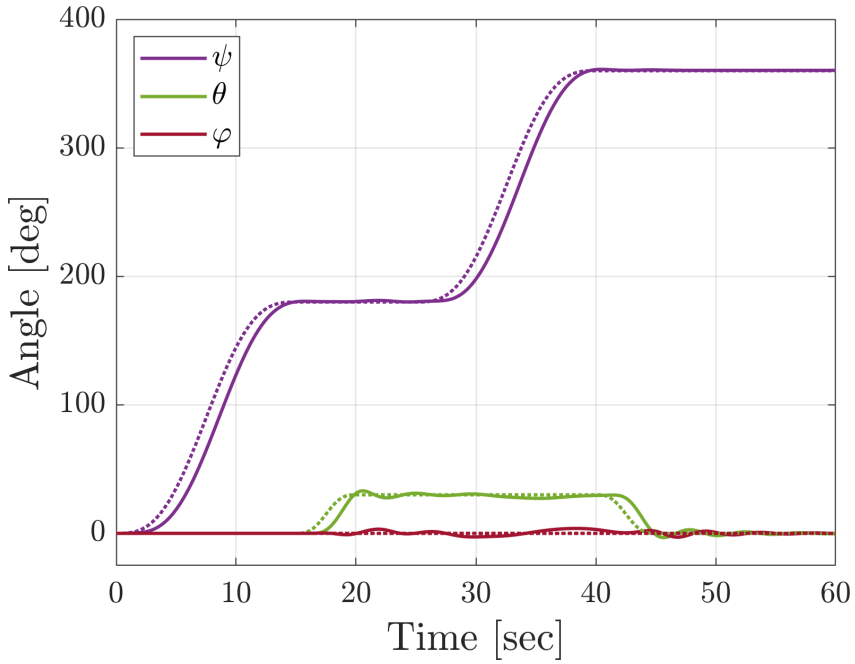

(a) Full trajectory showing all three angles.

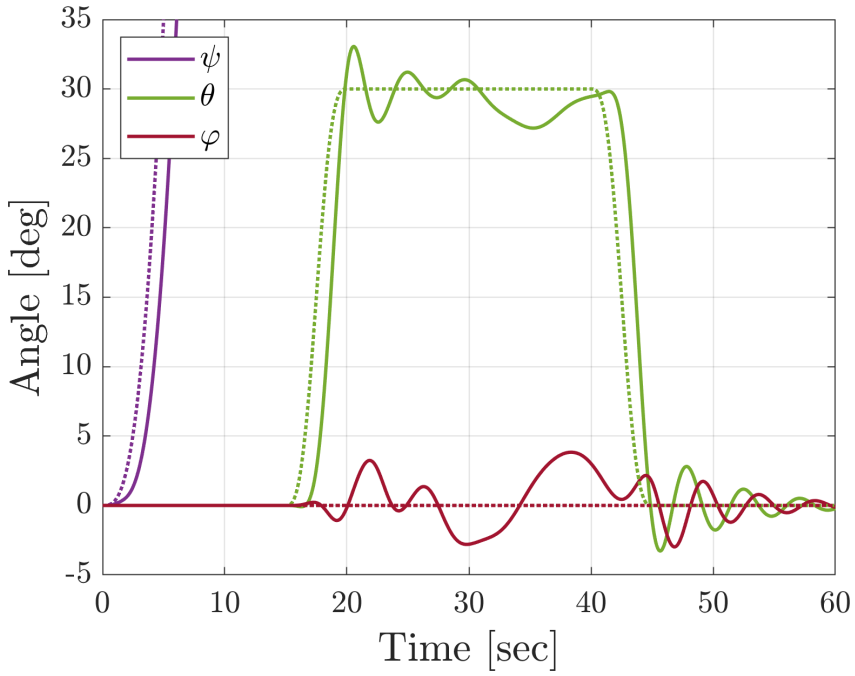

(b) Details of pitch and roll tracking.

Figure 4.5: Simulated tracking performance of base link rotation for a simple attitude trajectory with cycloid position profiles. The copter yaws 180°, pitches 30°, yaws another 180°, and pitches back −30° to return to the starting state. Desired roll angle remains zero throughout. Target trajectory is shown as dashed, while simulated measurements are shown as solid. Though the perturbations visible in the roll and pitch axes are correlated with motion in the yaw axis, there is a distinctive coupling between the roll and pitch which is most visible in the damped oscillations beginning at 45 sec.

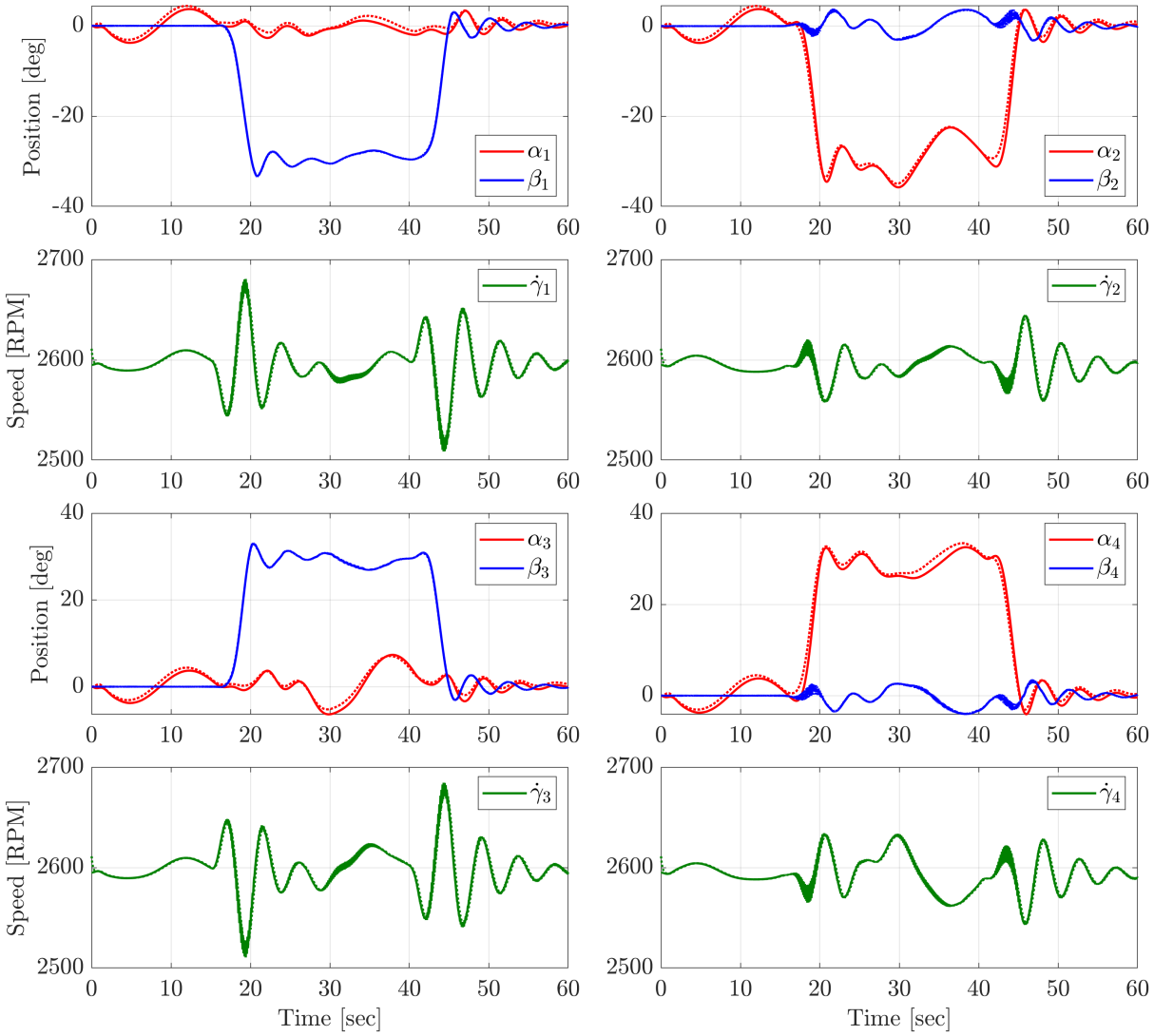

Figure 4.6: Simulated behavior of all four arms to generate the base motion shown in Fig. 4.5. Reference values, shown as dashed, are generated by the wrench mapper and inverse kinematics scheme in order to create the desired control wrench about the base. Clear symmetries are visible between the roll-axis arms and between the pitch-axis arms, which is the expected behavior to minimize conflicting thrust components.

shown in Fig. 4.5. Starting from level hover, the copter yaws 180°, pitches 30°, yaws another 180°, and pitches back −30°, returning to the starting state. All transitions follow the cycloid profile described by Equation (3.13), and the roll angle is meant to remain zero throughout. From Fig. 4.5a it is clear that the copter attitude generally tracks the target trajectory. Fig. 4.5b shows a zoomed-in view of the roll and pitch coordinates, where it can be seen that the maximum error is approximately 4°. Fig. 4.6 shows the behavior of the arm coordinates in response to the set-points generated from the wrench mapper and inverse kinematics scheme. The tracking is extremely close, with a maximum error of approximately 2°. The arm coordinates were intentionally tuned to operate on a faster time scale than the base coordinates, since the generation of an effective control wrench $\boldsymbol{\tau}_{\mathcal{B}}$ depends on fast response of the arms, similar to a multi-loop control architecture.

A second trajectory is shown in Fig. 4.7, which is identical to the first trajectory but with the pitch and roll axes swapped; the copter yaws 180°, rolls 30°, yaws another 30°, and rolls back −30°, returning to the starting state. The performance is extremely similar between the two trajectories and achieves a similar maximum error. The associated arm behaviors are shown in Fig. 4.8, which also mimic the performance of the first trajectory.

One notable feature visible in both Fig. 4.5b and Fig. 4.7b is the damped oscillation beginning at 45 sec. The two cases begin with very different initial conditions, but quickly enter a coupled oscillation with both the pitch and roll angles oscillating at the same frequency, and the pitch angle leading in phase by 90°. This is directly attributable to the gyroscopic coupling between these two axes; an attitude error in the $+\theta$ direction will elicit a control torque in the $-\theta$ direction, resulting in gyroscopic precession towards the $+\varphi$ direction, eliciting a control torque in the $-\varphi$ direction, resulting in gyroscopic precession towards the $-\theta$ direction, and so on until the oscillation is damped out by the derivative action of the controller. The behavior mimics precession of a spinning top under the influence of a gravitational torque, though with the direction flipped because the control torques act to stabilize the copter rather than overturn it as gravity would.

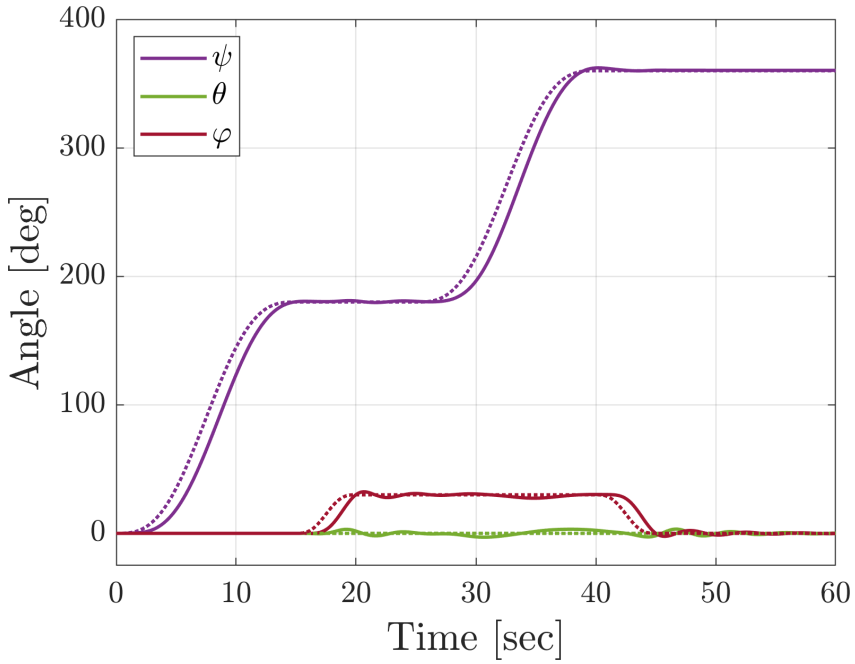

(a) Full trajectory showing all three angles.

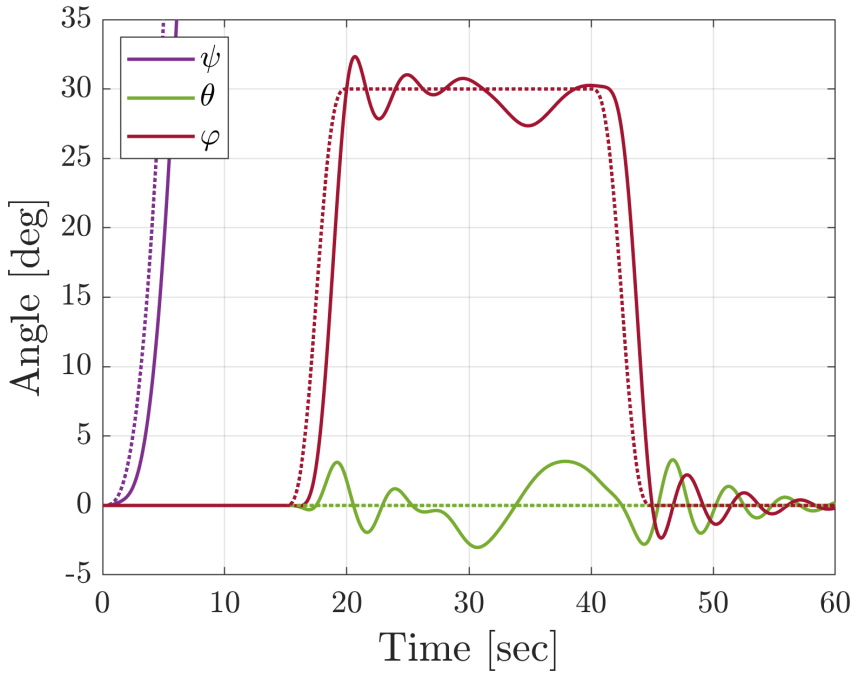

(b) Details of pitch and roll tracking.

Figure 4.7: Simulated tracking performance of base link rotation for a variant of the trajectory shown in Fig. 4.5 where the pitch and roll axes have been swapped. Target trajectory is shown as dashed and simulated measurements in shown as solid. The variant shows similar tracking performance to the original, and the same roll-pitch couplings are clearly visible. A notable feature is the damped oscillation beginning at 45 sec, which is nearly identical to that seen in Fig. 4.5 and corresponds to gyroscopic precession of the whole copter.

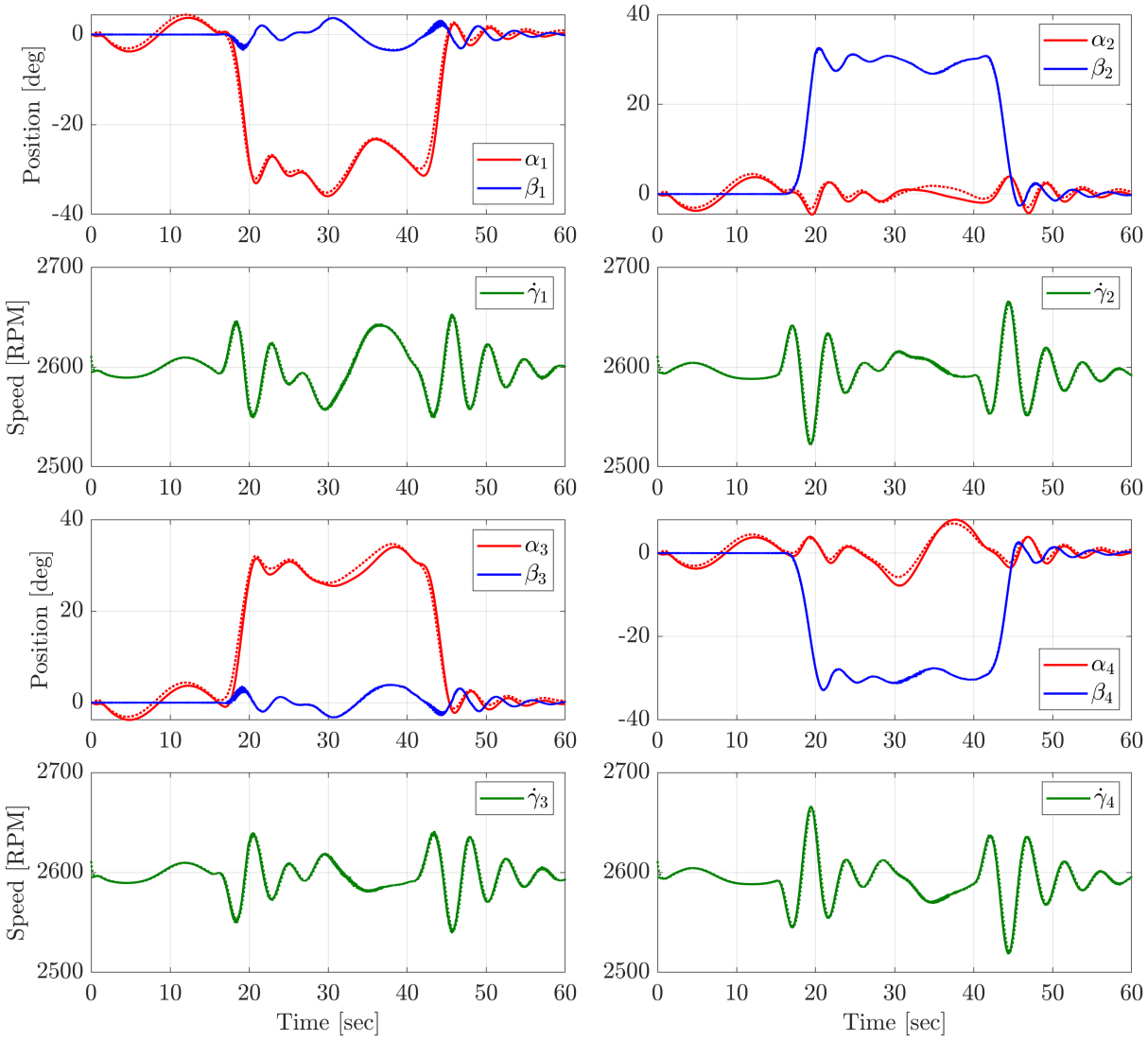

Figure 4.8: Simulated behavior of all four arms to generate the base motion shown in Fig. 4.7. Tracking is similar Fig. 4.6 and mimics the performance of the single-arm control design presented in Section 3.3.

This chapter developed equations of motion for the full copter with all four arms and a base link constrained by a spherical joint. Many simplifying approximations were made to reduce the complexity of the resulting equations of motion for use in control design. A sample trajectory with prescribed motion was used to verify the predictive power of the equations despite the simplifying approximations. Finally, a modified control architecture was developed to track a 3-DOF attitude trajectory with a single centralized control law that accounts for both configuration-dependent inertia fluctuations and gyroscopic couplings. The performance was demonstrated on two simple trajectories which illustrate both the capabilities and challenges associated with the copter. The final generalization with this platform is to remove the spherical joint constraint and allow full 6-DOF motion of the copter.

Chapter 5

Full Copter 6-DOF

Having developed a full copter controller which can track attitude trajectories for the base link, the last step in this work focuses on expanding the controller to include position trajectories for the base link, resulting in full 6-DOF pose control. This requires expanding the equations of motion from Chapter 4 to include translational coordinates.

5.1 Base Translation

Removing the spherical joint constraint allows the base link to translate in 3D space. The position of the base link center of mass with respect to the origin $\mathcal{O}$ is denoted

$$\boldsymbol{r}^{\mathcal{B}/\mathcal{O}} = x\,\hat{\boldsymbol{n}}_1 + y\,\hat{\boldsymbol{n}}_2 + z\,\hat{\boldsymbol{n}}_3, \tag{5.1}$$

and the linear velocity of the base as seen in the inertial frame is

$$\boldsymbol{v}^{\mathcal{BN}} = \dot{x}\,\hat{\boldsymbol{n}}_1 + \dot{y}\,\hat{\boldsymbol{n}}_2 + \dot{z}\,\hat{\boldsymbol{n}}_3. \tag{5.2}$$

The kinetic energy of the base link now includes both translational and rotational components

$$T_{\mathcal{B}} = T^{v}_{\mathcal{B}} + T^{\omega}_{\mathcal{B}}, \tag{5.3}$$

with the translational component given by

$$\begin{aligned} T_{\mathcal{B}}^{v} &= \frac{1}{2} m_{\mathcal{B}} \left(\boldsymbol{v}^{\mathcal{BN}}\right)^{T} \left(\boldsymbol{v}^{\mathcal{BN}}\right) \\ &= \frac{1}{2} m_{\mathcal{B}} \left(\dot{x}^2 + \dot{y}^2 + \dot{z}^2\right). \end{aligned} \tag{5.4}$$

This equation depends only on the translational speeds, leading to the trivial set of kinetic energy speed partials given by

$$\frac{d}{dt}\left(\frac{\partial T_{\mathcal{B}}^{v}}{\partial \dot{x}}\right) = m_{\mathcal{B}} \ddot{x}, \qquad \frac{d}{dt}\left(\frac{\partial T_{\mathcal{B}}^{v}}{\partial \dot{y}}\right) = m_{\mathcal{B}} \ddot{y}, \qquad \frac{d}{dt}\left(\frac{\partial T_{\mathcal{B}}^{v}}{\partial \dot{z}}\right) = m_{\mathcal{B}} \ddot{z}, \tag{5.5}$$

and all other partial derivatives are zero. The rotational component of the base kinetic energy is unchanged from Equation (4.9) and is not dependent on the new translational coordinates, therefore all partial derivatives from Section 4.2 remain valid.

The base link potential energy is

$$\begin{aligned} U_{\mathcal{B}} &= m_{\mathcal{B}} g_0 \, \boldsymbol{r}^{\mathcal{B}/\mathcal{O}} \cdot \hat{\boldsymbol{n}}_3 \\ &= m_{\mathcal{B}} g_0 z, \end{aligned} \tag{5.6}$$

with the only nonzero partial derivative given by

$$\frac{\partial U_{\mathcal{B}}}{\partial z} = m_{\mathcal{B}} g_0. \tag{5.7}$$

5.1.1 Effects on Arm Energy

Allowing base translation introduces an additive vector component to the positions of the arm bodies. Beginning with the arc, the new position vector is given by

$$\boldsymbol{r}^{\mathcal{A}^i/\mathcal{O}} = \boldsymbol{r}^{\mathcal{B}/\mathcal{O}} + \boldsymbol{r}^{\mathcal{A}^i/\mathcal{B}}, \tag{5.8}$$

where the position of the base relative to the origin is given by Equation (5.1), and the position of the arc relative to the base is unchanged from Equation (4.15). The new

velocity vector is

$$\boldsymbol{v}^{\mathcal{A}^i\mathcal{N}} = \boldsymbol{v}^{\mathcal{B}\mathcal{N}} + \boldsymbol{v}^{\mathcal{A}^i/\mathcal{B},\mathcal{N}}, \tag{5.9}$$

where $\boldsymbol{v}^{\mathcal{A}^i/\mathcal{B},\mathcal{N}}$ denotes the linear velocity of the arc with respect to the base, as seen in the $\mathcal{N}$ frame. It is equivalent to Equation (4.17) derived under the assumption of zero base translation. The translational kinetic energy can then be written as a sum of three components

$$\begin{aligned} T^v_{\mathcal{A}^i} &= \frac{1}{2} m_{\mathcal{A}} \big(\boldsymbol{v}^{\mathcal{A}^i\mathcal{N}}\big)^T \big(\boldsymbol{v}^{\mathcal{A}^i\mathcal{N}}\big) \\ &= \frac{1}{2} m_{\mathcal{A}} \big(\boldsymbol{v}^{\mathcal{B}\mathcal{N}}\big)^T \big(\boldsymbol{v}^{\mathcal{B}\mathcal{N}}\big) + \frac{1}{2} m_{\mathcal{A}} \big(\boldsymbol{v}^{\mathcal{A}^i/\mathcal{B},\mathcal{N}}\big)^T \big(\boldsymbol{v}^{\mathcal{A}^i/\mathcal{B},\mathcal{N}}\big) + m_{\mathcal{A}} \big(\boldsymbol{v}^{\mathcal{B}\mathcal{N}}\big)^T \big(\boldsymbol{v}^{\mathcal{A}^i/\mathcal{B},\mathcal{N}}\big). \end{aligned} \tag{5.10}$$

The first component captures the kinetic energy of the arc due to translation of the base, and is equivalent in form to Equation (5.4) with the mass of the base replaced by the mass of the arc. Its nonzero partial derivatives are thus of the same form as Equation (5.5).

The second component captures the kinetic energy of the arc due to translation about the base, and is unchanged from Equation (4.19). All partial derivatives from Section 4.3 therefore still apply. A similar statement can be made about the rotational kinetic energy of the arc, which is unchanged from Equation (4.20).

The last component is a cross-term between the linear velocities due to base translation and base rotation. In general this term can depend on many generalized coordinates/speeds and lead to complicated partial derivatives. For example, the cross-terms for arc 1 are given by

$$\big(\boldsymbol{v}^{\mathcal{B}\mathcal{N}}\big)^T \big(\boldsymbol{v}^{\mathcal{A}^1/\mathcal{B},\mathcal{N}}\big) = \big(\dot{x}\,\hat{\boldsymbol{n}}_1 + \dot{y}\,\hat{\boldsymbol{n}}_2 + \dot{z}\,\hat{\boldsymbol{n}}_3\big)^T \Big(\ell_{\mathcal{A}}\big(\dot{\psi} c_\theta c_\varphi - \dot{\theta} s_\varphi\big)\hat{\boldsymbol{b}}_2 - \ell_{\mathcal{A}}\big(\dot{\psi} c_\theta s_\varphi + \dot{\theta} c_\varphi\big)\hat{\boldsymbol{b}}_3\Big), \tag{5.11}$$

which is dependent on all three base velocities, all three base angles, and two of the three base angular velocities. Clearly evaluation of partial derivatives would prove formidable,

however consider the same cross-terms evaluated for arc 3, resulting in

$$\left(\boldsymbol{v}^{\mathcal{BN}}\right)^T\left(\boldsymbol{v}^{\mathcal{A}^3/\mathcal{B},\mathcal{N}}\right) = \left(\dot{x}\,\hat{\boldsymbol{n}}_1 + \dot{y}\,\hat{\boldsymbol{n}}_2 + \dot{z}\,\hat{\boldsymbol{n}}_3\right)^T\Big(- \ell_{\mathcal{A}}\big(\dot{\psi}c_\theta c_\varphi - \dot{\theta}s_\varphi\big)\hat{\boldsymbol{b}}_2 + \ell_{\mathcal{A}}\big(\dot{\psi}c_\theta s_\varphi + \dot{\theta}c_\varphi\big)\hat{\boldsymbol{b}}_3\Big), \tag{5.12}$$

which is equal and opposite to the cross-terms for arc 1. Because the masses of all arcs are identical, these cross-terms exactly cancel when assembling the full Lagrangian according to Equation (4.2), so the last term of Equation (5.10) has no effect on the final equations of motion. This is a direct consequence of selecting the $\mathcal{B}$ frame origin to be the copter center of mass, and any other choice of origin would result in some apparent translation as the copter rotates about its center of mass. The cancellation also occurs between arcs 2 and 4, as well as between opposing shafts. It does not occur between the propellers due to the variable distance between the propeller origin and the base origin, however the translational kinetic energy of the propeller can again be neglected due to its small magnitude relative to the rotational kinetic energy. The result is that allowing base translation does not introduce any additional terms to the rotational equations of motion.

The potential energy of the arm components is dependent on the position of the base, however the dependence is linear and therefore does not contain any cross-terms which would complicate the partial derivatives. All partials derived in Section 4.3 still apply, with one additional partial due to the base position. For example, the arc potential energy satisfies

$$\frac{\partial U_{\mathcal{A}^i}}{\partial z} = m_{\mathcal{A}} g_0, \tag{5.13}$$

and the same form holds for the shafts and propellers.

5.1.2 Generalized Forces

Of the generalized forces discussed in Section 4.4, only the thrusts have an effect on the base translation. To find the net effect of the thrusts on the translation coordinates,

consider the resultant vector obtained by combining all four thrusts

$$\begin{aligned}
\sum_{i=1}^{4} \bar{\boldsymbol{F}}_i &= c_p\dot{\gamma}_1^2\,\hat{\boldsymbol{s}}_3^1 + c_p\dot{\gamma}_2^2\,\hat{\boldsymbol{s}}_3^2 + c_p\dot{\gamma}_3^2\,\hat{\boldsymbol{s}}_3^3 + c_p\dot{\gamma}_4^2\,\hat{\boldsymbol{s}}_3^4 \\
&= c_p\dot{\gamma}_1^2\big(s_{\beta_1}\,\hat{\boldsymbol{b}}_1 - s_{\alpha_1}c_{\beta_1}\,\hat{\boldsymbol{b}}_2 + c_{\alpha_2}c_{\beta_2}\,\hat{\boldsymbol{b}}_3\big) \\
&\quad + c_p\dot{\gamma}_2^2\big(s_{\beta_2}\,\hat{\boldsymbol{b}}_2 + s_{\alpha_2}c_{\beta_2}\,\hat{\boldsymbol{b}}_2 + c_{\alpha_2}c_{\beta_2}\,\hat{\boldsymbol{b}}_3\big) \\
&\quad + c_p\dot{\gamma}_3^2\big(-s_{\beta_3}\,\hat{\boldsymbol{b}}_3 + s_{\alpha_3}c_{\beta_3}\,\hat{\boldsymbol{b}}_2 + c_{\alpha_2}c_{\beta_2}\,\hat{\boldsymbol{b}}_3\big) \\
&\quad + c_p\dot{\gamma}_4^2\big(-s_{\beta_4}\,\hat{\boldsymbol{b}}_4 - s_{\alpha_4}c_{\beta_4}\,\hat{\boldsymbol{b}}_2 + c_{\alpha_2}c_{\beta_2}\,\hat{\boldsymbol{b}}_3\big) \\
&= c_p\big(\dot{\gamma}_1^2 s_{\beta_1} - \dot{\gamma}_3^2 s_{\beta_3} + \dot{\gamma}_2^2 s_{\alpha_2}c_{\beta_2} - \dot{\gamma}_4^2 s_{\alpha_4}c_{\beta_4}\big)\hat{\boldsymbol{b}}_1 \\
&\quad c_p\big(-\dot{\gamma}_1^2 s_{\alpha_1}c_{\beta_1} + \dot{\gamma}_3^2 s_{\alpha_3}c_{\beta_3} + \dot{\gamma}_2^2 s_{\beta_2} - \dot{\gamma}_4^2 s_{\beta_4}\big)\hat{\boldsymbol{b}}_2 \\
&\quad c_p\big(\dot{\gamma}_1^2 c_{\alpha_1}c_{\beta_1} + \dot{\gamma}_2^2 c_{\alpha_2}c_{\beta_2} + \dot{\gamma}_3^2 c_{\alpha_3}c_{\beta_3} + \dot{\gamma}_4^2 c_{\alpha_4}c_{\beta_4}\big)\hat{\boldsymbol{b}}_3 \\
&\triangleq F_{b_1}\,\hat{\boldsymbol{b}}_1 + F_{b_2}\,\hat{\boldsymbol{b}}_2 + F_{b_3}\,\hat{\boldsymbol{b}}_3.
\end{aligned} \tag{5.14}$$

This resultant can be rotated into the inertial frame using the appropriate DCM

$$\boldsymbol{\Xi} = \begin{bmatrix} F_x \\ F_y \\ F_z \end{bmatrix} = \boldsymbol{R}_{\mathcal{NB}} \begin{bmatrix} F_{b_1} \\ F_{b_2} \\ F_{b_3} \end{bmatrix}, \tag{5.15}$$

so that F_x, F_y, and F_z are the resultant thrusts along the x, y, and z directions, denoted $\boldsymbol{\Xi}$ for convenience.

As with the base rotation axes, no dedicated actuators exist for base translation, and the motor input torques have no effect on the translation axes.

5.2 Equations of Motion

Because the rotational and translational dynamics are essentially decoupled by the appropriate choice of coordinates, it is possible to write down a separate equation of motion

for the base position, given by

$$m \begin{bmatrix} \ddot{x} \\ \ddot{y} \\ \ddot{z} \end{bmatrix} + mg_0 \begin{bmatrix} 0 \\ 0 \\ 1 \end{bmatrix} = \begin{bmatrix} F_x \\ F_y \\ F_z \end{bmatrix}, \tag{5.16}$$

where m is the mass of the full copter

$$m = m_{\mathcal{B}} + 4m_{\mathcal{A}} + 4m_{\mathcal{S}} + 4m_{\mathcal{P}}. \tag{5.17}$$

Defining a position state vector, Equation (5.16) can be rewritten as

$$\boldsymbol{p} = \begin{bmatrix} x \\ y \\ z \end{bmatrix}, \qquad \dot{\boldsymbol{p}} = \begin{bmatrix} \dot{x} \\ \dot{y} \\ \dot{z} \end{bmatrix}, \tag{5.18}$$

$$\begin{bmatrix} \dot{\boldsymbol{p}} \\ \ddot{\boldsymbol{p}} \end{bmatrix} = \begin{bmatrix} \boldsymbol{0} & \boldsymbol{E}_3 \\ \boldsymbol{0} & \boldsymbol{0} \end{bmatrix} \begin{bmatrix} \boldsymbol{p} \\ \dot{\boldsymbol{p}} \end{bmatrix} + \begin{bmatrix} \boldsymbol{0} \\ \boldsymbol{E}_3 \end{bmatrix} \boldsymbol{\Xi} - \begin{bmatrix} \boldsymbol{0} \\ \boldsymbol{W} \end{bmatrix}, \tag{5.19}$$

which is in the typical state-space form with

$$\boldsymbol{W} = \begin{bmatrix} 0 \\ 0 \\ mg_0 \end{bmatrix}. \tag{5.20}$$

5.3 6-DOF Tracking Control

The state-space form in Equation (5.19) is already amenable to the LQR framework, which could be used to calculate gain matrices that regulate the position and velocity of the base link to zero. The objective, however, is not to remain at zero but to track a given position trajectory $\boldsymbol{p}_d$. To achieve this, consider an integrated position error signal defined by

$$\boldsymbol{e_i} = \int \left(\boldsymbol{p}_d - \boldsymbol{p}\right) dt. \tag{5.21}$$

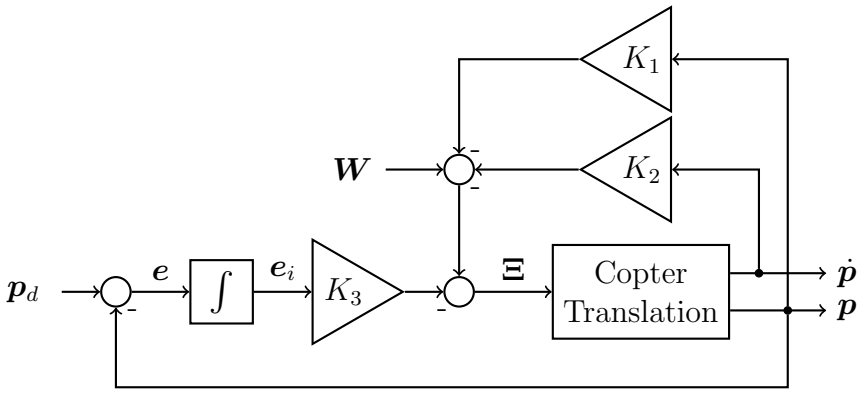

Figure 5.1: Block diagram for the copter translational dynamics in Equation (5.19) and the LQI control law in Equation (5.23).

Adding the integrated error to the state-space equation yields the augmented system

$$\begin{bmatrix} \dot{\boldsymbol{p}} \\ \ddot{\boldsymbol{p}} \\ \dot{\boldsymbol{e}}_i \end{bmatrix} = \begin{bmatrix} \boldsymbol{0} & \boldsymbol{E}_3 & \boldsymbol{0} \\ \boldsymbol{0} & \boldsymbol{0} & \boldsymbol{0} \\ -\boldsymbol{E}_3 & \boldsymbol{0} & \boldsymbol{0} \end{bmatrix} \begin{bmatrix} \boldsymbol{p} \\ \dot{\boldsymbol{p}} \\ \boldsymbol{e}_i \end{bmatrix} + \begin{bmatrix} \boldsymbol{0} \\ \boldsymbol{E}_3 \\ \boldsymbol{0} \end{bmatrix} \boldsymbol{\Xi} + \begin{bmatrix} \boldsymbol{0} \\ \boldsymbol{0} \\ \boldsymbol{E}_3 \end{bmatrix} \boldsymbol{p}_d - \begin{bmatrix} \boldsymbol{0} \\ \boldsymbol{W} \\ \boldsymbol{0} \end{bmatrix}. \tag{5.22}$$

Let the augmented state-feedback plus weight compensation control law be given by

$$\boldsymbol{\Xi} = -\boldsymbol{K}_1 \boldsymbol{p} - \boldsymbol{K}_2 \dot{\boldsymbol{p}} - \boldsymbol{K}_3 \boldsymbol{e}_i + \boldsymbol{W}, \tag{5.23}$$

where the gain matrices are obtained by applying the LQR framework to Equation (5.22). The resulting control block diagram is shown in Fig. 5.1. By including the integrated error as a state variable, the controller regulates the system to a steady-state where the position $\boldsymbol{p}$ asymptotically approaches $\boldsymbol{p}_d$, under the assumption that the latter is constant. This is an application of LQR with integral action, and the control law is dubbed the linear quadratic integrator (LQI).

The commanded base force $\boldsymbol{\Xi}$ from Equation (5.23) can be combined with the commanded base torque $\boldsymbol{\tau}_{\mathcal{B}}$ from Equation (4.294) to form the overall control wrench for the base link, denoted $\boldsymbol{u}$. This wrench is then fed to the same wrench mapper and inverse kinematics scheme used in Section 4.9 to generate set-points for the arm angles and propeller speeds. The full block diagram for the control architecture is shown in Fig. 5.2.

To tune the gain matrices in Equation (5.23), the LQR framework is applied with the

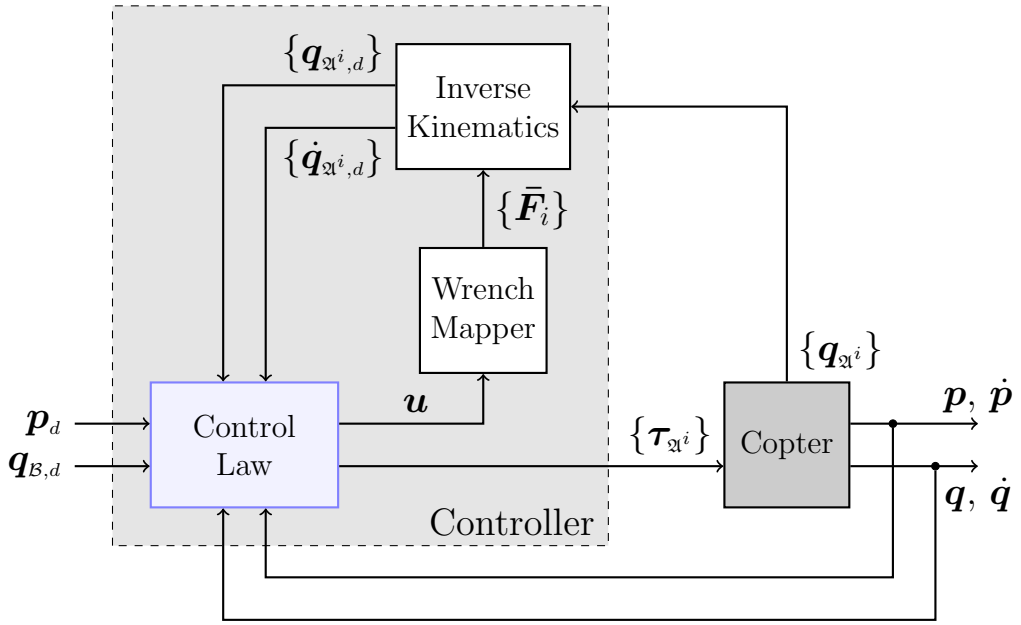

(a) Full control architecture.

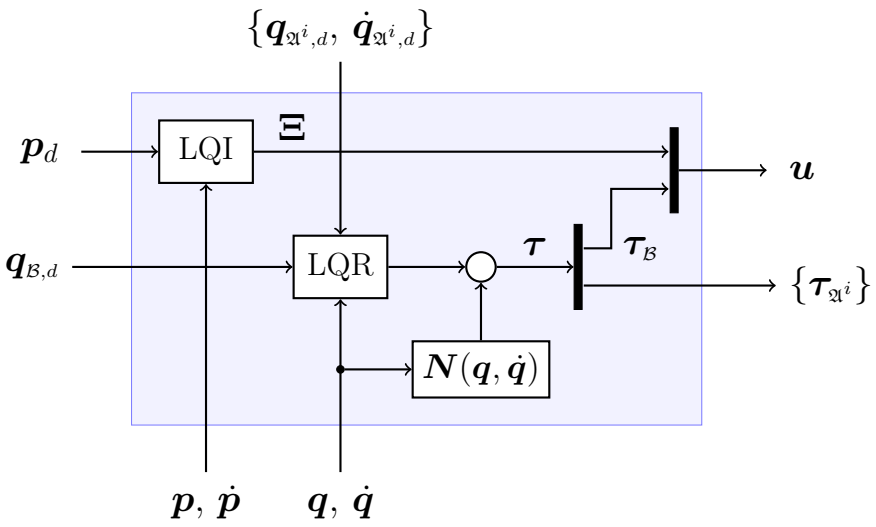

(b) Control law details.

Figure 5.2: Hierarchical control model for combined position and attitude tracking (compare Fig. 4.4). The commanded base force is computed by the LQI control law in Equation (5.23). The vector $\boldsymbol{\tau}$ is computed with the LQR plus nonlinear compensation in Equation (4.294), and is separated into the commanded base torque $\boldsymbol{\tau}_{\mathcal{B}}$ and the motor torques $\boldsymbol{\tau}_{\mathfrak{A}^i}$. The base force and torque are combined into a control wrench $\boldsymbol{u}$ and used to computed the desired arm angles and propeller speeds, which are fed back to the control law as set-points.

position state weightings $\boldsymbol{Q}_p = \text{diag}\,(1,\ 1,\ 1,\ 20,\ 20,\ 20,\ 5,\ 5,\ 5)$ and the control weightings $\boldsymbol{R}_p = \text{diag}\,(0.1,\ 0.1,\ 0.1)$. The attitude controller is unchanged from Section 4.9.

5.3.1 On-point Rotation

The control architecture is tested with two trajectories that demonstrate capabilities of the twist-tilt copter which would not be possible with a conventional quadrotor. The first is the on-point rotation trajectory shown in Section 4.9 with a spherical joint constraint, repeated here with base translation enabled. Fig. 5.5 shows the desired attitude trajectory, consisting of alternate yaw and pitch motions while maintaining zero roll. The simulated performance is very similar to Fig. 4.5 without base translation, which is expected because the translational dynamics are not coupled with the rotational dynamics, and the attitude controller is identical in both cases.

The simulated translation is shown in Fig. 5.4. It can be seen that during the initial yaw movement, all displacements remain essentially zero. During the first pitch motion occurring at 15 sec, the propeller speeds (shown in Fig. 5.5) are varied differentially to change the pitch angle while maintaining zero roll. This temporarily results in a net thrust which displaces the copter along the x axis, but is quickly corrected by altering the tilt angles on the roll-axis arms. A similar position perturbation is seen at 40 sec when the copter pitches back to its original attitude. The x displacements for these two events occur in the same direction despite reversed pitching action because the copter yaw angle changes 180° between the two maneuvers. In both cases the maximum displacement error is approximately 7 cm, but could be decreased by reducing the $\boldsymbol{R}_p$ cost in the LQR tuning. The cost of the base force $\boldsymbol{\Xi}$ relative to the cost of the base torque $\boldsymbol{\tau}_{\mathcal{B}}$ determines how strongly the arm set-points are influenced by position tracking and attitude tracking respectively. This can be exploited to create specialized controllers for real-world applications where precise position control is more important than attitude control, or vice versa.

Fig. 5.6 shows another variation of on-point rotation, consisting of alternating yaw

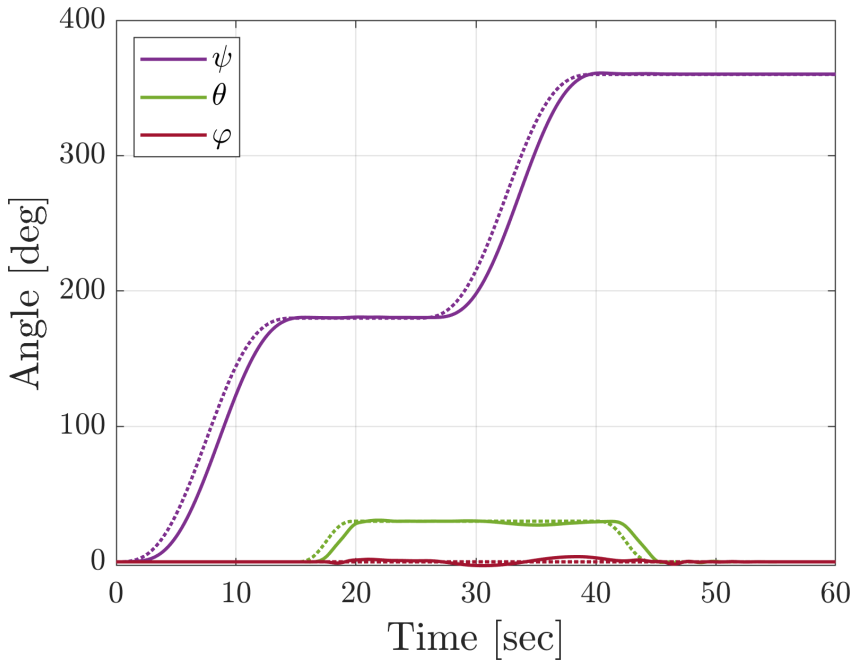

(a) Full trajectory showing all three angles.

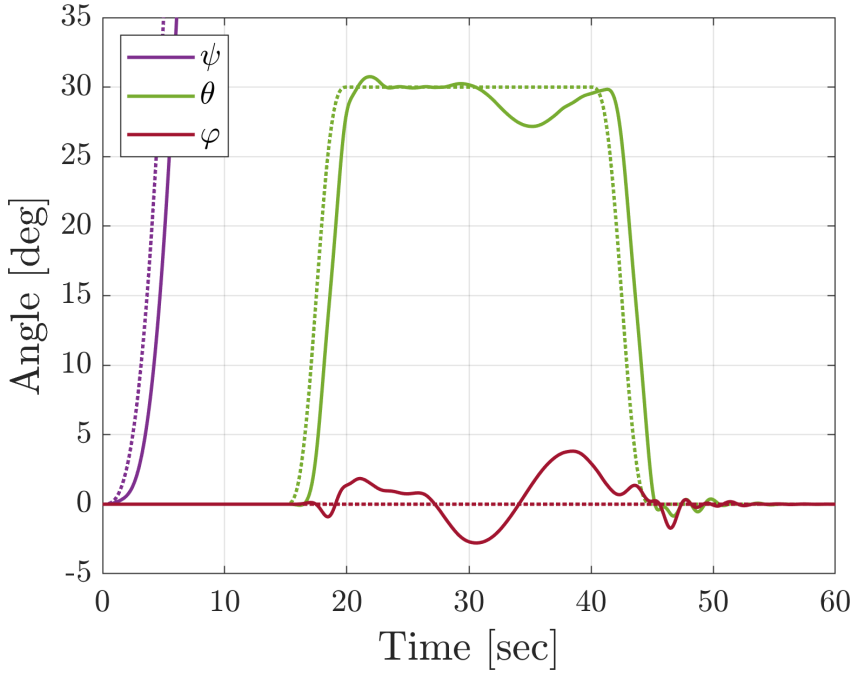

(b) Details of pitch and roll tracking.

Figure 5.3: Simulated tracking performance of base link rotation for a sequential yaw and pitch trajectory at zero roll. Target trajectory is shown as dashed, simulation measurements are shown as solid. While coupled perturbations exist in the roll and pitch axes, the tracking performance has improved by including an additional control objective for position regulation (compare Fig. 4.5b.

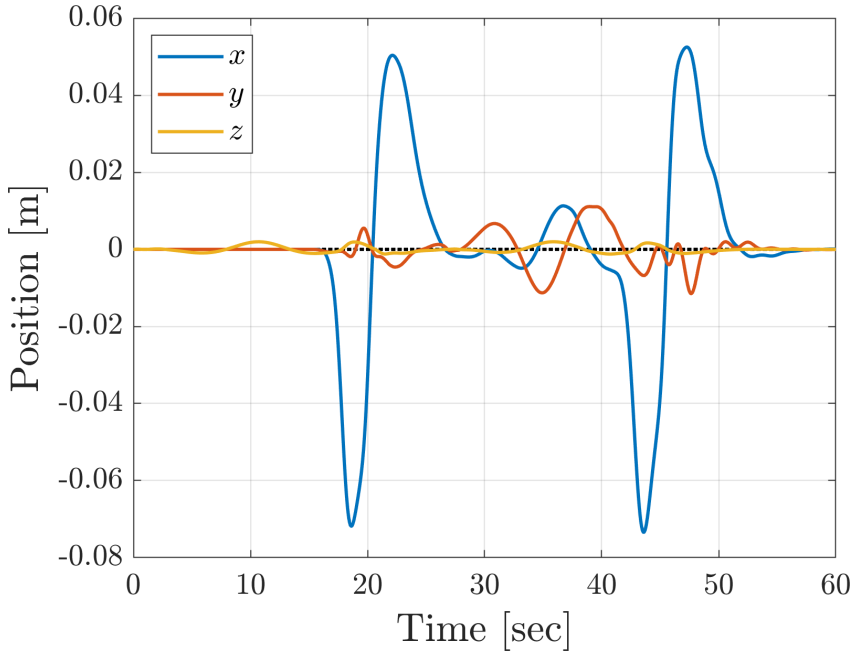

Figure 5.4: Position tracking performance for the attitude trajectory shown in Fig. 5.3. The desired displacement set-points are all zero, indicated by a black dashed line. Perturbations in the x axis occur during periods of pitching motion, where rotation of the full copter momentarily leads to a net thrust in the horizontal plane before being counteracted by the appropriate tilt angles.

and roll motions while maintaining zero pitch. The performance is again very similar to Fig. 4.7, which is the same trajectory simulated with a spherical joint constraint on the base link. The associated base translations and arm behaviors are shown in Fig. 5.7 and Fig. 5.8. Similar to Fig. 5.4, the position tracking remains nearly unperturbed during the initial yawing motion, and two position perturbations appear during the active rolling phases at 15 sec and 40 sec. The first roll is initiated at 15 sec by differentially varying the propeller speeds, briefly resulting in a net thrust in the positive y direction which is soon compensated by altering the tilt angles on the pitch arms. A similar y perturbation is seen during the negative pitch action at 40 sec, with translation occurring in the same direction due to the copter having yawed 180° in the interim. The maximum tracking errors for the position and attitude are approximately 7 cm and 4°, similar to the yaw-pitch trajectory variant.

One noteworthy feature of these simulations is the reduced overshoot in attitude tracking compared to the identical trajectories simulated with a spherical joint constraint

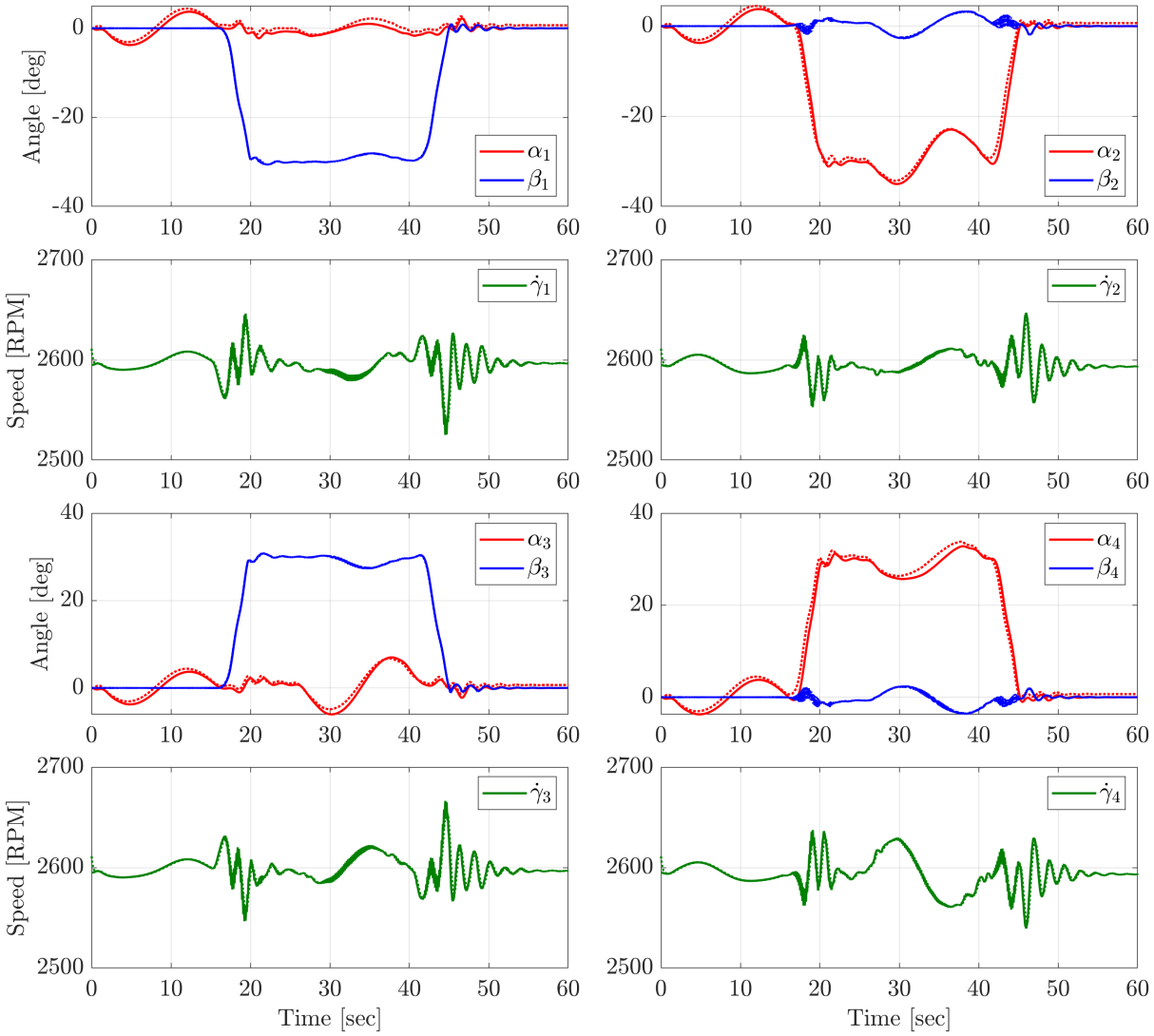

Figure 5.5: Simulated arm behavior for the attitude trajectory shown in Fig. 5.3. Reference values, generated by the wrench mapper and inverse kinematics scheme, are shown as dashed. Simulated measurements are shown as solid. Symmetries are clearly visible between opposing arms during the pitch motions, and between all arms during the yaw motions.

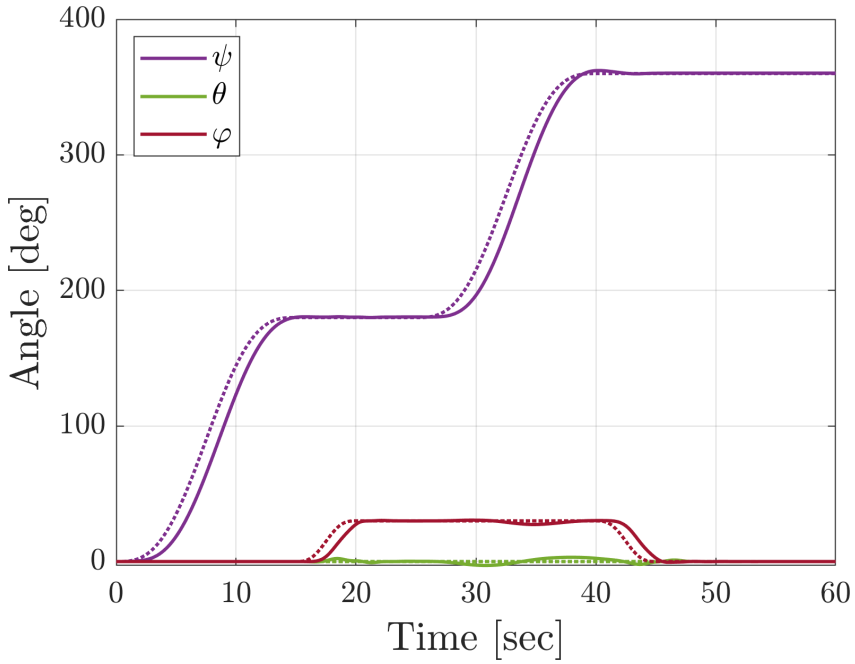

(a) Full trajectory showing all three angles.

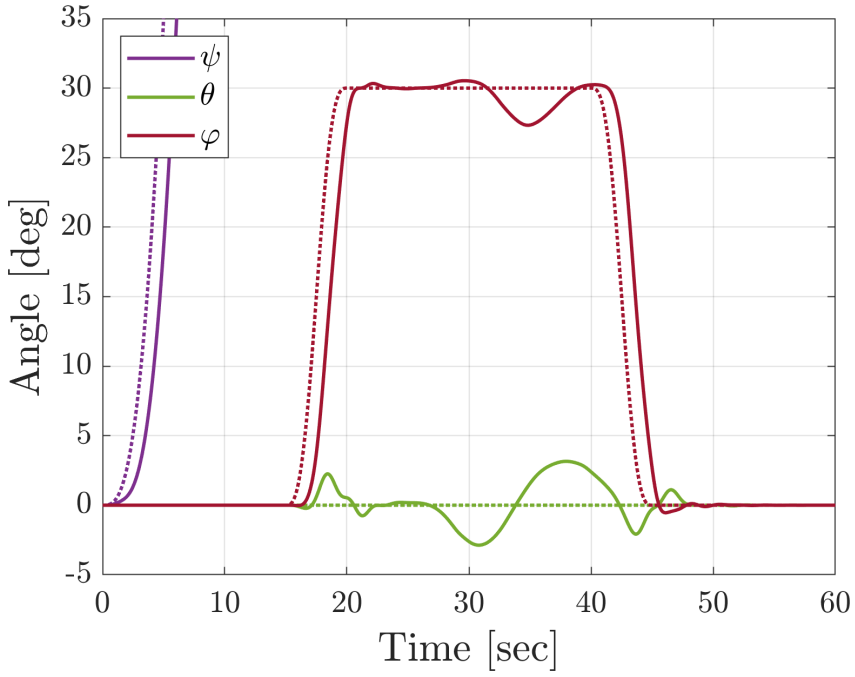

(b) Details of pitch and roll tracking.

Figure 5.6: Simulated tracking performance of the base link rotation for a variant of the trajectory shown in Fig. 5.3, with sequential yaw and roll motions at zero pitch. Tracking performance has improved over Fig. 4.5 by inclusion of the position regulation control objective.

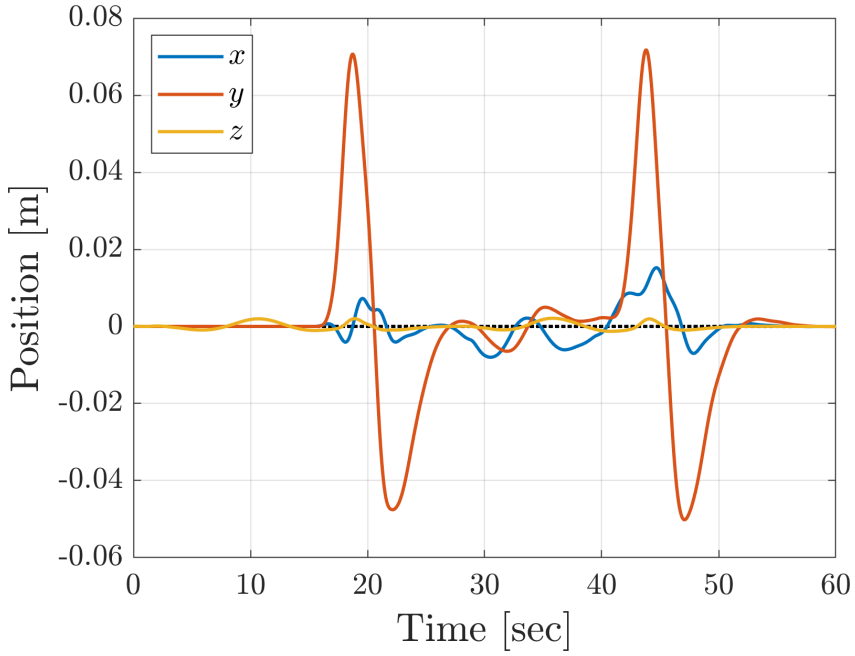

Figure 5.7: Position tracking performance for the attitude trajectory shown in Fig. 5.6. All desired displacements are zero, indicated by a black dashed line. Perturbations in the y axis arise during rolling motion of the base, where rotation of the full copter momentarily leads to a net thrust in the horizontal plane before being counteracted by the appropriate tilt angles.

(Fig. 4.5b and Fig. 4.7b). The addition of position tracking as a control objective has improved the performance in the attitude tracking objective. While it seems counterintuitive that adding multiple, possibly conflicting control objectives would improve performance, consider that the attitude dynamics are extremely complex and contain many unmodeled behaviors such as centrifugal and Coriolis couplings. Any attitude control input will thus have unexpected consequences which can ripple throughout the many degrees of freedom and lead to prolonged oscillations. In contrast, the position dynamics are relatively well-behaved, with the only major assumptions being those related to inertial properties of the various bodies (which also affect the attitude dynamics). By selecting the control weightings for the base force to be relatively cheap compared to the base torque, the controller generates control wrenches which favor the well-behaved position objective over the ill-behaved attitude objective. The direct result is less variation in set-points for the arm coordinates, visible by comparing Fig. 4.6 to Fig. 5.5 and Fig. 4.8 to Fig. 5.8; giving rise to overall smoother motion, lower overshoot, and reduced oscillation.

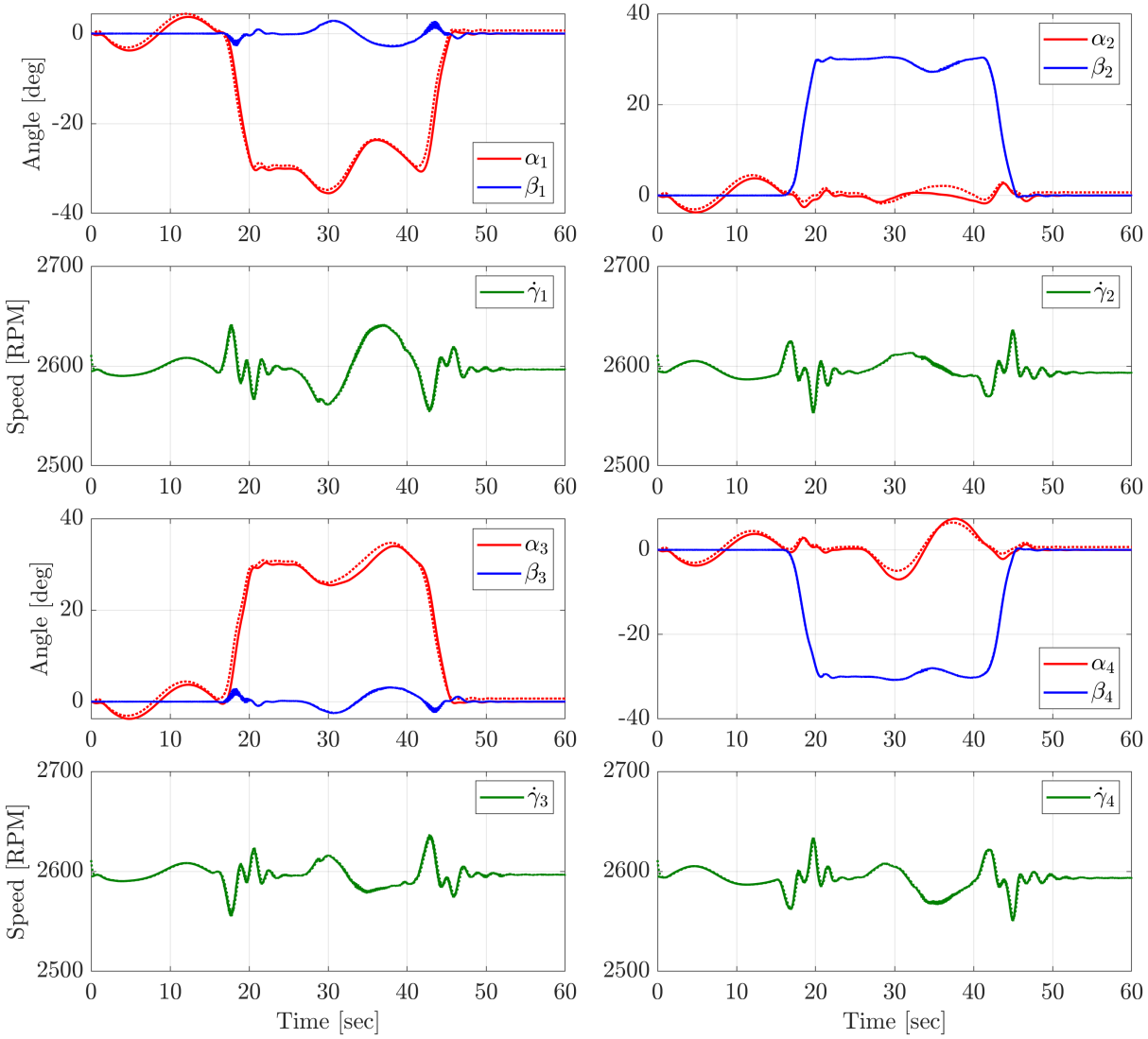

Figure 5.8: Simulated behavior of the arm coordinates to generate the base motion shown in Fig. 5.6. Performance is similar to Fig. 5.5, which is a variant of the same trajectory.

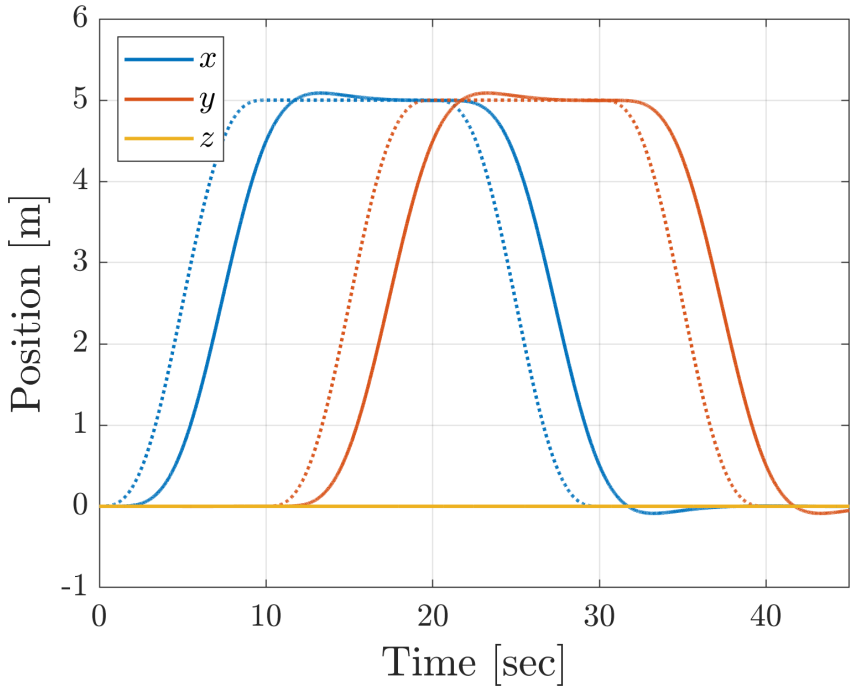

Figure 5.9: Simulated tracking performance for a simple position trajectory at zero attitude, tracing a 5 m square in the horizontal plane with edges interpolated by cycloid splines. The x and y tracking resembles the expected behavior for a rigid body, and the z displacement is maintained within 1 cm of nominal for the entire simulation.

5.3.2 Level Flight

The second type of trajectory which distinguishes the twist-tilt copter from a traditional quadrotor is the capability for full 3-DOF translation at a fixed attitude. Fig. 5.9 shows a position trajectory which traces out a 5m square in the horizontal plane, with interpolation between corners according to the cycloid in Equation (3.13). The associated base attitude and arm behaviors are shown in Fig. 5.10 and Fig. 5.11. Clearly the copter position tracks the desired trajectory, and the attitude is maintained within 0.6° of nominal throughout the entire simulation. The initial transient followed by near constant offset in the yaw angle is due to approximation of the arm centers of mass as being fixed along the twist axes. The true center of mass for arm i lies slightly in the positive $\hat{\boldsymbol{b}}_2^i$ direction, resulting in an initial disturbance to the twist angles that causes a thrust-induced yawing moment about the base. The yaw offset generates twist commands which are counteracted by the arm gravitational torque, leading to a steady-state offset of approximately 0.3°.

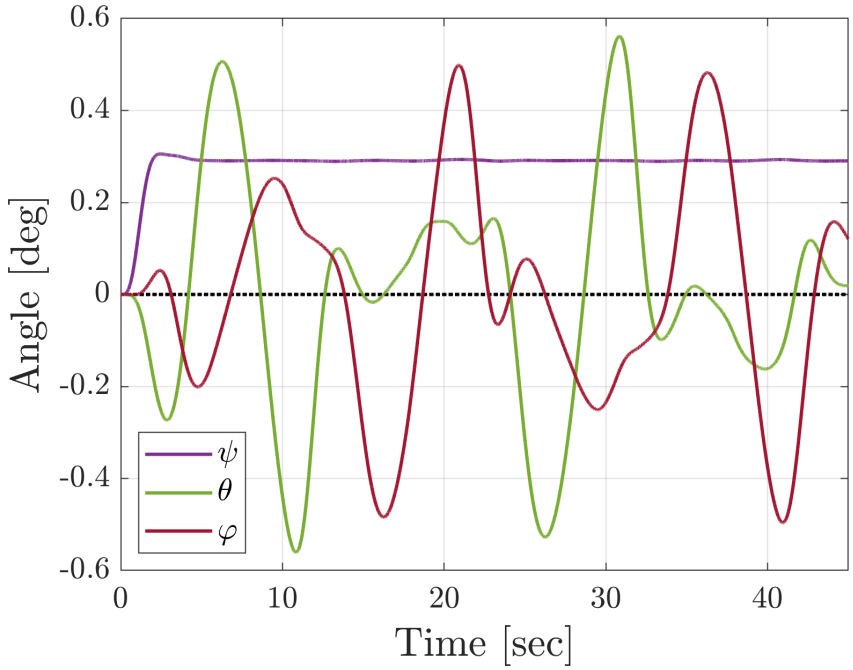

Figure 5.10: Simulated base link attitude for the position trajectory shown in Fig. 5.9. All rotation set-points fixed at are zero, indicated by a black dashed line. The initial transient followed by a near constant offset in the yaw angle is due to the unmodeled position of the arm centers of mass.

At the scale shown in Fig. 5.11 it is possible to see the details of the arm behavior. The near constant offset of approximately 0.4° in the twist angles is once again due to the approximation in the arm center of mass location, resulting in a pseudo steady-state offset where the corrective control signal cancels the gravitational torque. The most notable feature of the tilt and propeller motors is the small, high frequency variation in the reference signals. This is a result of the matrix pseudoinverse and inverse tangent functions present in the wrench mapper and inverse kinematics scheme. While these inversions are relatively well-behaved for small angles, they can become very sensitive near singularities and lead to violent divergence of the closed-loop system.

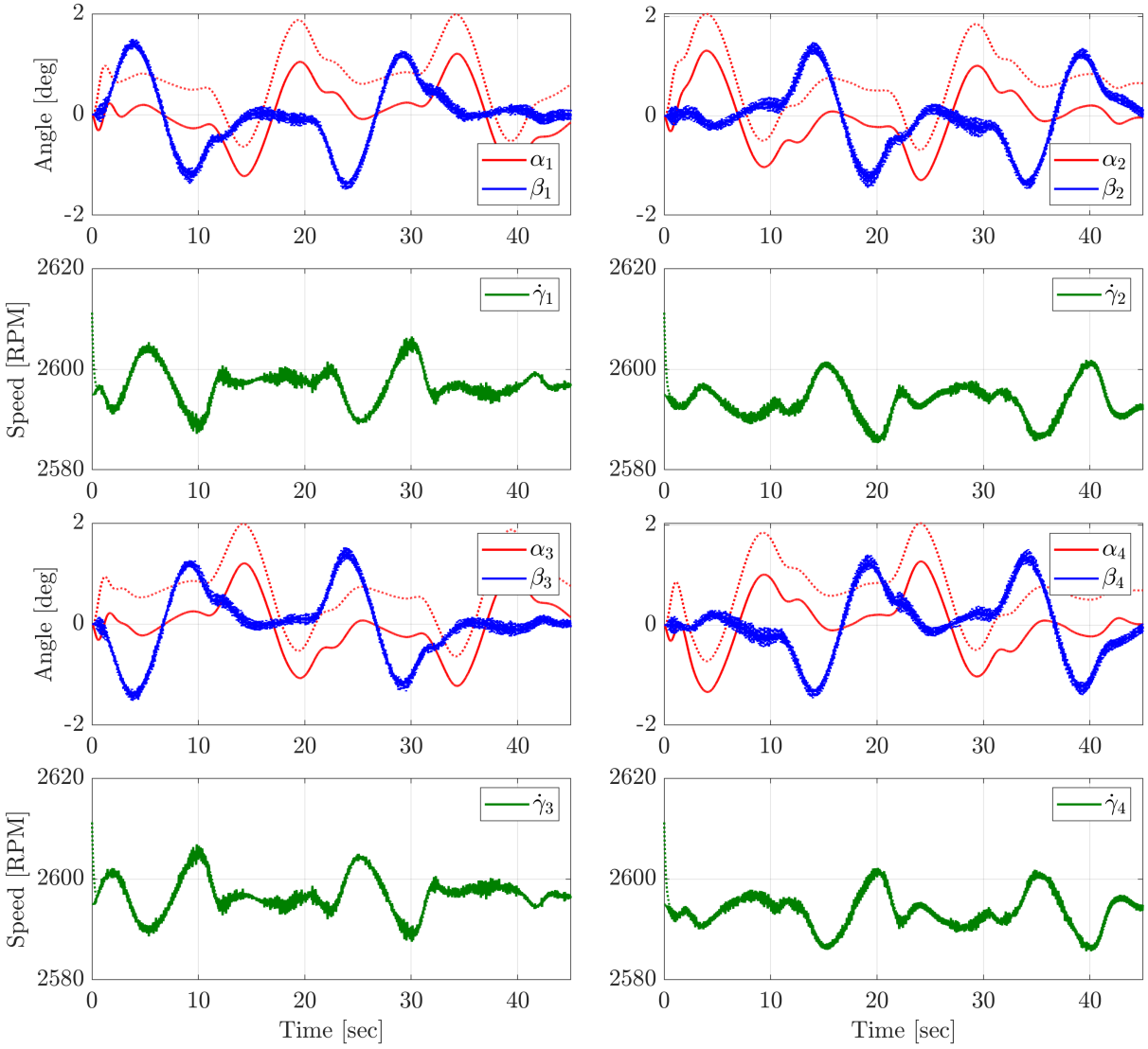

Figure 5.11: Simulated arm behavior associated with the position trajectory shown in Fig. 5.9. The near constant offset in the twist angles is due to the true location of the arm centers of mass, which lie slightly offset from the twist axes. Small, high frequency variations are visible in the set-points for both the tilt and propeller motors due to the matrix pseudoinverse in the wrench mapper and the inverse tangent functions in the inverse kinematics scheme.

Chapter 6

Conclusion

This work aimed to design a control architecture for the twist-tilt copter which could track arbitrary position and attitude trajectories in 3D space. The copter was modeled as four identical arm assemblies each composed of an arc, shaft, and propeller, all attached to a base link. General approximations were made about the centers of mass for the various bodies, namely that the centers of mass all lay at fixed distances along various motor axes due to symmetry. This greatly simplified the system dynamics by eliminating many possible Coriolis terms and other couplings between translational and rotational motion. These assumptions well approximate the real system, which was designed with such symmetries in mind.

A simulation was developed in Simscape Multibody for conducting virtual experiments on the twist-tilt copter. The simulation is built using an imported CAD assembly connected by specified joints. Inertial properties are extracted directly from the CAD files and therefore do not conform to the approximations made for modeling purposes. The equations of motion are formulated and solved within the software, completely uninfluenced by the equations derived in this paper. Actuator torque limits were also included to better approximate the mechanical behavior of the true system. This platform then serves as an independent basis for all control design and validation.

The control design problem was first approached for a single arm under the assumption that the base link was fixed to ground, leaving three degrees of freedom to be controlled.

Three independent LQR controllers were designed based on highly simplified linear models for each arm motor, treated as decoupled single-input-single-output systems. While the independent controllers performed well in isolation, tracking performance suffered when multiple motors were active simultaneously. Thus a more thorough modeling approach was deemed necessary for control design, one which could capture the nonlinear couplings between the three motor axes.

To derive the coupled equations of motion for a single arm on a fixed base, a Lagrangian formalism was applied with the three motor angles as the generalized coordinates. One valuable simplification was that the angular velocity of the propeller motor is several orders of magnitude greater than the angular velocities of the twist and tilt motors. The expression for the kinetic energy of the propeller could then be well approximated solely by the component due to $\dot{\gamma}$ rotation, eliminating many terms which would complicate the ensuing partial derivatives. This not only simplified the final equations of motion by removing some negligible centrifugal and Coriolis effects but also eliminated dependence on the rotor angle entirely, a critical feature for implementation where measuring the position of a fast moving rotor is impractical. Generalized forces were evaluated for each coordinate by projecting the various end-effector torques, applied motor torques, and internal gyroscopic torques onto each axis.

Evaluating the partial derivatives and assembling the Euler-Lagrange equations resulted in a system of coupled nonlinear equations including the remaining centrifugal, Coriolis, and gyroscopic coupling effects. The system satisfied known relationships pertaining to symmetries and definiteness of the matrix terms. A sample trajectory was then prescribed to the Simscape model to test the predictive accuracy of the derived equations of motion. Despite the approximations made for modeling purposes, the equations of motion reproduced the motor torques generated in simulation almost identically, affirming the accuracy of the derived model.

The same LQR framework used for the decoupled SISO control designs was applied to the coupled equations of motion to synthesize a single MIMO controller for the trajectory

tracking of the arm subsystem. The state and control tuning weights were selected to be identical between the SISO and MIMO implementations so that comparison between the two was as direct as possible. The resulting MIMO controller successfully maintained tracking performance of each motor axis even during simultaneous motions, compensating for the nonlinear couplings with feedback linearization and demonstrating the potential benefits of a thorough model-based control design for the full copter.

The dynamic model was next generalized to cover all four arm subsystems and allow for 3-DOF rotation of the base link, increasing the number of generalized coordinates to 15. Derivation of a general system of 15 coupled equations of motion may be nearly intractable, however the physical construction of the twist-tilt copter led to a simplified structure; the dynamics of each arm are dependent on the coordinates of that arm as well as the coordinates of the base, but are independent of the three other arms. The resulting inertia matrix and coupling matrix are thus mostly block diagonal, containing zeros in the elements which would relate any two arms, and with the remaining blocks related by simple substitutions due to symmetry. In addition, most of the quadratic velocity terms were deemed negligible compared to the gyroscopic effects of the propellers, which appear in every row of the equations and dominate the dynamics. The predictive accuracy of the new model was then evaluated using the same approach as the single arm model: prescribing a simulated trajectory and comparing the expected motor torques with the measurements from simulation. Despite many approximations and neglected dynamics, the derived equations of motion successfully reproduced the required motor torques to within the necessary accuracy for control design, even for a trajectory which overemphasized the neglected effects.

While the matrix equation of motion for the full copter with base rotation was similar in form to the matrix equation for a single arm with fixed base, a key difference is that the base rotation coordinates did not include a dedicated motor input and thus could not be controlled with the same LQR structure from previous chapters. The hierarchical control model introduced in [17] was then modified and applied to the coupled equations

of motion. Both the high-level rigid body controller and the low-level motor controllers were replaced by a single centralized control law based on the existing LQR framework. Torque commands for the arm coordinates were sent directly to the relevant motors, while the torque command for the base link was converted through a least-norms and inverse kinematics scheme to a set of desired set-points for the arm coordinates, fed back to the controller as arm trajectories. Use of least-norms leveraged the overactuated nature of the twist-tilt copter to realize a desired control wrench with a set of propeller thrusts having minimal Euclidean norm, equivalent to minimizing conflicting thrust components between arms.

The tracking performance of the modified hierarchical control scheme was tested on two variants of an attitude trajectory composed of sequential yaw-pitch motion or yaw-roll motion. In both cases the copter attitude successfully followed the trajectory within a satisfactory error envelope of a few degrees. Coupling between the roll and pitch axes was visible as a dual oscillation with identical frequency and constant phase offset. The behavior was consistent with control of a spinning top, a good approximation for the twist-tilt copter when all arm angles remain near constant.

Finally, the dynamic model was generalized to allow for unconstrained motion of the base link, bringing the number of generalized coordinates to 18. The choice of coordinate frames and assumptions on the inertial properties resulted in position dynamics which were completely decoupled from the attitude dynamics, with the translational behavior under the influence of thrust and gravity being linear in the three base link position coordinates.

The hierarchical control model was expanded to include a separate LQI position controller. Tracking performance was then evaluated on two types of trajectories which showcase maneuvers of the twist-tilt copter that would be impossible on a traditional quadrotor: on-point rotation and level flight. In both cases, the copter tracks the specified trajectory while maintaining nominal levels in the unspecified coordinates. Furthermore, addition of position tracking as a second control objective has improved upon the

performance of the attitude controller in isolation. By favoring the commands from the position controller over those from the attitude controller, the generated set-points for the arms are more influenced by the well-behaved translational dynamics as opposed to the ill-behaved rotational dynamics, resulting in smoother overall motion. This confirms the development of a model-based controller for the twist-tilt copter which effectively tracks position and attitude trajectories in SE(3).

This work has focused on modeling and control of the twist-tilt copter itself, however the true utility of the twist-tilt architecture is in maneuvering through a complex environment and manipulating a potential payload. While the inertial approximations are appropriate for the copter, adding a payload could significantly offset the center of mass for the overall system, causing shifts in the attitude dynamics and coupling the position dynamics to the attitude. Future work on the applications of this platform must involve adapting the control architecture to tolerate massive payloads, either through explicit modeling of the shifted center of mass or through feedback methods such as disturbance-observer-based control.

Another area with potential for great improvement is the inverse kinematics scheme. Use of inverse trigonometric functions to calculate angular set-points is highly sensitive to noise and can lead to violent divergence near singularities. One potential solution is to make use of the extensive work on inverse kinematics developed for robotics. For example, Kajita et al. present a singularity-robust inverse kinematics scheme in [19] which is based on damped least-squares. Alternatively, the Euler-angle parameterization used in this work could be replaced by a quaternion representation, completely eliminating the potential for singularities but requiring rederivation of the equations of motion.

A final comment is made regarding implementation of the proposed control architecture. While the terms in the nonlinear control law are easy enough to program in low-level hardware, dependence on many trigonometric terms is computationally expensive and could limit the effective bandwidth of the system subject to computing constraints. Alternate representation in terms of quaternions has the benefit of eliminating trigno-

metric elements, but at the expense of a further expanded set of generalized coordinates. Another avenue could be to selectively linearize those elements of the dynamics which are slowly evolving and only employ nonlinear compensation for the elements which vary more rapidly. These concessions or others may prove necessary for implementation of a stabilizing controller on real hardware.

Appendix A

Simulation Parameters

The multibody simulation first described in Chapter 3 and used throughout this work is based on an imported CAD assembly with the following parameters.

Base link:

- Mass: $m_{\mathcal{B}} = 318.43 \times 10^{-3}\,\text{kg}$
- Center of mass: coincident with $\mathcal{B}$ frame origin
- Inertia: $\boldsymbol{I}_{\mathcal{B}} = \begin{bmatrix} 1437005.46 & 0 & 0 \\ 0 & 1437005.46 & 0 \\ 0 & 0 & 2729652.26 \end{bmatrix} \times 10^{-7}\,\text{kg}\,\text{m}^2$ in $\mathcal{B}$ frame

Arc:

- Mass: $m_{\mathcal{A}} = 339.21 \times 10^{-3}\,\text{kg}$
- Center of mass: $\boldsymbol{r}^{\mathcal{A}/\mathcal{B}} = \begin{bmatrix} 284.62 & 48.66 & -.01 \end{bmatrix}^T \times 10^{-3}\,\text{m}$ in $\mathcal{B}$ frame
- Length from $\mathcal{B}$ to $\mathcal{A}$ on twist axis: $\ell_{\mathcal{A}} = 284.62 \times 10^{-3}\,\text{m}$
- Inertia: $\boldsymbol{I}_{\mathcal{A}} = \begin{bmatrix} 13679869.50 & 2819764.95 & 314.00 \\ 2819764.95 & 3870659.52 & 73.24 \\ 314.00 & 73.24 & 17511408.70 \end{bmatrix} \times 10^{-7}\,\text{kg}\,\text{m}^2$ in $\mathcal{A}$ frame

Shaft:

- Mass: $m_{\mathcal{S}} = 220.47 \times 10^{-3}\,\text{kg}$
- Center of mass: $\boldsymbol{r}^{\mathcal{S}/\mathcal{B}} = \begin{bmatrix} 414.77 & 11.61 & 1.27 \end{bmatrix}^T \times 10^{-3}\,\text{m}$ in $\mathcal{B}$ frame

- Length from $\mathcal{B}$ to $\mathcal{S}$ on twist axis: $\ell_{\mathcal{A}} = 414.77\,\mathrm{m}$
- Inertia: $\boldsymbol{I}_{\mathcal{S}} = \begin{bmatrix} 1986082.91 & -416.87 & 2.19 \\ -416.87 & 39339.47 & -3249.96 \\ 2.19 & -3249.96 & 1993493.04 \end{bmatrix} \times 10^{-7}\,\mathrm{kg\,m^2}$ in $\mathcal{S}$ frame

Propeller:

- Mass: $m_{\mathcal{P}} = 49 \times 10^{-3}\,\mathrm{kg}$
- Center of mass: $\boldsymbol{r}^{\mathcal{P}/\mathcal{B}} = \begin{bmatrix} 414.78 & 0 & 28.59 \end{bmatrix}^T \times 10^{-3}\,\mathrm{m}$ in $\mathcal{B}$ frame
- Length from $\mathcal{S}$ to $\mathcal{P}$ on propeller axis: $\ell_{\mathcal{P}} = 28.59 \times 10^{-3}\,\mathrm{m}$
- Inertia: $\boldsymbol{I}_{\mathcal{P}} = \begin{bmatrix} 5162.11 & 0 & -6.57 \\ 0 & 57.81 & 0 \\ -6.57 & 0 & 5199.18 \end{bmatrix} \times 10^{-7}\,\mathrm{kg\,m^2}$ in $\mathcal{P}$ frame

Assumed aerodynamic coefficients:

- Thrust: $c_p = 9.14 \times 10^{-5}\,\mathrm{kg\,m}$
- Torque: $c_t = 4.04 \times 10^{-6}\,\mathrm{kg\,m^2}$

Maximum motor torques:

- Twist motor: $2.3520\,\mathrm{N\,m}$
- Tilt motor: $2.3520\,\mathrm{N\,m}$
- Propeller motor: $0.5968\,\mathrm{N\,m}$

References

[1] F. Ruggiero, V. Lippiellol, and A. Ollero, "Aerial manipulation: A literature review," *IEEE Robotics and Automation Letters*, vol. 3, no. 3, pp. 1957–1964, 2018. DOI: 10.1109/LRA.2018.2808541.

[2] R. Rashad, F. Califano, and S. Stramigioli, "Port-hamiltonian passivity-based control on se(3) of a fully actuated uav for aerial physical interaction near-hovering," *IEEE Robotics and Automation Letters*, vol. 4, no. 4, pp. 4378–4385, 2019. DOI: 10.1109/LRA.2019.2932864.

[3] M. Ryll, G. Muscio, F. Pierri, E. Cataldi, G. Antonelli, F. Caccavale, and A. Franchi, "6d physical interaction with a fully actuated aerial robot," in *2017 IEEE International Conference on Robotics and Automation (ICRA)*, 2017, pp. 5190–5195. DOI: 10.1109/ICRA.2017.7989608.

[4] G. Jiang and R. Voyles, "A nonparallel hexrotor uav with faster response to disturbances for precision position keeping," in *2014 IEEE International Symposium on Safety, Security, and Rescue Robotics (2014)*, 2014, pp. 1–5. DOI: 10.1109/SSRR.2014.7017669.

[5] D. Brescianini and R. D'Andrea, "Design, modeling and control of an omni-directional aerial vehicle," in *2016 IEEE International Conference on Robotics and Automation (ICRA)*, 2016, pp. 3261–3266. DOI: 10.1109/ICRA.2016.7487497.

[6] S. Rajappa, M. Ryll, H. H. Bülthoff, and A. Franchi, "Modeling, control and design optimization for a fully-actuated hexarotor aerial vehicle with tilted propellers," in

2015 IEEE International Conference on Robotics and Automation (ICRA), 2015, pp. 4006–4013. DOI: 10.1109/ICRA.2015.7139759.

[7] B. Crowther, A. Lanzon, M. Maya-Gonzalez, and D. Langkamp, "Kinematic analysis and control design for a nonplanar multirotor vehicle," English, *Journal of guidance, control, and dynamics*, 2011, ISSN: 0731-5090.

[8] S. Park, J. Lee, J. Ahn, M. Kim, J. Her, G.-H. Yang, and D. Lee, "Odar: Aerial manipulation platform enabling omnidirectional wrench generation," *IEEE/ASME Transactions on Mechatronics*, vol. 23, no. 4, pp. 1907–1918, 2018. DOI: 10.1109/TMECH.2018.2848255.

[9] D. Sanalitro, H. J. Savino, M. Tognon, J. Cortés, and A. Franchi, "Full-pose manipulation control of a cable-suspended load with multiple uavs under uncertainties," *IEEE Robotics and Automation Letters*, vol. 5, no. 2, pp. 2185–2191, 2020. DOI: 10.1109/LRA.2020.2969930.

[10] H.-N. Nguyen, S. Park, J. Park, and D. Lee, "A novel robotic platform for aerial manipulation using quadrotors as rotating thrust generators," *IEEE Transactions on Robotics*, vol. 34, no. 2, pp. 353–369, 2018. DOI: 10.1109/TRO.2018.2791604.

[11] L. Ruan, "Independent position and attitude control on multirotor aerial platforms," Ph.D. dissertation, University of California Los Angeles, 2020.

[12] S. L. Jae, D. Lee, J. Kim, D. Kim, I. Jang, and H. J. Kim, "Fully actuated autonomous flight of thruster-tilting multirotor," *IEEE/ASME Transactions on Mechatronics*, vol. 26, no. 2, pp. 765–776, 2021. DOI: 10.1109/TMECH.2020.2999586.

[13] M. Nigro, F. Pierri, and F. Caccavale, "Preliminary design, modeling and control of a fully actuated quadrotor uav," 2019, pp. 1108–1116. DOI: 10.1109/ICUAS.2019.8798092.

[14] M. Ryll, H. H. Bülthoff, and P. R. Giordano, "A novel overactuated quadrotor unmanned aerial vehicle: Modeling, control, and experimental validation," *IEEE Transactions on Control Systems Technology*, vol. 23, no. 2, pp. 540–556, 2015. DOI: 10.1109/TCST.2014.2330999.

[15] M. Kamel, S. Verling, O. Elkhatib, C. Sprecher, P. Wulkop, Z. Taylor, R. Siegwart, and I. Gilitschenski, "The voliro omniorientational hexacopter: An agile and maneuverable tiltable-rotor aerial vehicle," *IEEE Robotics Automation Magazine*, vol. 25, no. 4, pp. 34–44, 2018. DOI: 10.1109/MRA.2018.2866758.

[16] K. Bodie, Z. Taylor, M. Kamel, and R. Siegwart, "Towards efficient full pose omnidirectionality with overactuated mavs," *Proceedings of the 2018 International Symposium on Experimental Robotics*, pp. 85–95, 2020, ISSN: 2511-1264. DOI: 10.1007/978-3-030-33950-0_8.

[17] M. J. Gerber and T.-C. Tsao, "Twisting and tilting rotors for high-efficiency, thrust-vectored quadrotors," *Journal of Mechanisms and Robotics*, 2018.

[18] B. Siciliano, L. Sciavicco, L. Villani, and G. Oriolo, *Robotics Modelling, Planning and Control*, ser. Advanced Textbooks in Control and Signal Processing. Springer-Verlag London, 2009, ISBN: 978-1-84628-641-4.

[19] S. Kajita, H. Hirukawa, K. Harada, and K. Yokoi, *Introduction to Humanoid Robotics*, ser. Springer Tracts in Advanced Robotics. Springer-Verlag Berlin Heidelberg, 2005, pp. 63–65, ISBN: 978-3-662-50166-5.